Formation Mechanisms of Cockade Texture in Breccias and Their Relation to Similar Hydrothermal Mineral Textures

Levent Tosun

School of Earth and Ocean Sciences,

Cardiff University

Submitted in partial fulfilment of the requirements for the degree of

Doctor of Philosophy (PhD)

1983059

June 2024

Dedicated to the part of my youth and the thousands of coffee beans that fuelled this journey...

Acknowledgements

This thesis would not have been possible without the invaluable contributions of many individuals over the past four years. I would like to take this opportunity to express my deepest gratitude to all of them. This study was carried out with the sponsorship of the Turkish government. I thank the Turkish Ministry of Education (MEB) authorities and the Institute of Mineral Research and Exploration (MTA) for their financial support.

I am deeply grateful to my supervisor, Prof. Thomas Blenkinsop, for his unwavering patience, invaluable guidance, encouragement, and continuous advice throughout this PhD journey. Working with him has been an honour and a joy. I feel fortunate to have firsthand experience of how a caring and supportive mentor can truly make a difference, especially during challenging times.

I wish to express my gratitude to my examining committee members, Prof. Zoe Shipton and Dr. Katherine Daniels, for their valuable recommendations and constructive criticism. I would also like to extend my thanks to Dr Katie McFall and Dr James Lambert-Smith for their significant contributions to the fluid inclusion study and to Dr Alexandra Nederbragt for her analyses of carbon and oxygen stable isotopes. Additionally, I am deeply thankful to Mr. Anthony Oldroyd for his kind support during sample preparations. I would like to extend my gratitude to Akın Çil, a PhD student in the Department of Geological Engineering at Middle East Technical University, and his advisor, Assist. Prof. Dr. Ali İmer, for sharing the data from the Gicik field. In addition, I would like to thank Prof. Erdin Bozkurt, Head of the Department of Geological Engineering at Middle East Technical University, and Assoc. Prof. Dr. Fatma Toksoy K., Deputy Head of the Department, for opening the doors and facilities of METU, which I can call my second home. Lastly, I am deeply grateful to Dr. Özcan Dumanlılar for his support during my doctoral scholarship application process.

I am incredibly grateful to my friends in the UK, MD Ruhal Yetişir and Veysel Bozan, and my housemates Faisal and Sam, for their endless patience with my grumpiness and for always being there to answer my countless (and sometimes insane) questions. And, of course, to the Güneş family, I can't thank you enough for your unwavering support over the past four years. I'm so lucky to have you all in my life. I am deeply grateful to Mustafa Kaplan, who has taught me so much, not just during this study but throughout my life. When he told me, "I am by your side no matter what happens," it was the moment I began to truly believe in myself and my ability to complete this work. I am incredibly thankful to Zehra Deveci Aral for her unwavering and cheerful friendship throughout this journey. Her ability to bring a smile to anyone's face

is truly special. I am certain that we will continue to share many wonderful experiences together as we move forward in our careers.

I want to express my deepest gratitude to my long-time friends who have been my anchor during this challenging journey: Ezgi Özten K., M. Bedirhan Koyuncu, Hilal Doğanülker B., Abidin U. Yücel, M. Anıl Payan, N. Anıl Üçer, Deniz Dündar M., Merve Özköse E., Gökhan Özdemir, and Rıdvan Yıldırım. Your support has kept me grounded. I also want to extend special thanks to the Kaymakcı and Ertepınar family and Meryem Dilan İnce for opening their home to me and believing in me throughout this journey. Endless thanks to Gökçe, who came into my life during a pretty challenging stretch of this journey and has stood by my side with steady love and support, and to Mr. TJ, our grumpy and old companion, who has been an irreplaceable part of our little world.

Finally, I want to express my deepest and most profound gratitude to my parents, Haydar Tosun and Zekiye Karakoç T. . Their endless sacrifices have been the cornerstone of my journey. This thesis is not just a culmination of my efforts; it is a testament to their belief in me, which has given me the strength to overcome every challenge and persevere.

'Pluralitas non est ponenda sine necessitate.'

Ockham's Razor

Abstract

Cockade texture refers to a fault-infill breccia texture, where individual core clasts are surrounded by concentric layers of cement and/or fine-grained sediment infill, with the central clasts remaining separated from one another. Cockade textures are commonly found in fault zones, where fracturing and subsequent fluid flow create open spaces for their development. Understanding their formation mechanisms is essential for improving interpretations of fault-controlled hydrothermal systems and their associated mineralisation processes.

Cockade textures have been widely used to infer sequential geological events, including mineralisation processes in vein-type deposits and, more recently, seismic cycles in paleoearthquake studies. However, their use in interpreting temporal sequences of events depends on the assumed formation mechanisms. Models such as suspension in fluid and rotation-accretion propose that cockade textures develop under dynamic fluid conditions driven by episodic deformation. In contrast, the force of crystallisation model suggests that cockade textures can form in static fluid environments without requiring seismic activity, implying that they do not necessarily record deformation-driven geological events. Additionally, partial metasomatic alteration, involving recrystallisation and replacement, plays a key role in modifying their final structure, further complicating their interpretation in sequential geological event reconstructions. These uncertainties highlight the need for a comprehensive evaluation of cockade formation mechanisms before using them to infer deformation history or mineralisation processes.

This study investigates the formation of cockade textures in cement-dominated breccias, addressing two primary objectives: (1) to examine how well existing theories explain why the central fragments of cockades remain separated, considering the assumptions and identification criteria of proposed mechanisms, and (2) to assess the reliability of cockade textures as proxies for interpreting temporal sequences of events, such as syntectonic mineral precipitation in vein-type deposits and seismic cycles in paleoearthquake studies. The research incorporates findings from two contrasting geological settings: Oxwich in Gower (South Wales), a carbonate-dominated system, and the Gicik low-sulphidation epithermal Au deposit in Ankara (North-Central Anatolia, Turkey), a silica-dominated system. These sites provide a valuable framework for evaluating the interplay of different formation mechanisms under varying lithological and fluid conditions, offering a more comprehensive understanding of cockade texture development.

To test the validity of these formation models, this study integrates field observations, microscopic analyses, fractal dimension analysis, fluid inclusion microthermometry, and stable isotope geochemistry. Field and petrographic evidence does not support the suspension in fluid mechanism, as the conditions required for sustained clast movement in rapidly ascending hydrothermal fluids were absent at both localities. The rotation-accretion model is partially supported by local truncations on the rims, suggesting episodic movement; however, no conclusive evidence indicates that the central fragments underwent significant rotation or shearing. In Oxwich, geopetal structures within central fragments confirm that they remained in their original orientations, while in Gicik, no evidence suggests relative rotation between the clasts. The role of partial metasomatic alteration is evident at both sites, with recrystallisation and replacement textures observed in carbonate-dominated Oxwich veins and silica-dominated Gicik veins.

These findings indicate that central fragments, which remained unrotated, were progressively enclosed by successive rim layers. In Oxwich, the well-defined overgrowth faces of these rims suggest that fracture opening and rim precipitation occurred gradually, with mineral growth sustained by a solution film consistently present between rim crystals. This implies that the force of crystallisation mechanism was capable of separating the central fragments without requiring repeated hydrofracturing associated with seismicity following initial faulting. At Gicik, an alternative explanation for the separation of clasts, which can result in cockade textures in breccias within low-sulphidation epithermal systems, is the infiltration and subsequent precipitation of highly viscous silica gel-like hydrothermal solutions into a fracture system.

Quantitative fractal dimension analysis reveals a progressive decrease in complexity from the central fragments to the outermost rims, supporting the hypothesis that cockade textures developed through open-space precipitation. In Oxwich, fluid inclusion microthermometry and stable isotope analyses provide further constraints on the palaeo-fluid conditions responsible for cockade formation. The homogenisation temperatures (155°C–285°C) from carbonate rims are consistent with previously documented cockade textures, while stable carbon and oxygen isotope values indicate a marine carbonate source with no evidence of magmatic fluid mixing. However, pervasive recrystallisation likely altered the isotopic composition, suggesting that the measured geochemistry reflects post-depositional processes rather than primary fluid signatures. Additionally, the similarity between cockade textures and oolites, where both central fragments and ooids remain separated by cement growth into open space, further supports the force of crystallisation mechanism as a viable explanation for fragment separation without requiring seismicity.

These findings underscore the complexity of cockade texture formation, emphasizing that no single mechanism can fully explain their development. While suspension in fluid and rotation-accretion models are widely accepted and often used as frameworks for interpretation, strictly adhering to their underlying assumptions may lead to overgeneralised or misleading conclusions. Cockade textures can form through various interacting processes, including force of crystallisation, open-space precipitation, and secondary alterations such as recrystallisation and replacement, all of which may contribute to their final structure. Recognizing the interplay of these mechanisms is essential for accurate geological interpretations. Future research should focus on quantifying the relative contributions of these mechanisms under varying geological conditions to refine the use of cockade textures as indicators of deformation history and hydrothermal activity.

Table of Contents

List of Figures

List of Tables

List of Appendices

Glossary

Amorphous Silica Types: Variations in silica texture indicative of different depositional environments in hydrothermal systems

Moss: Fine, delicate silica texture resembling moss, typically formed under rapid cooling conditions in hydrothermal systems.

Massive: Dense, structureless silica with no visible internal texture, indicating uniform precipitation.

Zonal: Silica displaying distinct compositional or textural bands, reflecting episodic or cyclic deposition.

Comb: Silica crystals that grow with elongated, parallel arrangements resembling a comb.

Colloform: Silica with concentric, layered textures, indicative of low-temperature precipitation.

Crustiform: Layered silica with contrasting composition or texture, commonly formed in hydrothermal veins.

Quartz Textures: Indicative of quartz recrystallisation and hydrothermal growth.

Mosaic: Interlocking, equant grains of quartz, forming a uniform texture.

Feathery: Delicate, wispy formations associated with rapid growth or recrystallisation.

Ghost Sphere: Rounded inclusions or outlines within quartz, indicating earlier growth interruptions or replaced phases.

Plumose: Feather-like quartz textures formed during deformation, indicative of dynamic recrystallisation.

Replacement Textures: Textures indicative of mineral replacement processes during hydrothermal alteration

Pseudo Bladed: Blade-like forms retained after replacement of an earlier mineral phase.

Pseudoacicular: Needle-like forms preserved through replacement processes.

Lattice Bladed: Intersecting, blade-like structures indicative of specific geochemical replacement conditions.

Ghost Bladed: Faint blade-like structures, remnants of partially replaced original minerals.

Parallel Bladed: Blade-like textures aligned parallel to structural or depositional controls.

Adularia: A low-temperature K-feldspar typically associated with epithermal systems

Authigenic Mineral Reactions: Reactions within a system leading to the formation of new mineral phases from pre-existing minerals

Botryoidal texture: A mineral texture resembling a cluster of grapes, commonly seen in chalcedony.

Cataclasite: A brittle fault rock formed by mechanical fragmentation.

Cockade texture: A concentric texture in breccia, formed by mineral precipitation around clasts.

Epithermal: A type of hydrothermal deposit formed at shallow depths and low temperatures.

Gangue Mineral: Non-valuable minerals that occur with ore minerals in a deposit.

Geopetal Infills: Sedimentary structures that indicate the original orientation of depositional layers in a sedimentary rock sequence.

Grain Elutriation: The process of separating finer particles from coarser ones through fluid flow, often in sedimentary environments.

Interstitial: Material occupying the space between larger grains or crystals.

Isochore: A line on a diagram representing constant volume conditions.

Mammillary: A mineral habit characterised by smooth, rounded protuberances.

Metastable: A state of a mineral or system that persists outside its equilibrium conditions.

Monomictic: A conglomerate or breccia composed of clasts of a single rock type.

Mylonite: A foliated fault rock formed under ductile shear conditions.

Polymictic: A conglomerate or breccia composed of clasts of multiple rock types.

Prophyllitic Alteration: Hydrothermal alteration characterised by chlorite, epidote, and pyrite, often in the peripheral zones of a deposit.

Pseudotachylite: A glassy or very fine-grained fault rock formed by frictional melting during seismic events.

Reniform: A mineral habit resembling a kidney shape.

Size Grading: A vertical change in grain size within a sedimentary layer, often indicative of depositional energy variations.

Sulphidation: A chemical reaction involving sulfur, critical in mineralisation processes.

Chapter 1: Thesis Overview

1.1 Introduction

Fault zones function as high- or low-permeability pathways controlling subsurface fluid flow, and studying these zones provides essential insights into deformation processes in the upper crust (e.g. Caine et al., 1996; Sheldon and Micklethwaite, 2007; Faulkner et al., 2010). Microstructural, mineralogical, and geochemical characteristics of these zones can provide detailed information about episodic events along fault structures and the history of hydrothermal fluids. Understanding these processes is crucial for reconstructing past tectonic activity, evaluating mineralisation systems, and assessing fluid migration pathways in fault-controlled reservoirs. This study focuses on the formation of cockade texture, a specific fault breccia infill texture. In economic geology, cockade textures have been studied as indicators of mineralisation sequences (Leroy et al., 2000) and syntectonic mineral growth (Van Alstine, 1944; Genna et al., 1996), providing a basis for correlating mineralisation with deformation. More recently, they have also been used in paleoearthquake research as potential records of seismic cycles (Berger and Herwegh, 2019; Masoch et al., 2019). Although these structures are widely recognised as important records of fluid-rock interaction, their formation remains poorly understood, with ongoing debate over the relative roles of different mechanisms and the conditions under which they develop. Investigating cockade textures offers a means to better understand fault-controlled fluid dynamics, hydrothermal ore deposition, and the structural evolution of deformation zones, making them a key subject in structural geology, economic geology, and fault zone research.

Cockade texture, a subtype of crustiform vein texture (Dong et al., 1995), is typically associated with open-space filling processes (Perelló, 1994), where successive mineral growth forms concentric rims around a central fragment. Cockade breccia, or cockade texture-bearing breccia, consists of polymictic or monomictic fragments mantled by successive overgrowths of vein material, with interstitial phases that may include sulphide, oxide, quartz, and carbonate minerals (Genna et al., 1996; Jébrak, 1997; Leroy et al., 2000; Frenzel and Woodcock, 2014; Blenkinsop et al., 2020). Core fragments may include wall rock, veins, or vein breccias, reflecting the reworking of hydrothermal and tectonic breccias formed earlier in the evolution of the vein system. These breccias are generally cement-supported, with crustiform overgrowth rims in contact with one another, while core fragments remain separated. Additionally, they may contain stratified void-filling sediments and geopetal infills (Frenzel and Woodcock, 2014) with varying abundances of chalcedony or well-developed cement minerals, as observed infilling the spaces between cockade fragments (e.g. Gillespie et al., 2011; Gülyüz et al., 2018) (Figure 1).

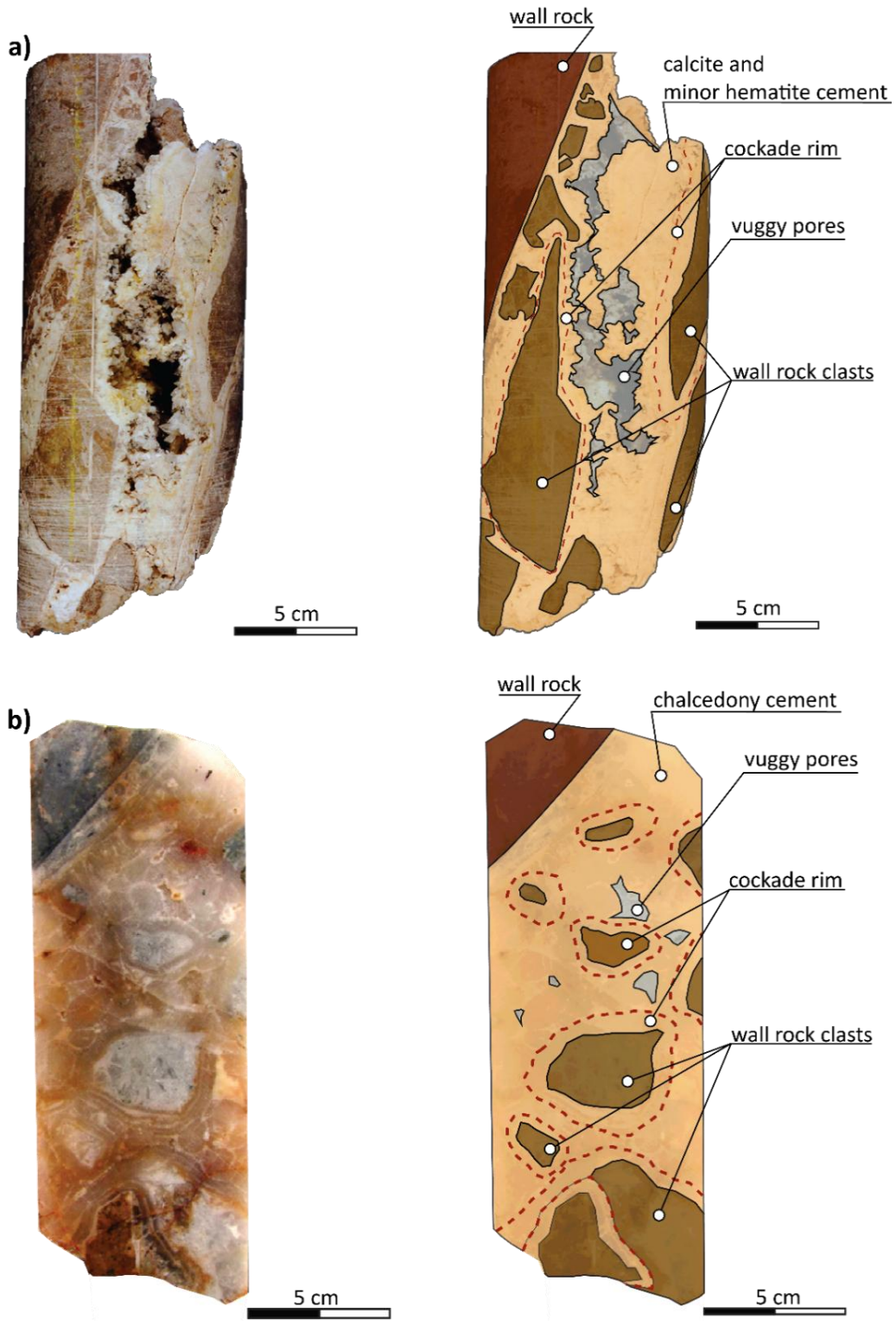

Figure 1: Example of fault infill cockade textures in boreholes; a) borehole core shows the cockade textures in a fault breccia with carbonate cement from Sellafield, Cumbria, UK (Gillespie et al., 2011); b) borehole core shows the cockade textures in a fault breccia with calcedony cement from Kestanelik Epithermal Gold Mine, Çanakkale, Türkiye (Gülyüz et al., 2018).

Since cockade textures were identified in a Pb-Zn-Ag vein in Germany (Weissenbach, 1836), they have been documented in many vein-style mineralisations, particularly in epithermal type deposits, which developed in near-surface environments (Sillitoe, 1985; Laznicka, 1989; Genna et al., 1996; Frenzel and Woodcock, 2014; Cox and Munroe, 2016). Veins in epithermal districts typically form late in the displacement history of the host faults when the faults have achieved maximum connectivity and structural permeability (Blenkinsop et al., 2020). While varying by district, common vein-filling textures in low- and intermediate-sulphidation veins comprise open space-filling hydrothermal textures, such as cockade, crustiform, colloform, and comb textures, and late carbonate replacement textures, such as lattice bladed textures (Dong et al., 1995). Among them, due to their concentric banding of mineral cement around breccia clasts, cockade texture may record characteristics of successive episodes of hydrothermal fluid flux and episodes of brittle deformations in syntectonic mineralisations (Genna et al., 1996; Leroy et al., 2000).

According to Genna and coauthors (1996), ore deposition occurs throughout the structural evolution in a pulsating manner, involving fracturing, mineral deposition, and fragment rotation. The growth of concentric rims in cockade texture depends on factors such as fluid pressures, local structural conditions, and the volume of newly formed materials within the hydrothermal channel. Therefore, the gradual formation of cockades reflects a pulsating mechanism of fluid addition within the slowly opening channel. Leroy's mineralogical and fluid-inclusion-based study on Mn-rich breccias from low-sulphidation epithermal gold deposits in Cirotan (Indonesia), Orcopampa (Peru), and Cavnic (Romania) reveals that the concentric rims of cockades, comprising ore and gangue minerals, can help in subdividing deposition sequences. This mineralogical zonation depicted by cockades provides insights into the general evolution of the depositional process over time.

Cockades have recently been the focus of palaeo-earthquake research because they may be related to seismic cycles (Berger and Herwegh, 2019; Masoch et al., 2019). According to those studies, the rims around core clasts are notably susceptible to chemical and mechanical variations in hydrothermal fluids, and they may relate to specific precipitation conditions, allowing the investigation of various phases of seismic cycles. According to Cox and Munroe (2016), injection-driven swarm seismicity, rather than mainshock-aftershock seismicity, is associated with the formation of cockade texture due to the characteristic response of host rock to fluid-rock interaction resulting in crack-seal vein textures by the episodic injection of over pressured fluids into fault zones.

All the proposed mechanisms for the formation of cockades need to find an explanation for the peculiar appearance of the texture: the core clasts do not touch each other. Although there is no clear consensus on the mechanisms involved in their formation, the general view among the most likely proposed mechanisms is that syntaxial crystallisation of infill into open, filled spaces occurs. This means that the rims surrounding the core clasts form in situ growths resulting from different mechanisms as follows.

Six mechanisms (Figure 2) promoting the cockade texture formation were identified by (Frenzel and Woodcock, 2014): (1) cut effect (Posepný, 1895; Taber, 1918), (2) infall of clast during cementation (Kutina and Sedlackova J., 1961), (3) Partial metasomatic replacement of clast minerals (Bateman, 1924; Bastin, 1925; Kutina and Sedlackova J., 1961; Rieder, 1969), (4) sustained suspension of clast due to rapidly ascending fluids(Farmin, 1938; Jobson et al., 1994; Cox and Munroe, 2016), or because of high viscosity or density of the fluid (Spurr, 1926; Dill and Weber, 2010), (5) repeated rotation and accretion of cockade clast due to repeated fracturing (Van Alstine, 1944; Kutina and Sedlackova J., 1961; Genna et al., 1996), and (6) crystallisation pressure exerted on the crystals during rims growth (Von Weissenbach, 1836; Cotta, 1859, 1870; Beck, 1903; Teber, 1918; Lingern, 1919; Bastin, 1925). Among the six proposed mechanisms, recent studies have largely focused on four (partial metasomatic replacement, clast suspension in ascending fluids, repeated rotation and accretion, and crystallisation pressure), while the cut effect and clast infall models are now considered less viable, as they do not align with the defining characteristics of cockade textures. Notably, these formation mechanisms reflect distinct geological environments and fluid conditions. Models such as clast suspension in fluids and repeated rotation-accretion suggest that cockade textures develop under dynamic fluid conditions driven by episodic deformation, which may be linked to seismic activity. Conversely, the crystallisation pressure model implies that cockade textures can form in static fluid environments, independent of deformation, meaning that they do not necessarily record tectonic events. Additionally, partial metasomatic alteration can overprint or modify primary structures, adding another layer of complexity to their interpretation in reconstructing geological histories. These variations underscore the importance of evaluating formation mechanisms carefully before using cockade textures as indicators of deformation history or mineralisation processes.

Despite the extensive study of cockade textures in both economic geology and paleoearthquake research, their formation mechanisms remain debated, particularly regarding the interplay of different processes under varying geological conditions. This study aims to address these uncertainties by systematically evaluating the proposed formation mechanisms using a combination of field observations, microstructural analyses, fluid inclusion microthermometry, stable isotope geochemistry, and fractal dimension analysis.

thin

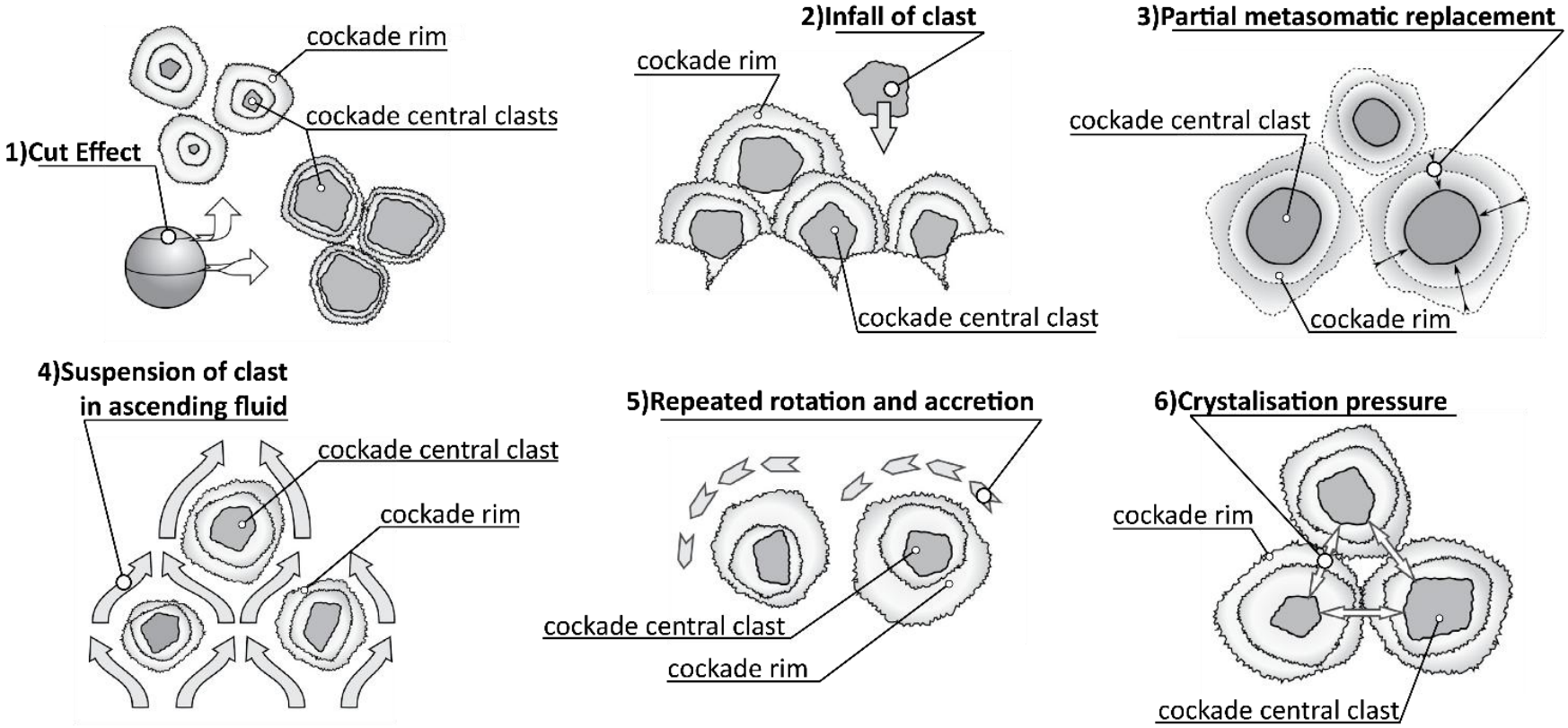

Figure 2: The six main hypotheses promoting the formation of cockade texture; 1) cut effect; 2) infall of clast; 3) partial metasomatic replacement of clast; 4) suspension of clast in ascending fluid; 5) repeated rotation and accretion; 6) crystallisation pressure (Frenzel and Woodcock, 2014).

1.2 Field Locations

Two field locations have been studied to test the previously proposed formation mechanisms of cockade texture. These are Oxwich in Gower (South Wales) (Figure 3 a) and Gicik low sulphidation epithermal Au deposit in Ankara (North-Central Anatolia, Turkey) (Figure 3 b). These locations host cockade textures of different ages and tectonic environments and provide comparisons of varying sizes and mineralogy of cockades. The selected locations provide interesting case studies for the following reasons:

Oxwich in Gower (South Wales)

- Extensive exposures of well-developed cockade texture are accessible, especially during low tide along the coastline.
- A comprehensive review, including the six proposed mechanisms promoting the cockade formation, was conducted by Frenzel and Woodcock (2014) in the same location. Their field-based observations and interpretations provide useful constraints for understanding the most likely formation mechanisms of cockade textures and for testing the favoured mechanisms of this study.
- Previous studies, including well-documented field observations and thermochronology in the same veins investigated in this study (Ault et al., 2016; Wright et al., 2009), provide useful constraints during fieldwork and the interpretation of fluid inclusion and stable isotope data.

Gicik low sulphidation epithermal Au deposit in Ankara (North-Central Anatolia, Turkey)

- Extensive exposures of well-developed cockades with other epithermal textures are accessible in the field. Due to the economic importance of the texture, this location provides useful data for investigating cockade in terms of mineralisation.
- The area has recently been studied in a M.Sc. Thesis (Çil, 2019), and petrography samples from the thesis are available for microscopical analyses, which is useful for enlarging the sample database used in this thesis.

Figure 3: a) View from Horton, east, to Porth-Eynon Bay, west, in Gower (South Wales) (417205 E, 5711550 N); b) View from southwest to Gicik low sulphidation epithermal Au deposit in Ankara (North-Central Anatolia, Turkey) (496910 E, 4428300 N). (Datum: WSG84 UTM Zone)

1.3 Aims and Objectives

The primary aim of this thesis is to address two reasons why cockade texture is of considerable geological interest, particularly for economic hydrothermal mineralisation. The first reason arises from the challenge of explaining how it forms, and especially the mechanisms resulting in the central fragments, surrounded by rims, not coming into contact with each other. Although competing mechanisms have been proposed to overcome that paradox, there is still no consensus. The second reason is based on the concept that the concentric rims around the fragments are formed by intermittent processes, and they can be used to reveal the temporal relationship of sequential geological events, such as fluid flow in epithermal mineralisation and seismic cycle determinations. However, without fully understanding the factors involving their formation and considering the possibility that the mechanisms could be effective simultaneously, there is a high likelihood of encountering significant contradictions in the temporal relationships of events inferred from the rims. This assessment is based on observations made in the Oxwich locality, where carbonate-dominated cockades are developed, and the Gicik locality, where silica-dominated cockades are developed.

1.4 Thesis Structure

This thesis is organised into seven chapters.

Chapter 1 is an introduction to the thesis, which includes a summary of approaches to study, field locations, aims and objectives, and an overview of the thesis structure (this chapter).

Chapter 2 reviews available literature outlining cockade texture and its accompanying hydrothermal textures, breccia classification, research on the formation of cockade textures, and the concept of the force of crystallisation with examples of the resulting geological processes.

Chapter 3 reviews the geological overviews of the aforementioned selected locations.

Chapter 4 reports the field observations, structural measurements, and mapping.

Chapter 5 reports the microstructural analyses, including thin section examinations, fractal dimensions of cockade samples from the selected locations, and a database created from previously published papers.

Chapter 6 presents and discusses fluid geochemistry with fluid inclusion and stable isotope results.

Chapter 7 presents and discusses the formation mechanisms of cockade texture in Oxwich and Gicik based on the findings in previous chapters.

Chapter 8 is a summary of the major findings. Responses to hypotheses are presented, and suggestions for further research are made.

The appendix files contain supporting information. The appendix includes all data used in the analysis and examples of calculations and software procedures used in chapters 4-5-6.

Chapter 2: Fault Infill Cockade Texture and Force of Crystallisation Review

This chapter provides an in-depth examination of cockade texture, fault breccia classification, and the concept of crystallisation force. The review of cockade texture, which has garnered significant interest among geologists over the years, encompasses three main aspects: (i) the nomenclature and identification of cockade texture-bearing breccias at both outcrop and hand-specimen scales, (ii) previously proposed formation mechanisms with their underlying assumptions, and (iii) their current applications in the field. Accurately identifying cockade textures and their components is crucial to ensuring a consistent nomenclature and preventing misclassification. Additionally, a critical review of past studies provides insight into the assumptions underlying different proposed formation mechanisms. The review of hydrothermal textures aims to provide insight into the formation conditions and spatial distribution of associated mineral textures. The review of fault breccia classification summarises the criteria used in different breccia classification schemes and evaluates why existing schemes may be insufficient for classifying breccias containing cockade textures. The concept of crystallisation force (or crystallisation pressure) encapsulates various geological processes influenced by the force exerted during crystal growth. It represents one of the earliest proposed mechanisms for cockade texture formation and provides an alternative perspective compared to other commonly accepted mechanisms, as it depicts a static fluid environment rather than dynamic fluid flow conditions. This review highlights the need to reassess the crystallisation force mechanism, which has often been overlooked or underemphasised, and underscores its potential importance in explaining cockade texture formation.

2.1 Formation of Cockade Texture-A Review

Cockades, cockade texture, cockade breccias, spar balls or ring ore are all referred to as a fault-fill texture in which clasts are completely surrounded by spheroidal hydrothermal overgrowth rims (Adams, 1920; Bastin, 1950; Kutina and Sedlackova, 1961; Genna et al., 1996; Leroy et al., 2000; Frenzel and Woodcock, 2014; Cox and Munroe, 2016). Cockade texture is of considerable interest due to its distinctive concentric rim bands, which can provide insights into fluid flux variations and their potential relationship with episodic deformation. However, the interpretation of these textures as direct indicators of deformation history depends on the assumed formation mechanisms. Among the various proposed models, suspension in fluid and rotation and accretion are widely accepted as the primary mechanisms responsible for cockade texture formation. Both models suggest that cockade textures develop in dynamic fluid environments, where episodic fluid movement and deformation events play a key role in their growth. In contrast, the force of crystallisation model proposes a static fluid environment, implying that cockade textures may not necessarily record deformation-driven processes. Additionally, partial metasomatic alteration, involving recrystallisation and mineral replacement, can modify the original structure of cockade textures, potentially overprinting primary growth features and complicating their use in geological reconstructions. Understanding these formation mechanisms is therefore essential for accurately deciphering the sequence of geological events and fluid-rock interactions in fault zone evolution during both seismic and non-seismic periods.

Cockade texture was first defined as concentric crustiform bands surrounding isolated fragments of wall rocks or early vein materials in breccias (Adams, 1920; Spurr, 1926). Dong and coauthors (1995) classified them as a subtype of crustiform texture, which is a primary growth into the open space and characterised by successive, narrow (up to a few centimetres), subparallel bands distinguished by the difference in texture, mineral proportions, and colour. As the cockade texture became an interest for economic geologists and they were mostly found in breccias in epithermal deposits (Genna et al., 1996), the term cockade breccia began to be used interchangeably with the term cockade texture. Frenzel and Woodcock (2014) discussed this issue regarding nomenclature and the classification of the faults that contain cockade texture, and they suggested that the term “cockade breccia” is a pragmatic choice that was unlikely to be misunderstood. The problem arising from the classification of cockade texture-bearing breccias will be discussed in the fault breccia classification section of Chapter 2.

An individual cockade texture comprises two components: the central clast and the rims (Figure 4). Central clasts can directly originate from the wall rock hosting the vein or from pieces of vein material previously

formed and refractured by episodic deformation. Their shapes can vary from angular to sub-rounded, depending on physical and chemical factors such as transportation or rotation in veins, internal rock chemistry, and the fluids they interact with. The rims may form in two ways: by growing crystalline material into an open space, characterised by sharp boundaries with the central clast or former cement generations, or by partial metasomatic replacement of the central clast minerals characterised by progressive, gradual contact due to fluid-rock interaction. The crystalline rims can exhibit different textures (e.g., cryptocrystalline, blocky, or fibrous) and compositions (e.g., quartz, calcite, or ore minerals), depending on a combination of factors including temperature, pressure, pH, and chemical composition of the fluid, as well as the growth rate of the minerals (Jourdan et al., 2009). The rim formed by inward partial replacement/alteration of the central clast may not be easy to detect, especially on the macro scale, and therefore requires microscopic analyses to differentiate from crystalline rims. Furthermore, although not included as a component in previous works, the void space between individual cockade textures, either remaining empty or filled with vein infills (matrix or cement), is an essential component to consider when examining the texture as a whole, especially for understanding the factors involved in its formation processes.

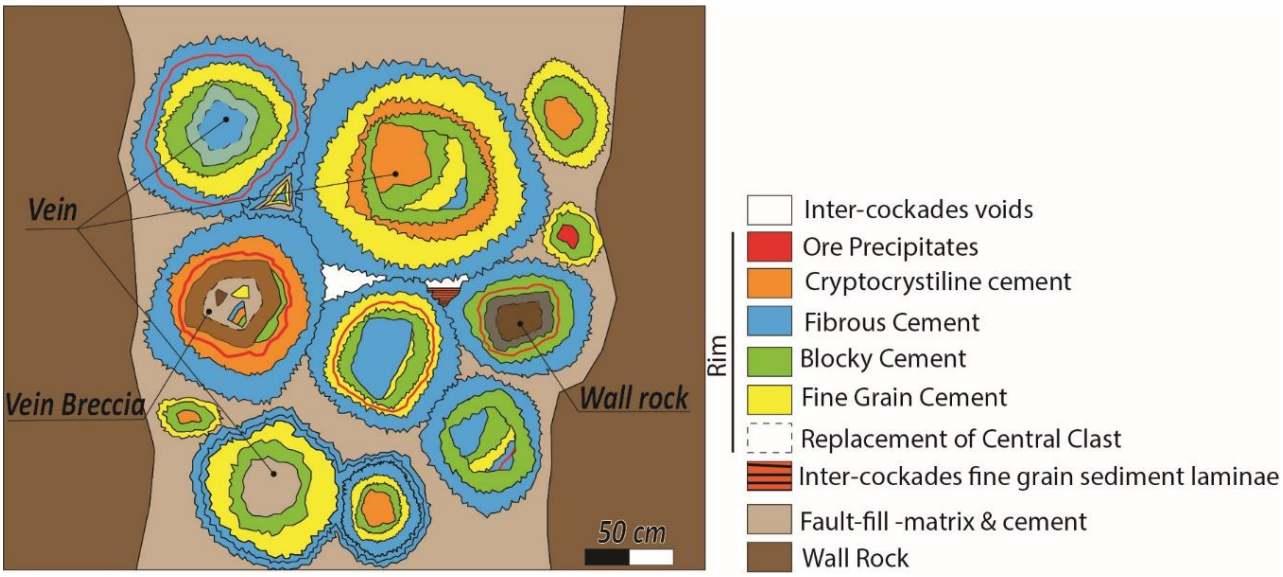

Figure 4: *Components of cockade texture in a breccia zone. The scale is determined based on the largest cockade texture presented in this study. Core fragments consist of wall rock, veins or vein breccias, and rims consist of cement materials with different textures and minerals. Dash lines show partial metasomatic replacement of the core fragments.*

Two of the six formation mechanisms (Figure 2), the cut effect and the infall of clasts, have been completely abandoned because they contradict the definition of texture. The cut affect mechanism contradicts the core fragments that do not touch each other in three dimensions (Talmadge, 1929), whereas the infall of

the clast mechanisms contradicts that rims completely surround the central fragments (Kutina and Sedlackova, 1961). However, in current studies on cockade textures, four of the six formation mechanisms for the formation of breccias containing this texture (Figure 2) have still been suggested: suspension in the fluid, repeated rotation and accretion, partial metasomatic replacement, and force of crystallisation. The background regarding the force of crystallisation will be discussed under a separate title in this chapter.

The suspension in fluid mechanism suggests that cockade textures with complete rims may develop when clasts are temporarily suspended in either highly viscous, dense mineralising fluids (Jobson et al., 1994) or rapidly ascending, low-viscosity hydrothermal fluids within dilatational cavities (Dill and Weber, 2010). However, for clasts to remain suspended throughout the cementation process, fluid flow must reach critical velocities sufficient to counteract gravitational settling. Dill and Weber (2010) proposed that highly viscous fluids, analogous to drilling muds (~6.0 –13.0 mPas at 25°C, compared to ~1 mPas for water at 25°C; Zhang et al., 2021), could suspend clasts during rim precipitation. However, this hypothesis lacks strong field evidence, as cockade texture-bearing breccia rarely contain the fine-grained sediments required to maintain such high viscosity (Spurr, 1926; Buerger and Maury, 1927). Furthermore, the intermittent nature of seismic agitation would lead to periodic settling and compaction during quiescent periods, making sustained suspension of clasts over extended timescales geologically improbable.

Frenzel and Woodcock (2014) conducted a series of calculations to determine whether cockades could be suspended in rapidly ascending, low-viscosity aqueous fluids. Their analysis was based on a fluid with a salinity of 20 wt.% NaCl (3.4 mol/kg) at 150°C, a relatively high salinity that results in a density of 1.0 g/cm^3 and a viscosity of 4.0 mPas (Roedder, 1984; Shepherd et al., 1985; Haas, 1970; Kestin et al., 1978; Mao and Duan, 2009). The study focused on evaluating the hydrodynamic conditions required to suspend cockades of typical size and assessing the physical constraints on maximum flow rates in hydrothermal fault systems.

The first calculation estimated the minimum velocity required for fluidisation of a loosely packed granular aggregate (void space, 50%) composed of quartz or calcite pebbles (density = 2.7 g/cm^3) with an equivalent hydraulic diameter of 5 cm, a size characteristic of cockades (Leroy et al., 2000). Using the fluidisation threshold relations from Eichhubl and Boles (2000), Frenzel and Woodcock (2016) estimated that a flow velocity of 0.24 m/s would be the absolute minimum required for fluidisation. This value remains largely unaffected by variations in fluid salinity or temperature, making it a robust threshold. The second approach involved calculating the minimum flow velocity required to keep clasts in suspension, which is equal to their terminal settling velocity. Based on the equations provided by Gaskell (1992) and Pettyjohn and Christiansen (1948) for cube-shaped particles, Frenzel and Woodcock (2016) determined that the

necessary velocity for suspending cockades in the described fluid is 0.88 m/s. This suggests that for bed fluidisation or suspension to be viable, fluid ascent velocities in the range of 0.1 to 1.0 m/s would be required. The third critical consideration was whether such high flow velocities could be realistically achieved and sustained in hydrothermal fault systems. Empirical data on fluid flow velocities in terrestrial systems is scarce, but Eichhubl and Boles (2000) estimated episodic upward fluid flow pulses ranging from 1.0^{-4} to 1.0 m/s in a carbonate vein along a strike-slip fault. However, these were transient, short-lived flow events rather than sustained flow. Using the Darcy-Weisbach equation, Frenzel and Woodcock (2016) approximated the maximum fluid velocity in a fault conduit (100 m long, 0.5 m wide) under over-pressured conditions. Assuming a rock density of 3.0 g/cm³ and a relative roughness of 0.1, their calculation yielded a maximum velocity of ~20 m/s. This exceeds the minimum requirements for fluidisation and suspension but is only achievable during short bursts of high-velocity flow triggered by seismic events.

Frenzel and Woodcock (2016) concluded that although their calculations indicate that intermittent fluidisation and cementation of clasts cannot be ruled out entirely, sustained suspension of cockades over extended periods is highly improbable. The required continuous flow velocities and discharge rates would be unrealistically high. Their analysis was further supported by observations from black smoker systems, where steady-state exit velocities reach 0.5–5 m/s (Macdonald et al., 1980; Converse et al., 1984; Hekinian et al., 1984). While hydrothermal faults could potentially discharge 10–45 m³⁄s at velocities of 0.2–0.9 m/s, these rates remain far below the values necessary to sustain clast suspension. Furthermore, Frenzel and Woodcock (2016) emphasised that natural fault systems typically exhibit much lower permeability than large open fractures, further constraining the possibility of sustained high-velocity flow. Based on these findings, Frenzel and Woodcock (2016) ultimately ruled out the possibility of sustained suspension and simultaneous cementation of cockades in a rapidly ascending hydrothermal fluid. Thus, the formation of cockade texture-bearing breccia via episodic fluidisation and clast mobility is feasible, but models invoking long-term suspension require reconsideration in light of field-based constraints and hydrodynamic limitations.

Cox and Munroe (2016) revisited the Dill and Weber (2010) model by examining cockade-bearing breccias in the Rusey Fault (Cornwall, UK) and the Roamane Fault (Porgera gold deposit, Papua New Guinea). Their study suggests that these breccias formed within upper crustal seismogenic regimes, undergoing repeated cycles of fault slip and fluidisation of fault damage products. They propose that high fluid fluxes (0.1 m/s to 1 m/s) in these settings are more likely associated with injection-driven swarm seismicity rather than mainshock-aftershock sequences. Based on their findings, Cox and Munroe (2016) acknowledge that in

cases where localised truncation of rims is observed, the rotation-accretion model remains a valid interpretation. However, they argue that cockade textures exhibiting completely continuous overgrowth rims are indicative of mineral accretion occurring while the fragments were in suspension within a fluid, suggesting that their formation was associated with a co-seismic event. The fluid in suspension model for cockade texture-bearing breccia formation is supported by two key observations (Cox and Munroe, 2016):

1) Continuous Overgrowth Rims: Hydrothermal overgrowths exhibit internally concentric bands that remain continuous around the spheroids, without the localised truncation typical of the rotation-accretion process. This indicates that mineral accretion occurred while the fragments were freely suspended in a fluid, rather than intermittently settling and being reoriented on a stable substrate.
2) Inverse Grading Due to Flow Velocity Variations: Cockade texture-bearing breccia layers exhibit inverse grading or banding, where the core clasts of cockades within some breccia layers appear to be organised in a way that suggests fluctuating flow velocities during co-seismic fluidisation of the fragmented rocks. These structures indicate that the breccia formed within a dynamic fluid environment, where episodic changes in flow energy influenced particle sorting and deposition.

The fluid flow that leads to cockade texture often plays a critical role in the formation of various types of hydrothermal ore deposits (Van Alstine, 1944; Genna et al., 1996; Leroy et al., 2000). One of the most notable previous studies examining the texture in terms of economic geology was conducted by Genna and coauthors (1995) on cockade texture-bearing breccia in the Cirotan vein of the West Java (Indonesia) gold district. Genna and coauthors (1995) also included a summary of earlier studies on the formation mechanism of the texture. In this study, cockades are described as a specific type of self-organised encrusted breccia, where rock and mineral fragments are concentrically coated by ore and gangue minerals, and their formation is related to hydraulic brecciation giving rise to the angular fragments forming the nuclei of the breccias (Sillitoe, 1985) and progressive encrustation of the nuclei into an open space, with the breccias becoming rounder as the cockades get larger (Laznicka, 1988). Additionally, they revealed that the dominant agitation mechanisms can be inferred from size grading in cockade texture-bearing breccia. Reverse grading indicates that fault movement was dominant due to the Brazil-nut effect (Möbius et al., 2001), whereas normal grading indicates that rapid ascending fluid was dominant due to the faster settling velocities of larger particles (Genna et al., 1995). The formation mechanism proposed by Genna and coauthors (1995) (Figure 5), strongly based on Sillitoe (1985) and Laznicka (1988), has been accepted as the most likely mechanism for cockade texture-bearing breccia, which is later referred to as "repeated rotation and accretion" by Frenzel and Woodcock (2014).

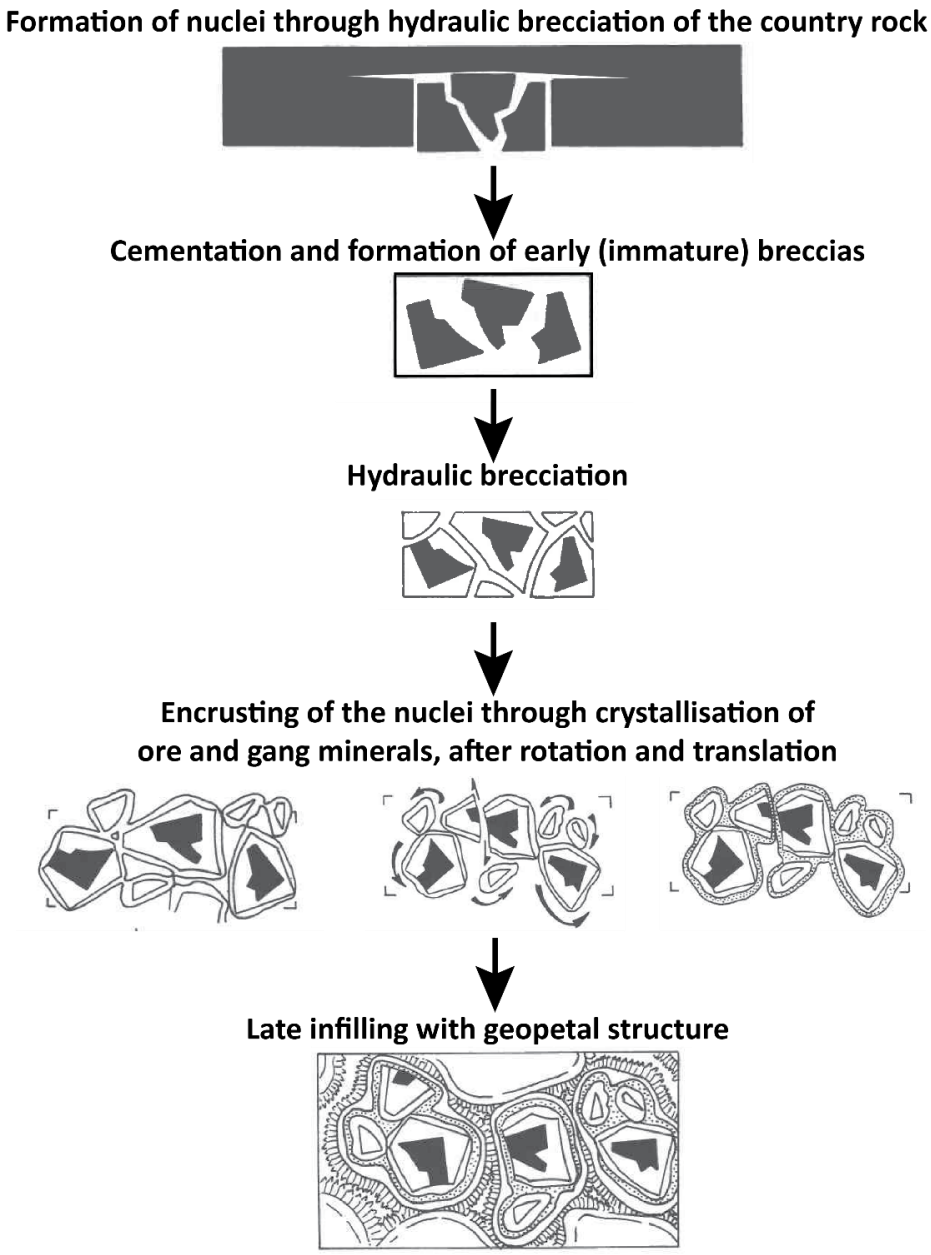

Figure 5: Repeated rotation and accretion mechanism of cockade texture-bearing breccia genesis proposed by Genna and coauthors (1995).

Frenzel and Woodcock (2014) provide a comprehensive review of cockade texture-bearing breccia formation, exploring six potential mechanisms (Figure 2). Their study, conducted on carbonate vein fills in the Gower Peninsula (Wales), which is also the focus area of this research. Frenzel and Woodcock (2014) suggest, based on two observations, that repeated rotation and accretion are the most likely mechanisms to explain the formation of cockade texture in their area of interest (Figure 2). The first observation involves rotated geopetal infills of hematitic sediments. The preservation of these rotated geopetal

sediments (or 'way up') between the euhedral calcite rims indicates that fracture cavities remained open for significant periods and were subject to episodic fluid fluxes with significant flow velocities, resulting in crystal growth either in suspension or through repeated accretion and rotation of clasts in an upward-flowing supersaturated fluid. The second observation relates to local truncations on the concentric growth rims of some cockade texture. These truncations were interpreted to result from the non-deposition of cockade layers where adjacent cockades were in contact. The irregular disposition of successive truncated segments of growth bands indicates that cockades are episodically rotated. This process is analogous to the formation of oolites on sand particles as they roll over a substrate in carbonate-saturated seawater. Frenzel and Woodcock (2014) have also postulated a list of criteria below to identify the cockade texture-bearing breccia form by repeated rotation and accretion mechanism, which depicts low rates of cement growth compared to a high rates of dilatational fault slip;

1) Concentric banding around clasts

2) Columnar cement and, or, other space-filling textures

3) Sharp boundaries between clasts and the first cement generation

4) Volume proportion of cement significantly higher than 50%

5) Clasts are not touching each other

6) Local truncations in cement layers where cockades were previously touching each other

7) Inverse grading of the core clasts of the cockades in some breccia layers, suggesting self-organisation of the core clasts controlled by seismic shaking (Genna et al., 1996)

8) Rotated geopetal indicators (For example of geopetal sediments, please see Figure 34, which illustrates sedimentary infill preserving original depositional orientation).

Previous work by Kutina and Sedlackova (1961) and Rieder (1969) revealed that the relative age of concentric rims of cockade textures is not straightforward because they can result from two processes occurring simultaneously: growth into open space and partial inward metasomatic replacement. They established sets of criteria to identify partial metasomatic replacements in cockade textures on macroscopic and microscopic scales. These criteria rely on observations of different localities from three cases of cockade textures from mineralised veins in Czechia and Slovakia, which contain either quartz minerals exclusively or a combination of quartz and ore minerals in the outer rim. According to Kutina and

Sedlackova (1961), the macro- and microscopic criteria for identifying Cockade texture formed by a partial metasomatic replacement are below.

Macroscopic criteria:

1) Irregular thickness of the layer of ore mineral around an individual rock fragment

2) The layer of the ore component in different rock fragments has significantly different thicknesses

3) Widening of the ore fringes around rock fragments is not regular in the plane section

4) Accumulation of the ore material between some close-lying fragments

5) Projecting of the layers or their continuation in veinlets in the direction of the main cementing component

Microscopic criteria:

1) Replacement along the grain boundaries

2) Replacement along the cleavage planes

3) Replacement across the grains without apparent relationship to the grain boundaries and to the cleavage

4) Simultaneous extinction of small relicts after replacement enclosed in the replacing mineral

5) Continuation of the layer into the main cementing component in the form of metasomatic veinlets, the connection with the lining band, was observed in the polished section

According to Frenzel and Woodcock (2014), while the partial inward replacement or alteration of clast minerals may lead to a texture resembling cockades, the authors argue against labelling the resulting product as cockade texture, and they called them cockade breccia-like textures. This is because it differs in genetic implications from their definition of cockade texture-bearing breccia, which specifies that rims surrounding central clasts consist solely of concentric layers of cement material.

The fluid flow resulting in cockade texture can provide insights into fault dynamics controlling repeated transitory fluid flow in the upper crust and, therefore, understanding processes related to palaeo-earthquake cycles (Berger and Herwegh, 2019b; Masoch et al., 2019). According to Berger and Herwagh, 2019), the initiation of a new cockade texture corresponds to the main seismic event, with subsequent

overgrowth events representing aftershocks and geopetal cement indicating periods of tectonic quiescence. These relationships provide relative age information, which can be calibrated using radiometric dating methods. The formation of cockade texture-bearing breccia and their cementation stages within fault zones suggests seismic activity in the upper crust, likely facilitated by fluid injection. Contrary to Berger and Herwegh (2019), Masoch and coauthors (2019) discuss the identification and conceptual model of cockade-bearing trans-tensional faults in the Col de Teghime area of Alpine Corsica by considering the effect of crystallisation force. Through field surveys and detailed microstructural and mineralogical observations, researchers established a model for cockade texture formation, encompassing various phases of the seismic cycle (Figure 6):

1) Co-seismic fragmentation of wall rocks at geometric irregularities, facilitated by CO_2- and Fe-rich fluids and mechanical wear, resulting in core clast formation.

2) Co-seismic fluidisation of rock fragments, leading to grain elutriation, sorting of finer clasts, and inverse grading within slipping zones. Inverse grading may result from clast collisions (Brazil-Nut Effect, (Möbius et al., 2001)) or shearing.

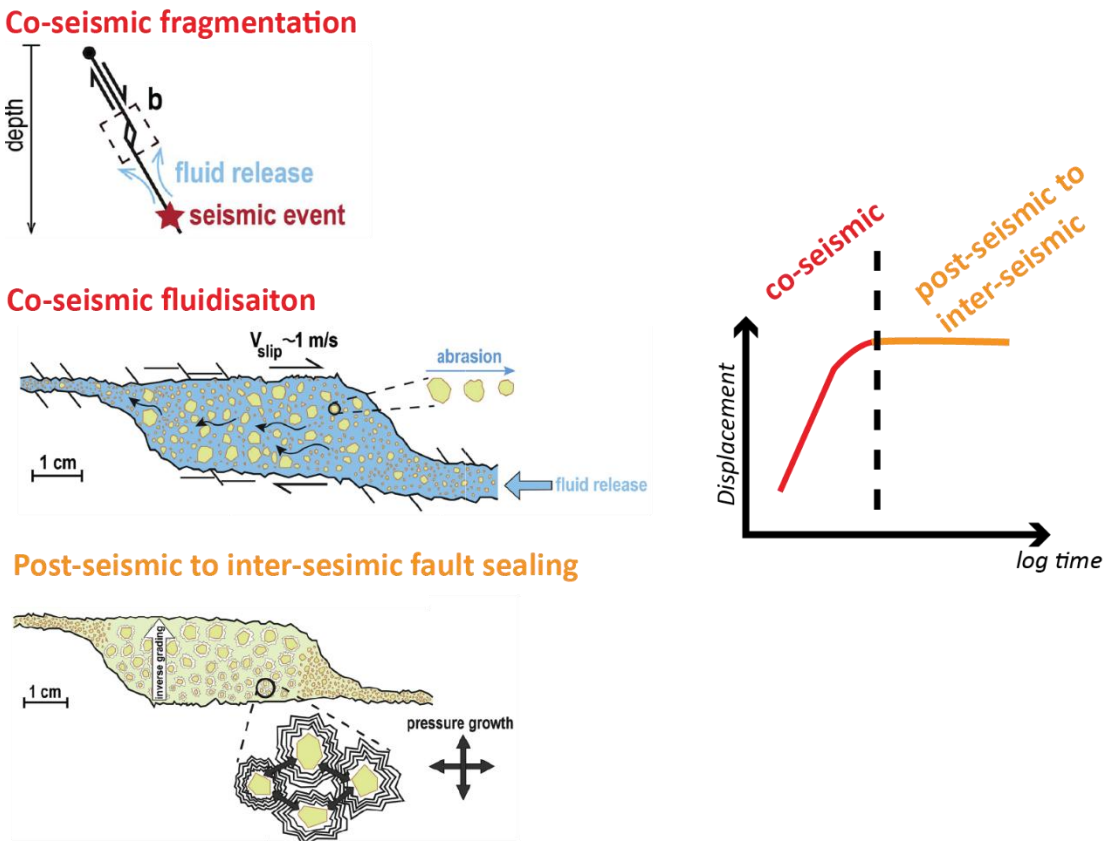

Figure 6: Conceptual model of the formation of cockade-bearing faults and its relationship to fault displacement and time during the seismic cycle (modified from Masoch and coauthors (2019)).

Overall, previous studies have shown that repeated rotation and accretion, suspension in the fluid, the crystallisation pressure and partial metasomatic alteration mechanisms can contribute to the formation of cockade texture. Although previous mechanisms lack a clear consensus on cockade formation, the repeated rotation and accretion mechanism proposed by Frenzel and Woodcock (2014) is widely accepted in the literature as the most likely mechanism, often cited in the study of vein-type mineral deposits and palaeo-earthquake studies (Berger and Herwegh, 2019), assuming rim growth corresponds to seismic activities. However, considering the other mechanisms support the growth of the rims into an open space, the deposition of rims around central clasts may originate from dynamic fluid flow in relation to syn-tectonic processes (repeated rotation and accretion, and suspension in fluid mechanisms) or may derive from a stagnant fluid during non-seismic periods, or the event does not require any seismic activity (the crystallisation pressure mechanism). Moreover, in a system where fluid is introduced episodically, it is quite possible that not only the central clast but also its rims will be exposed to this effect under different temperature and pressure conditions, and therefore, the final architecture of an individual cockade rims' repetition might be overprinted by replacement and recrystallisation processes, especially in a

hydrothermal system. Relying solely on a single mechanism of seismicity-related open space filling without fully understanding the mechanism of cockades may lead to misleading interpretations of their formation in epithermal mineralisations and seismic cycle determinations. For this reason, any geological inference to be made using cockade texture-bearing breccias requires a detailed description and analysis of the texture and the consideration of different mechanisms that may be effective in formation, sometimes even working simultaneously.

There are basically two issues regarding cockade texture that remain current in the literature. Firstly, while the rotation and accretion model proposed by Frenzel and Woodcock (2014) is the most recent and widely referenced explanation for cockade texture formation, there is still no complete consensus on the exact formation mechanisms of cockade textures as a whole. Other models, such as suspension in fluid, force of crystallisation, and partial metasomatic alteration, continue to be discussed and debated in different geological contexts. Secondly, existing breccia classifications fail to adequately categorize them as cement-supported breccias. To address this, a detailed examination of hydrothermal textures is provided below, elucidating the various hydrothermal textures found alongside cockade texture and their specific formation conditions. Additionally, a thorough review of fault breccia classifications and their defining criteria is presented to highlight the challenges in classifying cement-supported breccias containing cockade texture.

2.1.1 Hydrothermal Vein Texture

Textural identification and interpretation for hydrothermal veins consisting of ore and associated gangue minerals are tools necessary for understanding the processes involved in the genesis of these structures because the vein infills record the repeated cycles of mineralisation, sealing, replacement, brecciation, and fluid flow (Dong et al., 1995).

Since quartz is the most common gangue mineral precipitated through the life of many hydrothermal systems, the review and classification studies on vein textures are generally based on the characteristics, morphology, and crystal structure of quartz minerals (Dong et al., 1995). The first study into the textural characteristics of vein quartz was carried out by Adams (1920), which became the base for subsequent studies on hydrothermal quartz textures (Spurr, 1926; Shaub, 1934; Stillwell, 1950; Lovering, 1972; Boyle, 1979; Sander and Black, 1988; Saunders, 1990; Dowling and Morrison, 1990). Dong and coauthors (1995) carried out the most comprehensive study on the textures of veins, and they proposed a descriptive classification from a review of the literature and the examination of many samples from epithermal veins.

According to this classification, thirteen textural types have been differentiated and genetically grouped into three major classes: (1) primary growth textures are formed during crystal growth or the precipitation of amorphous silica (massive, crustiform, colloform, moss, comb, zonal), (2) recrystallisation textures are produced by the recrystallisation of chalcedony, or crystallisation and subsequent recrystallisation of amorphous silica to quartz (mosaic, feathery, plumose, ghost sphere), and (3) replacement textures are formed by the partial or complete pseudomorphs of other minerals by silica minerals (pseudo-bladed, pseudo-acicular, and lattice-bladed, ghost-bladed, and parallel-bladed) (Figure 7 a). Dong and coauthors (1995) further suggest that all silica minerals, except quartz, are metastable and have a tendency to convert to quartz after deposition, indicating recrystallisation (Figure 7 b). Moncada and coauthors (2012) studied the textures based on their fluid inclusion characteristics, and they suggest that the spatial correlation between boiling phenomena, gangue mineral characteristics within fluid inclusions, and the deposition of precious metal minerals presents a valuable exploration tool for epithermal precious metal deposits. Therefore, the presence of fluid inclusions or mineral textures indicating boiling (or flashing) in surface outcrops implies that the base of the boiling zone is situated below, and deeper levels within the hydrothermal system may host precious metal mineralisation. They further suggest that the cockade texture forms through slow crystal growth (non-boiling) towards open spaces, resembling textures like massive and comb textures (Moncada et al., 2012).

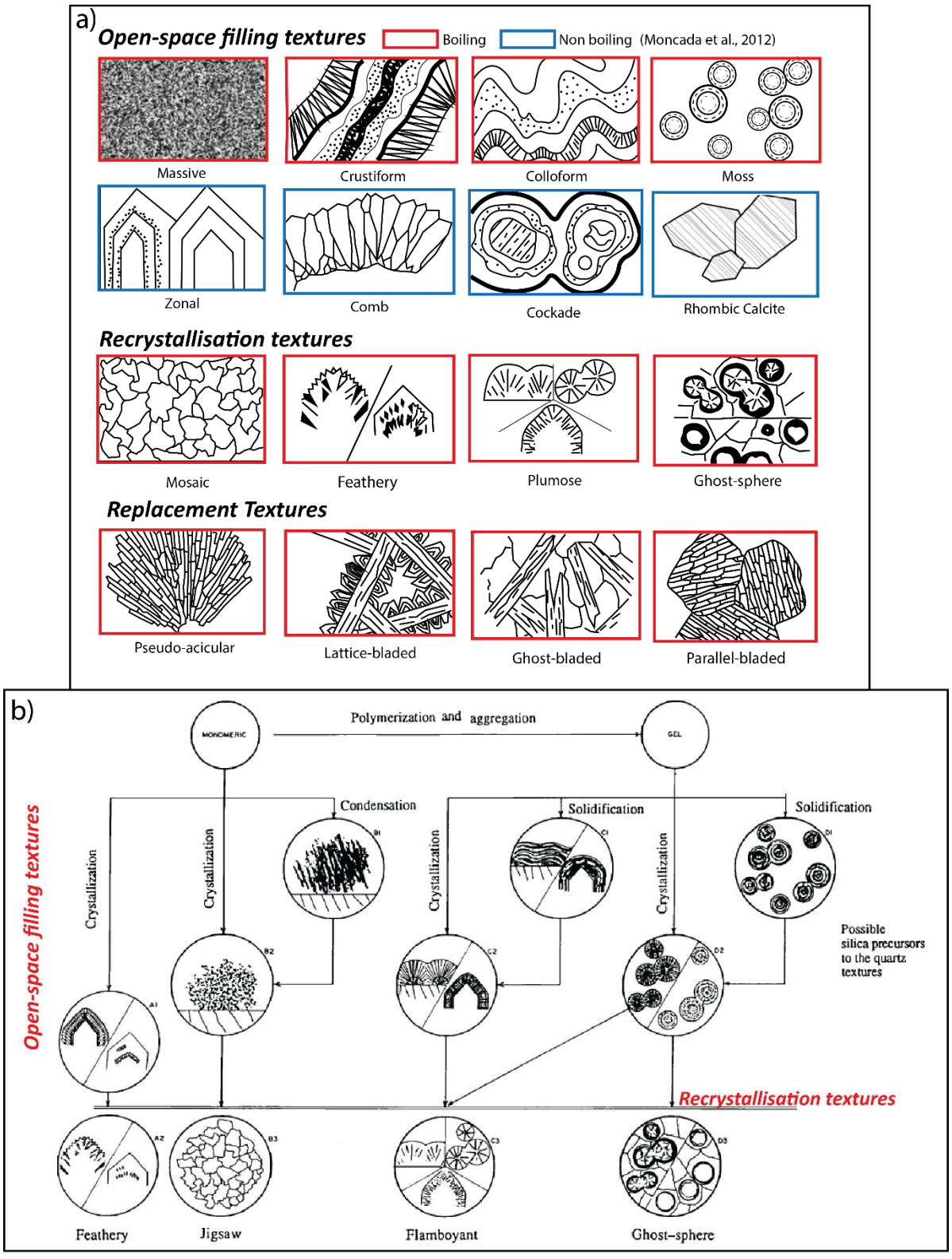

Figure 7: a) The classification of quartz texture by Dong (1995) the red and blue rectangles show their association with boiling and non-boiling processes (Moncada et al., 2012); b) The interpreted origin of recrystallisation texture (Dong et al., 1995).

Subsequent studies have classified textures based on their abundance and their spatial zonation in epithermal environments (Dowling and Morisson, 1989). In low-sulphidation epithermal systems, there is a clear zonation of alteration and mineralisation both vertically and horizontally (Buchanan, 1981; Hedenquist et al., 2000) (Figure 8). This zonation begins with ore-bearing veins containing crustiform quartz/chalcedony-carbonates ± adularia ± barite/fluorite (argillic alteration) and extends to the surrounding wall rock characterised by sericite/illite ± adularia, smectite/mixed-layer clay ± chlorite, and chlorite-carbonate ± epidote (propylitic alteration) in lateral directions. Textural and mineralogical zonation is also evident vertically. Gold grades are typically lower near the surface, where mineralisation occurs as rare native gold or gold associated with pyrite. Gold grades increase with depth in the system (closer to the boiling level), and the thickness of quartz veins decreases from top to bottom and may eventually terminate or be replaced by smaller carbonate veins (Hedenquist et al., 2000). Apart from these, the size of individual grains of minerals, particularly cryptocrystalline in some of these specific quartz textures, can be used to indicate boiling in shallow depths (Philips and Griffen, 1981; Bates and Jackson, 1987; Dong et al., 1995; Moncada et al., 2012).

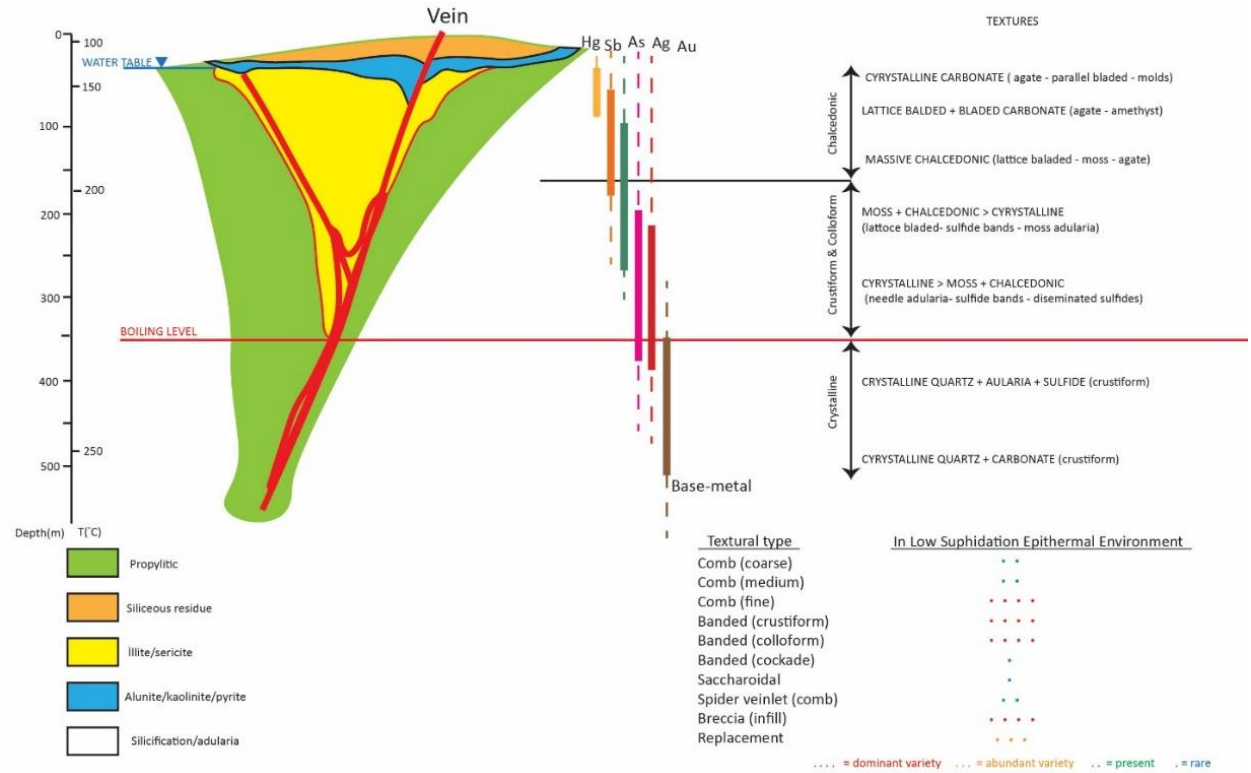

Figure 8: Alteration, textures, ore and gangue mineralogy in typical low–sulphidation epithermal vein deposits (Buchanan, 1981 and Sillitoe, 1993).

Cockades have been classified as a subtype of crustiform texture, a primary growth texture, by Dong and coauthors (1995). The primary growth texture is also known as open space filling textures, common at shallow depths where brittle rocks deform by fracturing rather than by plastic flow. The mixture of meteoric and magmatic waters may circulate freely within fractures, resulting in the precipitation of ore and gangue minerals by abrupt changes in pressure and temperature conditions. As such, open space-filling textures differ from those resulting from the replacement process. Contrary to open space filling textures, replacement textures are more common at high pressure and temperature, where open spaces are very limited and fluid flow is rather difficult. Their formation processes depend largely on the chemical composition and reactivity of the host rock and the hydrothermal solutions. According to Kutina and Sedlackova (1961), partial inward replacement of clast minerals may give rise to the formation of a cockade texture. For this reason, the presence or absence of the gradational boundary between the core clasts and rims, particularly the first one, is crucial for correctly identifying cockade texture to use them during the paragenesis of rim precipitations. In contrast, to open space filling texture, which produces abrupt contact between core clast and rims growing outwards, replacement is often accompanied by gradational boundaries between core clasts and rim-like replacement zone with colour contrast.

It has been emphasised that colloform texture is a primary growth texture in low-sulphidation epithermal systems that describes chalcedonic grains in fine rhythmic bands with spherical, botryoidal, reniform, and mammillary external surfaces (Rogers, 1917; Bobis, 1994; Dong et al., 1995; Sherlock et al., 1995; Moncada et al., 2012; Taksavasu et al., 2018). Under the microscope, colloform banded chalcedony has a microfibrous habit with sharp reentrant angles between touching spheroids (Dong et al., 1995). However, recent studies have also shown that different types of colloform textures that form by contrasting mechanisms can be distinguished (Zeeck et al., 2021). According to this study, petrographic investigations revealed the presence of relic microspheres within the colloform quartz bands that were originally composed of a noncrystalline, presumably gel-like, highly viscous silica precursor. Recrystallisation of the microspherical colloform bands showing a microfibrous habit can form colloform bands composed of mosaic quartz texture (Taksavasu et al., 2018; Zeeck et al., 2021). The analogy between the rhythmic bends of colloform texture and rims of cockades may contribute to revealing the processes in the formation of cockade texture.

2.2 Fault Breccia Classification

Breccia is an all-inclusive term that refers to an enigmatic rock group composed of a variety of individual mineral grains or broken fragments of rocks cemented together by a fine-grain or glassy matrix in any relative proportion (Fisher, 1961; Schmid, 1981; Laznicka, 1989; Knauth, 1994; Scholz, 2019; White and Houghton, 2006). The breccias are formed under several geological processes, such as igneous, sedimentary, and tectonic, which indicate different genetic origins (Shukla and Sharma, 2018). Attempts to define and classify tectonic, or fault, breccias are based on their genetic associations (Jébrak, 1997) and or diagnostic (non-genetic) features (Sibson, 1977; Wise et al., 1984; Killick, 2003; Mort and Woodcock, 2008; Woodcock and Mort, 2008) such as textures (primary cohesion and foliation), the size and relative proportions of their components (clasts, matrix, cement and voids). However, neither non-genetic (Sibson, 1977; Wise et al., 1984; Killick, 2003; Mort and Woodcock, 2008; Woodcock and Mort, 2008) nor genetic (Jébrak, 1997) classifications for fault breccias deal satisfactorily with fault rocks dominated by crystalline cement, like cockade texture-bearing breccias. The present review mainly focuses on the components of breccias, discusses the chronological development of fault breccia classifications and their criteria, and examines why they fail to adequately address the classification of cement-dominated breccias containing less than 30% large (>2 mm) clasts and less than 30% fine matrix.

Woodcock and Mort (2008) define the main components of the fault breccia, i.e., matrix, cement, and clast, in detail to avoid confusion regarding their recognition in the field. Although many relevant size limits are offered in previously published papers, they support the view of Laznicka (1989) and suggest that large clasts are any material larger than 2 mm in diameter or visible to the naked eye on an outcrop scale as a practical matter. Matrix is any fine-grained particulate material smaller than 2 mm in diameter, either derived directly from host rock or produced by local fragmentation of larger particles. Cement is a crystalline material grown in place, either as an infill of void space or a clast or matrix replacement. The term infill here refers to any post-faulting void-filling matrix or cement material.

Three prominent classifications are: (I) a descriptive (semi-quantitative) fault rock classification depending on textural features and cohesion at the time of fault movement, which is called primary cohesion (Sibson, 1977); (II) a quantitative fault classification mainly focusing on brecciation processes occurring in hydrothermal vein-type deposits allows for the discrimination between chemical and physical mechanisms (Jébrak, 1997), and (III) a non-genetic fault breccia classification principally based on clast size, relative rations between clasts, matrix and/or cement comprising the fault breccia (Woodcock and Mort, 2008).

Spry's (1969) review of metamorphic deformation mechanisms and textures and Higgins's (1971) cataclastic rock classification provided the basic nomenclature still used today. Higgins was the first to define the terms "fault breccia" and "fault gouge" as separate from the mylonite sequence and use primary cohesion as a criterion for classifying the fault-related rocks (Figure 9).

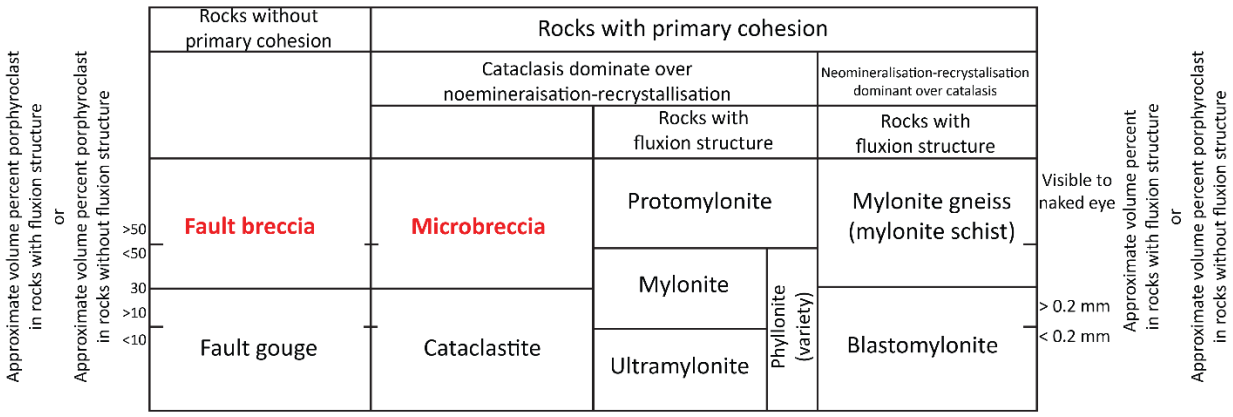

Figure 9: Classification of cataclastic rocks by Higgins (1971).

Sibson's (1977) classification, one of the most influential fault rock classifications, is based on Spry (2013) and Higgins (1971). He used the collective term "fault rock" instead of "cataclastic rocks" for rocks found in zones of shear dislocation. Although Sibson's study does not particularly aim to classify fault breccias, it was important in paving the way for future studies in the area. According to this classification, the fault rocks are subdivided into two main groups, cataclasites and mylonites, based on some distinctive and mostly descriptive features in macroscopic and/or mesoscopic scales (Figure 10 a). The criteria for this classification mainly comprise of the presence of primary foliation, cohesiveness, the nature of the matrix, the shape of the clast, and the nature of the contacts. By definition, the cataclastic series is generally considered to have been dominantly formed by the cataclastic processes (elastic-frictional) typical of the upper crust. In contrast, the mylonite series is more likely to have been dominantly formed by crystal-plastic processes (quasi-plastic), accommodated by recrystallisation, and generally found at upper to mid-crustal depth. Although each criterion was purposely selected to make it applicable in the field, a clear separation between cataclastics and mylonites is not always possible. For instance, rocks are generally not monomineralic, and nature makes it possible to see the different deformation styles side by side within a rock in certain circumstances. Additionally, foliation as a criterion to distinguish cataclasites from mylonites might be misleading since studies have documented the existence of foliated cataclasites, especially where the host rock is rich in micas (Chester et al., 1985). Breccias are included in the subclassification of cataclasites or brittle fault rocks. The main criterion for the classification of breccias is the fault rock's

cohesiveness; based on that, they can be subdivided into two groups: incohesive and cohesive breccias. The cohesive brittle fault rocks are usually found in faults that have been active at shallow crustal levels but relatively deeper than the incohesive ones. The cohesive nature of the rock is mainly due to the precipitation of minerals such as quartz, calcite, epidote, chlorite or K-feldspar from a fluid. According to Sibson's classification, cohesive rocks are included in the cataclasite series and subdivided into two main groups: crushed breccia and pseudotachylyte. Sibson (1986) added a genetic dimension to his fault breccia classification by subdividing it into attrition, distributed crush, and implosion breccias based on mechanical processes during brecciation, and he stated that fault breccias occur with increasing dilation through those mechanical processes (Figure 10 a-c).

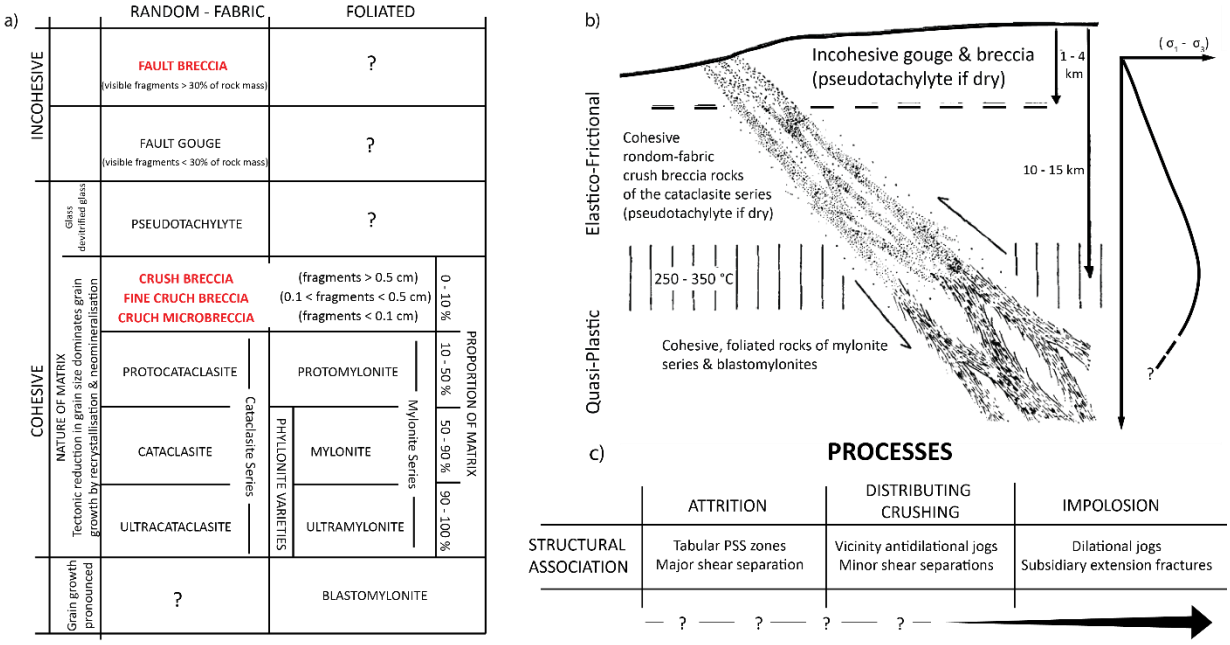

Figure 10: a) Textural classification of fault rocks (Sibson, 1977); b) conceptual model of fault zone (Sibson, 1977); c) possible structural associations for fault breccias derived from the different brecciation mechanisms (Sibson, 1986).

Wise and coauthors (1984) devised a graphical representation of the relationship between fault rocks on a plot of strain rate against recrystallisation rate, which provides a framework for understanding the relationships between the different fault rocks. Fault breccias fall in areas with higher strain rates against lower recrystallisation rates, with a non-foliated texture in the seismically active region. According to Wise and coauthors (1984) classification of fault rocks, the main discriminant and simple field criterion is the distinction of foliated versus non-foliated texture for separating mylonitic and cataclastic rocks, including fault breccia (Figure 11 a). However, although fault breccias typically lack a strong foliation, their clasts are commonly neither randomly aligned nor randomly distributed (Blenkinsop, 2000), and therefore, the

classification based firmly on the criterion that fault breccias must have a random non-foliated fabric is oversimplified and not very practical in the field. A modified version of Sibsons's classification suggested by Killick (2003) aims to propose a more applicable scheme for the economic geologist (Figure 11 b). In this version, since the terminology relating to crush breccias used by earlier systems is considered confusing and superfluous, it has been eliminated and included as a protocataclasites. Nonetheless, pseudotachylyte, a cohesive glassy or fine-grained fault rock with a distinct fabric (Magloughlin and Spray, 1992), is included in the cohesive fault rocks in both schemes. It forms exclusively on rapidly moving faults and is composed of a dark matrix material with minor mineral or wall rock inclusions. Its distinctive glassy or fine-grained texture, lack of significant mineral recrystallisation, and association with high-strain, high-velocity faulting allow it to be distinguished from other brittle fault rock types, such as cataclasites and breccias. According to this qualitative descriptive breccia classification, the breccias can be subdivided into three groups: cohesive, incohesive, and pseudotachylyte. When the pseudotachylyte is set aside considering its distinct formation process, it is seen that the cohesiveness of the rock is the main distinctive criterion which can be deduced from this classification scheme. Considering that the cohesiveness of rock is related to mineral precipitation, this classification can provide information about fluid interaction processes during the formation of the breccias. However, this classification is impractical due to the extreme difficulty distinguishing the fault rock's primary cohesiveness in the field. Furthermore, since a primarily incohesive fault rock can gain cohesiveness by secondary processes, such as pressure solutions or cementation in fractures, it can lead to misinterpretation.

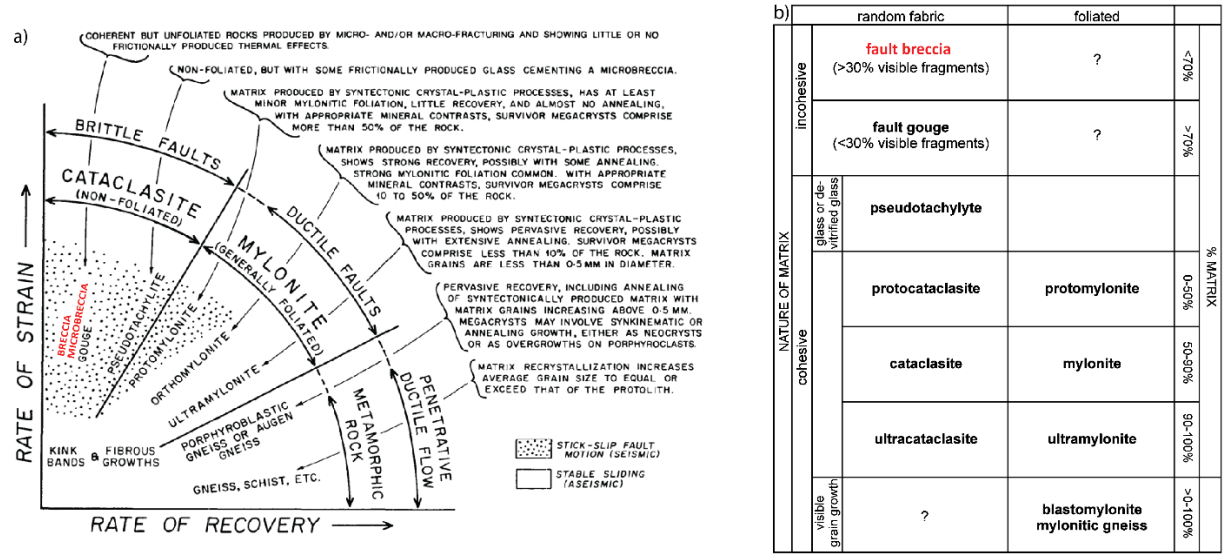

Figure 11: a) Terminology of fault-related rocks. Horizontal and vertical scales are variable depending on composition, grain size and fluids (Wise et al., 1984); b) a revised version of Sibson's (1977) textural classification of fault rocks (Killick, 2003).

Jébrak's (1997) classification of breccias is based on a qualitative approach, and this scope proposes a genetic classification of breccia by focusing on the main brecciation processes, particularly occurring in hydrothermal vein-type deposits. According to the Jébrak, there are two main mechanisms controlling the breccia formation in principle, physical and chemical, and the unravelling of the processes occurring during brecciation allows for the discrimination between chemical and physical mechanisms, including tectonic comminution, wear abrasion, two types of fluid-assisted brecciation (hydraulic and critical), volume expansion or reduction, impact and collapse (Figure 12 a). These mechanisms can be distinguished using nonscalar parameters that describe breccia geometry, including fragment morphology, the size distribution of the fragments, fabric, and dilation ratio. Two of those parameters (fragment morphology and fragment size distribution) are especially important. The fragments' morphology (the fractal dimension, roughness, Dr) allows for distinguishing chemical from mechanical breccias. The size distribution of the fragments (the particle size distribution, Ds) can be used to unravel the energy input during breccia formation. These parameters make the classification of different breccia formation mechanisms possible quantitatively; in other words, they provide insights into the environment in which the breccia formed (Figure 12 b). The Jébrak's (1997) classification is significant as it emphasises the importance of recognising different breccia types during mineral exploration. However, the dataset used to construct the conceptual graph (Figure 12 a), which illustrates the approximate distribution of different breccia types in hydrothermal vein-type deposits, is not well-defined. Additionally, the boundaries between the breccia types in the graph are not distinctly delineated. To ensure its reliability, the conceptual graph should be validated with a sufficient amount of data from natural examples.

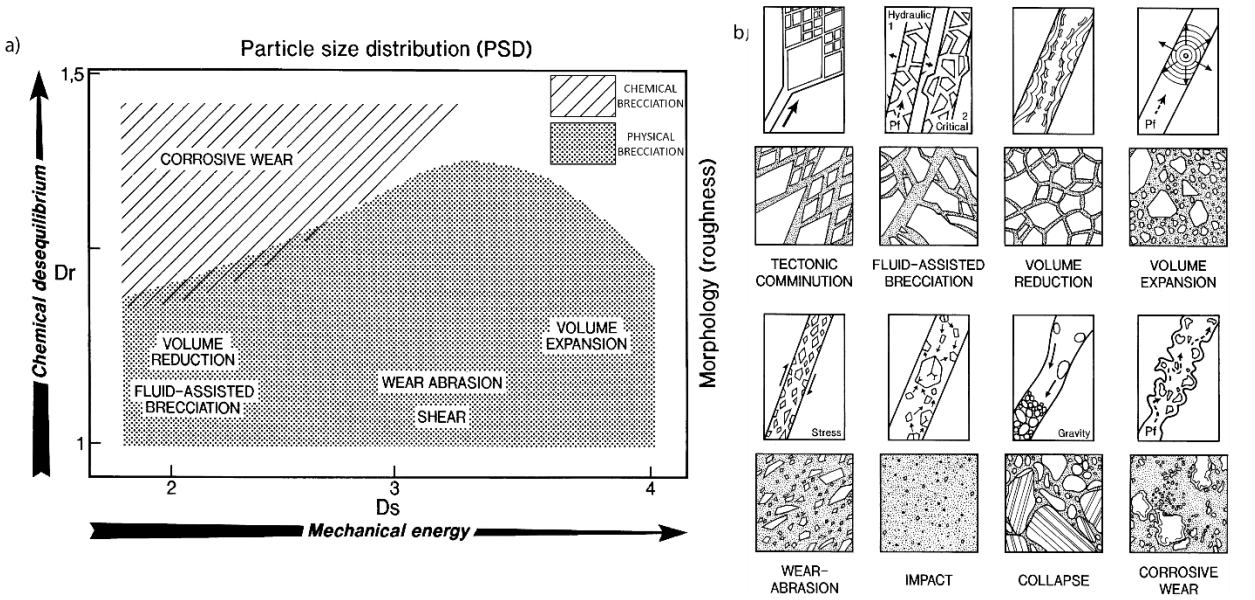

Figure 12: a) A quantitative breccia classification. Dr is the roughness fractal dimension, Ds is the particle size distribution. The zones are defined upon hydrothermal breccias with chemical brecciation the hatched zoned, and physical brecciation in the stippled zone. (Jébrak, 1997); b) The different types of brecciation mechanisms in hydrothermal vein deposits with resulting geometries. The thick black arrow indicates the direction of fault propagation, whilst small black arrows indicate the direction of the wall or fragments; Pf is fluid pressure (Jébrak, 1997).

Woodcock and Mort's (2008) classification of fault rocks is a semi-quantitative approach to non-genetic classification aimed at dealing with the weaknesses of the previously proposed classifications, especially regarding their practicability in the field (Figure 13). According to Woodcock and Mort's (2008) classification, the fault breccia can be cohesive or noncohesive, foliated or not foliated, and contain small clasts, fine-grained matrix or crystalline cement in some relative proportion. For this reason, instead of using primary cohesion and foliation as recognition criteria, they postulated the functionality of using textural terms adapted from the cave-collapse nomenclature (e.g. (Loucks, 1999), i.e. crackle, mosaic, and chaotic, in their fault breccia classification. They define the main components of the fault breccia, i.e., matrix, cement, and clast, in detail to avoid confusion regarding their recognition in the field. As a result, Woodcock and Mort (2008) proposed a revised classification of fault rocks (Figure 13 a) that uses the clast size as the primary criterion for distinguishing the fault breccia (>30% large clasts < 2 mm in diameter) from cataclasites (non-foliated, <30% large clasts < 2 mm in diameter) and mylonites (foliated, <30% large clasts < 2 mm in diameter). The fault breccias are further subdivided according to the settings of the clasts, into crackle, mosaic and chaotic breccias (Figure 13 b). In crackle breccia (>75% clasts), the clasts are little

rotated with respect to each other; in mosaic breccia (60-75% clasts), the clasts are more separated and rotated than crackle breccia. In the case of chaotic breccia (<60% clasts), the clasts are strongly rotated and have lost almost all geometric fit with adjacent clasts. Woodcock and Mort (2008) also proposed two ternary diagrams for alternative graphical displays of fault rock classification (Figure 13 c). The diagram on the left does not require distinguishing the cement from the fine-grain matrix and is more applicable in the field. The diagram on the right, which Laznicka (1988) previously used for breccias in general, might be helpful in breccias dominated by crystalline cement. However, the arbitrarily chosen line (30% cement) dividing the fault vein from cataclasite, mylonite, or fault gouge and the difficulty of distinguishing clast (>2 mm in diameter) from the matrix (<2mm in diameter) in the field limit the applicability of the diagram. Apart from these considerations, even though Woodcock and Mort (2008) emphasise that enhanced permeability created in breccia zones is important in channeling crustal fluids, they can be criticised for not considering the voids providing permeability to the breccia zones in their fault breccia classification.

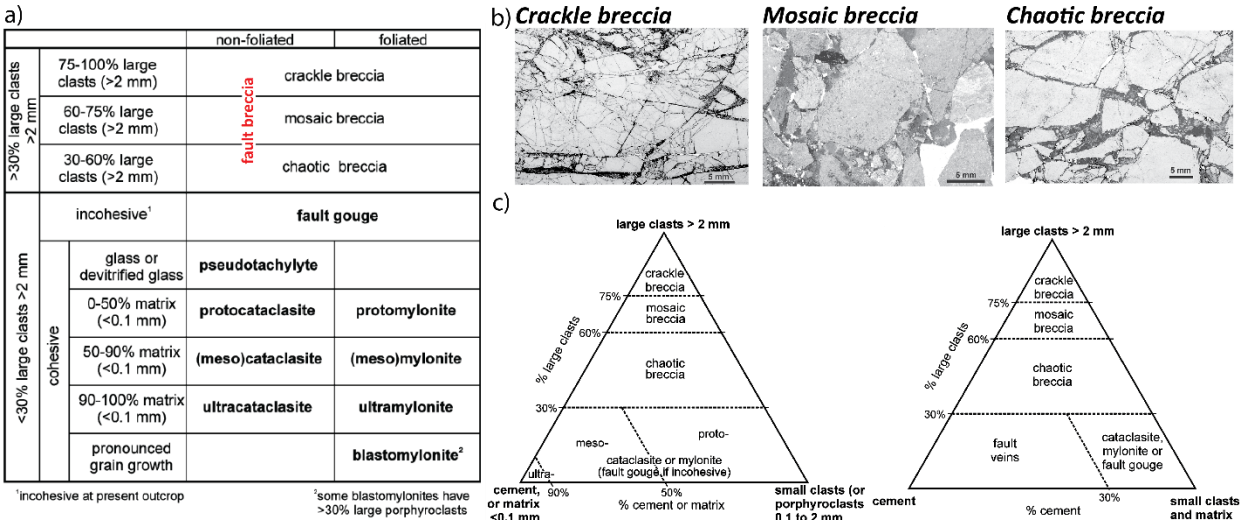

Figure 13: a) A revised version of Sibson's (1977) textural classification of fault rocks; b) Examples of crackle breccia, mosaic breccia and chaotic breccia from the Dent Fault Zone, NW England; c) Ternary diagrams showing the two alternative graphical displays of the proposed fault rock classification (Woodcock and Mort, 2008).

The present brief literature review provides a basic understanding of fault breccia classification and its related terminologies that will subsequently help in a variety of ways, especially for those seeking ore mineralisation. From the economic geology aspects, since fault breccias are the common structures developed by the progressive deformation of the fractures through which the ore-bearing fluids infiltrated into shallow depths, they provide crucial information regarding the formation of many hydrothermal ore deposits. Despite their evident importance in the upper crust, as discussed above, genetic and non-genetic

classifications still have some gaps due to their overarching criteria having exceptions and difficulties for their application in the field (e.g. Sibson, 1977). The lack of enough data from natural examples and the separation of chemical and physical processes that mostly occur by overprinting with each other, with an arbitrary line, is the weakness of the genetic classification (e.g., Jébrak, 1997). Although Woodcock and Mort's (2008) classification does not deal satisfactorily with fault rocks dominated by crystalline cement, as they mention in the articles (Mort and Woodcock, 2008; Woodcock and Mort, 2008; Frenzel and Woodcock, 2014), it is the most recent and easily applicable classification to use in the field. Additionally, the repeated rotation and accretion mechanism, which is favoured by Frenzel and Woodcock (2014), seems to be fit with the complementary crackle, mosaic and chaotic breccia classification. In this classification, the cement-rich breccias are classified as chaotic breccia (<60% clasts), which indicates that the clasts are strongly rotated and have lost almost all geometric fit with adjacent clasts or fault veins, which plot near the cement corner on the ternary diagram below the 30 % large clasts line (Figure 13).

All those classification schemes, either genetic or nongenetic, focus on the pre and syn-deformation factors affecting the resultant geometry of the fault breccia during their formation. Yet, they do not include the processes that might take place and affect their final architectures during interseismic or non-seismic periods, such as compaction, cementation, replacement, recrystallisation and dissolution. In this sense, the fault breccias, including cockade texture, dominated mainly by crystalline cement, might be good examples of why the available classification schemes do not satisfactorily deal with them because their formation mechanisms include both chemical (referring to the partial metasomatic replacement model) and physical factors (referring to the repeated rotation and accretion model) which can occur during interseismic periods) or not even require any seismic activity (referring to the force of crystallisation mechanism).

Both genetic and non-genetic classifications serve as fundamental tools for understanding breccias within fault zones. Despite their conceptual differences, both genetic classification terms and process-agnostic, non-genetic classification terms are frequently referenced in studies that infer formation processes. For example, Chauvet (2019) associates crackle breccias with early fragmentation stages due to tectonic stress or fluid overpressure, while categorizing collapse breccias as resulting from the gravitational collapse of fragments followed by subsequent cementation. This example highlights how the term "crackle breccia," derived from Woodcock and Mort's (2008) non-genetic classification, and the term "collapse breccia," adapted from Jébrak’s (1997) genetic classification, are both used in economic geology studies to infer formation processes. Similar classifications linking breccia terminology to formation mechanisms can be

found in other studies as well (e.g., Rhys et al., 2020). This demonstrates that, despite their distinct methodological foundations, genetic and non-genetic classification terms are frequently interconnected when interpreting breccia genesis. These overlaps underscore the need to critically evaluate the application of classification terminology and to address gaps in existing classification frameworks.

Cockade-textured breccias highlight these limitations, as their formation involves both primary deformation and secondary modification processes. Additionally, they typically contain open voids, which may be filled with matrix and cement or remain open throughout their formation history. While genetic classifications often overlook post-formational alterations, non-genetic classifications fail to account for voids, despite their significant influence on fluid migration and breccia connectivity. To improve classification frameworks, genetic approaches should integrate the impact of secondary processes, while non-genetic classifications should incorporate void percentage to provide a more comprehensive representation of breccia characteristics. Ultimately, the challenges in classifying cockade texture-bearing breccias underscore the need to refine existing classification methodologies, ensuring their methodological foundations align with genetic and non-genetic classification principles. Addressing these gaps will lead to a more accurate understanding of breccia evolution and its implications for fluid flow and mineralisation in fault zones.

2.3 Concept of Crystallisation Force

The concept of crystallisation force, also known as crystallisation pressure, has long been considered one of the earliest explanations for the formation of cockade textures. Initially proposed by Weissenbach (1836), this hypothesis has been echoed by many authors by suggesting that the central clasts in cockade texture-bearing breccias do not make contact with each other due to the pressure exerted by minerals precipitated during crystallisation in their growth direction. Moreover, crystallisation force has been widely documented in various geological settings, including crack-seal veins, stylolites, and frost weathering in porous rocks. In crack-seal veins, crystallisation pressure contributes to the progressive opening of fractures, influencing mineral growth in fault and hydrothermal systems. Similarly, in stylolites, the force exerted by crystal growth is known to play a role in pressure-solution processes, leading to selective dissolution and compaction of rock matrices. Additionally, in periglacial environments, crystallisation force is a key mechanism in frost weathering, where the expansion of ice crystals in rock pores generates sufficient pressure to cause mechanical fracturing. These examples highlight the broader geological significance of crystallisation force beyond cockade texture formation, underscoring its role in deformation, fluid-rock interaction, and mineral precipitation processes.

Frenzel and Woodcock (2014) dismissed this hypothesis based on textural analysis, discussing the resulting textures of rims depending on the surface energies and anisotropies of the minerals involved. The concept of surface energy and anisotropy govern the growth kinetics and morphology of crystals. Minerals with significantly higher surface energy and surface energy anisotropy, such as pyrite compared to quartz, tend to develop well-defined crystal faces projecting in all directions, except where grains of the same mineral are in contact. In contrast, when the minerals in a system have similar surface energy and low anisotropy, such as successive generations of quartz cement, they are more likely to exhibit anhedral textures without well-developed crystal faces, as seen in crack-seal veins (Spry, 1969). Based on this understanding, Frenzel and Woodcock (2014) argue that if the successive cement generation is caused by crystallisation force, the crystals would show anhedral textures due to their very similar surface energy and anisotropy. However, the cockades in their area of interest exhibit rims of crystals with well-developed growth faces projecting outward from the central clasts, taken to indicate growth into an open space. However, the concept of crystallisation force does not rule out growth into open space because the concept implies that a solution film, the thickness of several nanometres, exists between the surfaces of the crystals. In the absence of such a solution film, the growth of the crystal would stop, and no stress could be generated since it would be impossible to add material to the contact zone (Noiriel et al., 2010).

A crystal can exert pressure on its surroundings when increasing its size. Recent studies have shown that growing crystals from a supersaturated solution are capable of generating stress exceeding 150 MPa under laboratory conditions (Wolterbeek et al., 2017; Lambart, 2018; Skarbek et al., 2018; Zheng et al., 2018). As early as 1853, Jean Lavalle asserted the existence of such a force based on his observation of crystals in a saturated solution being pushed upward during their growth by precipitation on its bottom surface. It was first conceptualised as "*the force of crystallisation*" by (Beck, 1903), which is a pressure exerted by crystals in the direction they grow. In later years, many authors experimentally repeated this observation using simple or advanced laboratory experiment setups (Becker and Day, 1916; Taber, 1918; Correns, 1949; Schuiling, 1962; Ostapenko, 1976; Weyl, 2001; Wolterbeek et al., 2018). During early experiments, a single crystal was immersed in its own saturated solution and left growing by the potential supersaturation of the solution resulting from evaporation, cooling or depressurisation. Becker and Day (1905) demonstrated that confined crystals of "alum" ($KAl(SO_4)_2.12H_2O$) grow from a supersaturated aqueous solution. From experimental investigations, the authors concluded that when a crystal in an appropriate saturated solution grows in an open crack between walls with which it comes into contact on both sides, it exerts pressure to separate the walls, if a solution film also exists separating the loaded face from the wall (Correns, 1949; Weyl, 1959). The solution film acts as a diffusion path, allowing the exchange of ions between the crystal and the solution (Weyl, 1959). The linear force thus exerted is of the order of magnitude of the breaking strength of the crystal and, therefore, a geologic force of considerable magnitude and importance (Becker and Day, 1916). In recent experiments, with the help of advanced laboratory techniques, stress generated by growing crystals under adjustable pressure and temperature conditions can be measured. Wolterbeerk and coauthors (2018) directly measure the axial stress driven by a force of crystallisation, up to nearly 153 MPa, during confined hydration of porous CaO powder samples at 65 °C and atmospheric fluid pressure. The calculated stress value is well in excess of the tensile strength of most rock materials and corresponds to lithostatic stress at depths up to 6 km. Furthermore, it is possible to estimate that the force of crystallisation resulting from growing crystals could exceed several GPa under idealised conditions using the thermodynamic models and free energy of formation data from the literature (Robie and Hemingway, 1995; Wolterbeek et al., 2018). The outcomes of these studies have been used to explain a variety of geological processes, including frost-shattering, mineral vein formation, pseudomorphic mineral replacement, spheroidal weathering, and reaction-driven fracture. The following sections review various geological processes affected by the force exerted during crystal growth.

2.3.1 Frost-Shattering

One of the most prevalent natural processes involving crystallisation force is mechanical weathering through frost-shattering, which induces structural stress on the rock matrix, potentially compromising its integrity. In freezing conditions typical of cold or wintry climates, water within rock crevices and pores freezes, forming ice crystals. However, due to repulsion, a thin layer of water persists between the ice crystal and the crevice or pore walls (Gilpin, 1979; Lydon, 1984.; Webber et al., 2007; Sibley et al., 2021). This phenomenon, termed ice segregation, occurs as ice crystals preferentially grow in larger pores, leaving a film of unfrozen water (Gerber et al., 2022). With continued ice growth, the volume expands, applying pressure on the surrounding rock walls. This pressure arises from water expansion upon freezing and ice confinement within the pore space (Scherer, 1999). The resulting pressure from ice growth within pores and cracks induces mechanical stresses in the rock, leading to fracture or failure, a process called frost cracking (Everett, 1961; Derjaguin and Churaev, 1986; Kjelstrup et al., 2021). Frost cracking contributes to the gradual disintegration of rocks in cold regions. By comprehending ice segregation mechanisms and the role of crystallisation pressure in frost cracking, scientists and engineers can better anticipate and address the impacts of freezing conditions on rock stability and infrastructure. Therefore, as a form of physical weathering, frost-shattering substantiates the relevance of crystallisation force hypotheses in driving rock breakdown in high-altitude and high-latitude environments.

2.3.2 Mineral Replacement by Dissolution and Precipitation

Replacement refers to the process of fluid-rock interaction taking place by the dissolution of a host phase and precipitation of authigenic mineral reactions. Those processes are mainly driven by changes in P–T conditions and the chemical environment. During authigenic crystal growth at a stressed crystal face, the presence of at least several nanometres of solution film between the crystal face and host phase is required to facilitate mass transfer and mineral replacement reactions, allowing continuous crystal growth in a chemically evolving environment (Weyl, 2001). Ostapenko (1976) measured the excess pressure associated with the force of crystallisation, exerted by the replacement of periclase (MgO) by brucite ($Mg(OH)_2$) at various temperatures and pore water pressures. In experiments, periclase (MgO) samples were packed in steel cylinders of different wall thicknesses and subsequently hydrated, causing bulging or rupturing of the cylinders. The force of crystallisation-related stress, from 20 to 200 MPa, resulting in the deformation of cylinders, was estimated based on the strength of the steels with varying thicknesses. (Maliva and Siever, 1988) proposed an alternative to conventional models for diagenetic replacements

based on pore water undersaturation with respect to the bulk host phase. The concept is that when a new authigenic crystal begins to grow at some point in a rigid rock, it exerts stress on its surroundings, leading to the pressure-induced dissolution of the adjacent host. The dissolution of the host phase increases the supersaturation of the fluid relative to the growing crystal, causing a decrease in the growth rate of the crystal. The growth rate of the crystal and dissolution of the host phase operate in opposite directions until they reach an equilibrium state at some point in time. Fletcher and Merino (2001) developed a quantitative approach and modelled possible feedback between the growth of crystals in rocks, the local stress induced by the growth, and the possible effects of this stress. According to this model, the growth of garnets in schist or the growth of pyrite in shale can cause pressure solutions of the host grains, viscous creep of the host, or fracture propagation at the vein tips, thus allowing space for the replacement to take place depending on different physicochemical conditions. Furthermore, the genesis of self-organised zebra textures, or rhythmites, in burial dolomites proposed by Merino and coauthors (2006) is similar to this mechanism. According to this model, dolomitic zebra veins are displacive veins that forcibly make room for themselves by force exerted during syntaxial crystal growth. Their parallel equidistant fabric originates in pressure-induced dissolution, which compensates for the veins represent the volume increase. Consequently, the force of crystallisation is a major controlling factor for replacement processes principally driven by dissolution and precipitation reactions (Putnis, 2009).

2.3.3 Displacive Fibrous Veins

Fibrous crystals in veins can record displacement histories during vein opening (Wickham and Elliott, 1970; Durney, 1972; Wickham, 1973; Ramsay and Huber, 1983). This was recognised by Taber (1916) during a laboratory experiment in which he grew fibrous crystals by evaporation of salt solutions in pore spaces of porcelain substrates. He noticed that as the vein-like structures grew where fibres grew from both sides of a crack in the porcelain, the crack began widening by force exerted during crystal growth. Hence, he concluded that: (1) the syntectonic fibres in such veins grow during vein opening, (2) the fibres extend as they grow in the direction of the current vein opening, and (3) earlier-formed fibres segments maintain their growth orientations relative to the vein walls during subsequent vein widening, thus locking in a record of successive vein opening history. Today, there are two well-accepted models addressing the mechano-chemical conditions for the formation of fibrous veins. Ramsay (1980) proposed that fibrous mineral veins owe their origin to a crack-seal mechanism related to episodic crack opening by oscillations in fluid pressure. As an alternative explanation for the openings of fibrous veins, the force of crystallisation mainly depends on the degree of supersaturation of the stagnant fluid and does not require fluid flow or

high fluid pressure (Watts, 1978; Means and Li, 2001; Wiltschko and Morse, 2001). According to this model, the necessary space for fibres to grow incrementally without significant void space is created during the growth of the crystal (Bons and Jessell, 1997). Notably, Meng and coauthors (2017) suggest that the fibrous bedding parallel calcite veins, known as "beef veins", in shale become widened by the induced stress of crystallisation as a subsequent process of fracture sealing rather than by fluid overpressure.

2.3.4 Porphyroblasts

Metamorphic petrologists have adapted the "force of crystallisation" concept to explain the displaced and deformed preexisting schistose matrix around post-tectonic porphyroblasts developed by the concretionary growth (Misch, 1971; Yardley, 1974; Ferguson and Harvey, 1980). It has commonly been stated that idiomorphically growing porphyroblasts are able to deform the surrounding matrix or push the adjacent rock apart as it grows by its force of crystallisation. Spry (1969) opposed the concept on the grounds that the experiments in support of the force of crystallisation are not analogous to the growth of crystals in metamorphic rocks, and the work supposed to be done by a growing porphyroblast is too large to deform its surroundings under a large confining pressure. However, those objections had no physicochemical basis. Additionally, the microscopic evidence of post-tectonic porphyroblasts with the deformed surrounding matrix supports the concept of the force of crystallisation (Prior, 1987).

2.3.5 Vein Textures

Crystal fibre growths normal to the vein walls are distinctive textures that might be explained with the force of the crystallisation concept. Fletcher and Merino (2001) state that fibrous veins can form not only in veins making room for themselves by growing, but also in veins passively growing in open space. Therefore, the critical question here is whether a vein with fibrous texture is formed by incremental passive cementation of episodic cracking events driven by fluid flow and elevated pore pressure in an open space or is formed predominantly by the supersaturation-driven widening of the vein caused by the cement growth itself. The septarian concretion (Astin and Scotchman, 1988; Fletcher and Merino, 2001) is a diagenetic texture in mudrocks caused by progressive burial-driven localised excess pore pressure (Hounslow, 1997). The shape of concretions is a response to this local anisotropic pore pressure and might reflect the permeability anisotropy of the concretion and surrounding mudrock. As the excess pore pressure achieves the condition for tensile failure, the cracks in septarian concretions begin to form. Herein, during the separation of septarian cracks by radial fibrous calcite crystal, displacive calcite growth causes the widening and separation of septarian cracks (Fletcher and Merino, 2001).

Chapter 3: Regional Geology of Field Locations-A Review

This chapter provides a comprehensive review of previous studies conducted in Oxwich (South Wales) and Gicik (Ankara, Turkey), highlighting their geological evolution and the depositional, structural, and geodynamic settings in which they developed.

The selection of Oxwich and Gicik as field sites was driven by both scientific and practical considerations, particularly in response to the challenges posed by the COVID-19 pandemic. Initially, my research was intended to focus on a different geological topic in Saudi Arabia. However, due to travel restrictions and logistical uncertainties, I had to redefine my field approach and select alternative study sites that would align with the new research objectives while remaining accessible during the pandemic.

From a scientific perspective, Oxwich and Gicik represent contrasting geological settings, allowing for a comparative analysis of their depositional histories and the geological processes that shaped them. Oxwich is a carbonate-rich system and serves as the type locality where Frenzel and Woodcock (2014) first proposed the rotation and accretion model. In contrast, Gicik is a silica-dominated low-sulphidation epithermal system, offering insights into hydrothermal processes in a different mineralogical environment. Additionally, Gicik is particularly significant from an economic geology perspective, as mineralisation in this setting is closely associated with epithermal processes. This aspect enhances the relevance of the study by linking structural and hydrothermal evolution to ore deposition mechanisms. Furthermore, collaboration with a researcher who previously conducted geochemical studies at Gicik provided access to existing thin sections, further supporting the comparative nature of this research.

From a practical standpoint, these sites were also chosen based on accessibility and cost-efficiency. Oxwich, being close to Cardiff, enabled daily field visits using public transportation, while Gicik's proximity to Ankara allowed for daily fieldwork using private transport, minimising logistical challenges and optimizing the research budget. This strategic selection ensured that field investigations could proceed efficiently despite external constraints.

By selecting these sites, this study benefits from a comparative analysis of their geological histories, emphasizing their depositional settings, structural evolution, and the broader tectonic context in which they formed. This background information is essential for understanding the environmental and geodynamic conditions that may have influenced the development of various hydrothermal and fault-related textures.

3.1 Regional Geology of Oxwich

The study area in South Wales lies on the southern coast of Gower Peninsula (Figure 14). The area lies between the Bristol Channel Basin to the south which was related to the early Mesozoic extension (Brooks et al., 1988; Nemčok et al., 1995), and the southern margin of South Wales Coalfield to the north, which is a Late Carboniferous peripheral foreland basin, (Kelling, 1988; Gayer and Jones, 1989). Some authors call this province "the Mendip Shelf" area (Cossey et al., 2004).

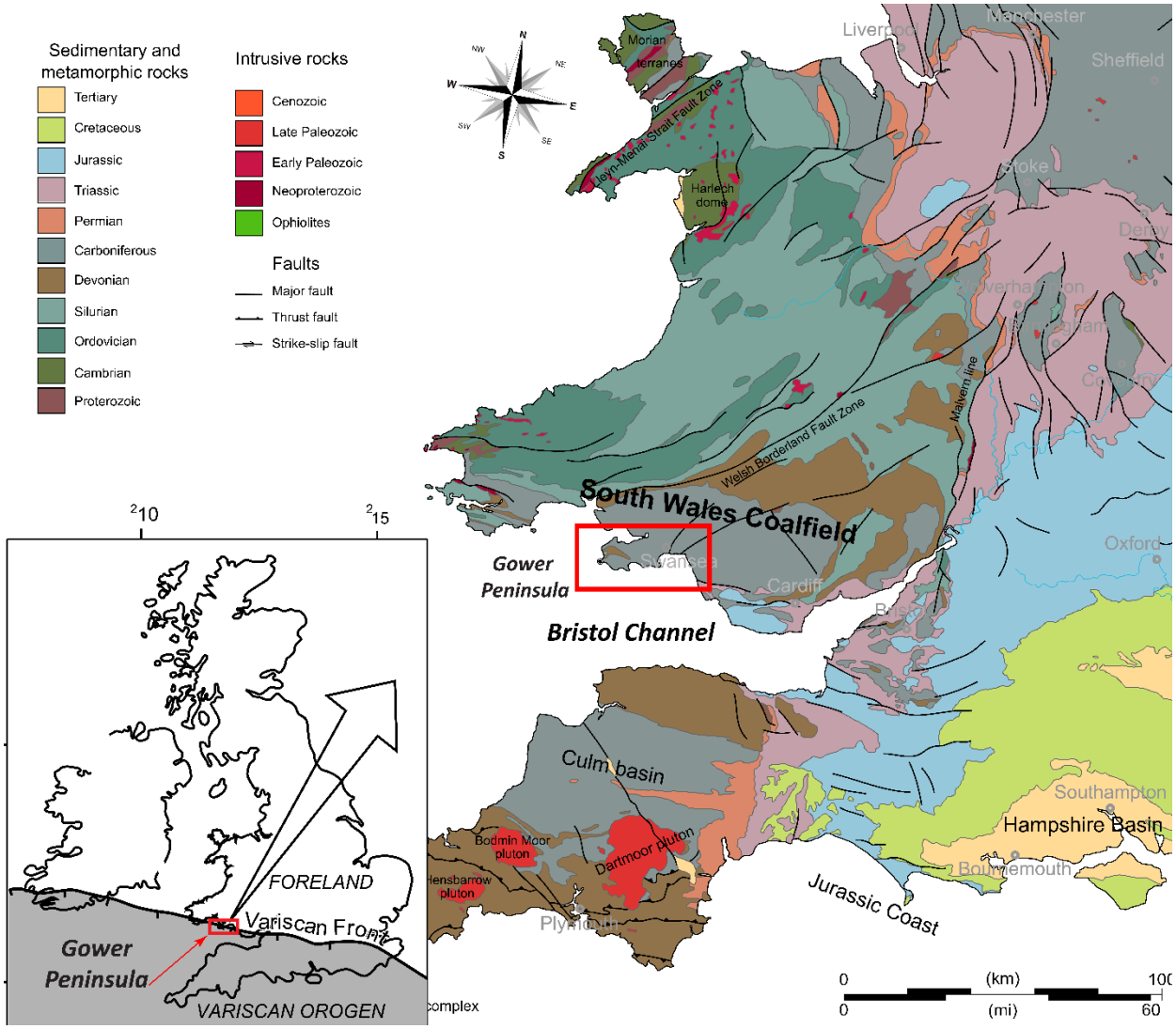

Figure 14: Bedrock geology map of England and Wales - 1:625 000. Red rectangle showing the location of the study area (British Geological Survey, 2002). The inset map shows the major tectonic division of Variscan Orogeny (Woodcock et al., 2014).

During the end of the Neoproterozoic and early Palaeozoic eras, the continents were geographically divided into Gondwana and Baltica to the south and Laurasia and Siberia to the north (Figure 15) (Cossey

et al., 2004; Mitchell, 2004; Groom, 2020). The lower Palaeozoic landmass of modern-day Wales originated from Eastern Avalonia at the edge of the continent of Gondwana, which straddled the south pole. During most of the Cambrian, the Iapetus Ocean separating the Gondwana and Laurasia landmasses began subducting beneath the margins of both continents (McKerrow et al., 2000). In the early Ordovician, subduction beneath eastern Avalonia led to a major shift from a collisional to an extensional regime along the northern margin of Gondwana, resulting in the northwards drifting of Avalonia by the opening of the Rheic Ocean towards the south (Cocks and Fortey, 1982; Scotese and McKerrow, 1990). The upper Neoproterozoic and lower Proterozoic rocks of Avalonia comprise arc-related calc-alkaline plutons, lavas, and inter-arc basin sediments cropping out as isolated inliers in Central England and Southwestern Wales along major active faults and are referred to broadly as British Avalonian (Horák, 1993). In the Late Ordovician, Avalonia and Baltica amalgamated along the Thor Suture by the closure of the Tornquist Sea, which had separated these palaeocontinents during most of the Ordovician, and they started migrating towards Laurasia (Cocks et al., 1997; Torsvik and Rehnström, 2003). Finally, during the late Silurian – early Devonian period, the progressive convergence of Avalonia and Baltica with Laurasia resulted in the Caledonian Orogeny, in which Scotland, England, and Wales connected along the Iapetus suture. The culminating stage of the orogeny, called the Acadian phase, continued until the mid-Devonian, leading to the folding, metamorphism and uplifting of the British Avalonian (Brenchley and Rawson, 2006; Howells, 2007).

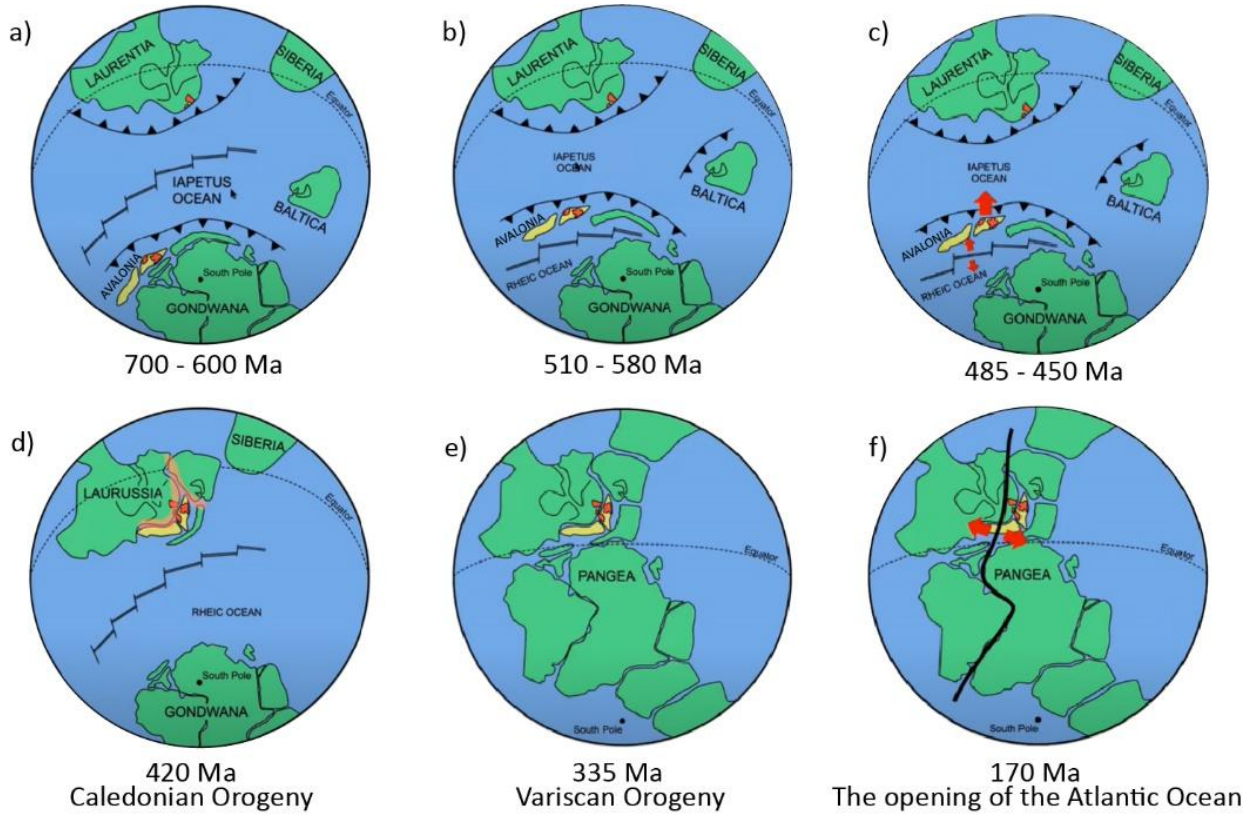

Figure 15: Distribution of continents in Late Proterozoic and Mesozoic time. Note: England and Wales are greatly exaggerated in size, adapted from Mitchell (2004) and Groom (2020).

In the early Devonian, the Anglo-Welsh Basin, fed from the Caledonides, was uplifted by the last phase of orogeny in the north, formed on the northern margins of the evolving Rheic Ocean (Barclay et al., 2015). This tropical sea bordering the southern margin of the newly amalgamated Laurasia from the early Devonian to Early Carboniferous persisted through the transgression northwards, resulting in flooding over the remnants of the Precambrian rocks of Avalonia and lower Palaeozoic sequence, which are the basement rocks of the passive margin (Barclay et al., 2015). The Anglo-Welsh basin is interpreted as a load-generated flexural subsidence foreland basin in the distal setting relative to the Caledonian Orogen (James, 1987; Friend et al., 2000). It accumulated thick Devonian-Early Carboniferous basin fills constituting continental classics, called Old Red Sandstone, at the base and was gradually overlaid by shallow marine Lower Carboniferous platform limestones and deltaic deposits with coal measures (Cossey et al., 2004). In the mid-Devonian, the progressive convergence of Laurasia with Gondwana by the northward subduction of the Rheic Ocean inverted the basin and started to thrust the Devonian-Early Carboniferous basin fills northwards. The closure of the Rheic Ocean towards the end of the Carboniferous, northward-moving Gondwana collided with the southern margin of the Laurasia continent and formed the supercontinent

Pangea. The mountain chain from Southern Ireland through South Wales into England and forming part of the east-west arc of northwestern Europe is the product of this collision and marks the Variscan Orogeny (Cossey et al., 2004).

Following the Variscan Orogeny, the supercontinent Pangea started fragmenting due to the thermal relaxation of the crust, which gave rise to the formation of the grabens along the preexisting Variscan structures. The Bristol Channel basin, for example, was formed by the reactivation of underlying Late Palaeozoic Variscan thrusts in early Mesozoic. The extreme arid climatic conditions of the Permo-Triassic interval resulted in the deposition of red beds shed from the Old Red Sandstone and Carboniferous rocks (George, 1970).

The Cretaceous opening of the North Atlantic Ocean and the Alpine Orogeny are global tectonic events that reactivated the Variscan faults and influenced the late Mesozoic basin development. (Brenchley and Rawson, 2006).

3.1.1 Local Geology of Oxwich

The coastal sections of the Gower Peninsula are well known as classical study areas for Upper Palaeozoic strata of Devonian and Carboniferous ages, deposited during the Caledonian and Variscan Orogenies, and mainly shaped by the effects of the latter (Wright et al., 2007). The study area lies between the coastal section from Porth Eynon to Oxwich, Gower (Figure 16). The area hosts a complete set of deformation structures from the Lower Carboniferous to the early Cretaceous. The bedrock geology of the region is comprised almost entirely of Upper Palaeozoic strata of Devonian and Carboniferous ages, and a small outlier of Triassic sediments underlies part of the village of Port Eynon.

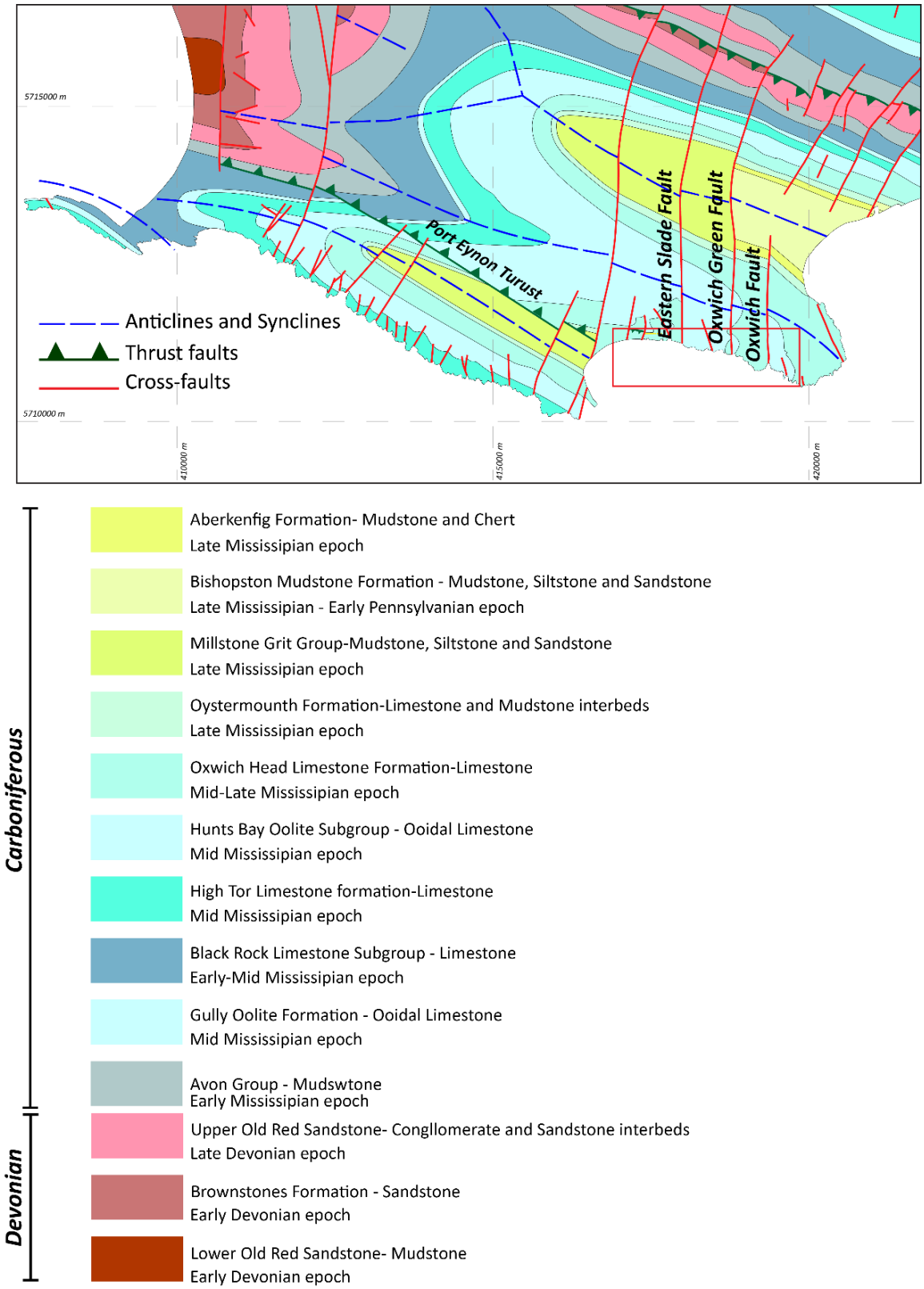

Figure 16: Geology and Structural Map of Gower (Modified from George (1940)) with fault names and British Geological Survey 1:50 000 maps (British Geological Survey, 2002). The red rectangle shows the study area. (Datum: WSG84 UTM Zone)

The Old Red Sandstone Supergroup (ORSS), the lowermost strata, is exposed at the core of anticlines as inliers and along the hanging wall block of the thrust faults near the study area (Cossey et al., 2004). It predominantly comprises siliciclastic strata of the late Silurian to Carboniferous age. It is subdivided into two groups, the Lower Old Red Sandstone and the Upper Old Red Sandstone, separated by a regional unconformity resulting from the Acadian phase of the Caledonian Orogeny (Kellaway and Welch, 1955; Barclay et al., 2015). The ORSS is conformally overlain by the Carboniferous Limestone Supergroup (CLS), cropping widely out in the peninsula, deposited during the Dinantian Epoch of the Carboniferous period (Cossey et al., 2004). The supergroup is subdivided into the Avon Group at the base; this is the earliest Carboniferous strata and is represented by a shale-dominated shelf succession deposited during the early Tournasian (Waters et al., 2007). The Pembroke Limestone Group, a typical platform carbonate succession, overlies the Avon group in the CLS showing an evolution from ramp to shelf facies with sea-level fluctuations (Waters et al., 2007). The overlying Namurian Marros Group, formerly known as the Millstone Grit Series, comprises siliciclastics derived from the north uplifted during Variscan deformation (Waters et al., 2014). The South Wales Coals Measures Group, deposited during the end of the Carboniferous period cropping out to the north of the peninsula, overlies the Morros Group and is represented by fluvial-deltaic facies with varying thickness of coal interbeds (Waters et al., 2014). Towards the end of the Triassic, the post-Carboniferous cover was eroded, as constrained by an Early Triassic unconformity. A small outlier of this period underlies part of the village of Port Eynon, which is on the eastern boundary of the study area (George, 2008). A simplified stratigraphical section of rock sequences in South Wales (Cleal and Thomas, 1996) is presented in Figure 17 a.

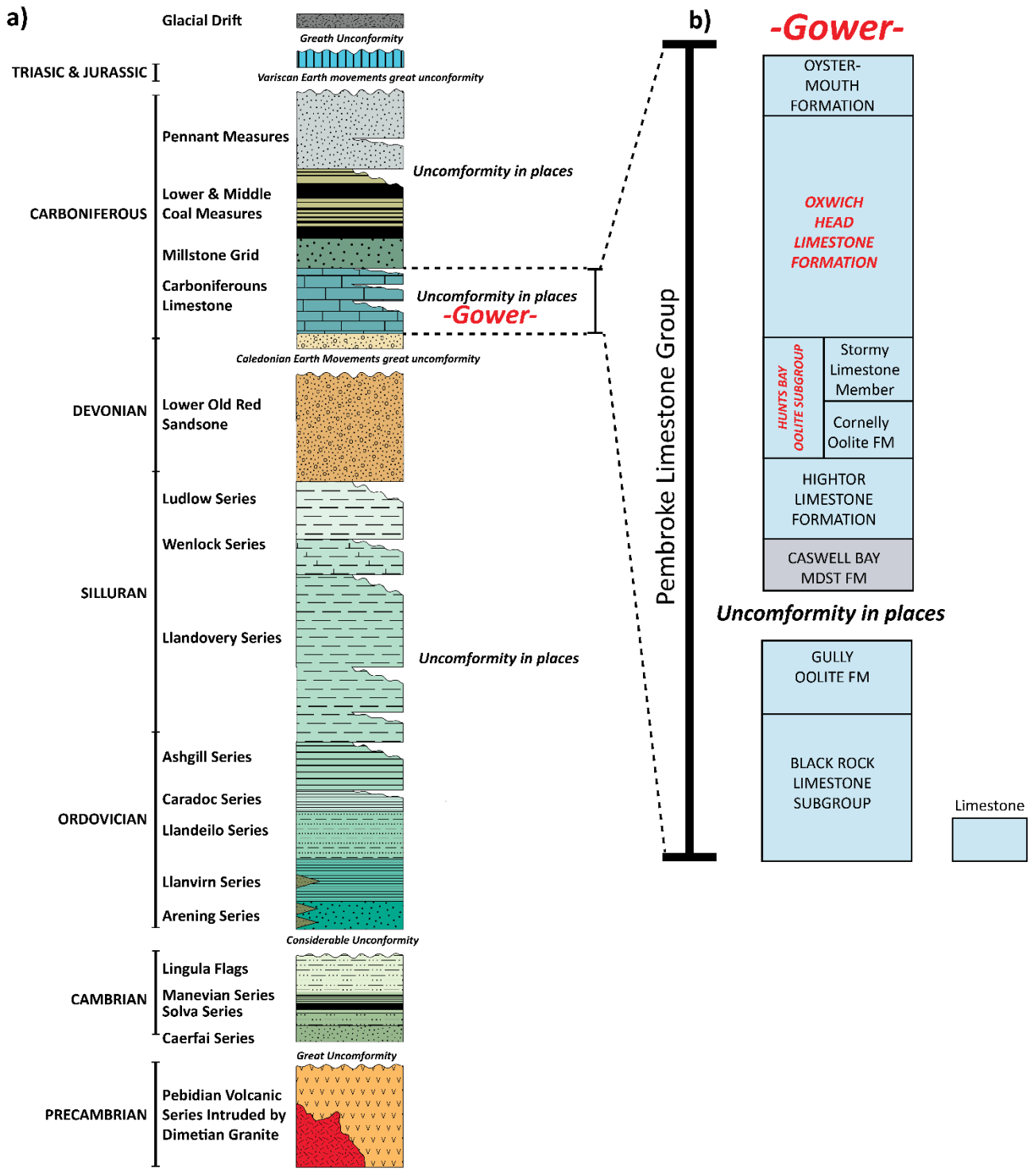

Figure 17: a) Simplified and generalised stratigraphical column of the rock sequence in South Wales, Cleal and Thomas (1996); b) vertical sections illustrating the Lower Carboniferous of Gower, South Wales, adapted from Waters and coauthors (2007).

The Hunts Bay Oolite Subgroup and the Oxwich Head Limestone Formation, from older to younger, are the lithostratigraphic units of to the Pembroke Limestone Group that crop out within the area of interest in this study (Figure 17 b). The Hunts Bay Oolite Subgroup exhibits two main formations. The lower formation is the Cornelly Oolite Formation, mainly dominated by oolitic sequences interbedded with bioclastic and peloidal limestones and calcite mudstones. The Stormy Limestone member represents the upper part of the Hunts Bay Oolite Subgroup and is mainly dominated by limestones with micritic and crypt microbial lithofacies. The Oxwich Head Limestone Formation is the younger unit in direct contact with the underlying Stormy Limestone Formation, the boundary between the two being marked by a palaeokarstic surface related to periodic emersions of the unit during its deposition (Wilson et al., 1990; Waters et al., 2007). It is dominated by thickly bedded, fine to coarse-grained, recrystallised, grey-mottled, skeletal packstones (Howells, 2007), with distinctive pale-dark grey pseudo-brecciation (Waters et al., 2007).

The area experienced Variscan deformation in the late Carboniferous, resulting in the formation of folds slightly plunging to the E or ESE, south-dipping thrust faults oriented to the E-W or ESE, and cross faults oriented to the NNW or NNE. Wright and coauthors (2009) conducted a comprehensive field-based study on the NNW or NNE-oriented cross-faults and their infills in Gower, which are also the main subjects of this study. Based on the field evidence of this and previous studies, the temporal distributions of structures in an overlapping time sequence are as follows. The folds formed primarily during NNE-directed Variscan shortening (George, 1940), inferred from minor ductile shear zones (Srivastava et al., 1995), conjugate shears and the stylolite seams perpendicular to the shortening direction (Roberts, 1979) developed in Lower Carboniferous limestones. Thrusts striking parallel to fold axes then formed, indicating northward vergence during progressive shortening (Roberts, 1979). The cross-cutting relationships of the wide vein, breccia or sediment-filled fissures with host rock along some cross-faults indicate that they developed later in the kinematic history (George, 1940; Roberts, 1979; Wright et al., 2009). The seismic data collected from the extensional Mesozoic Bristol Channel Basin, south of the study area, show that faults striking parallel to the Variscan thrusts and cross-faults bound and cut through the Mesozoic sedimentary rocks in the basin (Brooks et al., 1988). The existence of those faults reveals that the inversion of Variscan structures controlled the evolution of the basin during Mesozoic extension, and NNE-NNW transfer faults that cut through the Mesozoic infills in the basin are formed by the reactivation of the similarly oriented cross faults in the Palaeozoic basement that accommodated differential displacement between two adjacent segments of the Variscan thrust faults (Brooks et al., 1988). A recently published study by Ault and coauthors (2016) supports this reactivation during the Mesozoic based on multiple low-temperature thermochronometric data in fault-related feature fills on the Gower Peninsula. This study documented

early Cretaceous hydrothermal fluid circulation in an originally NNW or NNE trending Variscan cross-fault. This hydrothermal fluid flow event is coeval with tectonic and seafloor spreading events associated with the opening of the North Atlantic Ocean (Doré et al., 1999).

Sibson and coauthors (1982) conducted one of the earliest studies aiming at explaining the formation mechanisms for fissures up to several metres wide, including the one at Gower Peninsula, and he proposed the famous "fault-valve model" explaining the occasional presence of large hydrothermal veins hosted on faults often with a clear textural record of the incremental deposition. In this study, he examined the fault vein in Limeslade Bay, located east of our study area, showing the same geological and mineralogical characteristics as the cross-faults and their infills at Oxwich. In this study, he described the vein fills of calcite with subordinate hematite and their textures, which indicates complex movement history and the passage of large volumes of hydrothermal fluid. He observed the initially banded crustification texture from the walls of fissures followed by episodic brecciation and recementation of vein fill, recording at least nine episodes of extensional opening. Sibson interpreted the early banded crustification with inwardly terminated crystals as characteristic of intermittent crystal growth from the walls of progressively opening fissures. He suggested that this feature resulted from a fault that originated as a hydraulic extension fracture and opened incrementally in the direction of the least principal compressive stress when fluid pressure periodically exceeded it. The episodic brecciation of vein fill afterwards resulted from the shear stress component acting along the fracture due to the change in stress field orientation. Thus, he concluded that the formation of veins on cross-faults at Gower was in accordance with the fault-valve model in terms of the pattern of veining and their textural characteristics.

According to Wright and coauthors (2009), the origin and infill of large fissures along or around faults in the upper few kilometres of the crust, such as in the Gower Peninsula, can be explained by two mechanisms: by the geometric mismatch between displaced fault walls (Newhouse, 1940) or by solution widening along inactive faults (Loucks, 1999). To test this hypothesis, they discussed the origin and infill of NNE-SSW-oriented fissures using lithological components and fault zone architectures. The lithological components, including dendritic hematite growth and elongated calcite growth into open voids, cockade texture including breccia formation, laminated sediment infill, and void-collapse breccias, provide evidence for growth into open fluid-filled phreatic fissures, metres wide in some cases. On the other hand, polyphase deformation history along cross-faults and their fillings record that fault displacement overlapped in time with fissure filling. Based on those observations and the lack of void geometries and

speleothem related to karstic processes, they concluded that NNE-SSW-oriented cross-faults are formed by a geometric mismatch across faults during their slip rather than by solution.

3.2 Regional Geology of Gicik

The present-day Anatolian plate is composed of three main continental fragments (Anatolide-Tauride Block, Arabian Platform and Pontides) (Ketin, 1966; Şengör and Yilmaz, 1981), separated by curvilinear belts marked by the presence of ophiolitic rocks (Figure 18). The Anatolide-Tauride Block and the Arabian Platform were derived from the northern margin of Gondwana; in contrast, the Pontides to the north were one part of Laurasia. The Anatolide-Tauride Block and the Arabian Platform in the south were separated by the southern branch of Neotethys, also known as the Bitlis-Zagros Ocean. The northern margin of the Anatolide-Tauride Block accreted to the Pontides along the Izmir-Ankara-Erzincan Suture Zone, representing the closed northern branch of Neotethys. This early classification of the Turkish tectonic units was later revised to include several other subdivisions, i.e. Kırşehir Massive, Menderes Massive, Tavşanlı Zone, Afyon Zone and Bornova Flish Zone, based on profound stratigraphic, palaeogeographic, structural, magmatic and metamorphic breaks (Okay and Tüysüz, 1999; Moix et al., 2008). The Gicik low sulphidation epithermal gold deposit, the area of interest in this study, is within the Sakarya Zone and makes up the Pontide fragment of Laurasian affinity together with the İstanbul and Rhodope-Stranja Zones (Figure 18).

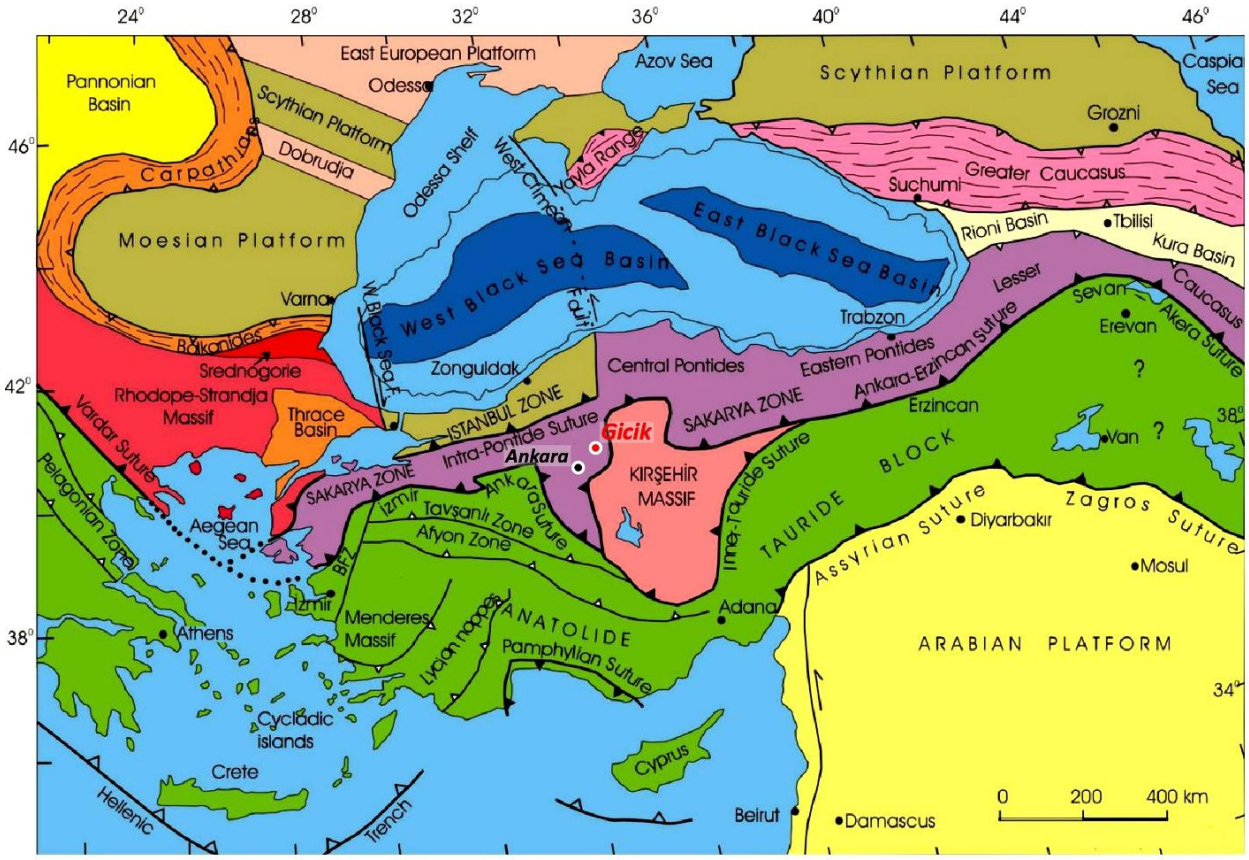

Figure 18: Map showing Turkey's major tectonic units and suture zones (Okay and Tüysüz, 1999). (Datum: WSG84 UTM Zone)

The opening and closure of the Palaeo-Tethys and Neotethys oceans strongly control the geology and metallogeny of the Anatolian Plate, which is also known as Asia Minor (Şengör and Yilmaz, 1981; Bozkurt and Mittwede, 2001; Yigit, 2009; Richards, 2015). Subduction and collision of many small continental fragments derived from Gondwana in the south and Laurasia in the North resulted in their amalgamation during the Late Jurassic to Miocene when the Neo-Tethys Ocean reached its peak and later started to close progressively following the initiation of the northward drifting of the Afro-Arabian platform (Figure 19). Within this geological framework, the record relating to the Palaeo-Tethys Ocean was poorly preserved in most parts of Anatolia, but the rock units associated with Neo-Tethys comprise the major geological entities of the region. Therefore, Tethyan metallogeny in Turkey has been much better constrained overall by the cyclic rifting, subduction and closure of the Neo-Tethys oceans (Yigit, 2009; Richards, 2015; Rabayrol et al., 2019; Kuşcu et al., 2019).

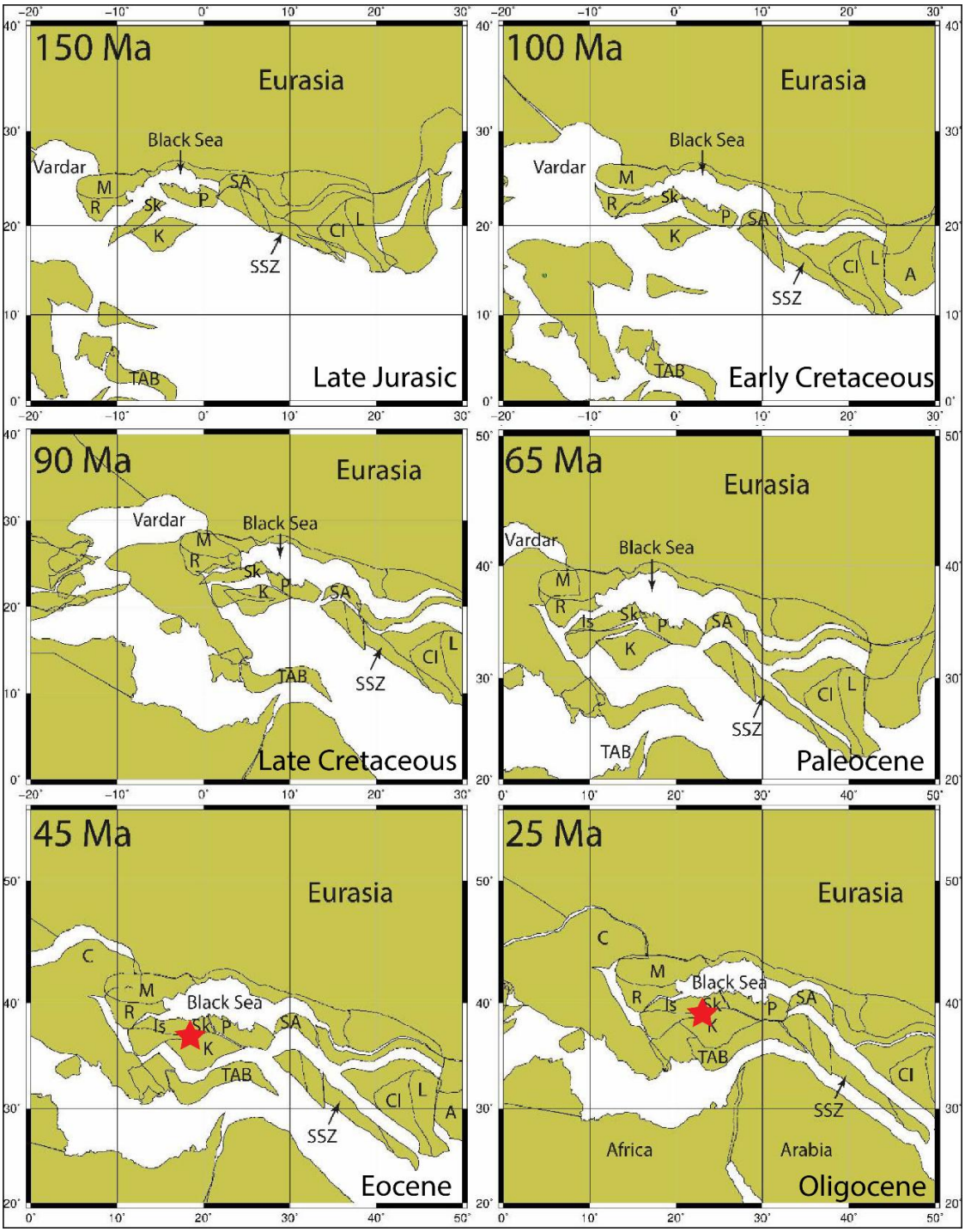

Figure 19: Paleogeographic reconstructions of Anatolia and its neighbouring regions between 150 and 25 Ma as obtained from the Ocean Drilling Stratigraphic Network's Plate Tectonic Reconstruction Service. Red stars showing location of Gicik Low-Sulphidation Epithermal Au Deposit. Abbreviations: A: Afghan Block; C: Carpathians; CI: Central Iranian Block; Is: Istanbul Zone; K: Kırşehir Block; L: Lut Block; M: Moesian Platform; P: Pontides; R: Rhodopes; SA: South Armenian Block; Sk: Sakarya Zone; SSZ: Sanandaj-Sirjan Zone; TAB: Tauride-Anatolide Block. (www.odsn.de/odsn/services/paleomap/paleomap.html) (modified from Çil, 2019)

The Sakarya Zone remained a part of the active Laurasian margin until the Late Triassic. Widespread development of subduction-accretion complexes, called the Karakaya and Küre complexes, occurred during the Permo-Triassic and Early Jurassic period (Okay and Göncüoğlu, 2004; Okay et al., 2006). The opening of the marginal Küre Ocean in the Late Triassic resulted in the rifting of the Sakarya Zone from Laurasia (Robertson et al., 2021), but the Sakarya Zone and other Pontic fragments re-accreted to the Laurasian margin in the Early Jurassic following the closure of the Küre Ocean due to subduction beneath the Sakarya Zone. Therefore, the Pre-Cenozoic tectonic basement of the Sakarya Zone consists of Variscan (330-310 Ma; Okay et al., 2006) metamorphic basement units and cross-cutting Palaeozoic granitoids (Delaloye and Bingöl, 2000; Okay et al., 2006).

The closure of the Küre Ocean initiated the opening of the Izmir-Ankara-Erzincan Ocean, the northern branch of Neo-Tethys, to the south of these fragments due to the northward roll-back of the subducting slab (Okay and Tüysüz, 1999; Moix et al., 2008). By this time, the Anatolide-Tauride Block (TAB) and the Kırşehir Massive already occupied the north-facing southern margin of the Izmir-Ankara-Erzincan Ocean. Closure of the northern branch of Neo-Tethys was initiated during the Cretaceous, which resulted in the development of arc complexes mainly in the eastern Pontides (Okay and Şahintürk, 1997; Rice et al., 2009; Sipahi et al., 2018) and less commonly in western (e.g. Yaylaçalı Formation, NW Turkey; Rice et al., 2006) and central Pontides (e.g. Beypazarı Granitoid; Helvacı et al., 2014). The continent-continent collision between the Sakarya Zone and the Kırşehir Block occurred in the Late Cretaceous (Kaymakcı et al., 2010) Rice et al., 2006). The Late Cretaceous collision is generally regarded as a "soft collision", meaning that subduction was still active, and deformation was accommodated primarily by distributed shortening, thrusting, and under-thrusting, rather than large-scale crustal thickening (Kaymakci et al., 2009; Rice et al., 2006). This phase was followed by the ultimate "hard collision" in the late Palaeocene-Early Eocene, when the complete consumption of the Izmir-Ankara-Erzincan Ocean resulted in a more rigid continental collision, leading to intense crustal thickening, widespread metamorphism, and large-scale thrusting (Okay and Tüysüz, 1999; Rice et al., 2006; Kaymakci et al., 2009). Late Cretaceous-Palaeocene elimination of the Izmir-Ankara-Erzincan Ocean was followed by two major episodes of magmatism in north-central Anatolia.

The first of the major episodes is represented by middle Eocene volcanic and plutonic rocks generated in response to the Sakarya-Tauride Anatolide Block collision. Magmatic products of this stage include andesitic-dacitic lavas and agglomerates exposed to the north of Ankara (Ach, 1982; Seyitoğlu and Büyükönal, 1995; Dönmez et al., 2009) and calc-alkaline monzonitic-granitic plutons further northwest (Sherlock et al., 1999; Altunkaynak et al., 2012; Demirbilek et al., 2018). Two competing models have been

proposed to explain the source of middle Eocene magmatism in northern Anatolia. Among these models, synchronous or diachronous collision during either the Late Cretaceous and/or Eocene, followed by Eocene slab breakoff and post-collisional magmatism, is one of the most widely accepted (Keskin et al., 2008). The recently developed renewed under thrusting model (continued shortening and collision), however, challenges this hypothesis and proposes another explanation for the magma generation (Mueller et al., 2019).

The second stage of magmatism was mainly effective between the central and western part of the collisional belt and is responsible for the formation of the post-collisional Galatean Volcanic Province to the northwest of Ankara. This covers an area of approximately 6500 km^2 and consists primarily of Early–Late Miocene calc-alkaline trachyandesite-andesite to trachydacite-dacite volcanic and volcaniclastic sequences with minor rhyolite (Varol et al., 2014). The Galatean Volcanic Province is developed around several main volcanic eruption centres during post-collisional crustal extension following the subduction of the northern branch of Neo-Tethys (Varol et al., 2014).

The volcanic complex to the north of Ankara, where the Gicik gold mine is located, was initially named "Ankara Volcanics" by Ach (1982) and belongs to the first episode of magmatism in north-central Anatolia. Eocene calc-alkaline intermediate composition volcanic rocks were formed in a post-collisional tectonic setting following the thickening of the crust at eastern Anatolia, resulting in the collapse by slab-breakoff during middle Eocene (Keskin et al., 2008).

3.2.1 Geology of Gicik Gold Mine

Gicik low-sulphidation epithermal Au deposit is situated approximately 15 km north of Ankara city centre, Central Anatolia, along the southern margin of the Laurentian affinity, Sakarya Zone (Figure 20). The mine site lies adjacent to the densely populated urban centre, so settlements and recreational areas at least partly conceal the mineralised system.

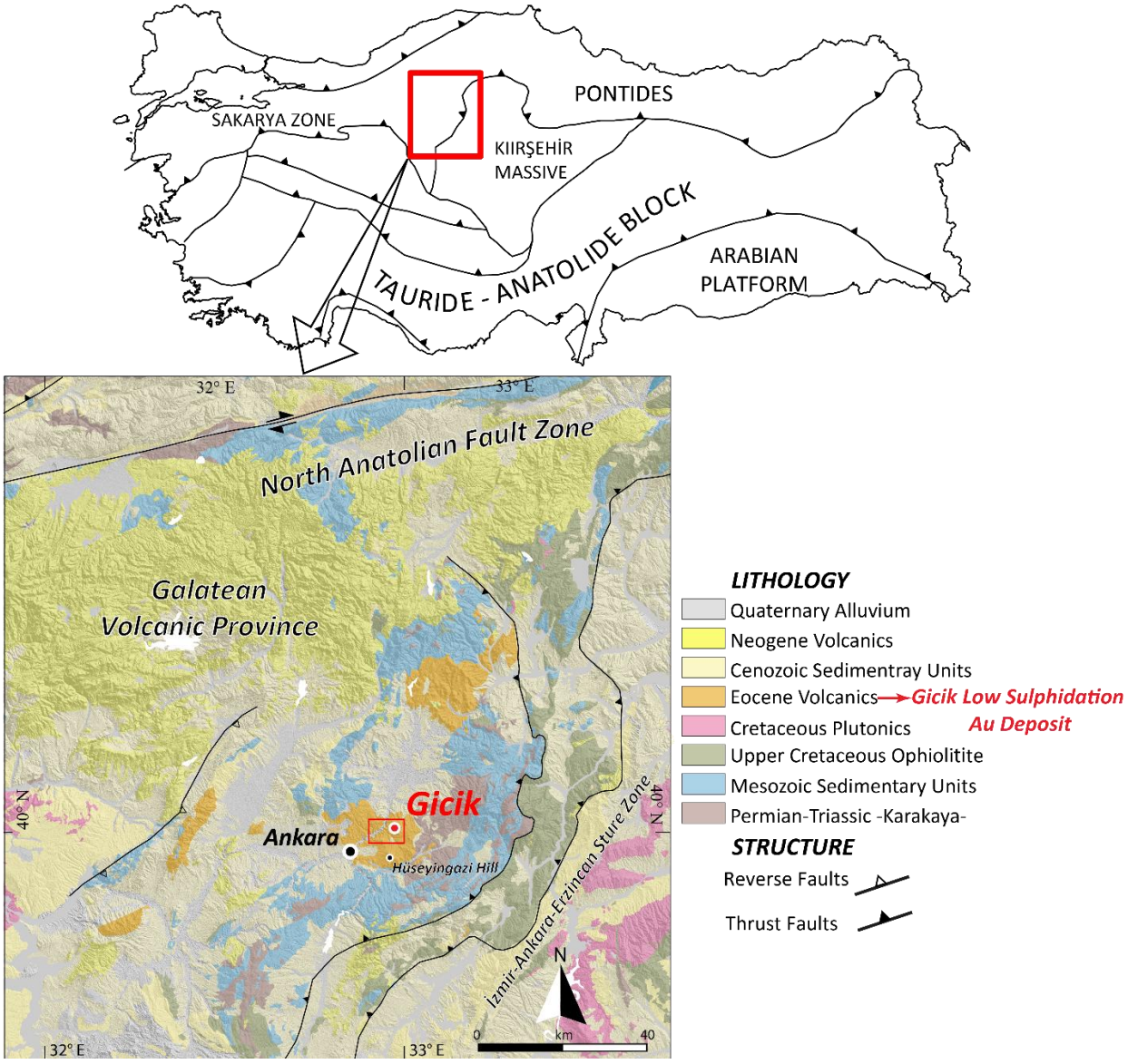

Figure 20: Geological setting of north-central Anatolia (Çil, 2019). The inset map shows the major tectonic divisions of Turkey (Okay and Tüysüz, 1999, Moix et al., 2008). (Datum: WSG84 UTM Zone)

The Gicik low-sulphidation epithermal system was first identified by Eurogold following stream sediment and Bulk Leach Extractable Gold (BLEG) sampling in the late 1980s and early 1990s. Positive anomalies from sediment sampling methods led to the discovery of a low-sulphidation epithermal-style vein system in the Gicik area. Subsequent exploration efforts included detailed geological mapping, predominantly channel rock sampling, and drilling at 22 locations, totalling approximately 2.5 km of core length, aimed at delineating the extent of mineralisation and assessing the prospect's economic potential. In 2005, Eurogold encountered environmental challenges, leading to Koza Gold Company's acquisition of the Gicik area license. This transition prompted an acceleration of exploration activities, notably drilling, resulting in nearly 49 km of additional drilling at 144 locations by 2009. In August 2008, Koza Gold commenced open-pit mining operations, producing nearly 10 thousand tonnes of ore and yielding 2800 ounces of gold and 4100 ounces of silver. However, the Gicik open-pit mine was shut after a year of operation. In 2016, the company underwent a change in ownership and became a state-owned company. Reserve development activities persisted until 2020, yet fieldwork was discontinued due to the absence of economically viable findings from drilling operations. The company, which is currently under state control, has not shared data obtained from previous studies in the field for privacy reasons.

Hüseyingazi Hill, located 4–5 km south of Gicik, is one of the several volcanic vents around Ankara and is considered the most likely eruptive centre of the volcanic rock sequences of Gicik and its environs (Figure 21). This volcanic sequence of andesitic-dacitic lava flows, tuffs, and agglomerates, also called the Tekke Volcanics, was previously included in the Ankara Volcanics (Ach, 1982) and was suggested to be Miocene as constrained by stratigraphic relationships with interbedded sedimentary units (Akyürek et al., 1984; Tankut, 1985; Besbelli and Varol, 2002). However, K-Ar and $^{40}Ar/^{39}Ar$ geochronological data from least-altered and altered lithologies yielded ages between 42 and 47 Ma (Ach, 1982; Ach and Wilson, 1986; Dönmez et al., 2009; Çil, 2019), much older (Middle Eocene) volcanic activity north of Ankara. The mineralisation in the Gicik Gold mine is hosted in andesitic-dacitic lavas of this age and agglomerates widely exposed in the region.

Figure 21: View from Gicik towards Huseyingazi Hill to the south.

Although accurately determining contact relations and lateral continuities is challenging due to widespread agricultural cover and recreational gardens, the host volcanic sequence is divided into three distinct units based on contact relationships and textural differences, from older to younger, respectively: lower yellowish-coloured massive lava flows, middle agglomerates with lava flows and tuff intercalations, and upper massive pinkish lava flows (Çil, 2019). (Figure 22). All volcanic units unconformably overlie the Pre-Cenozoic metamorphic basement (Akyürek et al., 1982, 1984), which does not crop out near Gicik and is not intersected in any of the exploration drill holes (Çil, 2019). The volcanic sequence is locally cut by NE-SW-oriented isolated andesitic dykes, having a similar orientation to the mineralised veins.

The hydrothermal system in Gicik is characterised by a large alteration footprint almost over the entire study area, manifested by widespread hydrothermal alteration of volcanic lithologies. Gold mineralisation is limited to narrow silicified vein segments in a restricted area of the mine site. The three major alteration types that are widely observed in epithermal type mineralisations were identified in the Gicik gold mine: propylitic, argillic, and silicification (Çil, 2019) (Figure 22). Propylitic alteration is observed in almost the

entire volcanic sequence and is characterised by chlorite, epidote and carbonate replacement with minor disseminated pyrite. The alteration intensity increases significantly around the vicinity of mineralised veins, almost completely replacing original volcanic lithologies while preserving the original porphyritic texture. Argillic alteration is developed throughout immediate volcanic wall rocks adjacent to the siliceous veins and is characterised by quartz-clay/sericite mineral assemblages. It appears as light grey/beige to slightly pinkish and is commonly coated with Fe-(hydr)oxide phases due to the surface oxidation of sulfides, particularly pyrite. Adularia is rare and observed only in colloform banded vein textures. Silicification is the alteration type most associated with gold mineralisation. Various types of silicification developed along mineralised veins with cores consisting of massive milky white quartz in most veins. Colloform banded veins are characterised by alternating very fine-grained to medium-grained quartz layers. Recrystallisation into quartz is evident in colloform banded veins. Quartz varieties similar to those observed in colloform banded veins are also present as cement in hydrothermal breccias as well as in lattice-bladed aggregates (developed after calcite) associated with boiling hydrothermal fluids. Dark grey varieties of quartz are associated with the common pyrite-arsenopyrite assemblage. Higher-grade gold-silver mineralisation at Gicik is intimately related to either the dark grey quartz-sulphide veins or the colloform banded quartz-pyrite-tetrahedrite veins. The final stage of silica addition into the system is marked by the presence of amethyst quartz and vitreous coarse-grained quartz, identified as late-stage open-space filling phases.

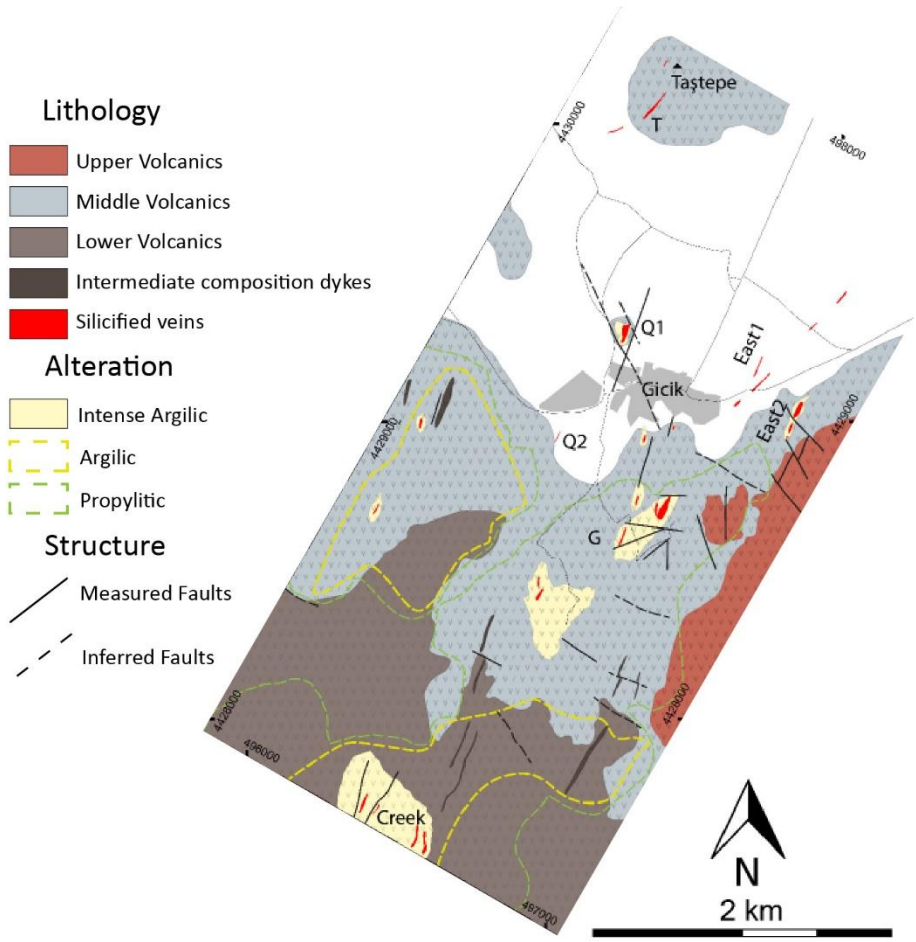

Figure 22: Detailed outcrop geology map of the Gicik area. The Blank area represents agricultural fields and recreational gardens where there is no exposure (Çil, 2019). The vein segments are named T, Q, G, East, and Creek veins by Eurogold (1990). (Datum: WSG84 UTM Zone)

The siliceous vein sets have thicknesses varying from 1 to 10 metres at the surface. Several hydrothermal textures, including colloform banding, hydrothermal brecciation, comb, cockade, drusy quartz, stockwork veinlets and lattice–bladed, are widely present in these veins. These hydrothermal textures display zonation where massive quartz veins at the inner parts gradually change to stockwork veinlets, hydrothermal brecciation, cockade, and colloform banding towards the outer sections. Each vein system has broadly similar mineralogy and texture to others. However, some significant differences and specific textures are better developed in certain vein sets. The table below presents the characteristics of veins with their orientations (Table 1) (Çil, 2019).

Table 1: Summary of the veins in terms of textures and ore mineralogy (Çil, 2019).

Vein	Segment	Thickness (m)	Exposed Strike Length (m)	Orientation	Description	Textures	Ore Minerals	Gangue Minerals
T	-	~2-3 m	~120 m	NE-SW	Blocks and boulders of silicified intermediate-composition volcanic rocks	2-5 cm thick massive quartz veinlets	-	Quartz
Q	Q1	~5-15 m	~65 m	N-S	Siliceous vein surrounded by intensely altered host rock	Stockwork, colloform banding, lattice bladed, cockade, open space filling, hydrothermal breccia	Pyrite	Quartz, amethyst quartz
	Q2	~2-3 m	~37 m	NE-SW	Two vein sets merging at the south forming the main vein	Colloform, massive, open space filling, cockade, hydrothermal breccia	Pyrite	Quartz
G	-	~1-3 m	~10-60 m	NE-SW	Comprises of several small veins	Colloform banding, grey coloured silicification, open space filling	Pyrite, arsenopyrite, tetrahedrite	Quartz
East	East1	~1-3 m	~15-40	NE-SW	Blocks and boulders of silicified host rock	-	-	Quartz
	East2	~2-7 m	~140 m	NE-SW	Several thin veins in the same orientation form the main vein	Hydrothermal breccia, gray-coloured silicification, stockwork	Pyrite, arsenopyrite	Quartz
Creek	-	~3-4 m	~40 m	NE-SW	Silica vein with intensely silicified host rock	Massive, open space filling	Minor pyrite	Quartz

Chapter 4: Field Observations

This chapter comprises field observations, descriptions, and structural data interpretation from Oxwich in Gower (South Wales) and Gicik low sulphidation epithermal Au deposit in Ankara (North-Central Anatolia, Turkey). Both study areas were investigated within their limitations as circumstances allowed.

The outcrops visited and sampled in Oxwich, designated as a natural reserve, are located on the southern coast of Bristol Channel, known for having the world's second-highest tidal range (~12 m). Therefore, access to the outcrops depends on the tide and the thickness of the beach sediments, which vary from season to season. Additionally, due to the natural reserve status of the field site, studies on the outcrops were conducted delicately.

The outcrops visited and sampled in Gicik were within an abandoned mine site; these were very close to settlements, and some of the veins mapped in previous works have since been covered by urbanisation. During the field study, the outcrops, including cockade texture, were described in detail and documented with photographs indicating locations and orientations.

A total of seven veins from Oxwich and two from Gicik were mapped to understand better the mechanisms involved in their formations (Appendices 1). The scale of mapping evidence, both challenging and supporting the proposed formation mechanisms of cockade texture-bearing breccias, is presented for both locations.

4.1 Oxwich Field Observation

4.1.1 Fissure Fills in Oxwich

Field investigations were conducted along approximately 2.5 km of coastline on the eastern shore of Port Eynon Bay, situated within the Gower Peninsula (Figure 23). This coastal segment exhibits a variety of breccias, including mosaic, crackle, chaotic, and cockade-textured breccias, distributed along both NNE-SSW and E-W trending sub-vertical fault zones, with widths ranging from a few centimetres to 2.5 metres (Figure 24). Detailed geological mapping was undertaken at five representative localities (Appendix 1.1 and Appendix 1.5).

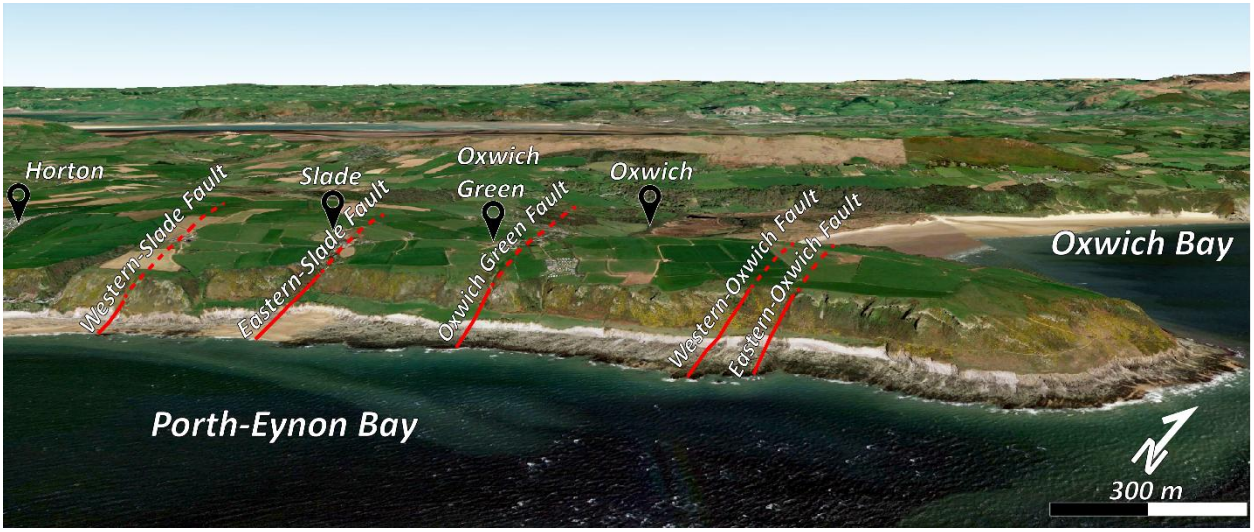

Figure 23: Google Earth's 3-D view from the south to the north shows the fissure cropping out on the eastern shore of Port Eynon Bay.

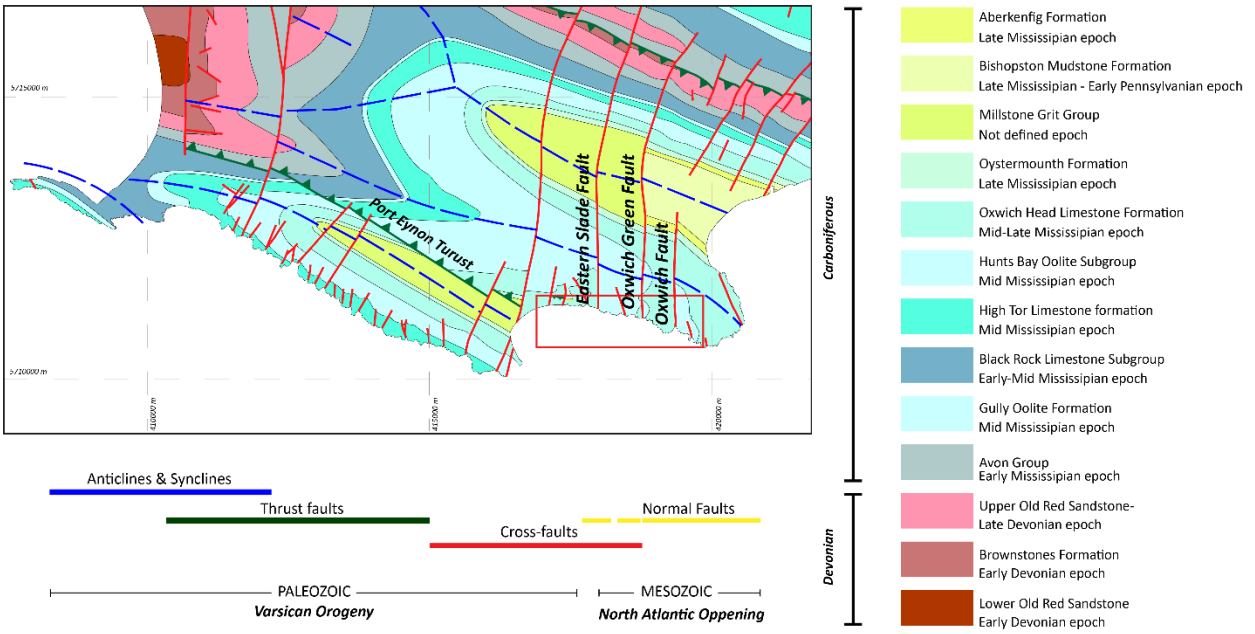

Figure 24: Geology and structural map of Gower (Modified from George (1940)) with fault names and British Geological Survey 1:50 000 maps (British Geological Survey, 2002), and beneath, structural paragenesis is modified from Wright and coauthors (2009). The red rectangle shows the study area. (Datum: WSG84 UTM Zone)

The beds within the southern limb of the eastward-plunging anticline primarily dip towards the south and SSE. However, the primary orientations of these beds and their joint sets undergo significant alteration around north-south trending cross-faults, resulting in the cutting and displacement of the limestone host rock. The walls and subsequent infill of calcite precipitates exhibit slickenside striations consistent with the dominance of strike-slip oblique fault zones (Figure 25).

Figure 25: a-c) Fault and slickenside lineation orientations in limestone host rock (a- 418922 m E 5711180 m N; b- 417831 m E 5711424 m N; c- 419228 m E 5711053 m N); d) Fault and slickenside lineation orientation in calcite vein infill (418624 m E 5711285 m N). (Datum: WSG84 UTM Zone)

The well-defined growth faces of large calcite crystals grow syntactically towards the centre of the vein, perpendicular to the fissure walls (Figure 26). These crystals display no evidence of stretching or oblique growth associated with the syntectonic precipitation of vein material due to the episodic opening of veins caused by strike-slip deformation. The presence of well-defined growth faces perpendicular to the vein wall suggests growth into a wide fluid-filled void space rather than through an incremental crack–seal mechanism (Ramsay, 1980).

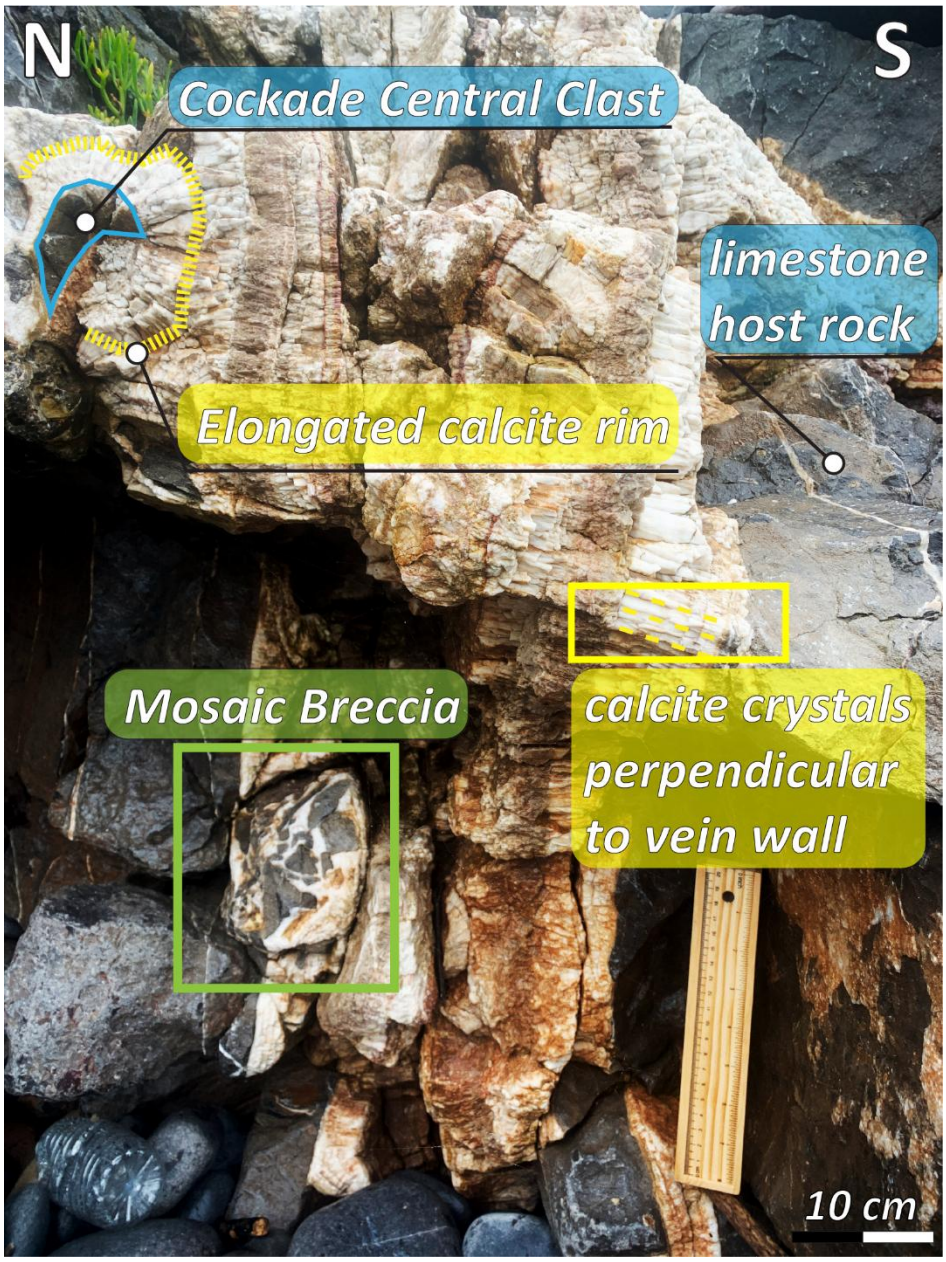

Figure 26: Well-defined growth calcite faces perpendicular to the vein wall and around the cockade crystal. This is the same zone as the photo in Figure 33, in which mosaic and cockade texture-bearing breccia are seen together (419252 m E 5711088 m N). The included ruler shows a length of 20 cm, providing a reference scale for size measurements within the image. (Datum: WSG84 UTM Zone)

In the westernmost part of the study area, a south-dipping thrust fault strikes parallel to the fold axis and is characterised by hanging wall block deformation on its low angle (20°) movement surface. The thrust conforms to the regional top to the north vergence and is cut by both N-S cross faults and E-W trending

faults. Its relationship with the other structures is apparent in the field and consistent with the paragenesis of the faults (Figure 27).

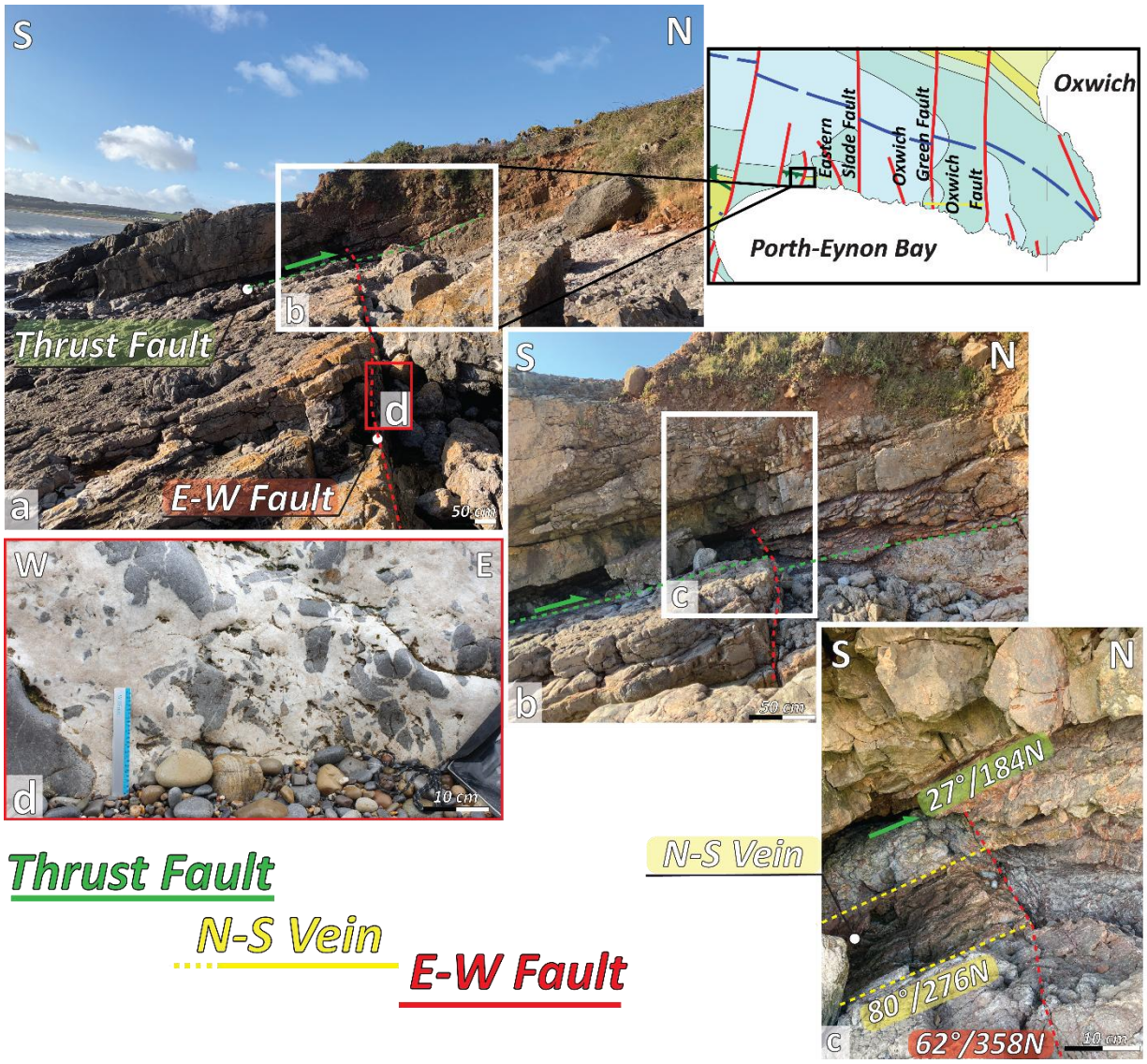

Figure 27: The temporal evolution of the thrust fault, N-S trending veins, and E-W trending faults based on crosscutting relationships.

The West-Oxwich fault provides a clear illustration of the relationship between the NNE-SSW trending vein fillings and the E-W trending vein system. The accompanying figure visually demonstrates this relationship. Notably, the widest vein observed in the field, measuring approximately 2.5 metres, is intersected vertically by E-W trending calcite-filled veins, causing interruptions along its strike. This cross-cutting relationship (Figure 28) akin to the previous figure, indicates that the E-W trending system is younger.

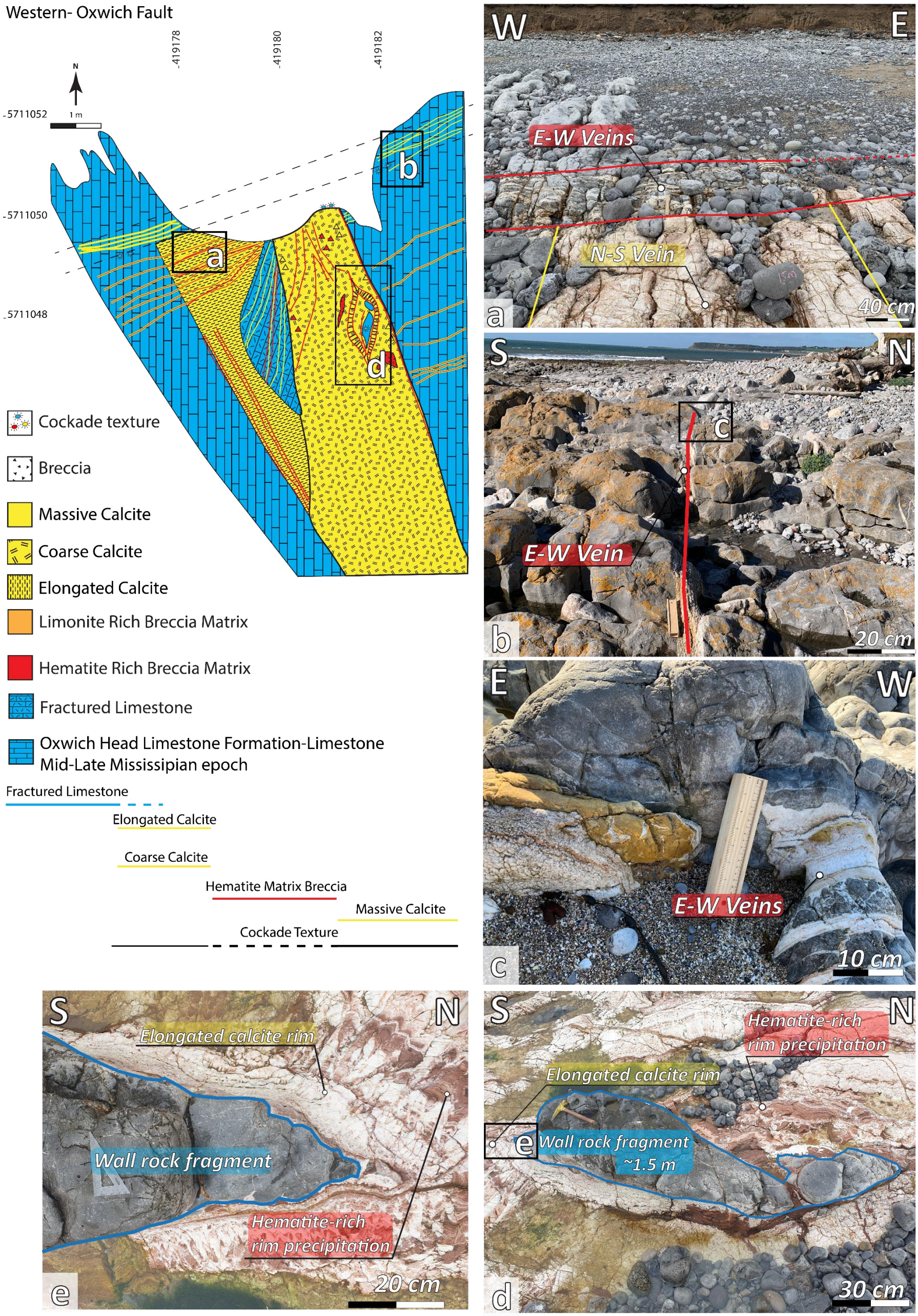

Figure 28: a) Field photograph showing the cross-cutting relationship between NNE–SSW-trending vein fillings and E–W-trending vein systems; b) E–W-trending vein; c) Close-up view of E–W-trending vein; d and e) Cockade texture with well-developed elongate calcite rims alternating with hematite-rich precipitate rims (419188 m E, 5711042 m N). (Datum: WGS84 UTM Zone)

The breccias found within fissures generally comprise angular and subangular clasts ranging from a few millimetres to 10 centimetres in diameter (29 a-c). A unique giant cockade texture featured a central clast of 1.5 metres (Figure 28 d and Figure 28 e). Clasts within crackle and mosaic breccias originate from the limestone host rock (29 a and Figure 29 b), while chaotic breccias contain a mixture of host rock and previously deformed vein fills (29 c).

29: Breccia photos from the field and their UTM coordinates; a, b and c are the crackle, mosaic, and chaotic breccia respectively, (a- 419402 m E 5711059 m N; b- 417381 m E 5711370 m N; c- 419346 m E 5711056 m N); d- f) cockade texture having elongated, fine grain and hematite precipitate rims with wall rock originated limestone central clasts (d- 419245 m E 5711083 m N; e- 419410 m E 5711048 m N; f- 417098 m E 5711475 m N). (Datum: WSG84 UTM Zone)

The central clasts of cockades are generally angular to sub-rounded, vary in size from 1 cm to 1.5 m, and are derived generally from wall rock (Figure 28 d-e and 29 e-f). As seen in 28 e and d, although it is not possible to test whether the block derived from the wall rock is in contact with the wall rock or any other clast in 3D, the size individual cockade clasts with well-developed rims fulfil the criteria of cockade texture on its surface projection.

Close to the host rock, crackle and mosaic breccias dominate, signifying the initial phases of brittle fragmentation within the examined veins. In contrast, chaotic breccias tend to occur towards the centre of the veins, indicating their formation in the later stages of vein development. This paragenetic relationship among different breccia types is particularly evident in the East-Oxwich fault, where all three types coexist. Cockade textures are observed across all breccia types, suggesting that their formation is not restricted to any specific deformation stage (Figure 30).

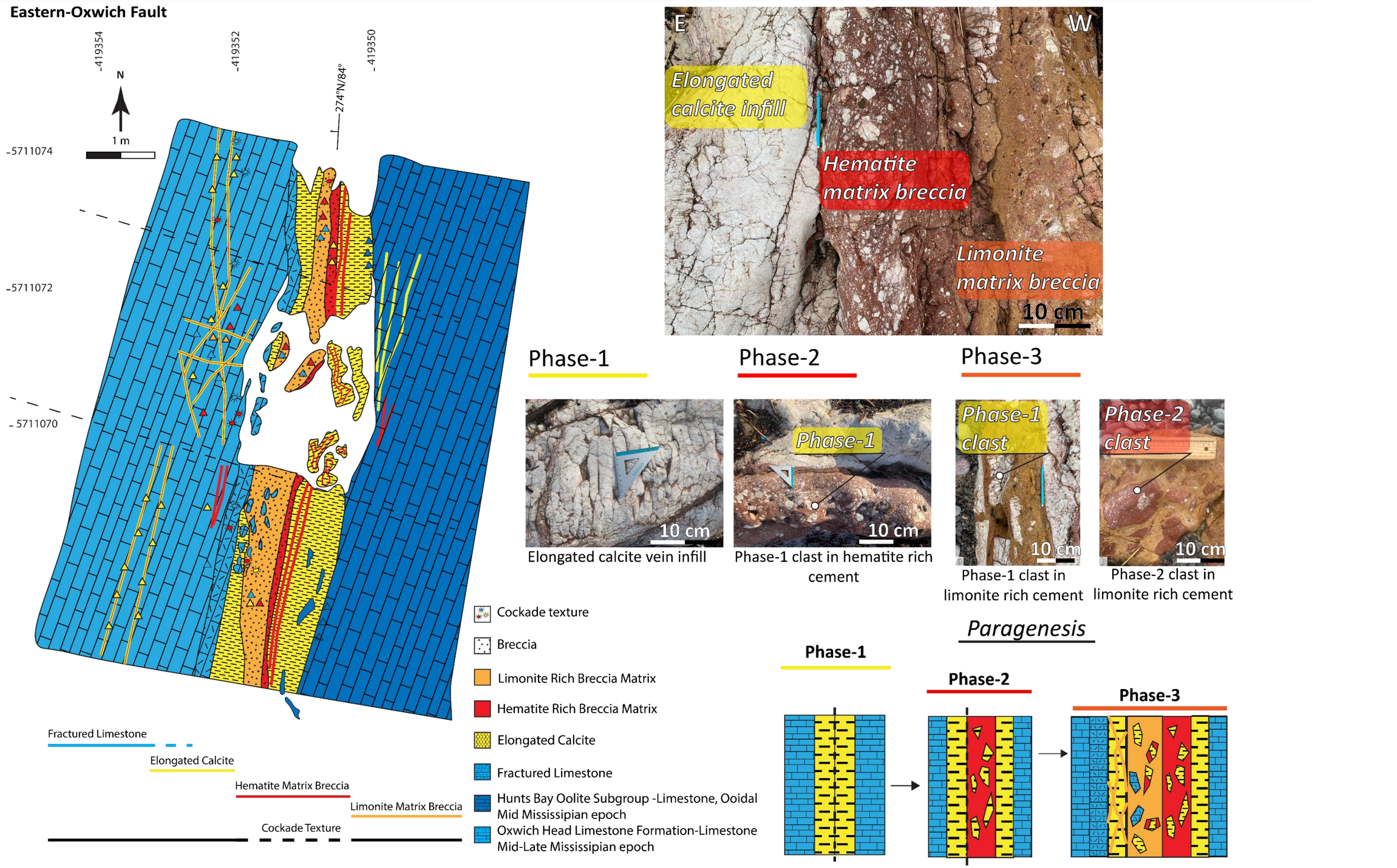

Figure 30: The paragenesis of veins on the Eastern-Oxwich Fault.

The monomictic and polymictic breccia zones are typically exposed along with fault parallel layers, each from centimetres to metres thick. The monomictic breccias are mostly observed close to the wall rock and are characterised by calcite cement fill and fragments derived from the wall rock (Figure 31 a). The cockade textures are mostly observed in this type. The polymictic breccias are observed mostly away from wall rock and are characterised by distinct clasts of different origins with cement and fine grain matrix, indicating that the brecciation was episodic and separated by periods of cementations (Figure 31 b). In Figure 31, both cockade texture-bearing and non-cockade texture bearing breccias exhibit jigsaw-fit clast textures, indicating a low degree of rotational misfit of the clasts characteristic of mosaic and crackle breccias (Mort and Woodcock, 2008; Woodcock and Mort, 2008; Frenzel and Woodcock, 2014).

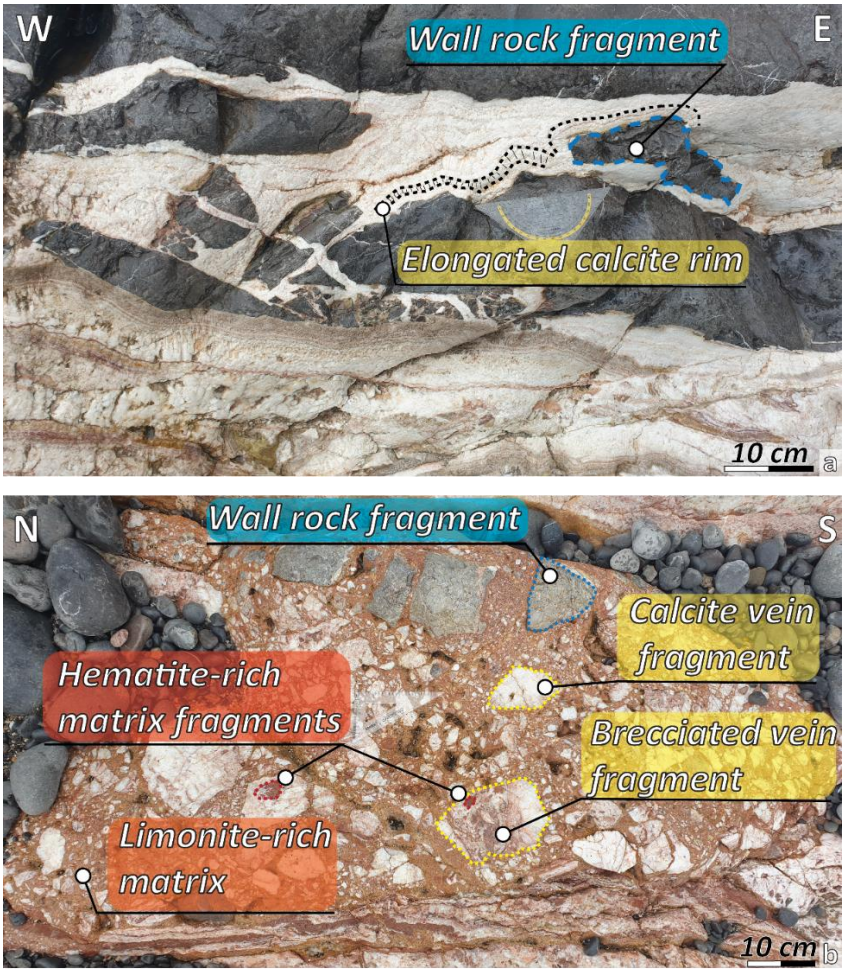

Figure 31: The monomictic and polymictic breccia photos from the field. a) The monomitic cockade texture-bearing breccia comprises angular fragments derived from wall rock and shows jigsaw-fit clast textures with a high cement-to-clast ratio. (419252 m E 5711088 m N); b) The polymictic chaotic breccia comprises angular to subrounded clasts driven from wall rock, and previously deformed vein fills in a limonite-rich matrix and shows a relatively lower-cement to clast ratio with respect to cockade texture-bearing breccia (Eastern-Oxwich Fault) (419344 m E 5711048 m N). (Datum: WSG84 UTM Zone)

The cockade clasts do not touch each other and fulfil the criteria for the correct identification of the texture (Frenzel and Woodcock 2014). The central clasts are separated by the surrounding rims, which are composed of calcite cement with different textures (i.e. blocky, elongated, or massive) and fine-grain hematite-rich precipitates. Blocky calcite occurs as masses of equant crystals with no preferred orientation. They have commonly grown inwards into an open space. The elongated calcite crystal growths have their long axes perpendicular to vein walls or pointing outwards, mimicking the shape of the central clasts of cockades (Figure 32), which indicates epitaxial growth. Both blocky and elongated textures are classified as open-space filling primary growth vein textures (Dong et al., 1995), and their formation is closely associated with the degree of saturation of the fluid and surface energy and anisotropy of the calcite crystal. Blocky texture growth tends to occur when there is ongoing nucleation of new crystals during growth, whereas elongated blocky textures are generally interpreted in terms of competitive crystal growth normal to the substrate (Oliver and Bons, 2001). Such competition implies a lower nucleation rate of new seed crystals than for the equant blocky calcite and a lower degree of supersaturation of the fluid. During the field study, the rims composed only of calcite cement were differentiated by the textural differences developed during their growths (Figure 32).

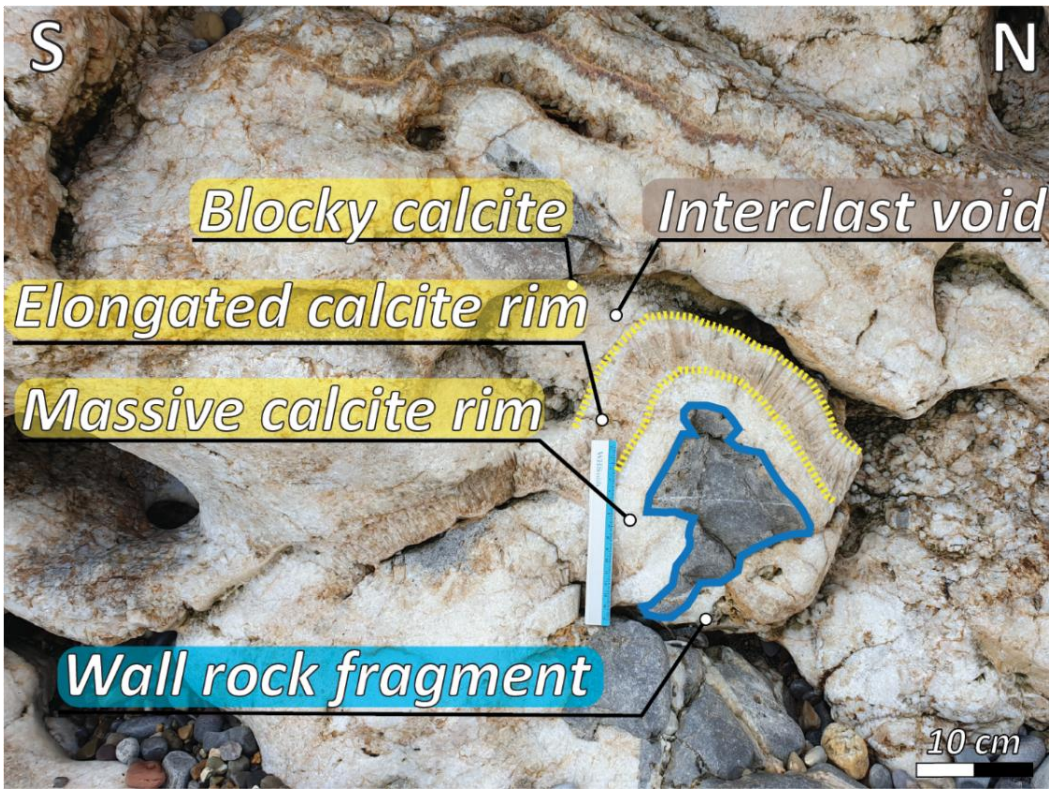

Figure 32: Cockade texture-bearing breccia with massive and elongated calcite rims with blocky calcite precipitates in interclast voids (417133 m E 5711479 m N). (Datum: WSG84 UTM Zone)

As the distance between vein walls increased, a vertical progression from jigsaw-fit to cockade textures was observed, correlating with increasing aperture in the breccia. Figure 33 illustrates the transition from mosaic breccia, characterised by a lower cement-to-clast ratio, to cockade texture-bearing breccia, with a higher cement-to-clast ratio as wall separation increased from 12 to 16 cm. Although both mosaic and cockade texture-bearing breccia have calcite cement, distinct textures emerge over short distances. The cement in mosaic breccia displays a massive, fine-grained calcite texture, whereas the cement in cockade texture-bearing breccia consists of elongated and blocky calcite crystals, indicative of open space-filling textures. The progression from crackle breccia to cockade texture-bearing breccia from bottom to top suggests that cockade texture can form without significant rotation as the open space between clasts increases with the widening vein aperture. Furthermore, as shown in Figure 31 a, elongated calcite rims surround the jigsaw-fit distribution of the fragments derived from the host rock, and the fragments are not in contact with each other. Cockade texture-bearing breccias composed of angular fragments exhibit jigsaw-fit clast textures, indicating a low degree of rotational misfit, which is characteristic of mosaic and crackle breccias (Mort and Woodcock, 2008) (Figure 31 a).

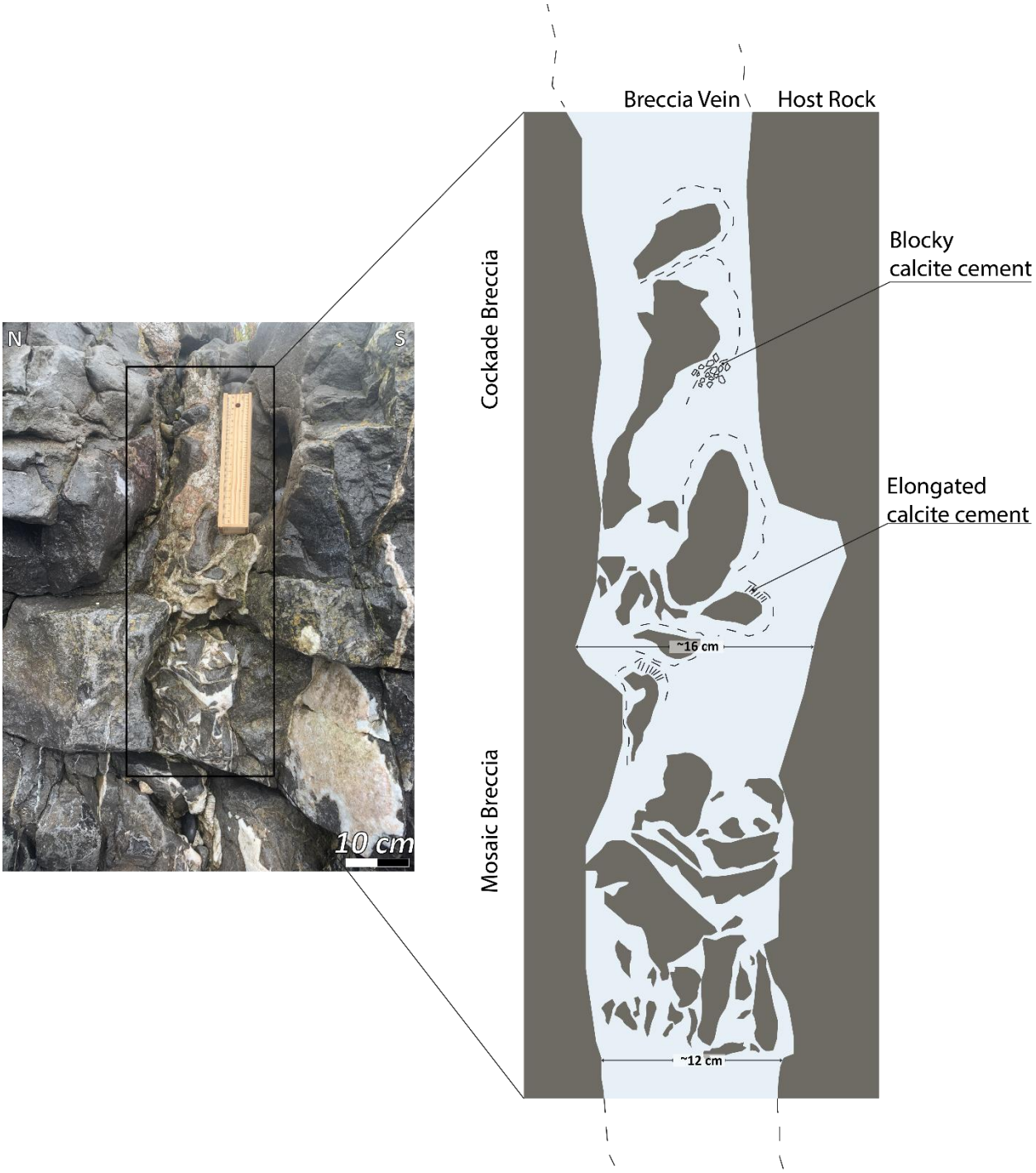

Figure 33: Transition from mosaic to cockade texture-bearing breccia in the same vein (419252 m E 5711088 m N). The included ruler shows a length of 20 cm, providing a reference scale for size measurements within the image. (Datum: WSG84 UTM Zone)

The ferruginous infills of breccias, typically reddish or orange-brown due to their hematite or limonite content, are found in both matrix and cement forms, i.e. fine (<2mm) sediment with lamination (Figure 34) and fine grain hematite precipitate (Figure 35) alternating with open space calcite textures,

respectively. The fine-grain geopetal sediments were observed as sub-horizontal laminated sediment in steeply dipping fissures and cockade texture (Figure 34). As seen in Figure 34 a and b, limonite and hematite-rich sediment fissure fills with lamination are deposited by gravitational settling and are not affected by shear deformation. Figure 34 d and e show the residual voids in veins filled by hematite-rich sediments. Figure 34 c is a clear example of unrotated geopetal sediments horizontally deposited on a clast surrounded by elongated calcite crystal growth, which indicates no significant rotation during rim precipitation after the depositing of this sediment on top of the central clast.

Figure 34: The photos of sediment infills in fissures; a-b) limonite and hematite-rich sediment fissure fill, respectively, deposited by gravitational settling in fissures.(a-418083 m E 5711422 m N;b-417830 m E 5711446 m N); c) Western Oxwich fault - unrotated geopetal infill deposited on top of a cockade texture central clast (419193.67 m E 5711059.01 m N); d-e) the residual voids in veins filled by hematite-rich sediments (d-419347 m E5711047 m N; e-419399.79 m E 5711053.40 m N). (Datum: WSG84 UTM Zone)

Figure 35 a and b show the precipitated hematite interlaminated with elongated calcite growing perpendicular to the steeply dipping fissure wall. The alternating calcite and hematite rims, which also surround the central clast of the cockade, ease the identification of cockade texture rims by creating colour contrasts in the field. Hematite-rich layers are observed as fine-grain precipitates interlaminated with

elongated carbonate minerals by mimicking the shape of the previously formed crystals. Interlaminated hematite-rich precipitates and large calcite crystals with well-defined growth faces indicate growing into an open space.

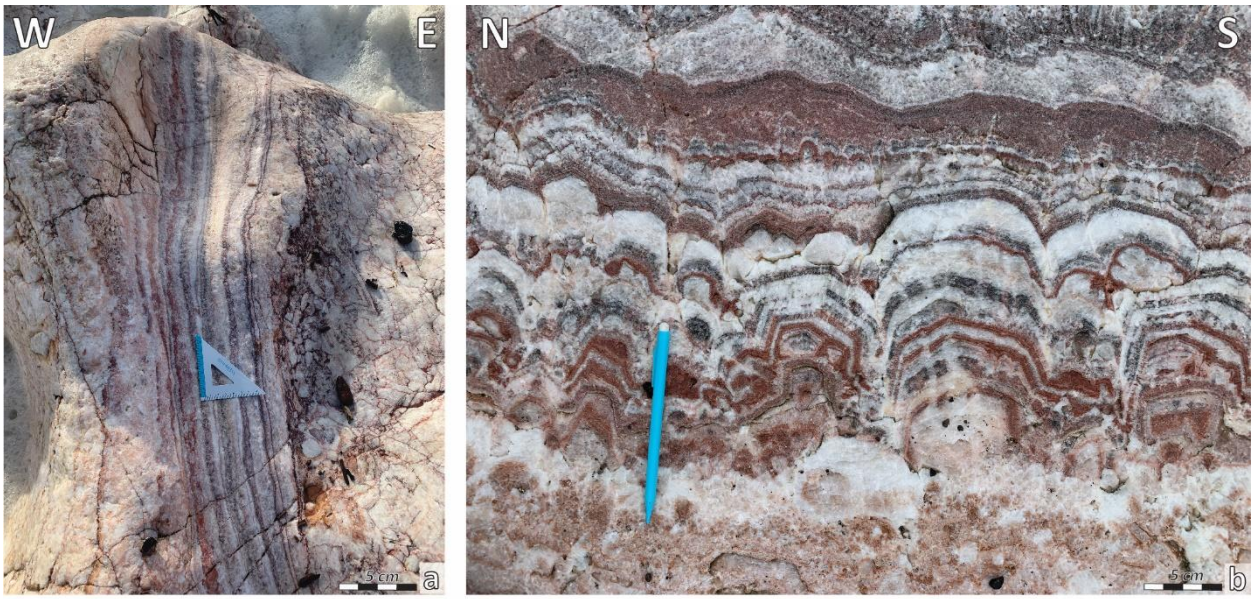

Figure 35: The precipitated hematite interlaminated with elongated calcites as vein infills on Western and Eastern-Oxwich faults, respectively (a- 419188 m E 5711037 m N; b-419352 m E 419352 m E). (Datum: WSG84 UTM Zone)

4.1.2 Discussion and Conclusion

The deformation history and related structures in Oxwich can be summarised as follows. Following the deposition of Lower Carboniferous platform limestones, the region was subjected to Variscan orogenic deformation during the Late Carboniferous, resulting in the formation of folds, thrust faults, and cross-faults, with some temporal overlap in their development (George, 1940; Roberts, 1979; Wright et al., 2009). Toward the end of the Triassic, post-orogenic sedimentary cover, including, was eroded, as evidenced by the Early Triassic unconformity. The N-S trending cross-faults exhibit brittle-ductile deformation, likely linked to tectonic thickening before erosion (Wright et al., 2009). During the Mesozoic extension associated with the opening of the North Atlantic Ocean (Dore et al., 1999), the region experienced renewed tectonic activity, leading to the development of E-W trending faults, which are identified for the first time in this study (Figure 27). Hydrothermal fluids circulated along both pre-existing fissures (Ault et al., 2016) and these newly developed E-W trending faults. Cockade textures, the primary focus of this study, are observed in both N-S trending cross-faults and E-W trending faults.

The formation of cockade texture-bearing breccias under the suspension in fluid mechanism is hypothesised to occur in two contrasting fluid conditions: (1) a highly viscous, dense mineralizing fluid, intermittently agitated by fault movement (Spurr, 1926; Dill and Weber, 2010), and (2) a low-viscosity, high-velocity hydrothermal fluid, capable of suspending clasts within dilatational cavities (Farmin, 1938; Jobson et al., 1994; Cox and Munroe, 2016). The first scenario requires a substantial amount of fine-grained argillaceous material to maintain a drilling-mud-like viscosity (~6.0 –13.0 mPas at 25°C, compared to ~1 mPas for water at 25°C; Zhang et al., 2021), which is essential to counteract gravitational settling. Similar to previous studies (Dill and Weber, 2010), our field observations in Oxwich do not support this hypothesis, as the fault fills lack significant argillaceous sedimentary infill. While it is possible that such material was initially present and later transported away, leading to a reduction in viscosity and potential breccia collapse, no field evidence suggests significant post-depositional removal. This absence indicates that high-viscosity fluid suspension is not a viable mechanism for the formation of cockade textures at this site. The second scenario involves fluidisation via low-viscosity, high-velocity hydrothermal fluids, where the required minimum flow velocity for clast suspension can be quantitatively constrained.

Hydrodynamic calculations suggest that for a 5 cm-sized clasts, a typical size range for cockades (Leroy et al., 2000), fluid velocities must exceed 0.88 m/s (Pettyjohn and Christiansen, 1948; Gaskell, 1992; Frenzel and Woodcock, 2014), with minimum fluidisation flow rates estimated at 0.24 m/s for a loosely packed aggregate (Eichhubl and Boles, 2000; Frenzel and Woodcock, 2014). However, to sustain continuous

suspension, considerably higher flow rates would be necessary, potentially reaching 10–20 m/s during peak fluidisation pulses (Frenzel and Woodcock, 2014). Although such transient high-velocity pulses may occur during seismically induced fault-valve cycles (Sibson, 1981, 1990), sustaining this over prolonged timescales remains hydrodynamically unrealistic (Frenzel and Woodcock, 2014). Additionally, our field observations from Oxwich reveal significant discrepancies between theoretical suspension models and natural clast sizes. For example, a ~1.5-metre-sized central clast from the East Oxwich Fault (Figure 28 e and Figure 28 d), while meeting the general morphological criteria of a cockade texture (i.e., being isolated and rimmed by cement overgrowth), would require fluid velocities orders of magnitude greater than those calculated for 1–5 cm clasts to remain suspended during rim accretion. Such an extreme scenario is physically implausible, reinforcing the conclusion that episodic fluidisation and transient clast mobility are more realistic processes than long-term suspension-driven growth.

The rotation-accretion hypothesis deals satisfactorily with the intermittent fluidisation and subsequent partial cementation, two needed sub-mechanisms for forming cockade texture (Frenzel and Woodcock, 2014). The three mainstays for this mechanism are the deposition of truncated segments of growth rims, rotated geopetal sediments and reverse size grading of clasts on the outcrop and the microscopic scale. It has been stated that truncation in outgrowth rims and the rotated geopetal sediment deposition between cements are direct evidence of the rotation of the clasts during the formation of cockade texture. Reverse grading of cockades within individual breccia units can result from either the Brazil-Nut effect, which is the tendency of larger particles in an agitated self-supporting mass of non-equigranular particles to migrate towards the top (Möbius et al., 2001), or simple shear granular flow. Reverse grading is compatible with the proposal that seismic shaking is the major mechanism for refracturing the breccia and rotating the clasts. Neither truncation on outgrowth rims nor reverse grading was observed on the outcrop scale in the field; on the contrary, a very clear example of unrotated geopetal sediment depositions was documented during the field study (Figure 34 c). This indicates that rotation of central clasts during the cement growth is not required to form cockade texture. Moreover, as the distance between vein walls increased, a vertical progression from jigsaw-fit crackle to mosaic to cockade texture-bearing breccia was observed in the direction of increasing aperture (Figure 26 and Figure 33). This transition in a single vein as the aperture opens is evidence of a lack of rotation. Therefore, the rotation and accretion hypothesis has also been ruled out for cockade texture formation due to the lack of rotation.

Pressure growth develops crystal faces projecting in all directions if the mineral phases have high surface energy and surface energy anisotropy (e.g., pyrite vs. quartz or calcite and quartz; Spry, 1969). The

hypothesis of pressure growth of crystals in stationary conditions within pressurised fluids is compatible with each criterion of cockades. It has been proven that crystallisation pressure is a mechanism that drives dilation in veins by exceeding the tensile strength of the rock and is sufficient to push vein walls apart (Wiltschko and Morse, 2001). Experimental studies indicate that crystallisation pressure can achieve magnitudes of 30 MPa (Zheng et al., 2018, 2019). Additionally, microstructural observations show that the rims surrounding the core clasts, and each rim grow in an epitaxial way over the previous one, and epitaxial growth in the presence of fluids is the most energetically favourable process of crystal growth, as proven by experiments and numerical modelling (Putnis and Putnis, 2007; Mithen and Sear, 2014). These experimental and mineralogical observations are also supported by conceptual and thermodynamic models suggesting that significant crystallisation pressures are associated with supersaturated fluids in diagenetic environments and high-fluid pressure crack-sealing veining. The pressure growth hypothesis depends on the availability of free pore space between particles and the supersaturation degree of the fluid, which may result in the precipitation of a concentric rim around cockade clasts. The well-defined growth faces as seen in the fissures of Oxwich and visible on the larger crystals, like in the elongated blocky calcite texture, indicate that they grew into a wide fluid-filled void space rather than by an incremental crack–seal mechanism, which is controlled by supersaturation of host fluid and refers to hydrothermal and meteoric water involved in the diagenetic process (Oliver and Bons, 2001). The transition from crackle to mosaic to cockade texture-bearing breccia within a single fissure can be explained through the influence of the crystallisation mechanism. Wiltchko and Morse (2001) suggest that the pressure generated by crystal growth can promote vein development, akin to how fluid pressure drives hydrofracture propagation. Notably, the concept of crystallisation force does not mandate dynamic fluid flow within the system; it can also operate effectively in a static fluid environment. Consequently, the development of a cement-dominated zone rich in cockade texture, accompanied by an expanding aperture between vein walls and the coexistence of crackle-to-mosaic breccia within the same vein, may be ascribed to the effects of crystallisation force.

Textural and kinematic observations of these fissures suggest that, while episodic opening was driven by external forces, the veining process was predominantly controlled by fluid chemistry, with subsequent diagenetic overprinting along fissure walls. Although E-W trending faults demonstrably cut and displaced N-S trending fissures, instances of the opposite crosscutting relationship were also observed in some locations. This suggests that N-S fissures were locally reactivated during hydrothermal fluid circulation in the Early Cretaceous, potentially operating in conjunction with E-W trending faults.

These observations highlight that the force of crystallisation must be considered as a key mechanism in the formation of cockade textures at Oxwich. Frenzel and Woodcock (2016) conducted their study in the same locality, proposing the rotation and accretion model as the primary mechanism for cockade formation. This model suggests that cockade textures develop through repeated clast movement and cement accretion. However, our findings indicate that the separation of central clasts is more plausibly explained by the force exerted during crystal growth. While this mechanism is not universally applicable to all breccias, and not all cockade textures are necessarily linked to the seismic cycle, our observations suggest that at Oxwich, the force of crystallisation played a more significant role than previously proposed. In fact, the preservation of cockades formed by the force of crystallisation may indicate prolonged stability within fissure fills near the Earth's surface.

4.2 Gicik Field Observations

4.2.1 Veins at Gicik

Gold mineralisation at Gicik is hosted within a series of discontinuous veins, with thicknesses typically varying between 1 and 5 metres and extending along strike for approximately 100 metres (Figure 36). The veins generally dip steeply and are mainly parallel within NE trending faults in the lower and middle volcanic series (Figure 37). The veins were named T, Q, G, East, and Creek veins during the early exploration stages of Gicik, done by Eurogold; for this reason, the names are kept the same in this study for convenience. The veins are hosted in porphyritic dacite lava flows, agglomerates, and tuff, and the associated hydrothermal alteration has produced a widespread alteration footprint covering most of the study area. Propylitisation, argillic alteration and silicification are three significant types of hydrothermal alteration in Gicik, and the cockade texture has been observed in the T vein, Q-1 vein, and Q-2 vein, adjacent to highly silicified regions. The cockades are accompanied by other open-space textures, such as colloform banding and replacement textures, such as lattice–bladed textures, which are considered to have characteristics of low to intermediate sulphidation systems (Simmons and Christenson, 1994; Hedenquist et al., 2000; Einaudi et al., 2003; Sillitoe and Hedenquist, 2003; Simmons et al., 2005).

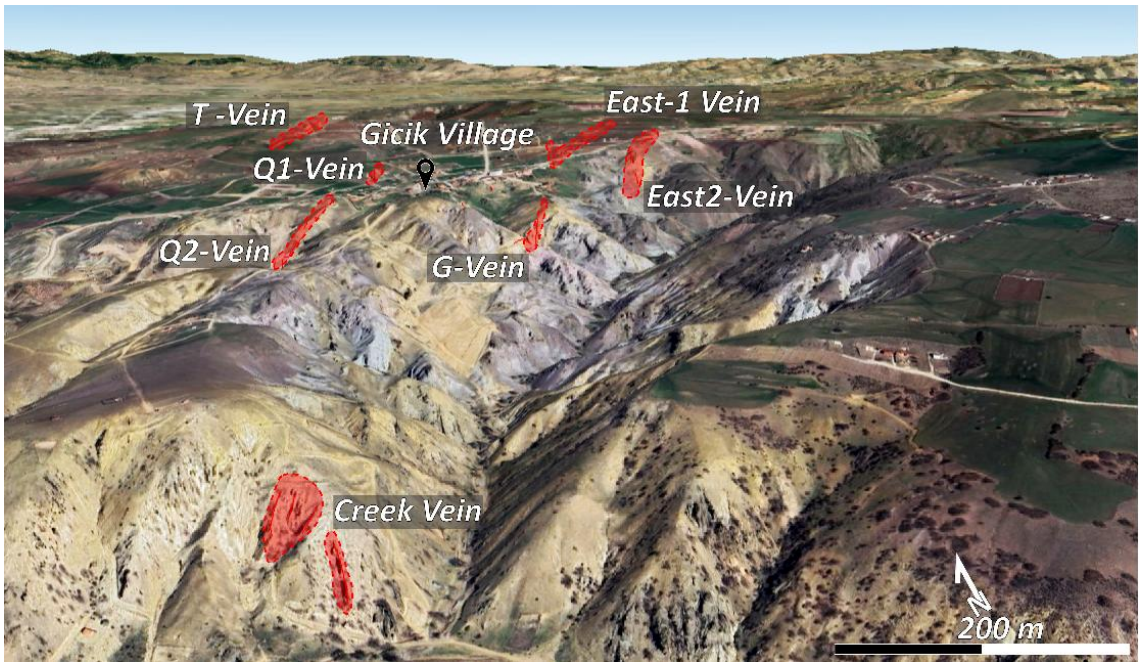

Figure 36: Google Earth image of the Gicik area displaying the siliceous veins. The red dashed lines indicate the T Vein, Q-1 Vein, Q-2 Vein, East-1 Vein, East-2 Vein and G Vein segments, named by Eurogold (1990) during the early exploration activities.

Figure 37: Field photographs of vein segments and their UTM coordinates. a) T vein exposed at the north of Gicik (497496 E, 4430126 N); b) Contact between prophylitic agglomerate and argillised andesite with silicious vein observed in the Q-1 vein segment at the north of Gicik Village (497249 E, 4429198 N); c) Q-2 vein cross-cutting upper volcanics at the south-west of Gicik Village(497035 E, 4428873 N); d) East-1 vein at the east of Gicik village (497711 E, 4429129 N); e) East-2 vein at the south-east of Gicik village (497809 E, 4428866 N); f) The best-exposed section of the NE-SW trending G-Vein exposed immediately to the south of Gicik village (497333 E, 4428844 N); g-h) Best exposed sections of northern Creek veins at the southernmost part of the study area(496521 E, 4427395N). (Datum: WSG84 UTM Zone)

Çil (2019) subdivided the volcanic lithologies into three sequences, i.e. lower, middle and upper volcanic, based on dominant lithological units, macro-textural observations and their topographic elevations. The lower volcanic series crops out in the southwestern part of the study area and is represented by pinkish and yellow-grey massive dacitic lavas. The middle volcanic series comprises agglomerate, tuff, and porphyritic dacite intercalations and hosts almost all siliceous veins associated with mineralisations. The upper volcanic series, seated at relatively higher elevations, caps the underlying lower and middle volcanic series at the eastern sector of the study area and is characterised by dacite flows with agglomerate intercalations. The entire volcanic sequence is cut by NE-SW-oriented mafic to intermediate composition dykes, which have similar orientations to mineralised veins (Figure 38).

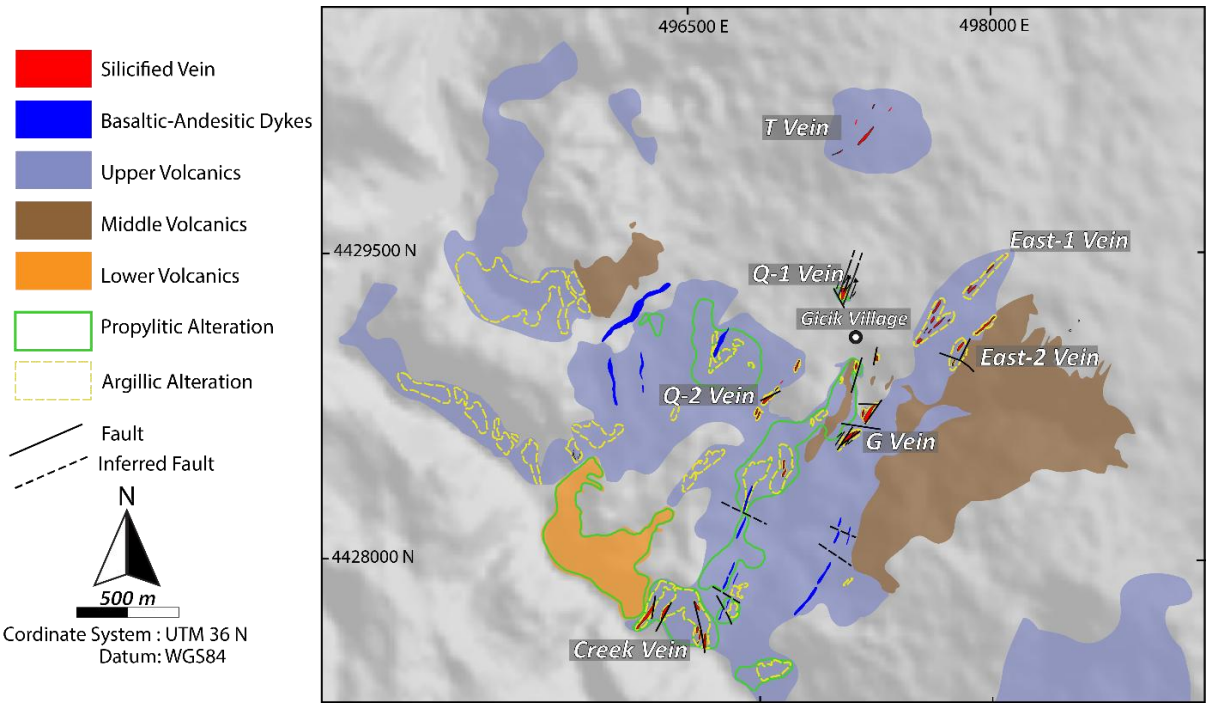

Figure 38: Detailed outcrop geology map of the Gicik area. Blank areas represent agricultural fields and recreational gardens where there is no exposure (modified from Çil, 2019). (Datum: WSG84 UTM Zone)

Three main alteration styles observed in Gicik are pervasive propylitisation, vein-proximal argillic alteration, and silicification. Propylitisation, the most widespread alteration style, intensifies significantly near mineralised veins and gradually transitions into argillic alteration, which is oriented perpendicular to the vein. It is primarily represented by chlorite replacing ferromagnesian minerals, accompanied by minor disseminated pyrite (Figure 39 a). Argillic alteration is predominantly observed adjacent to intense silicification, forming an envelope around quartz veins. The altered host rock exhibits a light grey/beige to slightly pinkish colouration and is commonly coated with Fe-(hydro)oxide phases. These coatings result

from the surface oxidation of sulfides, particularly pyrite. The alteration is characterised by the partial to complete replacement of primary igneous minerals, driven by the slightly to moderately acidic nature of hydrothermal fluids in low-sulphidation epithermal systems (Simmons et al., 2005) (Figure 39 b).

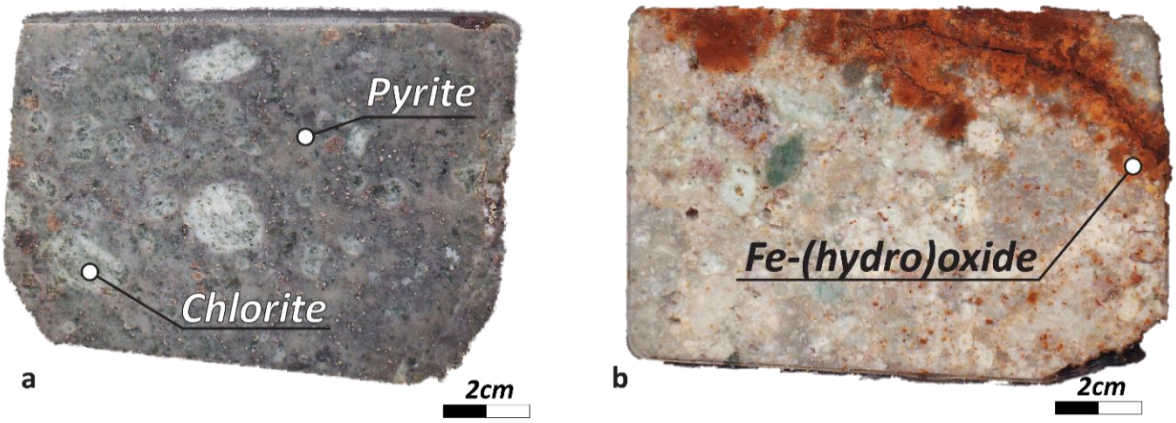

Figure 39: a) Typical appearance of prophylitic alteration in hand specimen close to the East-1 vein (497642 E, 4428778 N); b) typical appearance of argillic alteration in hand specimen close to the East-2 vein (497776 E, 4428760 N). (Datum: WSG84 UTM Zone)

Silicification is directly associated with gold mineralisation in Gicik. Petrographic microscopy studies reveal that microcrystalline quartz replaces the groundmass of andesitic wall rocks, whereas the phenocryst phases, e.g. hornblende, biotite, pyroxene, and plagioclase, are leached out, resulting in a vuggy texture (Figure 40 a and Figure 40 b) (Çil, 2019). The vuggs within the silicified host rock are partially filled with chalcedony and granular quartz (Figure 40 b).

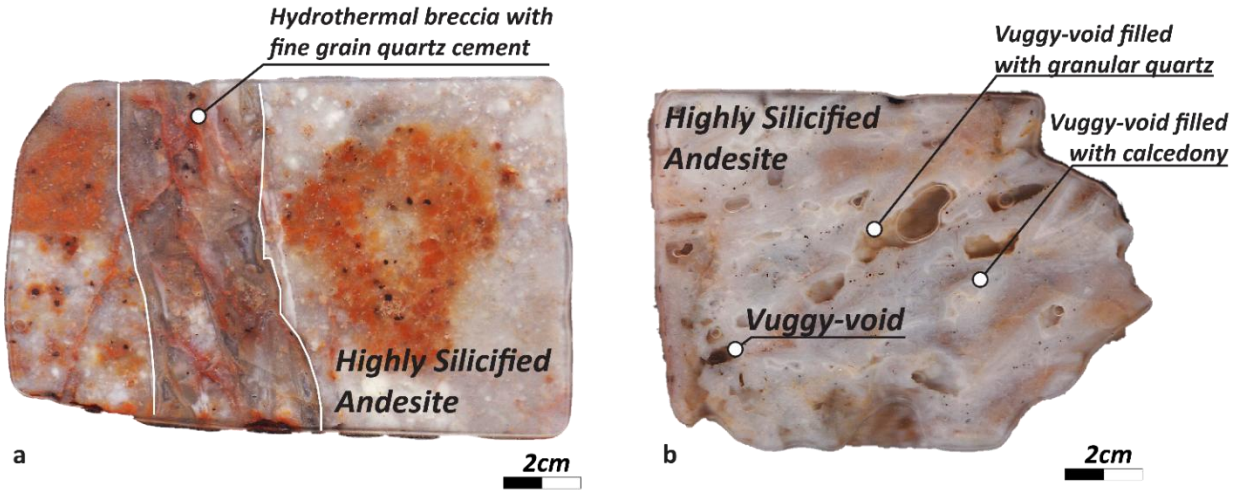

Figure 40: a) Typical appearance of silicified andesite from Q-1 vein in hand specimen (497223 E, 4429095 N); b) Typical appearance of silicified andesite from Q-2 vein in hand specimen (496999 E, 4428760 N). (Datum: WSG84 UTM Zone)

Various types of quartz developed along mineralised veins, which are also present as cement in hydrothermal breccias, including fine-grain grey quartz, fine-grain vitreous quartz and fine-grain milky quartz. According to Çil (2019), dark grey varieties of quartz are associated with the pyrite-arsenopyrite and quartz-pyrite-tetrahedrite mineral assemblages. Mineralisation at Gicik is intimately related to this early open space-filling phase. In contrast, vitreous and milky quartz is associated with late-stage open-space filling phases and is mostly seen after the dark grey quartz in colloform texture (Figure 41).

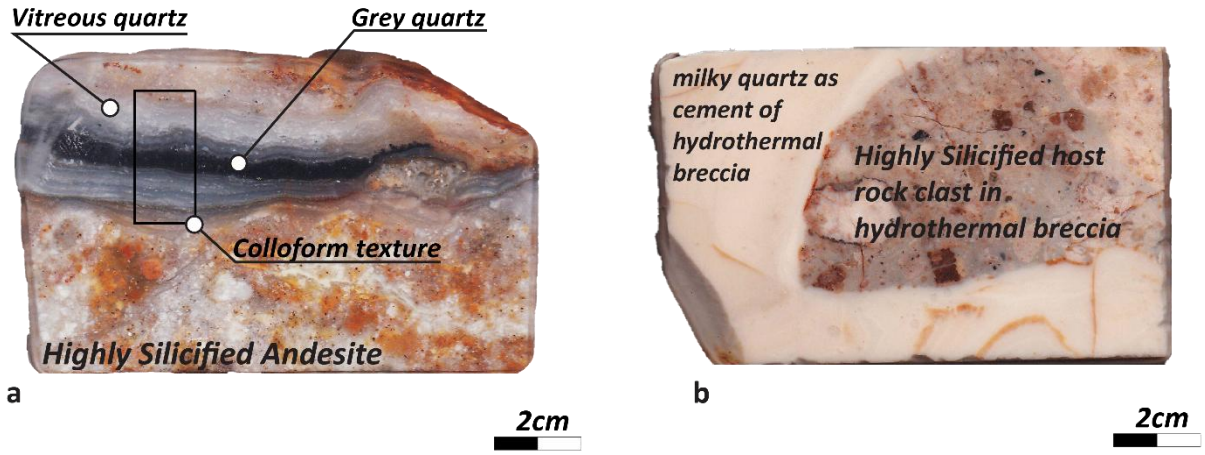

Figure 41: a) Typical appearance of dark and vitreous quartz in colloform texture from East-1 vein in hand specimen (497606 E, 4428877 N); b) Typical appearance of milky quartz from T vein in hand specimen (497326 E, 4429879 N). (Datum: WSG84 UTM Zone)

According to Eurogold's initial exploration program, towards the north of Gicik, T vein crops out at the surface as NE trending segments reaching the length of 120 m in a middle volcanic series; however, recently, it has been concealed mainly by the agricultural and recreational activity. Observations were made from locally derived loose blocks. T vein is characterised by a well-developed colloform, comb and cockade texture, and it is mostly made of cryptocrystalline milky quartz (Figure 42). The rock chip samples taken from the outcrop by Euroggold are barren, whereas significant assay values (16.8 g/t Au) were obtained from the core samples during early drilling operations (Çil, 2019).

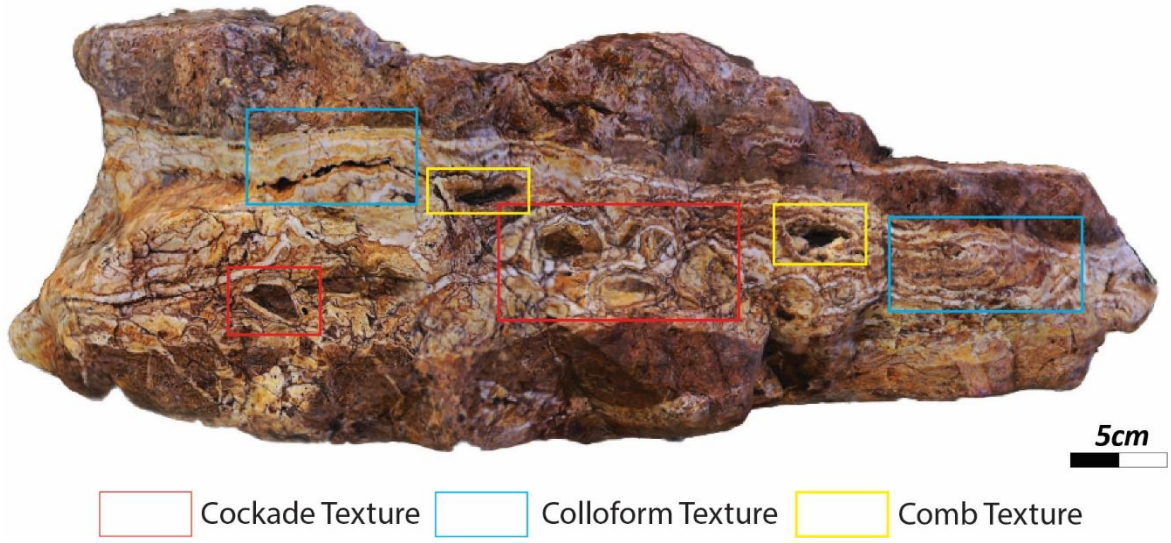

Figure 42: Open space filling texture observed in the not-in-situ block around T vein.

The NNE-trending Q vein, known as the original discovery vein, comprises two segments: Q-1 to the NNE and Q-2 to the SSW. Based on historical surface and core data, the Q-vein represents the most significant part of the mineralisation in Gicik. However, the continuity between the Q-1 and Q-2 segments along strike is completely covered by the Gicik village settlements. Koza Gold, the last license owner, operated the southmost part of the sector, finding ten ppm Au values from rock samples from the surface (Çil, 2019). The veins have a strike length of approximately 100 metres, with thicknesses ranging from 1 to 5 metres. No clear correlation was identified between vein thickness and the occurrence of cockade textures in this study. While cockade structures were observed in some narrow veins, they were not consistently present in wider ones, suggesting that vein thickness alone may not control their formation. The zone exhibiting the best zonation in terms of alteration presents an abrupt transition from the silicified quartz vein in the centre, passing into a few metre-wide zones of argillic and then propylitic alteration (Figure 39 b). Additionally, the Q veins contain the best hydrothermal open space and replacement textures, including colloform banding, comb, lattice bladed, and well-developed cockade texture. For this reason, the Q-1 segment (Figure 43) and the remnant northmost part of the Q-2 segment (Figure 44) were mapped in detail for this study (Appendix 1.6 and Appendix 1.7).

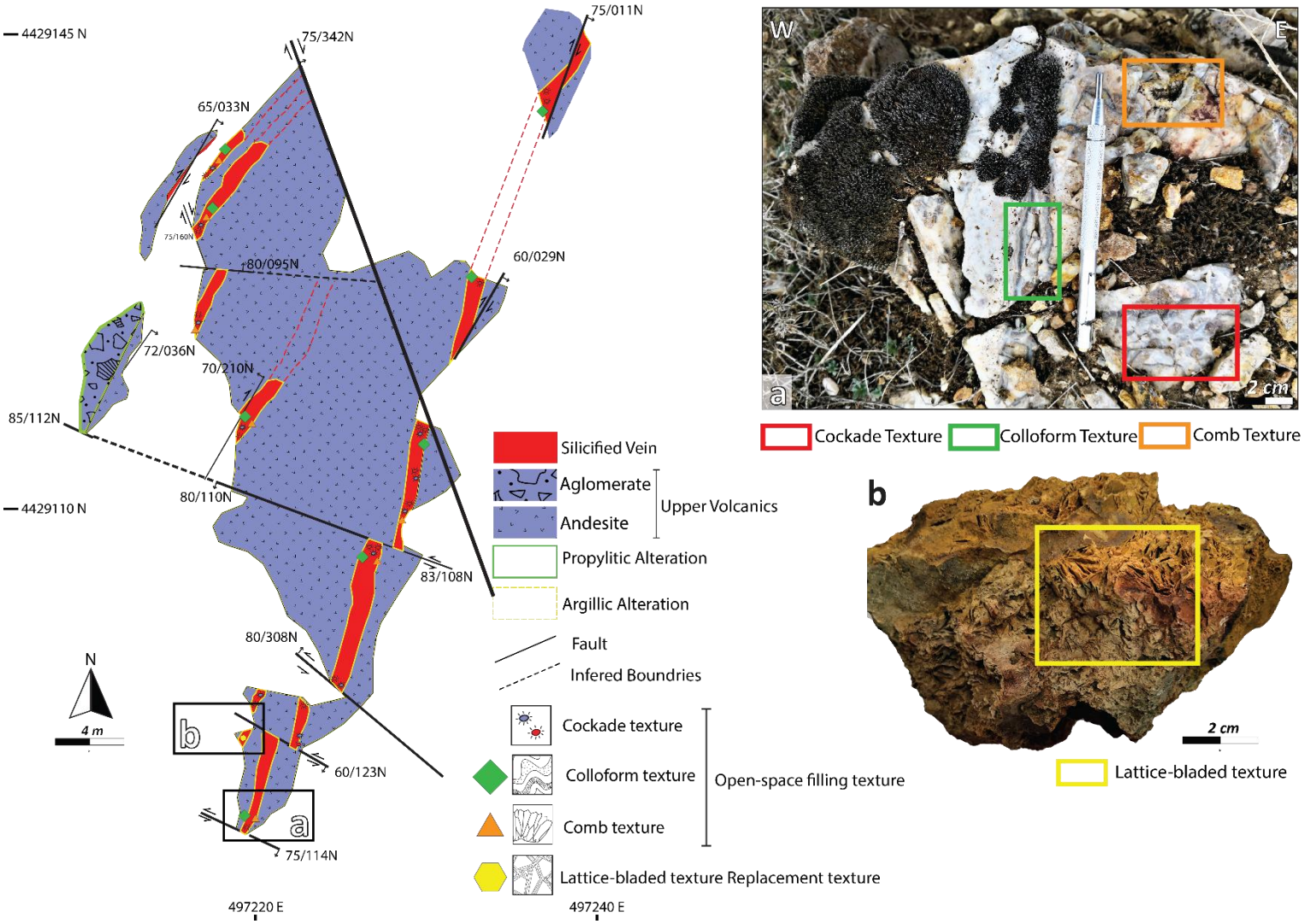

Figure 43: a) Open-space filling textures, including cockade, colloform, and comb textures, observed in the Q-1 vein. The black rectangle on the map indicates the location of the photo; b) Replacement texture, lattice-bladed texture, identified in the Q-1 vein (Çil, 2019). The black rectangles on the map correspond to the location of the hand specimen.

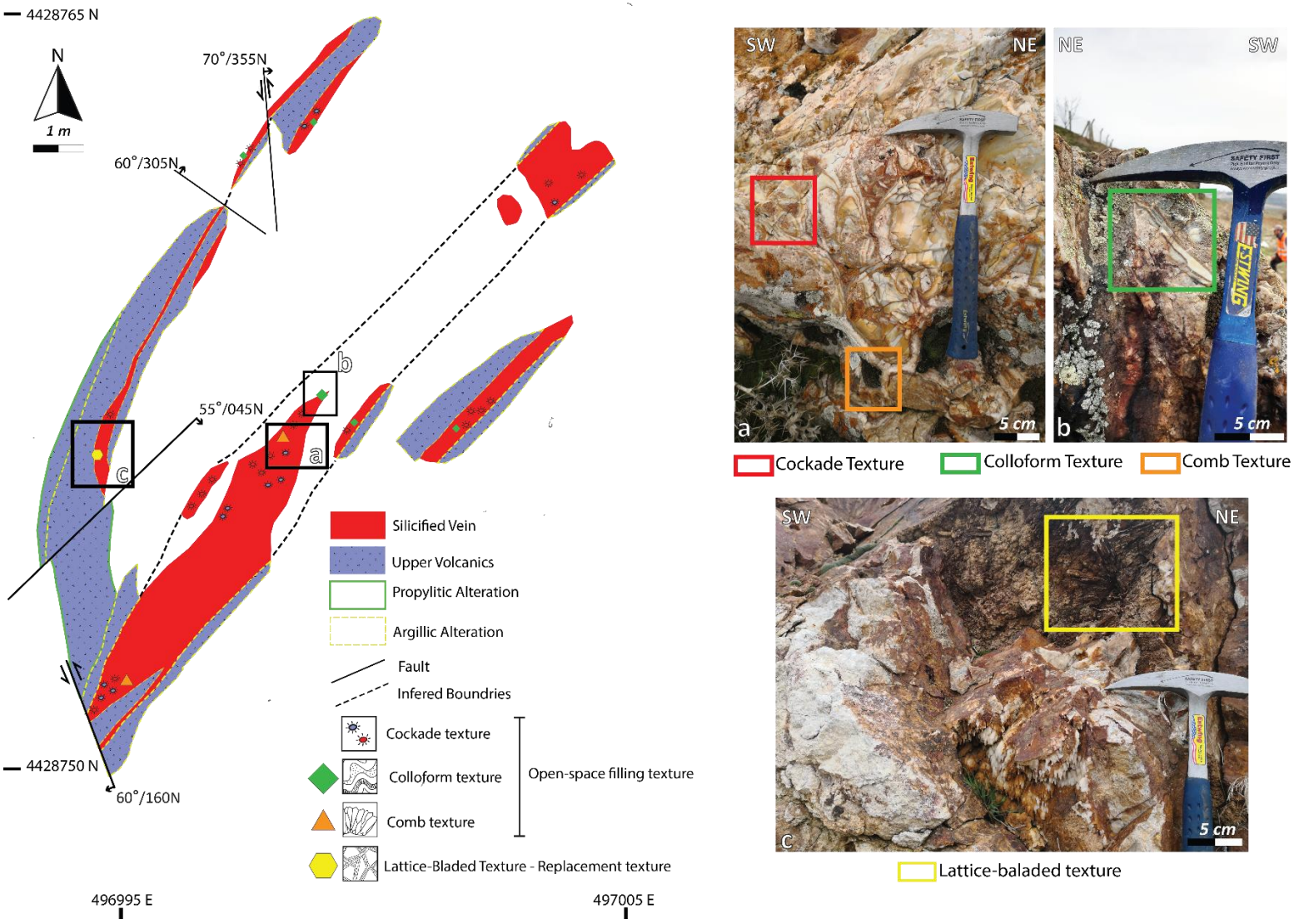

Figure 44: a-b) Open-space filling textures, including cockade, colloform and comb texture, observed in Q-2 vein. The black rectangle on the map indicates the location of the photo; c) Replacement texture, specifically lattice-bladed texture, identified in the Q-2 vein. The black rectangles on the map correspond to the location of the filed photos.

The East vein is composed of two segments, East-1 and East-2. The East-1 vein segment is represented by two separate NE-SW and ENE-SSW trending veins that show a stepping network, intersecting to the east of Gicik village (Figure 45). Gold assay values of 3-5 ppm were obtained from rock samples from the surface (Çil, 2019). Both branches could be intermittently followed up as outcrops with thicknesses between 1 and 2 m for approximately 500 m along strike. The branches are characterised by extensively silicified volcanic rocks, with a minor portion of thin quartz veins and veinlets (Figure 41 a). Sulphide minerals are visibly concentrated as disseminations where the branches intersect (Figure 45 a). The segment contains open space and replacement textures, including cockade and lattice blade texture on the northernmost small outcrop (Figure 45 b and Figure 45 c). To the east, the East-2 vein segment crops out parallel to the East-1 vein segment for a strike length of around 150 m. The NE-SW-oriented vein has a thickness of between 2 and 8 m. Contrary to the East-1 vein, the East-2 vein contains massive quartz veins up to 0.5 m thick, and the intensity of the silicification and appearance of argillic alteration is more apparent. This segment contains disseminated pyrite, similar to East-1, visible on the hand specimen scale, and arsenopyrite was also detected in this segment (Çil, 2019). Well-developed hydrothermal textures were not observed within the segment at the hand sample scale.

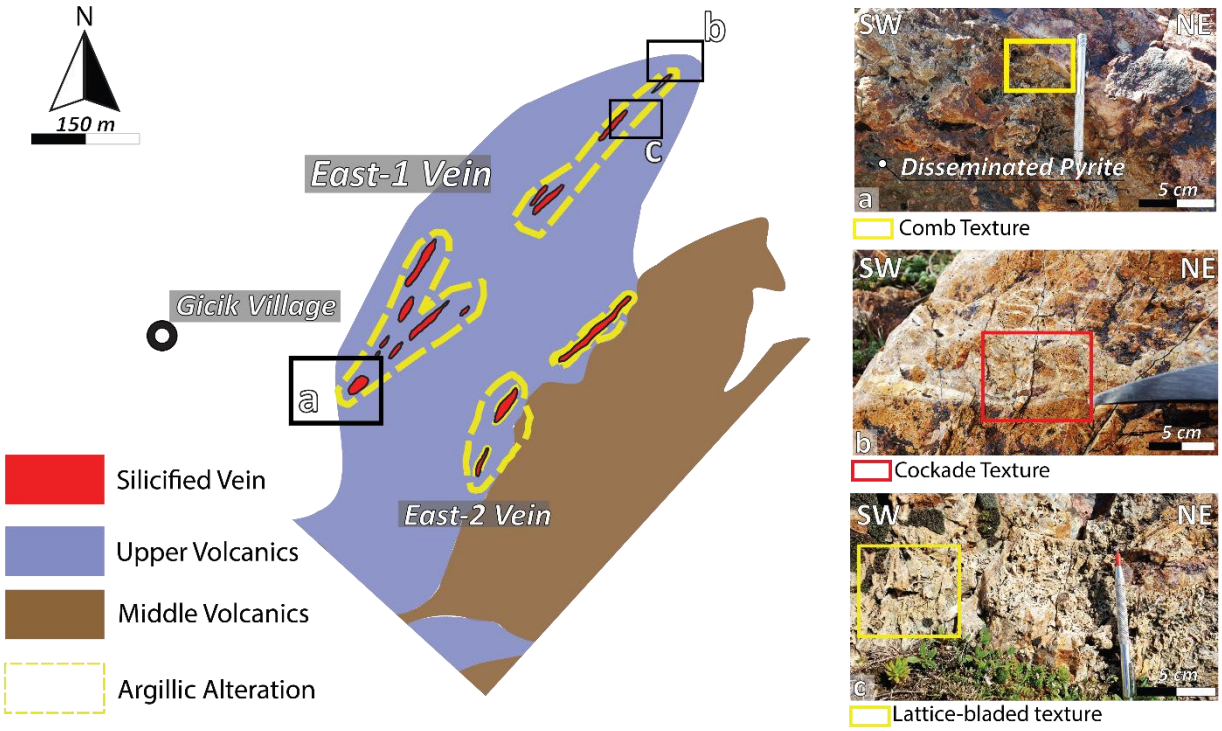

Figure 45: a) Comb texture and disseminated pyrite on the intersection of two sets of veins in East-1 segment; b) Cockade texture on East-1 vein segment; c) Lattice-bladed texture on East-1 vein segment. The locations of the photographs are shown on the outcrop map (modified from Çil, (2019)).

The G-vein is comprised of at least two segments hosted in the middle volcanic series agglomerates. They are steeply dipping and have a relatively consistent NE (NNE to NE) orientation, up to 3 m thick and 60 m long. Compared to the T, Q, and East veins, the G veins are at lower elevations, and therefore, the surface exposures may represent deeper levels of the mineralised system. It returned the highest assay results during the historical drilling operations by Eurogold, averaging 21.6 g/t Au (Çil, 2019). Koza Mining operated and backfilled a large part of this sector during previous years; for this reason, detailed observations of this vein could not be made. The southmost, unexploited part of the vein is represented by intense silicification of volcanic host rock (Figure 46). Well-developed hydrothermal textures were not observed within this segment.

Figure 46: Intensely silicified volcanic host rock photo from G vein (497226 m E 4428440 m N). (Datum: WSG84 UTM Zone)

The Creek veins crop out at the southern part of the system in the volcanic flow of the middle volcanic series (Figure 38). They are comprised of NNE-SSW and NNW SSE-oriented veins that are 3 m thick and have an average length of 40 m. The wall rock surrounding the veins is pervasively silicified, in which stockwork veinlets are found (Figure 47). Veins are mainly made up of massive quartz, up to 1 m thick, displaying rare comb and colloform-banding textures.

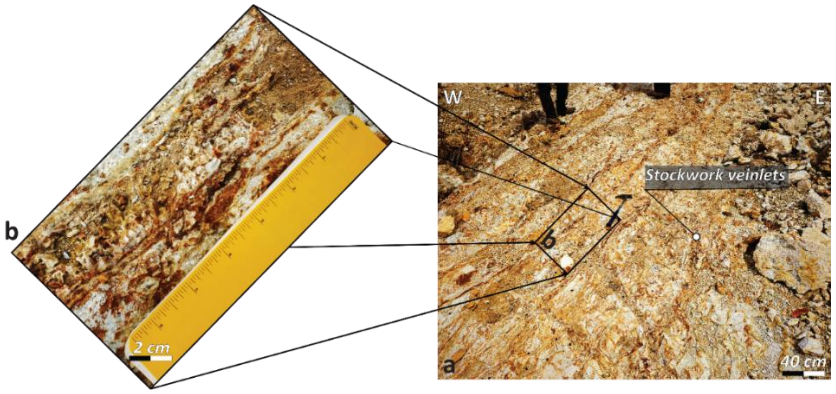

Figure 47: a) Stockwork veinlets from Creek vein; b) a close-up photo of quartz stockwork veinlet with Fe(hydro)oxide (496521 m E 4427412 m N). (Datum: WSG84 UTM Zone)

In Gicik, the cockade clasts do not touch each other, fulfilling the criteria for the identification of cockades (Frenzel and Woodcock 2014). Cockade textures, which include veins, are characterised by breccias dominated by crystalline cement. The central clasts are typically subrounded and are surrounded by rims composed of fine-grained quartz of varying colours (e.g., dark grey, vitreous, or milky) (Figure 41 a and Figure 41 b) and sulphide precipitates (e.g., pyrite, arsenopyrite, tetrahedrite) (Figure 48 h). The rims often grow inward into open spaces and are accompanied by other open space-filling textures, such as colloform banding and comb texture (Dong et al., 1995). The central clasts comprise altered fragments of host rock, early-generation cement, and early breccia clasts. The rims are composed of layers of dark grey, vitreous and milky silica accumulations and different forms of very fine-grain quartz cement alternations.

The observations made on both outcrops and hand specimens considered the criteria of Frenzel and Woodcock (2014) for the repeated rotation and accretion mechanism and the criteria for the partial metasomatic replacement mechanism (Kutina and Sedlackova, 1961). The contact boundary between the central clasts and the early generations of rims is often indistinct in hand specimen (Figure 48 a and Figure 48 f). Moreover, the hand specimen view of a cockade texture from the G vein (Figure 48 g) displays the irregular thickness of the dark grey sulphide-rich rim and its penetration through dissemination into surrounding quartz cement. In the plane section, the layers of dark grey sulphide-rich rims have different thicknesses around fragments from wall rocks and early veins (Figure 48 c), and the widening of these rims is not regular around rock fragments. Figure 48 h shows the accumulation of tetrahedrite on the triple junction of quartz rims around different fragments. However, the local truncations on the rims surrounding fragments exist on cockade texture (Figure 48 a, c and e), which are interpreted as cockades that were previously in contact with each other in repeated rotation and accretion model (Frenzel and Woodcock, 2014).

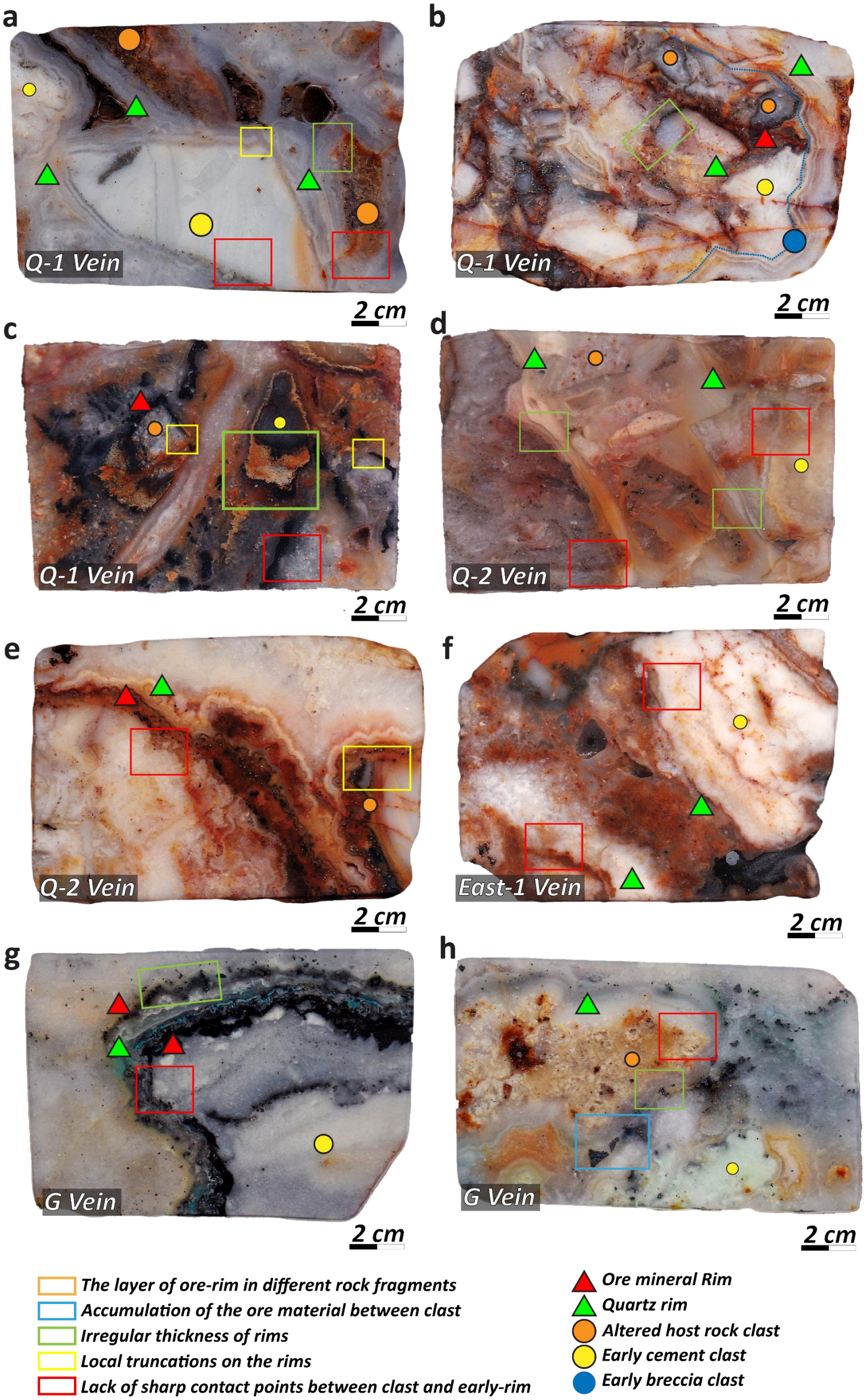

Figure 48: The hand specimen photos and their locations from Gicik low sulphidation epithermal mineralisation a) Q-1 vein segment (497264 m E 4429285 m N); b) Q-1 vein segment (497271 m E 4429297 m N); c) Q-1 vein segment (497035 m E 4428928 m N); d) Q-2 vein segment (497045 m E 4428934 m N); e) Q-2 vein segment (497026 m E 4428926 m N); f) East-1 vein segment (497330 m E 4428926 m N); g) G vein (497026 m E 4428926 m) N; h) G vein (497296 mE 4428666 m N). (Datum: WSG84 UTM Zone)

4.2.2 Structural Observations at Gicik

Structural observations were made to elucidate the relationship between faults and mineralised veins within the Gicik low-sulphidation epithermal system. A summary of orientation data for the seven identified vein segments is provided in Figure 49.

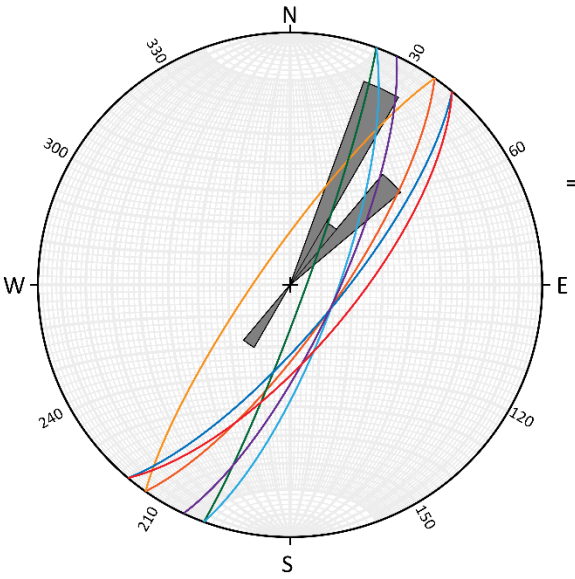

Vein	Segment	Easting	Northing	Average Orientation Strike	Dip
T-vein	-	493736	4430058	040	70
Q-vein	*Q-1 vein*	497263	4429308	035	75
	Q-2 vein	497046	4428931	215	80
G-vein	-	497430	4428972	020	85
East-vein	*East-1 vein*	497638	4429049	040	75
	East-2 vein	497880	4429066	020	75
Creek-vein	-	496552	4427573	025	75

Figure 49: Orientation of the veins and their segments on the stereonet. (Datum: WSG84 UTM Zone)

By mapping the Q-1 and Q-2 veins and systematically compiling fault data during fieldwork, we classified faults into three distinct orientations. The orientation of the fault plane, the pitch/rake of the slickenside, and the relative sense of movement were recorded along with their geographic coordinates (Figure 50). Detailed photographs of each fault were taken, and documentation of the site was completed. The direction of relative displacement on each fault plane was determined through the analysis of kinematic indicators, including grooves, chatter marks, tool marks, and fibrous minerals (Figure 51). The first orientation comprised NE-SW-oriented faults closely parallel to the vein structures (Figure 52 a-c and Figure 53 a). Fault slip data revealed that these faults exhibited dextral strike-slip movement with a reverse component. These faults were observed to cut across the veins with hydrothermal textures and the volcanic rocks with hydrothermal alterations.

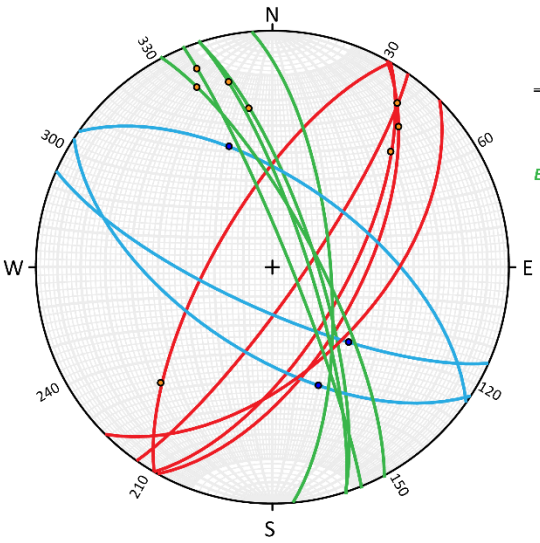

Fault	Easting	Northing	Strike	Dip	Dip Quad	Rake
Propylitically Altred Volcanic Rock	497312	4428753	342	78	N	22
East2-vein Argilic Altrted Volcanic Rocks	497768	4428772	35	80	N	14
G-vein Silicified Volcanic Host Rock	497236	4428397	338	84	N	12
East1-vein Silicified Vein with Hydrothermal textures	498128	4429392	332	75	N	20
Q-1 vein (a)	497222	4429129	30	65	N	34
Q-1 vein (c)	497226	4429122	210	70	S	35
Q-1 vein (d)	497241	4429126	29	60	N	25
Q-1 vein (e)	497236	4429110	342	75	N	34
Q-1 vein (f)	497225	4429101	123	60	S	55
Q-1 vein (g)	497223	4429091	114	75	S	55
Q-2 vein (a)	496983	4428734	355	70	N	-
Q-2 vein (b)	496980	4428731	305	60	N	55
Q-2 vein (c)	496955	4428704	45	55	N	-

NE-SW Faults
NNW-SSE Faults
NW-SE Faults
Dextral Strike slip with reverse component
Sinistral Strike slip with normal component

Figure 50: Orientation of the faults and their slip senses on the stereonet. (Datum: WSG84 UTM Zone)

Figure 51: Faults cutting a, b and c) volcanic rocks with hydrothermal alterations, prophylactic, argillic and silicification, respectively, (a- 497312 m E 4428753 m N; b-497768 m E 4428772 m N; c-497236 m E 4428397 m N); and d) veins displaying hydrothermal textures (d-498128 m E 4429392 m N). (Datum: WSG84 UTM Zone)

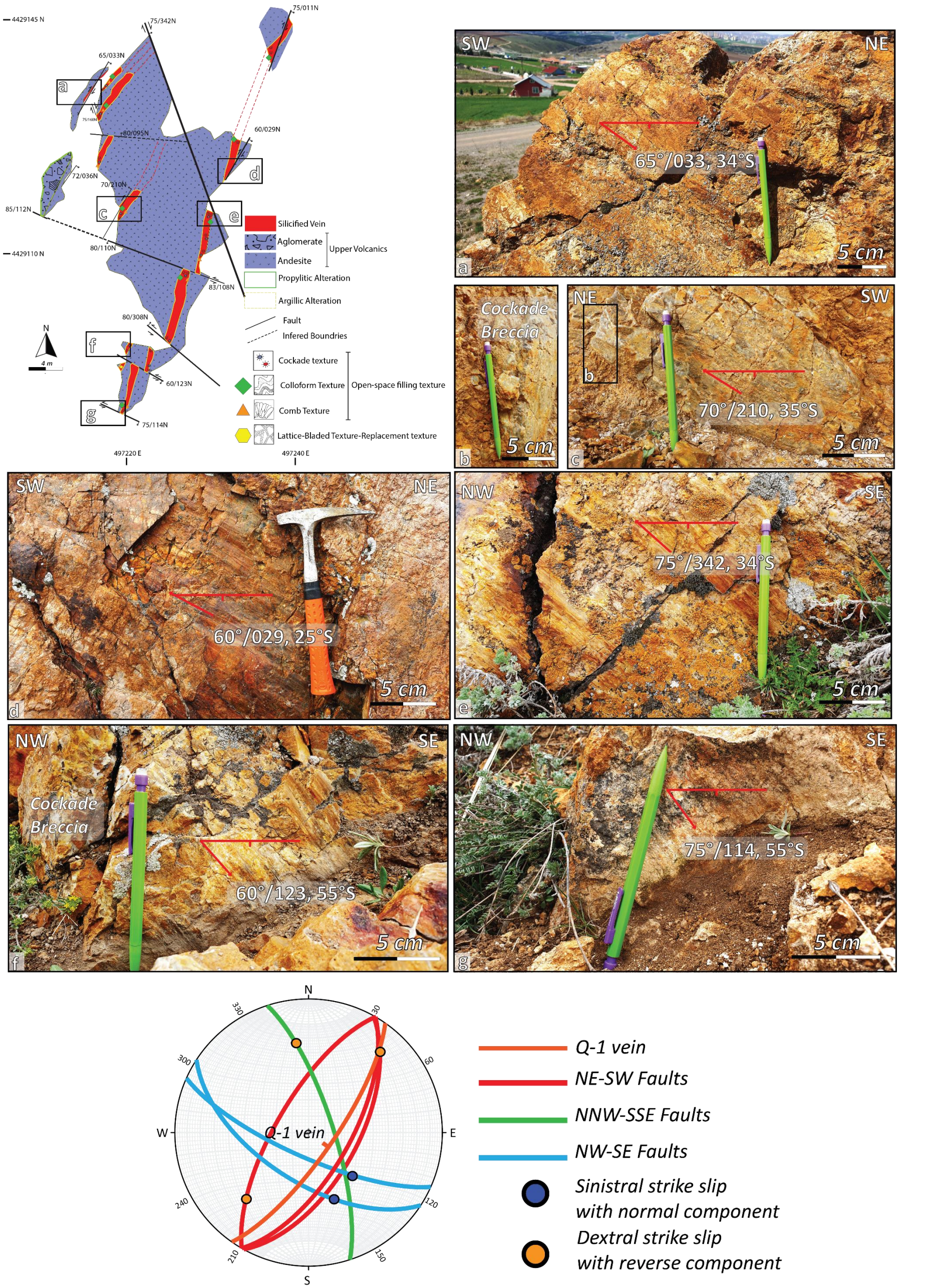

Figure 52: Views of fault surfaces from Q-1 vein. a-d) NE-SW trending dextral strike-slip fault with a reverse component having a similar orientation with vein; e) NNW-SSE trending dextral fault with the reverse component; f-g) NW-SE trending sinistral oblique strike-slip fault with the normal component. Orientation of the faults, their slip senses and the average orientation of the Q-1 vein segment on the stereonet.

The subsequent two fault sets exhibit orientations NNW-SSE (Figure 52 e and Figure 53 a) and NW-SE (Figure 52 e-g and Figure 53 b), although their paragenetic relationship was not clear. However, these faults cut and displaced the NE-SW-oriented faults and veins. The fault surface data of the NNW-SSE-oriented faults indicated dextral strike-slip movement with the reverse component, whereas the fault slip data of those with NW-SE orientation indicated sinistral strike-slip movement with the normal component. Additionally, these faults cut and offset andesitic-basaltic dykes parallel to the NE-SW-oriented ore veins (Figure 38).

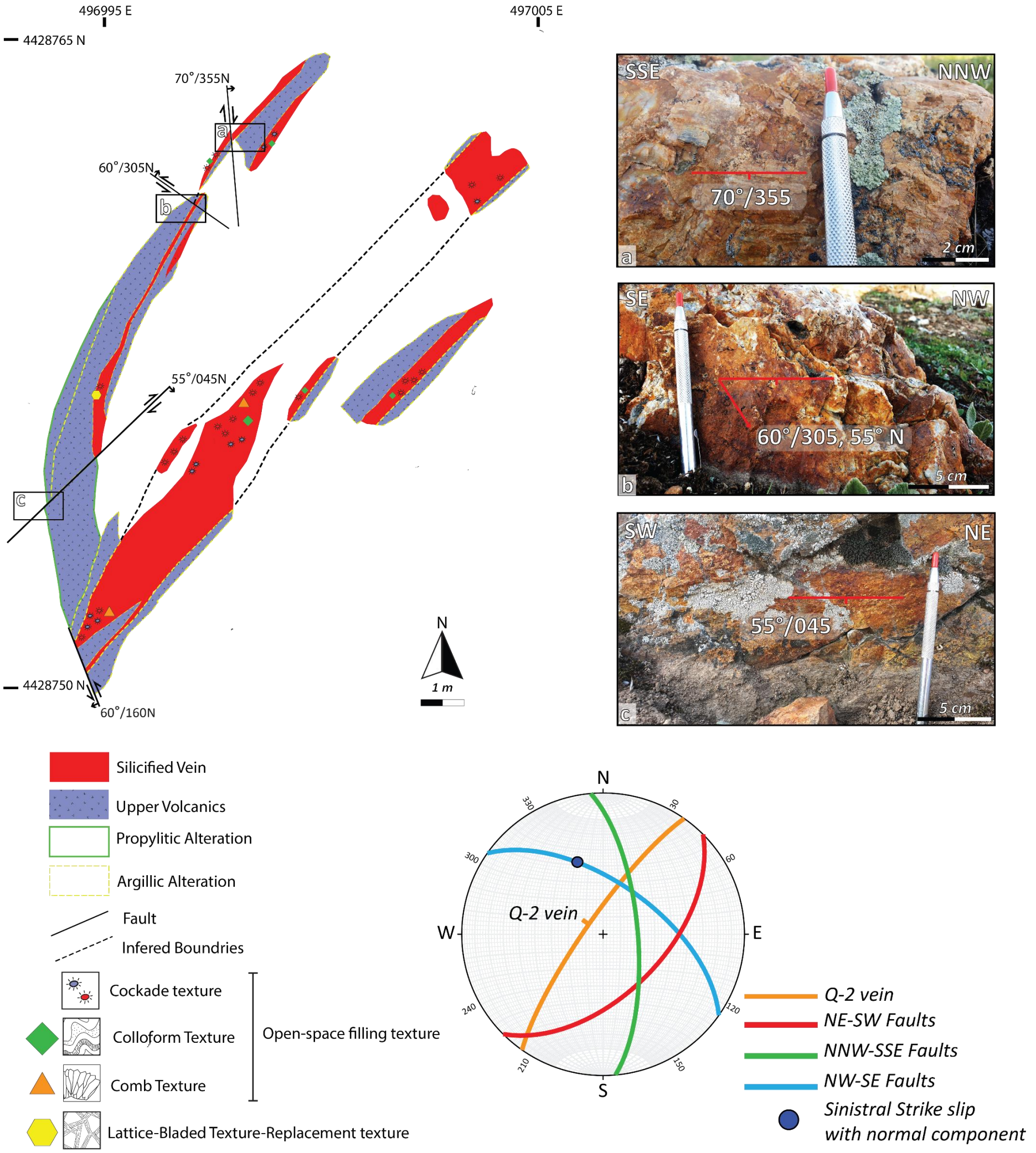

Figure 53: Views of fault surfaces from Q-2 vein; a) pure dextral NNW-SSE trending fault cuts quartz vein; b) NW-SE trending sinistral oblique strike-slip fault with normal component; c) dextral strike-slip NE-SW trending faults having a similar orientation to a vein. Orientation of the faults, their slip senses, and the average orientation of the Q-2 vein segment on the stereonet. (Datum: WSG84 UTM Zone)

4.2.3 Discussion and Conclusion

The mineralisation at Gicik was classified as low-sulphidation epithermal style Au mineralisation by Çil (2019), based on textures that are characteristic of low-sulphidation systems such as colloform banding, crustification, lattice bladed, and cockade textures. The mineralisation is hosted within silicified NE–SW trending veins, which are closely parallel to NE-SW-trending oblique faults with predominant strike-slip components, having reverse movement on their slip surfaces. Çil (2019) interpreted this colinearity as indicating that these faults served as permeable conduits for hydrothermal solution convection, which resulted in epithermal-style mineralisation. These faults and associated vein systems are cut by NW–SE and NNE–SSW trending faults, which are interpreted to have developed after mineralisation (Çil, 2019). He based these observations on the examples of systems formed under transpressional stress rather than extensional or transtensional conditions, such as McLaughlin in the western U.S. (Sherlock et al., 1995) and low-sulphidation epithermal systems in the Rosario-Bunawan district in the Philippines (Kolb and Hagemann, 2009); however most epithermal systems, especially low-sulphidation ones, typically develop in purely extensional or transtensional tectonic settings (Cooke and Simmons, 2000; Sillitoe and Hedenquist, 2003, Rhys et al., 2020). Our field observations confirm that the NE-SW faults show evidence of right-lateral reverse movement by cutting co-linear NE-SW ore-bearing veins. Additionally, we verified NW–SE and NNE–SSW faults in the field, with slip data indicating a dextral strike-slip with a reverse component and a sinistral strike-slip with a normal component, respectively. Although the temporal relationships of these features in the field are unclear, it is evident that they have cut and displaced both the veins and NE-SW faults. Our observations and detailed mapping in the Q-1 and Q-2 segments revealed that NE-SW faults cut and displaced the veins, including hydrothermal textures and alterations related to mineralisation. Subsequently, NNW-SSE and NW-SE faults cut and displaced both the veins and NE-SW faults. Therefore, we interpret all the exposed fault sets in the field as having been developed after mineralisation. The collinearity between NE-SW veins and faults may result from the inversion of an earlier fault system. The mineralised veins initially formed under an extensional stress regime and were later crosscut by subsequent faulting during a compressional phase, leading to fault reactivation and structural overprinting.

Cockade texture is commonly found in epithermal systems and is categorised by Dong and coauthors (1995) as a subtype of crustiform texture, indicating growth towards open space. Moncada and coauthors (2012) suggest that cockade texture forms through slow crystal growth (non-boiling) towards open spaces, resembling textures like massive and comb textures, based on fluid inclusion data. However, Kutina and

Sedlackova (1961) and Rieder (1969) demonstrated that the rings surrounding a single cockade texture can form due to growth into open space and partial metasomatic replacement together. They proposed that the lack of contact between central clasts in cockade textures could also be a result of inward partial metasomatic replacement processes affecting the outer parts of central clasts and surrounding rims. They also outlined criteria indicating partial metasomatic replacement in cockade texture based on observations of different cockade textures containing only silicate minerals, such as quartz and chalcedony, or both silicate and ore minerals, such as sulfides and oxides, as the outer rim. These criteria involve macroscopic and microscopic observations to identify key features, such as the absence of sharp contact points between the residual cores of the clasts and the surrounding rims, uneven rim thickness, variations in ore rim thickness, and the accumulation of ore material between cockade textures. All of these features are observed in the hand specimens presented in Figure 48. The contact boundary between the central clasts and the early generations of rims is often indistinct on the hand specimens in Gicik. The rims display the irregular thickness of the dark grey sulphide-rich rim and its penetration through dissemination into surrounding fine-grain silica cement, and the widening of the rims is not regular around central fragments (Figure 48 g). Macroscopic examination of cockade textures in the Gicik low-sulphidation epithermal system confirmed the presence of the inward partial metasomatic replacement criteria (for the full list of criteria, see *Formation of Cockade Texture* in Chapter 2, p.16), indicating that replacement processes play a significant role in forming cockade textures in the study area. Moreover, the local truncations on the rims surrounding fragments exist on cockade texture (Figure 48) and are interpreted as having been previously in contact with each other in repeated rotation and accretion model by Frenzel and Woodcock (2014) (for the full list of criteria, see *Formation of Cockade Texture* in Chapter 2, p.17). However, aside from the observed local truncations, no additional field evidence supporting the suspension in fluid or rotation and accretion models was encountered. Specifically, no rotated geopetal infill structures or other indicators of vein rotation were observed. Furthermore, while seismicity was undoubtedly present, the absence of inverse grading in the core clasts of cockades within breccia layers suggests that seismic shaking-driven self-organisation of clasts (Genna et al., 1996) and variations in flow velocity during co-seismic fluidisation (Cox and Munroe, 2016) did not leave identifiable structural or textural imprints in the study area.

Open space-filling textures, such as cockade, colloform, comb, and lattice-bladed replacement textures (Dong et al., 1995), were observed in close proximity within the same veins in Gicik (Figure 43 and Figure 44). The coexistence of replacement and primary growth textures in these veins suggests that partial inward metasomatic replacement played a role in vein formation. This overprinting likely resulted from the episodic deformation characteristic of epithermal systems, where repeated cycles of brittle

deformation and fluid influx initially promoted mineral growth, followed by partial replacement. Thus, field observations from Gicik indicate that partial inward metasomatic replacement and rotation and accretion mechanisms acted together in the formation of cockade textures.

4.3 Comparison of Oxwich and Gicik Localities on Outcrop and Hand Specimen Scale

The cockade texture-bearing breccias were examined on outcrop and hand specimen scales. The carbonate-dominated system in Oxwich, where Frenzel and Woodcock (2014) have favoured the rotation and accretion mechanisms, supports the crystallisation pressure hypotheses as discussed above in the relevant section. On the other hand, the silica-dominated system in Gicik supports the hypothesis that the rims surrounding the central fragments were formed by growing into an open space or by the inward metasomatic replacement of the central clasts and the early generation of the rims. The table below compares the macroscopic observations in the selected localities on the outcrop and hand specimen scales (Table 2). The examination on microscopic scales will be presented for both localities in Chapter 5 to support and reinforce the field observations.

Table 2: Comparison of the selected localities based on the observations on the outcrop and hand specimen scale.

Macroscopic Scale

	Oxwich	*Gicik*
Central Fragments	Limestone wall rock (e.g. Figure 26)	Volcanic wall rock, early generation cement and breccia (e.g. Figure a to h)
Rim mineralogy	Calcite and iron-rich carbonate cement (e.g. Figure 35)	Course to fine grain quartz and euhedral to disseminated opaque minerals, i.e. pyrite (e.g. Figure 48)
Rim texture	Massive, elongated and blocky calcite(e.g. Figure 32)	Open space-filling texture, i.e cockade, colloform, and comb, and replacement textures, i.e. lattice-bladed (e.g. Figure 43)
Criteria for mechanisms	Central fragments are separated (e.g. Figure 29 d-e-f) Rims surrounding the central fragments (e.g. Figure 33) No truncation on outgrowth rims No reverse or normal grading A very clear example of unrotated geopetal sediment deposition (Figure 34 c) Well-developed crystal face indicating growth into an open space (e.g. Figure 26) Sharp contact boundary between central fragments and rims (e.g. Figure 32)	Central fragments are separated (e.g. Figure 42) Rims surrounding the central fragments (e.g. Figure 44 a) Truncation on outgrowth rims (Figure 48 e) No reverse or normal grading No rotated geopetal sediment Not-well developed crystal face indicating rapid cooling (e.g. Figure 48 a) No sharp contact between central fragments and rims (e.g. Figure 48 g)
Operating mechanisms for the formation of cockade texture	Force of crystallisation	Partial metasomatic alteration by replacement Repeated rotation and accretion

Chapter 5: Microstructures and Geometry of Cockade-Texture Bearing Breccias

This chapter presents microscopic observations, descriptions, and interpretations from the two distinct localities, Oxwich and Gicik that were presented in Chapter 4 and represent carbonate and silica-dominated systems respectively. Thin sections from four samples collected at Oxwich and three at Gicik were prepared at Cardiff University's Thin Section Preparation Laboratory within the School of Earth and Environmental Sciences. And additional five thin sections, including cockade textures from Gicik, were shared by Çil (2019) with the hand specimens and locations. Microscopic investigations used transmitted light-polarised microscopes to highlight textures and reveal the structural and mineralogical relationships of central fragments and the surrounding rims.

This chapter also includes analyses of the geometric characteristics of the boundaries between central fragments and rim layers on microscopic and macroscopic scales. These analyses used fractal dimensions as a quantitative scale-independent parameter, aiming to show their complexity levels and potential associations with accompanying textures through the application of the box-counting method. The sample dataset covers the samples collected in this study and those shared by Çil (2019), alongside well-documented cockade textures from previous studies in 21 other locations.

5.1 Samples and Methods

5.1.1 Samples

5.1.1.1 Thin Sections from Oxwich and Gicik Localities

The study involved examining microscopic features in four thin sections from the Oxwich carbonate-dominated system and nine thin sections from the Gicik silica-dominated low-sulphidation epithermal system. The Gicik samples consist of four collected during this study and five from a prior study by Çil (2019). Table 3 provides a summary of the sample locations and their descriptions.

Table 3: The sample locations and descriptions from Oxwich and Gicik. (Datum: WSG84 UTM Zone

Oxwich

Sample ID	Easting	Northing	Description
OX-1	419188	5711042	Cockade texture in **Western Oxwich Fault**, alternating layers of rims composed of the red-stained micritic calcite and euhedral sparry calcite crystals in blocky or fibrous shape.
OX-2	419352	5711051	Cockade texture in **Eastern Oxwich Fault**, alternating layers of rims composed of the red-stained micritic calcite and euhedral sparry calcite crystals in blocky or fibrous shape.
OX-3	419345	5711044	Cockade texture in **Eastern Oxwich Fault**, from the rim of giant cockade texture (Figure 31), alternating layers of rims the red-stained micritic calcite and euhedral sparry calcite crystals in blocky or fibrous shape.
OX-4	419252	5711088	Cockade texture in **E-W trending Fault**, alternating layers of rims composed of the red-stained micritic calcite and euhedral sparry calcite crystals in a blocky or fibrous shape surrounding the central fragment of

Gicik

Sample ID	Easting	Northing	Description
GCK-1	497264	4429285	Cockade texture in **Q-1 Vein segment**, alternating layers of rims composed of microcrystalline to crystalline quartz surrounding the central fragments of highly silicified volcanic host rock and early quartz vein.
GCK-2	497262	4429284	
GCK-3	497260	4429287	
GCK-51	497260	4429291	
GCK-4	497045	4428934	Cockade texture in **Q-2 Vein segment**, alternating layers of rims composed of microcrystalline to crystalline quartz surrounding the central fragments of highly silicified volcanic host rock and early quatz vein and opaque minerals.
GCK-55	497045	4428937	
GCK-64	497043	4428933	
GCK-30	497026	4428926	Cockade texture in **G Vein**, alternating layers of rims composed of microcrystalline to crystalline quartz and disseminated opaque minerals surrounding the central fragments of highly silicified volcanic host rock, early quartz vein, and alteration minerals.
GCK-32	497026	4428926	

5.1.1.2 Fractal Dimension Database

A database was compiled from the literature of 21 locations, as well as the cockade texture images from Oxwich, and Gicik. The database categorises occurrences based on their types of veins, following the classification by Frenzel and Woodcock (2014). Table 4 summarises these occurrences, along with references and the number of rims analysed at microscopic or macroscopic scales.

Table 4: The summary of the database from the well-documented occurrences with references and the number of the rims.

Type	*Locality*	*Reference(s)*	*Scale*	*# Rims (n)*
Epithermal Au-(Ag-Cu) veins	Calera, Oropampa district (Peru)	Gibson et al., 1990	Macroscopic	1
	Baia Mare (Romania)	Grancea et al., 2002	Macroscopic	1
	Exploits subzone and Gander zone (Canada)	Squires, 2005	Macroscopic	1
	Cirotan mine (Indonesia)	Genna et al., 1996	Macroscopic	2
	Cirotan mine (Indonesia)	Leroy et al., 2000	Macroscopic	4
	Lebong Tandai mine (Indonesia)	Jobson et al., 1994	Macroscopic	2
	Cononish Au–Ag deposit (Scotland)	Tanner, 2012	Macroscopic	1
	Grimsel Pass, Aar massif (Switzerland)	Berger and Herwegh, 2019	Microscopic	5
	Porgera gold deposit (Papua New Guinea)	Cox and Munroe, 2016	Macroscopic & Microscopic	3
	Col de Teghime area (France)	Masoch, 2019	Microscopic	2
	Gicik Mine (Turkiye)	**Çil, 2019**	**Macroscopic & Microscopic**	5
Epithermal Pb-Zn-(Cu, Ag, Au, Sn) veins	Alacran mines (Mexico)	Spurr, 1926	Macroscopic	2
	Chocaya (Bolivia)	Buerger and Maury, 1927	Macroscopic	2
	Port au Port Peninsula, (Canada)	Watson, 1943	Macroscopic	1
	Pribram (Czech Republic)	Kutina and Sedlackova, 1961	Macroscopic	1
	Bianska Stavnica (Slovakia)	Rieder, 1969	Macroscopic	2
	Saint-Salvy/Noailhac deposit (France)	Munoz et al., 1994	Macroscopic	1
	Peyrebrunne (France)	Munoz et al., 1997	Macroscopic	2
Fluorite-Baryte veins	St. Lawrence, Newfoundland (Canada)	Van Alstine, 1944	Macroscopic	5
Low-T calcite veins	**Gower Peninsula (Wales)**	**Wright et al., 2009**	**Macroscopic**	2
	Gower Peninsula (Wales)	**Frenzel and Woodcock, 2014**	**Macroscopic**	4

5.1.2 Methods

5.1.2.1 Microstructural Analysis

Previous research has established that silica and carbonate phases within the epithermal setting exhibit a wide range of textures, often with distinctive characteristics that provide insights into the physical conditions associated with mineralisation (Adams, 1920; Bodnar et al., 1985; Sander and Black, 1988; Simmons and Christenson, 1994; Dong et al., 1995; Henley and Hughes, 2000; Camprubí and Albinson, 2007). These textures can be categorised based on their genesis: those formed during initial deposition, those resulting from recrystallisation processes, and those indicating replacement of previously deposited material. Additionally, some textures are readily observable in hand specimen, while others necessitate microscopic examination, with certain features only becoming apparent under crossed-polarised light.

Open space, recrystallisation, and replacement textures were identified during microscopic observations based on Dong and coauthors' (1995) classification in Gicik, and on diagenetic carbonate cement classification terminology adapted from (Folk, 1959; Scholle and Ulmer-Scholle, 2003) in Oxwich. During microscopic observations, the criteria for replacement from Kutina and Sedlackova (1961) and the criteria for rims growing into open space from Frenzel and Woodcock (2014) were also considered.

5.1.2.2 Fractal-Dimension Methodology

Fractal dimension analysis, a method for quantifying shapes independently of scale, aims to reveal the geometric complexities within central fragments and surrounding rim layers of cockade textures. This analysis also seeks to understand their potential associations with primary and secondary processes, as indicated by distinct textures. We determined the fractal dimensions of individual cockade textures by digitising the boundaries between central fragments and distinct rims. To conduct these analyses, we utilised ImageJ (Schneider et al., 2012), an open-source image processing program, and its FracLac plug-in (Balay-Karperien, 2004), specifically designed for calculating fractal dimensions within the ImageJ framework using the box-counting method.

Different calculation methods for fractal dimension were proposed by scientists from different disciplines (Longley and Batty, 1989; Carr and Benzer, 1991; Fowler and Roach, 1993; Baumann et al., 1994; Klinkenberg, 1994; Allen et al., 1995), and the validation of each method and related problems were discussed for the accuracy, reliability and the associated error margin of the various methods (Dubuc et al., 1989; Dutch, 1993; Gillespie et al., 1993; Klinkenberg, 1994; Allen et al., 1995; Bérubé and Jébrak,

1996). Bérubé and Jébrak (1999) analysed the validity of the widely used vector and matrix-based methods ideally suited for computerisation, including structured walk (Kaye, 1989), box-counting (Gangepain and Roques-Carmes 1986; Sarkar and Chaudhuri, 1994; Voss, 1986), dilation (Flook, 1979), and Euclidean distance mapping (EDM) (Danielsson, 1980). They proposed that EDM is the most effective algorithm for deriving fractal dimensions with high precision and low variability. Although the EDM is the most reliable method, it requires that the outlines to be analysed must be closed polygons. The box-counting method was thus felt to be more suitable in this study due to the discontinuous nature of cockade texture outlines and was chosen for use.

Box-counting is one of the first methods developed specifically for computerised fractal analysis. It is a widely used method due to its versatility in measurement type and ease of application. After the emergence of the algorithm on which the method is based, it was developed to obtain faster and more reliable results (Liebovitch and Toth, 1989; Block et al., 1990; Buczkowski, et al., 1998a; Buczkowski et al., 1998b; Gonzato, 1998). The method must be performed on a one-pixel outline that an image processing algorithm can generate. The difficulty of generating the outline varies with the chosen algorithm and depends on the desired precision, speed, and original image resolution; it is usually performed on an entire image containing only one feature (Bérubé and Jébrak, 1996). The box-counting method estimates the fractal dimension by systematically covering an object with grids of decreasing size and counting the number of occupied boxes. Mandelbrot (1982) originally defined the fractal dimension (*D*) in a general form as:

$$D = \lim_{r \to 0} \frac{\log N(r)}{\log 1/r} \quad . \qquad (1)$$

where *N(r)* represents the number of elements (e.g., segments, boxes, or other subdivisions) required to cover the object at a given scale *r*. This equation provides a theoretical foundation for calculating fractal dimensions in various contexts, but it was later adapted for practical use in the box-counting method. In the box-counting approach, this equation is reformulated as:

$$N_r = r^{-D_b} \quad . \qquad (2)$$

where a square mash of size *r* is placed over the perimeter of the image and N_r represents the number of boxes containing the pixels of the outline. Here D_B specifically refers to the fractal dimension obtained using the box-counting method. Taking the logarithm of both sides gives:

$$\log(N_r) = -D_b \,.\log\,(r) \quad . \qquad (3)$$

This logarithmic transformation enables a linear regression approach for determining the fractal dimension, where the slope of the line in a log (N_r) *vs.* log (r) plot corresponds to - D_B. An example of a log(r) vs. log (N_r) graph is given below for a digitised cockade texture rim from Frenzel and Woodcock (2014) (Figure 54). The graph shows that the data points fit a linear distribution as evidenced by the very high value of r^2 (0.9948) in the linear fitting, demonstrating that the interfaces are fractals and, as such, according to Bruno and coauthors (1994), the interface can be considered as a natural factor. This means that the identified fractal geometry indicates a self-similar structure across different scales, suggesting that the interface follows geometric properties characteristic of natural fractal systems, rather than exhibiting arbitrary irregularities.

Fraclac calculates the slope of regression (D_B) by applying the following equation (Balay-Karperien 2004):

$$m-= \frac{n\sum SC-\sum S\sum C}{n\sum S^2-(\sum S^2)} = -D_b \quad . \qquad (4)$$

Where S = log of size, C = log of count, and n = number of sizes. The correlation (r^2) of the regression line is calculated using (Balay-Karperien 2004):

$$r^2 = \left[\frac{n\sum SC-\sum S\sum C}{\sqrt{n\sum S^2-(\sum(S)^2(n\sum C^2-(\sum C)^2}}\right]^2 \quad . \qquad (5)$$

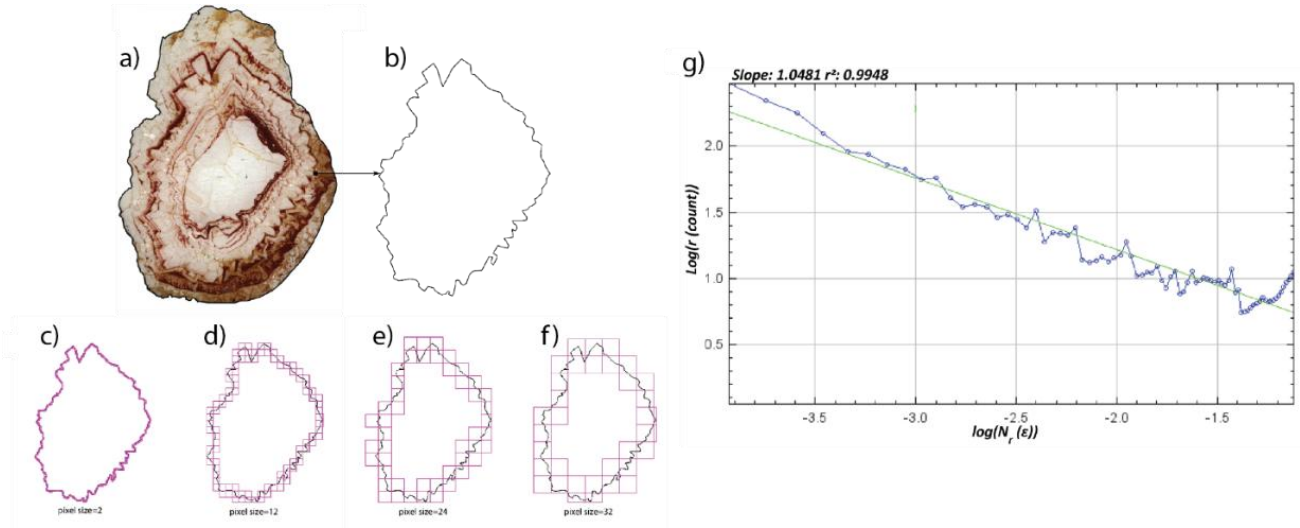

Figure 54 a) Original image of a cockade texture from Frenzel and Woodcock (2014); b) cockade texture rim outline produced in QGIS; c-f) the procedure used to measure the fractal dimension (D_B) via box-counting. Square meshes of different sizes (r) are laid over the digitised cockade texture rim. The number of boxes (N) containing black pixels with increasing pixel size is counted and shown in pink; g) Log (r (count)) vs. log (Nr (ε)) produced using FracLac, shows how fractal dimension (D_B) is calculated by linear regression; -D_B is equal to the slope of linear regression interpolation. The fractal nature of the interfaces is indicated by the linear fitting of data (r^2 > 0.95, Bruno et al., 1994). ε is the box scale = box size/image size.

This study yielded fractal dimension values using the FracLac plug-in (Balay-Karperien, 2004) in association with the ImageJ program. Shapes with known theoretical fractal values were tested using all five different scaling methods (Linear, Power, Scaled, Relative sizes, and Odd), allowing for varying the size of boxes in one grid of a series of grids in the FracLac plug-in. The known fractal shapes (Quadric and Koch fractals) were produced using the Fractal Generator plug-in (Balay-Karperien, 2004), and then they were vectorised in QGIS (3.28.0) (QGIS Development Team, 2009) to evaluate the effect of different stroke widths (0.1 mm and 0.2 mm) and image resolutions (53 and 120 dpi) on fractal dimension calculations. These specific values were chosen to ensure that the results are not significantly influenced by variations in line thickness and image resolution, which are common variables in digital image processing and vectorisation workflows (e.g., Bérubé and Jébrak, 1996; Buczkowski et al., 1998a). The 0.1 mm and 0.2 mm stroke widths represent a realistic range of line thicknesses used in geological image analysis and mapping applications, while the 53 dpi and 120 dpi resolutions were selected to reflect the lower and upper limits of typical raster resolutions used in similar fractal analysis studies. A square and a circle with stroke widths of 0.1 mm and 0.2 mm resolutions of 53 and 120 dpi, were also produced in QGIS (3.28.0). FracLac produced the most accurate fractal dimensions via box-counting; in particular, the default box sixes were the most accurate over the range of shapes and complexities tested, being consistently accurate between ±3%, averaging at -0.13%. The results showed that the in-built ImageJ box-counting system is the most inaccurate method when testing. During this process, the number of the different grids was set at 12 as a default in linear scaling method, the minimum box size was set at 5 pixels, and the maximum size was 45% of the image to obtain a consistent representative distribution across the different sizes of images analysed.

Fractal dimension measurements were conducted on a single, well-preserved cockade texture per study from the 21 publications included in the database. The selected cockade textures were chosen based on clarity and resolution, ensuring that the rims were distinguishable for accurate digitisation. The number of rims analysed per sample and whether the measurements were conducted at macroscopic (outcrop) or microscopic (thin section) scales are summarised in Table 4. Among these, only two studies (Cox and Munroe, 2016; Çil, 2019) included both macroscopic and microscopic analyses, where fractal measurements were performed on two separate cockade structures per dataset to compare their characteristics across different scales. For rim delineation in outcrop images, contrasts in mineralogical composition, crystal textures, and colour variations were used to identify rim boundaries wherever image resolution was allowed. In thin section images, rim identification was primarily based on variations in crystal growth, colour contrasts, and textural differences, which were best observed in cross-polarised thin section images. Although a single cockade per study was analysed, this selection was made to maximise

the number of rims that could be measured around an individual clast, ensuring a detailed assessment of fractal dimensions. While increasing the number of analysed cockade textures both within individual sites and across different locations would enhance the statistical robustness of the dataset, logistical constraints during this PhD research—including challenges related to the COVID-19 pandemic and time limitations—prevented further expansion of the dataset.

5.2 Microscopic Observations on Samples from Oxwich and Gicik

5.2.1 Microscopic Observations from Oxwich

The central clasts at Oxwich were derived from limestone wall rock (Figure 55 c), whereas the rims were composed of alternating layers of the red-stained micritic calcite (Figure 55 a1-a4, b1, b2, b4 and c1-c3) and euhedral sparry calcite crystals in blocky or fibrous shape. The blocky sparry calcites with euhedral crystal terminations are typically white, and they occur as masses of equant euhedral crystals with no preferred orientation (Figure 55 a1-a3 and b2). The fibrous sparry calcites are characterised by growth banding perpendicular to the fissure wall, which is obvious in thin sections. (Figure 55 a1, a1-a3, b1 and c). The red-stained micritic calcites precipitate along the concentric growth patterns of euhedral carbonate crystals by mimicking their shapes, and they have varying thicknesses in the same layer (Figure 55 a1-a4, b1, b2, c1-c3 and d). The layers are cut by euhedral sparry calcites in some places (Figure 55 a1 and Figure 55 a2). High-magnification views of adjacent areas of precipitated red-stained micritic calcite and euhedral sparry calcite show a gradational contact relationship (Figure 55 c1-c3). The thin section photo in Figure 55 c1 to c3 clearly shows the contact relationships between concentric rims, composed of red-stained micritic calcite and fibrous sparry calcite crystals, which grow outward from a central clast of fossiliferous limestone wall rock in a cockade texture. The first generation of fibrous sparry calcites has a sharp contact with central clasts. However, the layers of rims generally show size gradations from fine-grained micritic to course-grained blocky and fibrous sparry calcite with red-stained micritic calcite interlaminations. Figure 55 b3 shows the relationship between two central fragments of cockade textures that are separated by rims of micritic and blocky calcite crystals. The original clast boundaries are not very obvious, yet the rims are recognisable due to their different crystal size and colours.

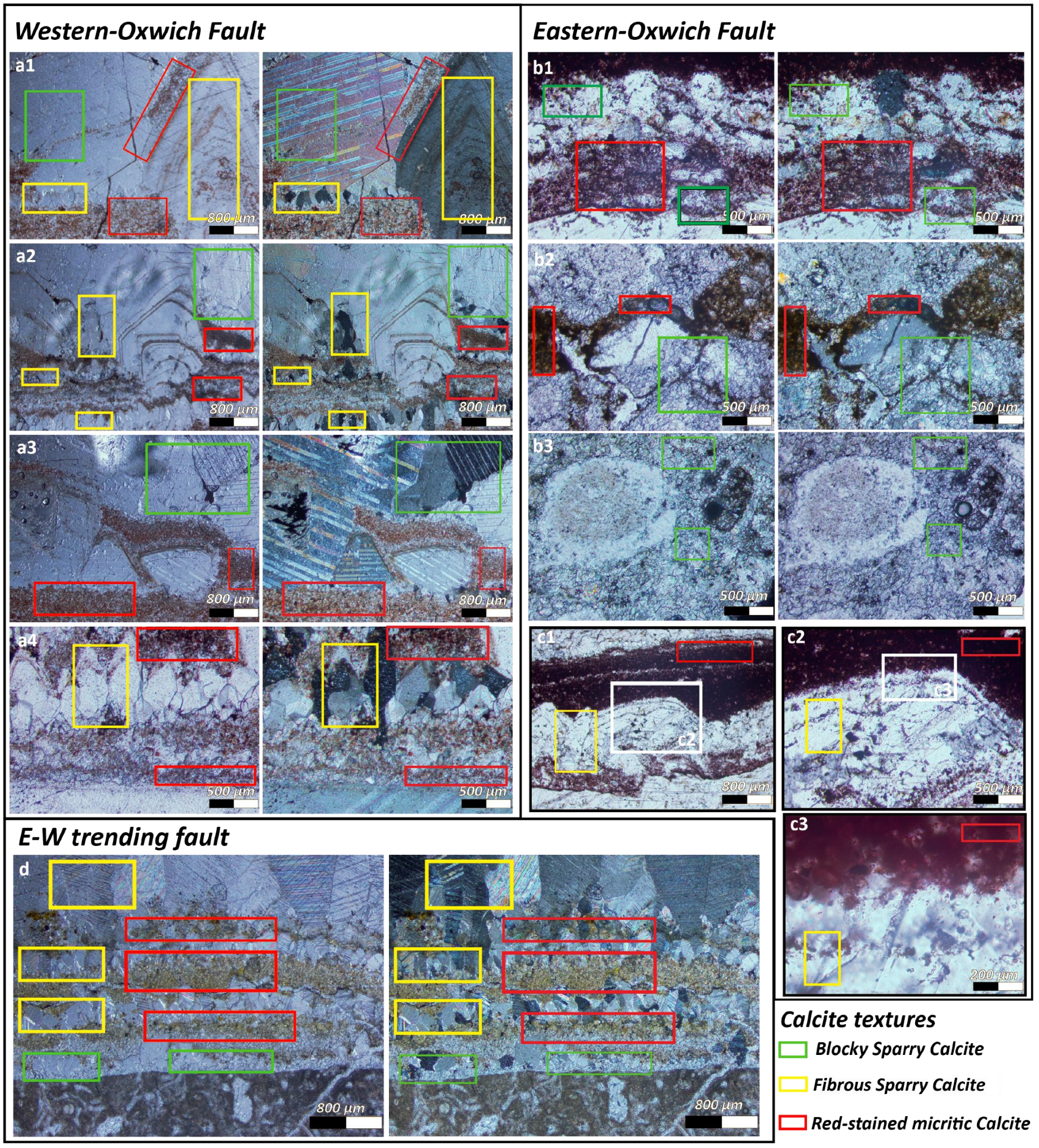

Figure 55: The thin section photos and their locations from cockade texture bearing-breccias in Oxwich. The photos on the left represent the plane polarised light and, on the right, represent cross-polarised light. a) Western-Oxwich fault (a-419188 m E 5711042 m N); b-c) Eastern-Oxwich fault (b-419352 m E 5711051 m N; c- 419345 m E 5711044 m N); c) E-W trending fault (d-419252 m E 5711088 m N). (Datum: WSG84 UTM Zone)

5.2.2 Microscopic Observations from Gicik

The most common mineral textures observed in thin sections prepared from cockade texture-rich zones in the Gicik low sulphidation epithermal system are recrystallisation textures, including mosaic, jigsaw, feathery, plumose, and ghost sphere. They are thought to result from the recrystallisation of originally amorphous or cryptocrystalline silica to form crystalline quartz (Sander and Black, 1988; Dong et al., 1995; Camprubí and Albinson, 2007). These textures are mainly characterised by microcrystalline to crystalline quartz crystals with distinct features, recognisable when observed under a microscope (Dong et al., 1995). Cockade texture is readily apparent in thin sections with concentric cement around central fragments, not in contact with one another (Figure 56). This format was chosen to illustrate the spatial relationships between multiple cockade textures. Additionally, the cross-polarised version provides the best visualisation of these relationships due to the enhanced colour contrast.

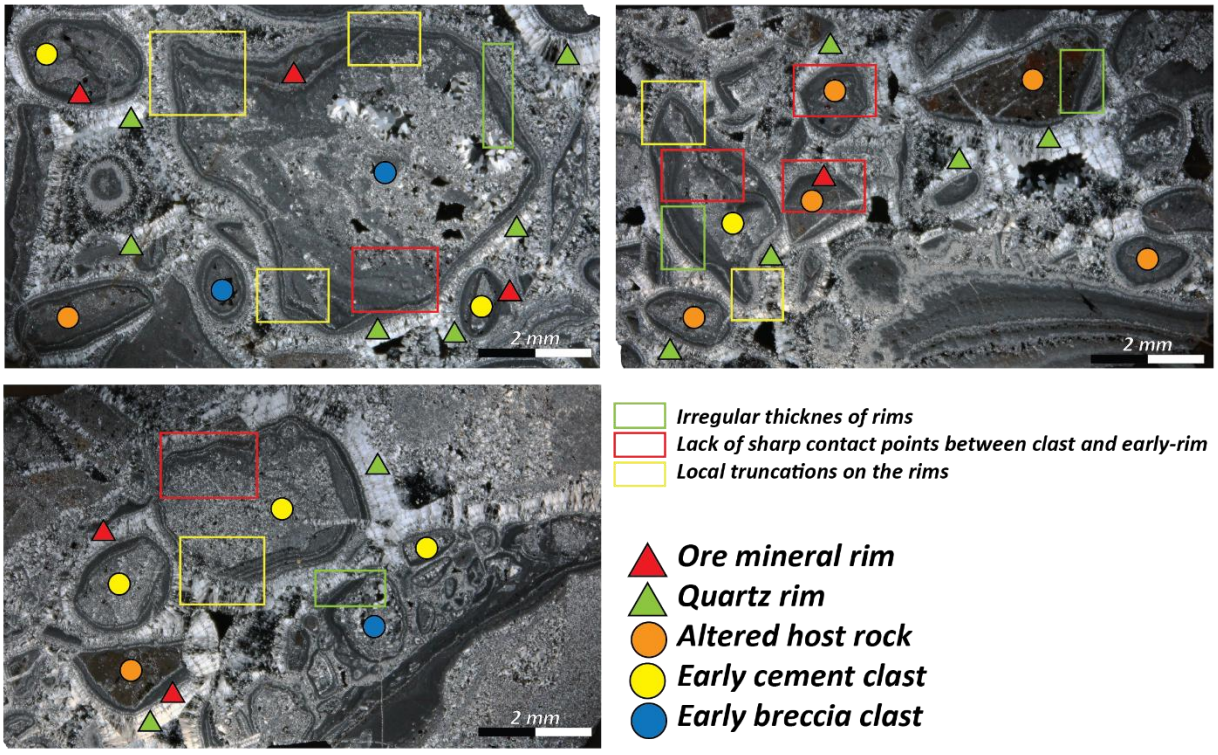

Figure 56: Cockade textures showing the relationships of concentric cement around self-supported central fragments in the Q-1 vein segment. (Datum: WSG84 UTM Zone)

Recrystallisation textures are observed on both central fragments and rims. Cental fragments are derived from highly silicified wall-rock (Figure 57 a3, b1 and b3), early quartz veins(Figure 57 a1, b4 and b5), and minerals such as euhedral pyrite or adularia (Figure 57 b2, c3 and c4), whereas rims are composed of zones of quartz (Figure 57 a-c) and disseminated pyrite plus very fine grain mosaic textured quartz (Figure 57 c3) that mimic the shape of central fragments. The predominant recrystallisation texture observed in the samples is mosaic-textured quartz. This texture is characterised by aggregates of microcrystalline to crystalline quartz crystals with interpenetrating grain boundaries (Dong et al., 1995). It commonly occurs in central fragments (Figure 57 c2), likely originating from early vein precipitates, with the rims (Figure 57 a1 and b2) partially or completely surrounding the fragments (Figure 57 b2 and b5). The next most prevalent texture is plumose quartz texture (Sander and Black, 1988), displaying patches or zones within the grain and radiating variable extinction positions when viewed under plain and crossed polars (Figure 57 a1, b1, b2, b4, and c2-c4). This quartz texture is also referred to as 'feathery' by Adams (1920) and 'flamboyant' by Dong and coauthors (1995). Additionally, the ghost sphere texture (remnants of primary moss textures) is observed on the quartz rims (Figure 57 b3, b5, c1 and c2), indicating recrystallisation from colloidal amorphous silica. It shows the radial extinction that occurs from silica gel crystallised to flamboyant texture.

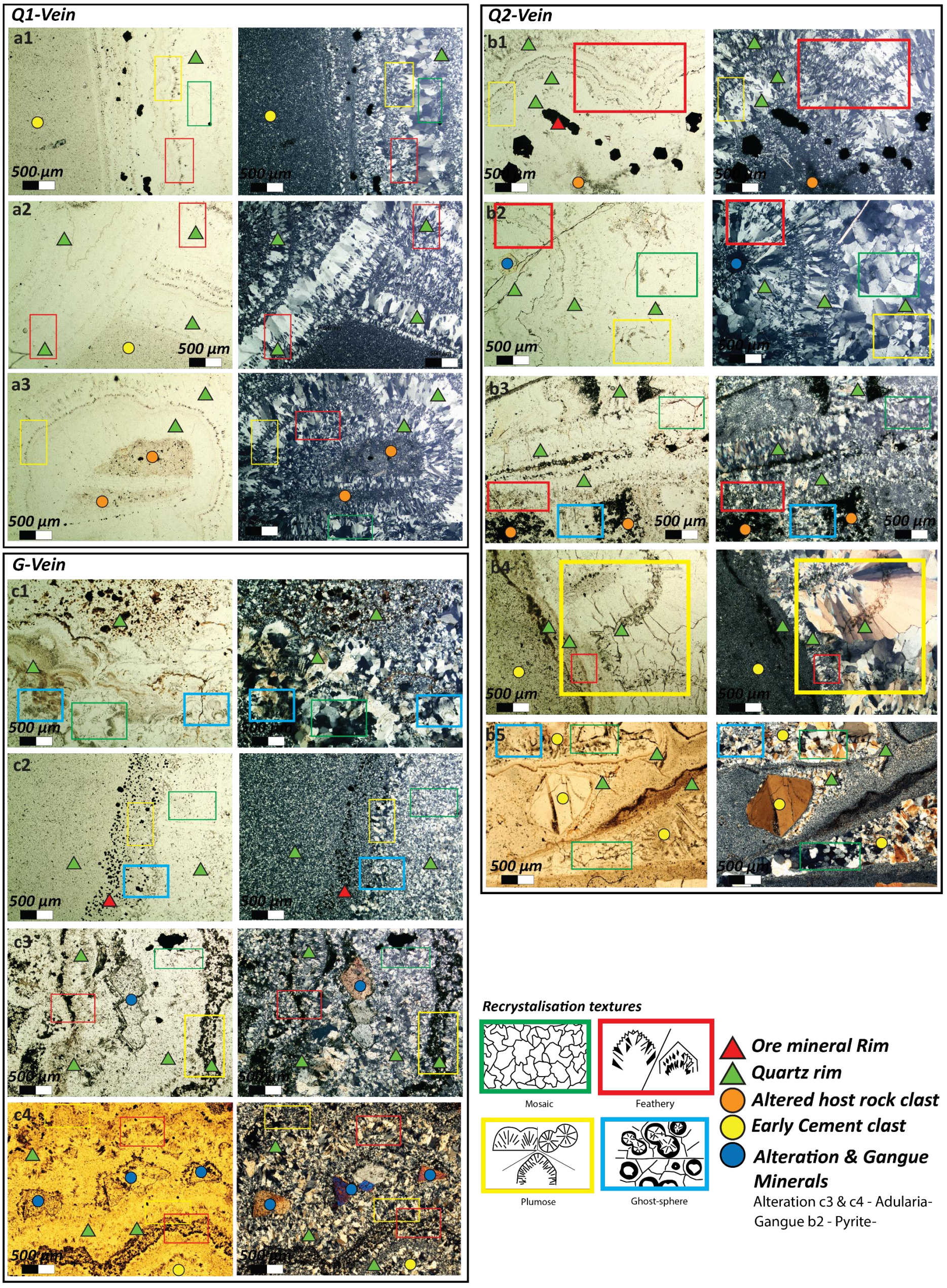

Figure 57: The thin section photos and their locations from cockade texture bearing-breccias in Gicik. The photos on the left represent the plane-polarised light and, on the right, represent cross-polarised light. a) Q-1 vein segment (497264 m E 4429285 m N); b) Q-2 vein segment (497045 m E 4428934 m N); c) G-vein (497026 m E 4428926 m). (Datum: WSG84 UTM Zone)

Microscopic observations of the cockade textures in Gicik reveal primary growth textures that have been largely overprinted by secondary recrystallisation processes. The comb texture is the most widely accompanying texture in cockade texture, especially growing into the void space created between the latest overgrowth rims. It is characterised by groups of parallel and subparallel quartz crystals, which are oriented perpendicular to the surface of a mineral or mineral aggregate. The crystals mostly display a uniform grain size and euhedral terminations at their free ends. The layers of euhedral quartz forming the comb textures also include, like the rims of cockade textures, the replacement textures, such as feathery and plumose textures (Figure 58).

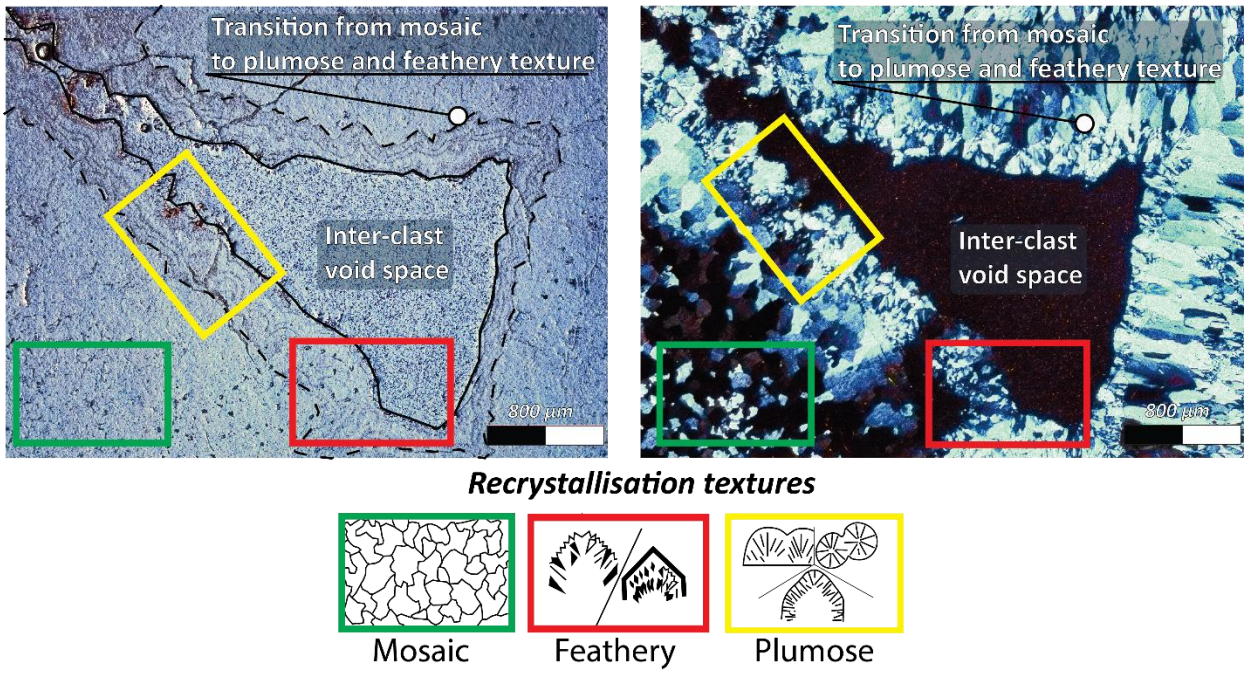

Figure 58: Thin section photo of comb texture accompanied by replacement texture in Q-1 vein segment (497264 m E 4429285 m N). (Datum: WSG84 UTM Zone)

5.3 Fractal Dimension Results

5.3.1 Database

The database was constructed by compiling 21 study areas where cockade textures have been documented (Appendix 2). Sixteen of these sites were selected based on Frenzel and Woodcock (2014), who classified them as well-documented cases containing either macroscopic or microscopic cockade textures. In addition to these, the study area Gicik (Çil, 2019) was included, along with two other key locations: the site where Frenzel and Woodcock (2014) proposed the rotation and accretion model and the same location studied by Wright and coauthors (2009). Furthermore, Cox and Munroe (2016), which proposed the suspension and accretion model, was incorporated to ensure the inclusion of diverse conceptual approaches. To construct the database, cockade texture images were extracted from the relevant publications and digitised for further analysis. These digitised images were then used to perform fractal dimension analysis to assess the geometric complexity of cockade textures across different sites.

In Figure 59, a predominant decreasing trend in fractal dimensions (D_B) is observed from central fragments to surrounding rims for silica-dominated and carbonate-dominated systems. However, exceptions are also noted in carbonate-dominated systems, where fractal dimensions increase from central fragments to surrounding rims on the macroscopic scale. This pattern is characterised by fluctuations in fractal dimensions between layers of the rim, although the general trend shows a decrease in fractal dimensions (Figure 59). Figure 59 displays the fractal dimension values of central fragments and the outermost rims on the box-and-whisker plot according to their occurrence types in the database and Gicik locality.

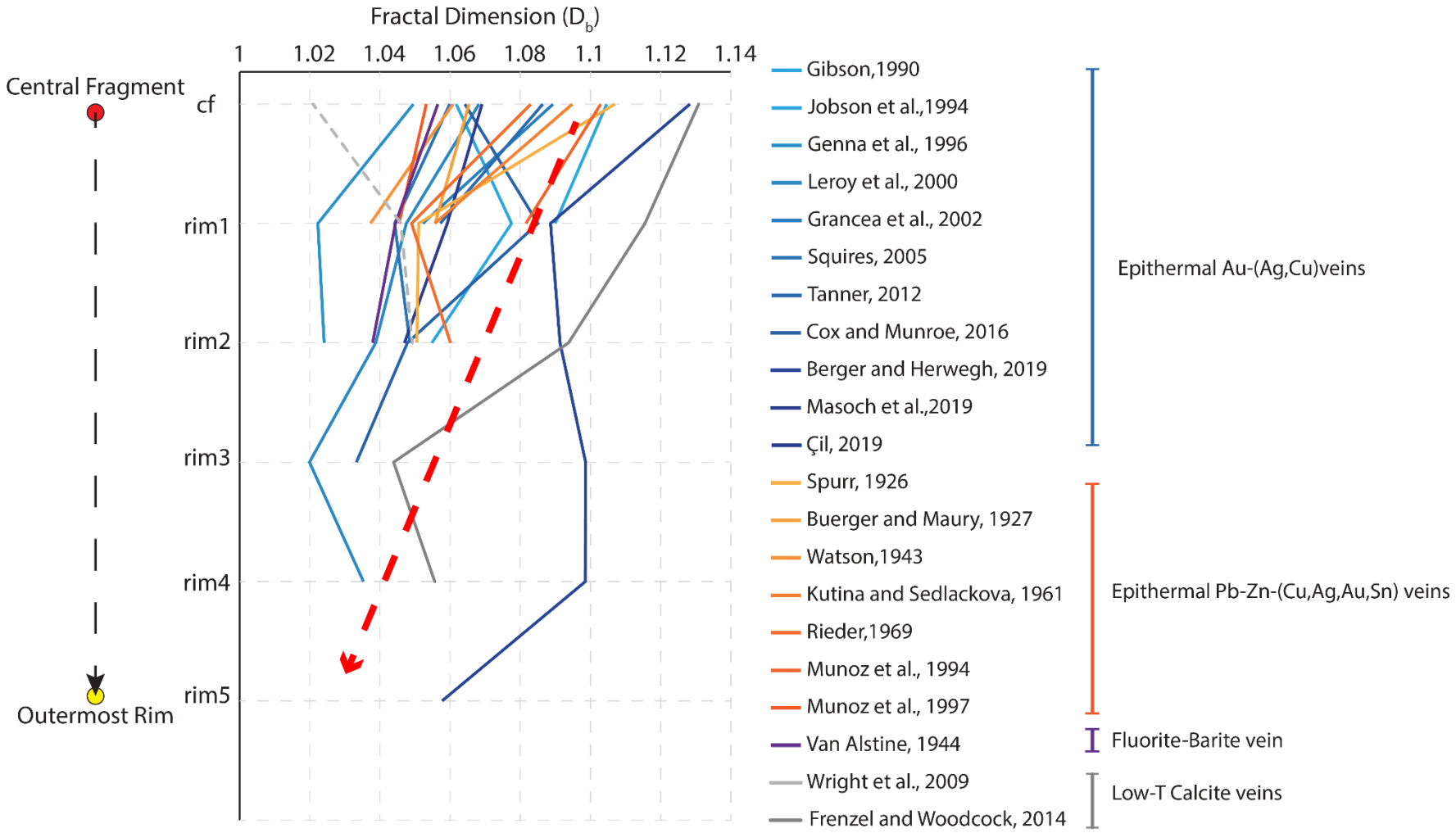

Figure 59: The fractal dimension values of the database from the central fragment to the successive rims. The standard deviations of the fractal dimension values are too small to show on the graph. The pale grey dashed line (Wright et al., 2009) represents the only cockade texture where the outer rim has a higher fractal dimension value than the central fragment. The dashed red line represents the decreasing fractal dimension trend from the central fragment to the outermost rim.

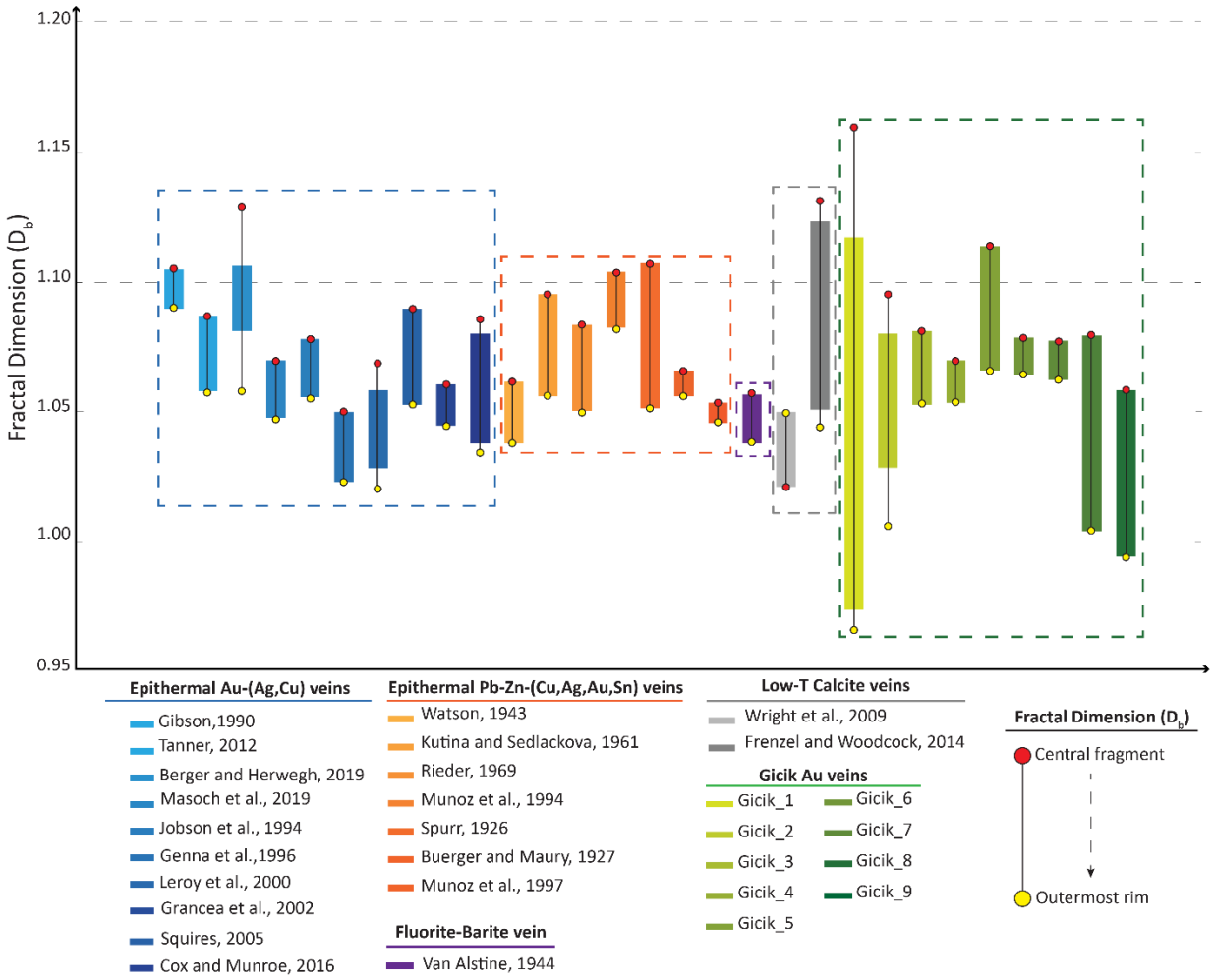

Figure 59: The fractal dimension values of the central fragments and outermost rims according to the occurrence types in the database and Gicik locality.

5.3.2 Oxwich

The comparison between Oxwich and the database examples refers specifically to cockade textures documented at macroscopic scales. The database examples were taken from studies conducted in the same study area, as reported by Frenzel and Woodcock (2014) and Wright and coauthors (2009), which also examined low-temperature calcite veins in Oxwich. The central fragments originate from limestone host rock and early vein material (Figure 60 a-d). The rims are composed of carbonate layers with distinct texture and colour differences due to their iron content (Figure 60 a and Figure 61 c) and crystal sizes (Figure 60 b and Figure 61 d). In Figure 60, the fractal dimension values show a consistent overall decrease from the first to the final rim except for a, b and d, while the central fragments have lower values than the first rim, except for c.

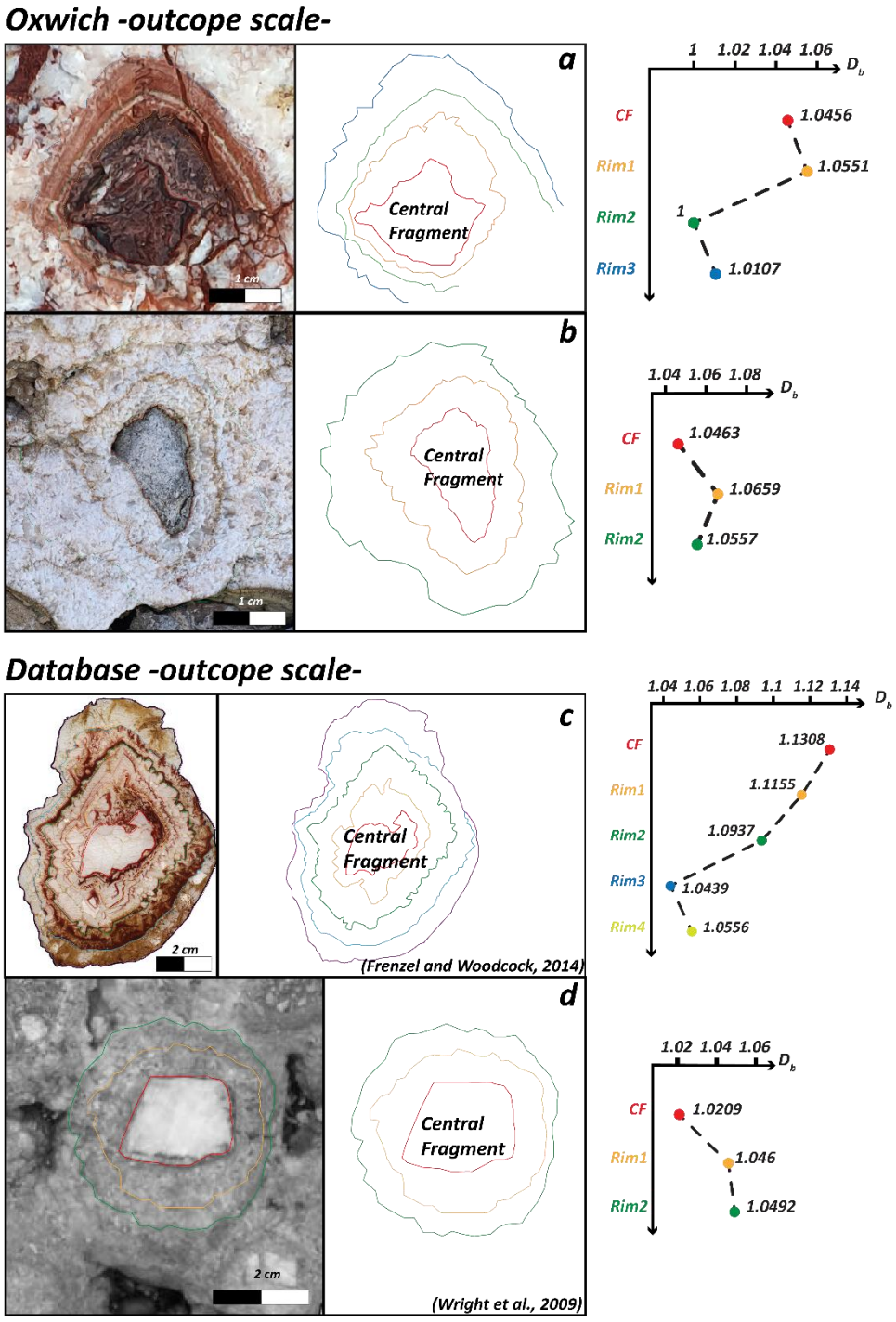

Figure 60: The fractal dimension values of cockade textures from this study and database information for Oxwich on the outcrop scale. The sample locations from this study were the Western Oxwich Fault: (419346 E, 5711079 N), and the Eastern Oxwich Fault: (419192 E, 5711056). The standard deviations of the fractal dimension values are too small to show on the graph (Appendix 2). (Datum: WSG84 UTM Zone)

5.3.1 Gicik

The comparison between the Gicik samples (this study) and the database examples from the Porgera Gold Deposit, Papua New Guinea (Cox and Munroe, 2016), (both documented in Au-rich hydrothermal deposits), include the cockade texture on macroscopic and microscopic scales. In Gicik, the central fragments are surrounded by very fine-grain silica layers with distinct colour differences at the microscopic scale, while at the macroscopic scale, they consist of fine-grained massive to elongated quartz crystals with distinct colours and textures. The fractal dimension values of cockades show a decreasing trend from the central fragments to the outer rims at both macroscopic and microscopic scales (Figure 61 a-d). This trend is characterised by an initial sharp decrease from the central fragment to the first rim, followed by a slight increase before decreasing again in the final rim. Figure 61 b highlights a slight increase in fractal dimensions within fine-grained dark silica layers, followed by a decrease with the transition to well-developed elongated quartz crystals on the microscopic scale. In the Porgera Au deposit (Papua New Guinea), the central fragments of cockades are surrounded by alternating elongated quartz crystals and pyrite-rich layers of rims. This pattern of alternating mineralogical layers is similar to the variations observed in Gicik, where successive rims exhibit distinct mineral compositions. At the macroscopic scale, there is an apparent decrease in fractal dimension from the central fragment to the first rim (Figure 61 c). Conversely, at the microscopic scale, a slight increase in fractal dimension from the central fragment to the first generation of elongated crystals precedes a decrease, leading to subsequent rims (Figure 61 d). In all cases, regardless of whether it is on a microscopic or macroscopic scale, the central fragments have higher values than the outermost rims.

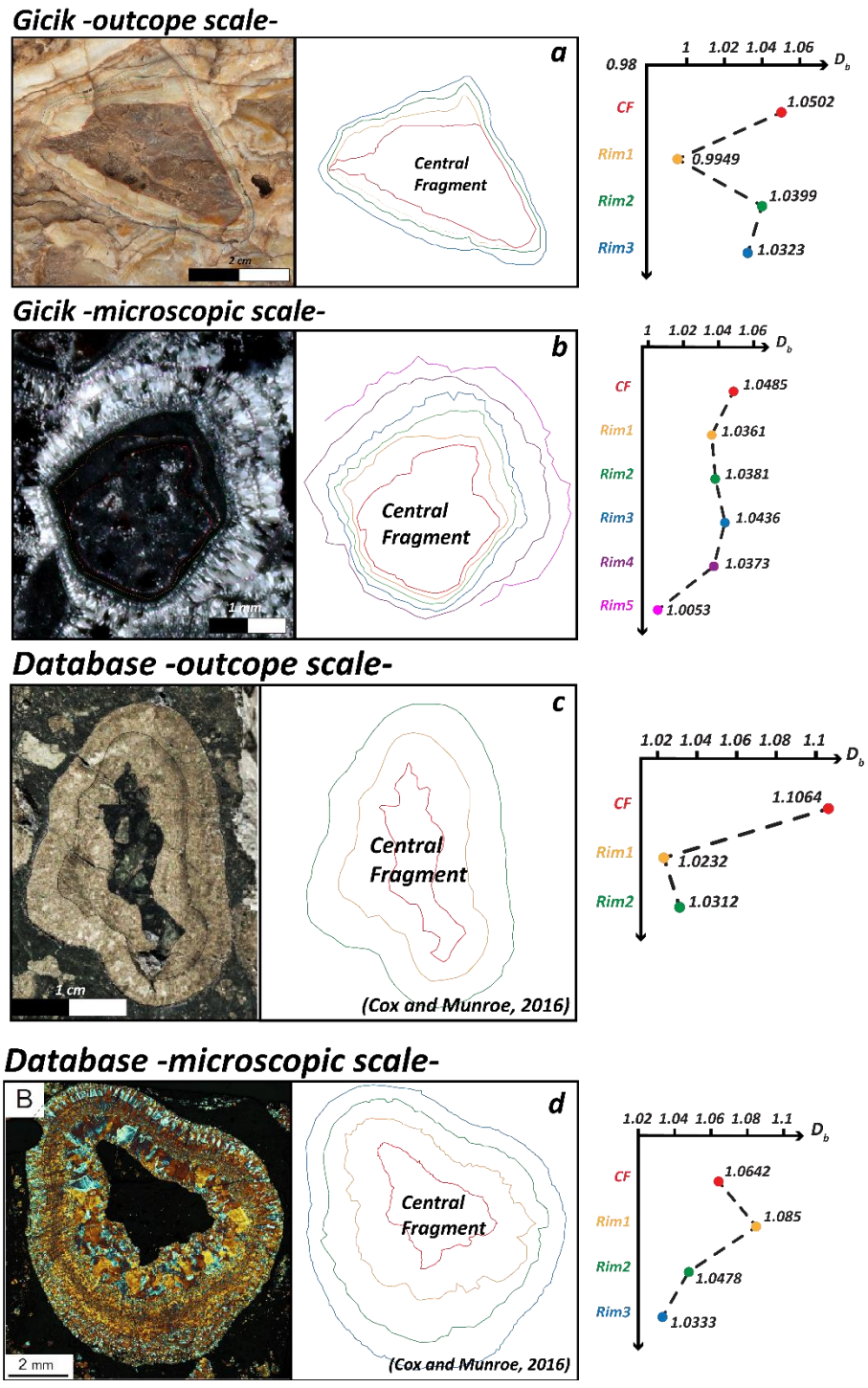

Figure 61: The fractal dimension values of cockade textures from Gicik and the database (Cox and Munroe, 2016) on outcrop and microscopic scale The sample locations from this study were the Q-2 vein segment on the outcrop scale: (497262 E, 4429264 N), and Q-1 vein segment on microscopic scale: (497262 E, 4428940 N). The standard deviations of the fractal dimension values are too small to show on the graph (Appendix 2). (Datum: WSG84 UTM Zone)

5.3.2 Oxwich and Gicik

Figure 63 illustrates variations in fractal dimensions of successive rims expanding outward from a central fragment at a microscopic scale in Oxwich and Gicik. In Oxwich, the fractal dimensions of carbonate precipitate rims originating from a fossiliferous limestone host rock fragment exhibit overall a slight decrease (from 1.0439 to 1.0233) with fluctuations (Figure 62 a). Conversely, in Gicik, the fractal dimension decreases (from 1.1641 to 0.9973) gradually from the central fragment of highly silicified host rock to fine-grain quartz and well-developed elongated quartz crystals with distinct textures (Figure 62 b).

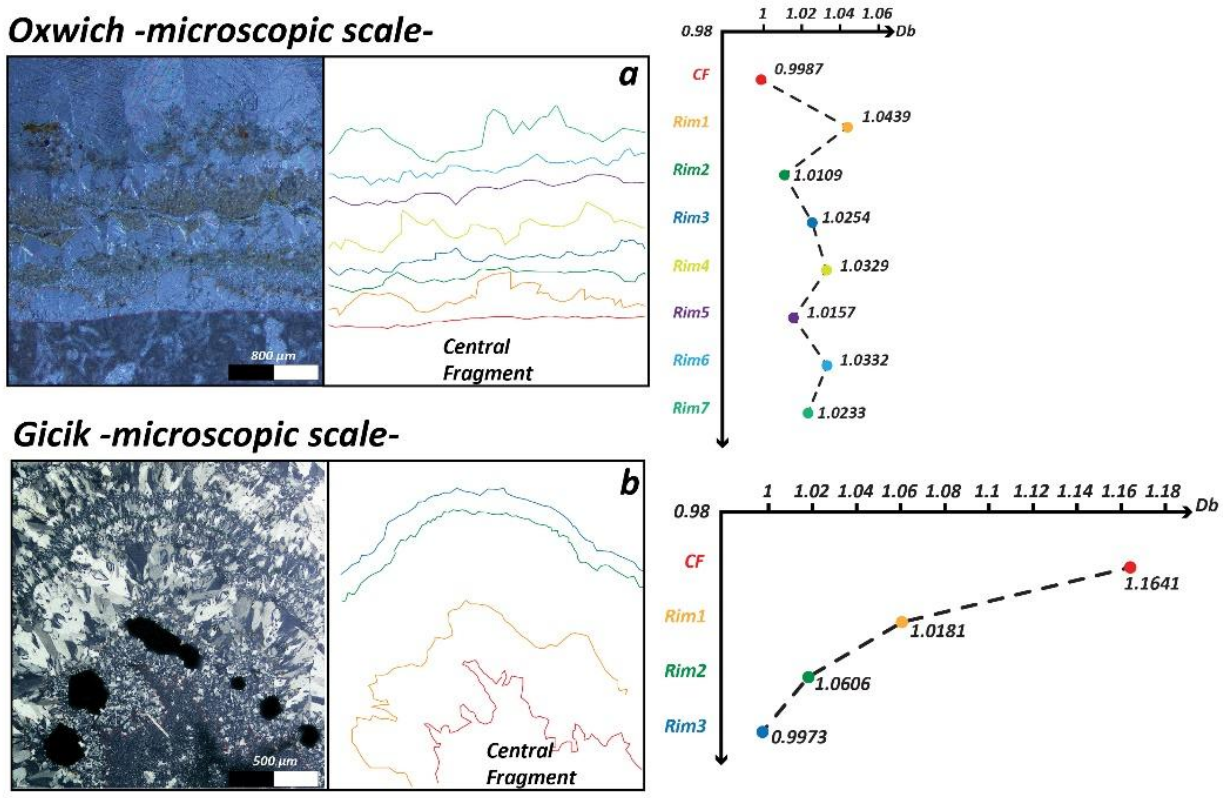

Figure 62: The fractal dimension values of cockade textures from Oxwich and Gicik on the microscopic scale. The sample locations from this study were Oxwich, E-W trending fault: (419252 E, 5711088 N), and Q-2 vein segment: (497045 E, 4428937 N). The standard deviations of the fractal dimension values are too small to show on the graph (Appendix 2). (Datum: WSG84 UTM Zone)

5.4 Discussion and Conclusion

Microscopic observations of cockade textures in silica-dominated Gicik veins and carbonate-dominated Oxwich veins reveal textures indicative of various geological processes, including primary growth into open spaces, recrystallisation, and replacement.

In Oxwich, the textures of surrounding rim layers around a wall rock fragment include various crystal forms of carbonate cement with different sizes and preferred orientations on a microscopic scale. The central fragments originate from limestone wall rock (Figure 55), while the rims consist of alternating layers of red-stained micritic calcite and euhedral sparry calcite crystals in blocky or fibrous shapes (see Figure 55). These two types of calcites, micritic and sparry, are commonly found in sedimentary rocks with diverse textures (Wright and Tucker, 1991). It is well-documented that micritic calcite forms through recrystallisation from a metastable precursor under diagenetic conditions (Wright et al., 1997; Gierlowski-Kordesch, 2010). Blocky crystal growth typically occurs during ongoing nucleation of new crystals, associated with high supersaturation of the host fluid (Oliver and Bons, 2001). Supersaturation can result from mechanisms such as the sudden halt of rapidly rising fluids (Bons, 2001) or a rapid drop in fluid pressure during hydraulic fracturing (Phillips, 1972). Fibrous sparry calcite textures, as opposed to blocky ones, are generally explained by competitive crystal growth perpendicular to the substrate (Oliver and Bons, 2001). This competition suggests that a lower degree of fluid supersaturation during deposition resulted in a lower nucleation rate for new seed crystals compared to equant blocky calcite (Oliver and Bons, 2001). Various mechanisms control the formation of micritic and sparry calcite, primarily related to diagenetic processes that alter crystal shape and size post-precipitation. The sequence of sparry calcite with micritic calcite laminae suggests recrystallisation, characterised by size increases and number decreases of distinct-coloured calcite crystals with different textures (Gonzalez et al., 1992). The red-stained micritic calcites precipitate along concentric growth patterns of euhedral carbonate crystals, mimicking their shapes and varying in thickness within the same layer (see Figure 55). These very fine-grained, randomly oriented calcite crystals decrease in number and increase in size outwardly, transitioning from blocky to fibrous euhedral crystals due to competitive growth (Dickson, 1993; Oliver and Bons, 2001). Additionally, well-defined growth faces visible on larger crystals indicate growth into a fluid-filled open space rather than through an incremental crack-seal mechanism. Local truncations on the surrounding rim layers or rotated geopetal indicators were not observed at the microscopic scale in Oxwich, as individual cockade textures did not fully fit within a single thin section. While geopetal structures were identified macroscopically, breakage points were not detected at either scale. If

continuously sealed and refractured systems formed the cockade rims due to mechanical actions of fault walls, one would expect local truncations on rims rather than the following growth faces precisely. Therefore, criteria supporting the repeated rotation and accretion mechanism proposed by Frenzel and Woodcock (2014) were not detected on the microscopic scale. However, the layers of red-stained micritic calcite exhibit varying thicknesses within the same layer and are intersected by euhedral sparry calcites in some areas (Figure 55 a1 and Figure 56 a2). High-magnification views of adjacent areas of precipitated red-stained micritic calcite and euhedral sparry calcite reveal a gradational contact relationship rather than a sharp one (Figure 55 d1-d3). The irregular rim thickness and lack of sharp contact points between layers support criteria for inward metasomatic alteration mechanisms, where alteration refers to recrystallisation rather than replacement processes. Hence, the cockade textures in Oxwich, a carbonate-dominated system, primarily illustrate rim growth into an open space around a central fragment. The absence of local truncations on the rims and rotated geopetal indicators suggest a diagenetic environment rather than repeated fault movement. Moreover, micritic and sparry calcite boundary relations and textures primarily point to recrystallisation as a diagenetic process. This suggests that while the rims of cockade textures initially grew into an open space, they are partially affected by inward alteration through recrystallisation as a secondary process. This underscores the importance of detailed microscopic analyses of cockade textures, considering both primary and secondary processes, to avoid misinterpretations, particularly when correlating successive fluid fluxes using concentric layers of rims.

In Gicik, microscopic observations show primary growth textures, albeit predominantly affected by recrystallisation. Recrystallisation textures such as mosaic, feathery, plumose, and ghost spheres are widely observed textures in silica-dominated systems at Gicik (Figure 57). The mosaic texture forms through the recrystallisation of massive chalcedony or amorphous silica (Dong et al., 1995; Camprubí and Albinson, 2007), suggesting recrystallisation temperatures exceeding 180°C, close to the upper stability limit for chalcedony (Fournier, 1985; Saunders, 1994). The feathery texture, characterised by aggregates of fibrous chalcedony with rounded external surfaces, is often accompanied by plumose and ghost sphere textures, indicative of silica gel precursors (Dong et al., 1995; Taksavasu et al., 2018; Zeeck et al., 2021). Silica gel precipitates due to rapid pressure decrease associated with fracturing and subsequent temperature decrease, leading to amorphous silica precipitation (Henley and Hughes, 2000). Depending on initial temperature and pressure conditions, the fluid may undergo rapid vaporisation, or pressure-temperature conditions may follow the liquid-vapour curve as the fluid continues to boil along its upward flow path (Brown, 1986). Camprubí and Albinson (2007) describes this type of silica as a transitional phase in the silica precipitation cycle, precipitating after the amorphous silica phase and before the later

crystalline quartz phase. These recrystallisation textures are also observed in the comb texture, classified as a subtype of crustiform texture similar to the cockade texture. This implies that the rims of cockade textures initially grew into an open space, akin to the growth of euhedral quartz crystals of comb texture into the void space created between the latest overgrowth rims (Figure 58). However, these textures are extensively overprinted by secondary processes, such as recrystallisation and replacement, observed on both central fragments and surrounding rims. This overlap can lead to misinterpretation, particularly when correlating different fluid fluxes using concentric layers of rims. Moreover, in Gicik, the cockade textures exhibit local truncations on the surrounding rims, interpreted as a criterion for the repeated rotation and accretion mechanism at a microscopic scale (Frenzel and Woodcock, 2014). Alongside these features, the cockade textures in Gicik primarily demonstrate criteria for replacement, such as replacement along grain boundaries, resulting in irregular rim thickness and a lack of sharp contact points between central fragments and surrounding layers of rims (Kutina and Sedlackova, 1961) (Figure 56). Thus, microscopic observations of cockade textures in Gicik provide evidence for both repeated rotation and accretion, and inward metasomatic alteration, indicating the simultaneous occurrence of these two favoured mechanisms.

Descriptions of the structures and texture of rocks are essential for advancing our understanding of them. These descriptions allow us to deduce the relative ages of successive events, identify those susceptible to secondary processes, such as replacement and recrystallisation, and discern geological processes involved in the formation of these structures and textures. However, the terminologies used in either microscopic or microscopic analyses to describe mineral structures and textures are subjective and, therefore, need some systematic numerical methods to make strict comparisons. As a shape parameter, the fractal dimension provides an enhanced understanding of the various processes that ultimately result in a final outline (Longley and Batty, 1989).

When fractal dimension was chosen as a method in this study, the primary goal was to distinguish between cockade rims formed by primary and secondary processes. To achieve this, a database was created using well-documented occurrences compiled by Frenzel and Woodcock (2014). Selected examples from this database were digitised, focusing on the central fragments and their surrounding rims. The box-counting method, used for fractal dimension calculations, required the boundaries of features to be represented as continuous, non-interrupted lines. However, this posed a limitation in microscopic-scale analyses, particularly for rims affected by secondary processes, as the traces of these processes did not consistently form a continuous structure. As a result, since these rims could not be delineated as a single uninterrupted

line, it was not possible to systematically distinguish between primary and secondary processes. Additionally, one of the biggest challenges encountered was that the resolution of the source images significantly influenced how rims were delineated. As a result, the initial objective of using fractal dimension analysis to systematically differentiate primary and secondary textures could not be fully achieved. The only consistent finding was that the fractal dimensions of central fragments were generally higher than those of the outermost rims. The only exception to this trend was Wright and coauthors (2009), where fractal dimension increased outward from the central fragment. However, this is likely an artefact of the low resolution of the selected cockade texture image rather than a genuine geological pattern. Furthermore, variations in fractal dimension between the central fragment and the outermost rim, which include intermittent increases and decreases in intermediate rims, and occasional values exceeding those of the central fragment, could not be directly linked to secondary processes.

The results showed a general trend of decreasing fractal dimensions from central fragments to rims in silica-dominated systems, with occasional increases in carbonate-dominated systems. The decrease in fractal dimension values of crystal layers is interpreted as they grew into an open space, which is a general consensus of many proposed formation mechanisms, repeated rotation and accretion, fluidisation in a fluid and crystallisation pressure, except inward metasomatic replacement. The fractal dimension measures how complex and irregular surfaces are, which are the outlines of central fragments and the rim fronts in this study, with higher values indicating more intricate shapes. When crystal layers experience a decrease in fractal dimension, it can indicate a transition from a highly irregular and branching growth pattern, typical of constrained growth within a confined space, to a more ordered and less complex pattern, which can occur when crystals grow in an open space where they have more room to expand without encountering any obstacles. Therefore, the value of decreasing fractal dimensions from central fragments to outermost rims aligns with the proposed mechanisms, suggesting primary growth of rims into the open space. As rims grow outward, their complexity decreases, progressively becoming smoother as they mimic the shape of the central fragment and appear increasingly rounded toward the outermost rims.

5.5 Comparison of Oxwich and Gicik Localities on Microscopic Scale

The cockade texture-bearing breccias were examined on microscopic scales. The carbonate-dominated system in Oxwich, where Frenzel and Woodcock (2014) favour the rotation and accretion mechanisms, supports the crystallisation pressure hypotheses, as discussed above in the relevant session, on a microscopic base. Moreover, the pervasive recrystallisation texture observed on rims indicates that the partial metasomatic alteration by recrystallisation also operates at Oxwich. On the other hand, the silica-dominated system in Gicik supports that the rims surrounding the central fragments are formed by growing into an open space and by the inward metasomatic alteration by replacement and recrystallisation of the central clasts and the early generation of the rims. The truncations on outgrowth rims indicate that the repeated rotation and accretion mechanism also operates at Gicik. Table 5 below compares the macroscopic observations in the selected localities on the microscopic scale.

Table 5: The comparison of the selected localities based on the observations on the microscopic scale.

Microscopic Scale

	Oxwich	***Gicik***
Central Fragments	Fosilliferrious limestone wall rock (e.g. Figure 55 d)	Volcanic wall rock, early generation cement and breccia (Figure 57)
Rim mineralogy	Carbonate and iron-rich carbonate cement (Figure 55 a to d)	Coarse to fine grain silica cement, alteration minerals, i.e. adularia, and euhedral to disseminated opaque minerals, i.e. pyrite by replacement (Figure 57 c3 and b2)
Rim texture	Blocky sparry, fibrious sparry and red-stained micritic carbonate (e.g. Figure 55 a)	Open space-filling texture, i.e cockade, comb, recrystallisation textures, i.e. feathery, plumose, ghost-sphare textures (Figure57a to c)
Criteria for mechanisms	Central fragments are separated Rims surrounding the central fragments No truncation on outgrowth rims No rotated geopetal sediments Well-developed crystal face indicating growth in to an open space (Figure 55 a) Sharp contact boundary between central fragments and rims (e.g. Figure 55 d)	Central fragments are separated (Figure 56) Rims surrounding the central fragments Truncation on outgrowth rims No rotated geopetal sediments Not-well developed crystal face indicating rapid cooling (Figure 57 c2) No sharp contact between central fragments and rims (Figure 56)
Operating mechanisms for the formation of cockade texture	Force of crystallisation Partial metasomatic alteration by recrystallisation	Partial metasomatic alterations by replacement and recrystallisation Repeated rotation and accretion

Chapter 6: Fluid Geochemistry-Fluid inclusions and Stable Isotopes

This chapter presents the analyses of fluid inclusion microthermometry and stable carbon and oxygen isotopes from Oxwich. Seven samples collected from carbonate rims of cockade textures were analysed at Cardiff University's Laboratories within the School of Earth and Environmental Sciences. These analyses aim to reveal the palaeo-fluid environment, focusing on the fluid source and temperature governing the precipitation of carbonate rims surrounding the central clasts in cockade textures. Due to the pervasive effects of replacement and recrystallisation observed in microscopic analyses, the fluid characteristics recorded in these samples primarily reflect secondary processes, particularly late-stage diagenetic modifications, rather than the original geochemical environment. No sample yielded fluid inclusions suitable for fluid inclusion microthermometry in Gicik (cf. Çil 2018)

Given the natural reserve status of the Oxwich Bay and Porth-Eynon Bay areas within the Gower Peninsula, all sampling activities were conducted with minimal impact on the environment. Sampling was carefully planned to avoid excessive material removal, ensuring that outcrops remained undisturbed for future research and conservation. In line with the best practices, the Geological Society’s Code for Geological Fieldwork and Sampling was strictly followed, which includes obtaining necessary permissions, limiting sample sizes, and prioritizing areas where natural erosion already exposes fresh surfaces. This approach aligns with previous geological studies conducted within the Gower Peninsula, where responsible sampling methods have been implemented to balance scientific research with environmental conservation.

6.1 Samples and Methods

6.1.1 Samples

Seven samples were obtained from carbonate cement within fissures, focusing on cockade textures for fluid inclusion microthermometry and stable carbon and oxygen isotopes in the Oxwich region. Both the double-polished thin sections and the stable isotope samples were prepared from the same hand specimens. The hand specimen photos are depicted in Figure 63, along with their corresponding locations on the map. (For the sample locations and descriptions, please see Table 6.)

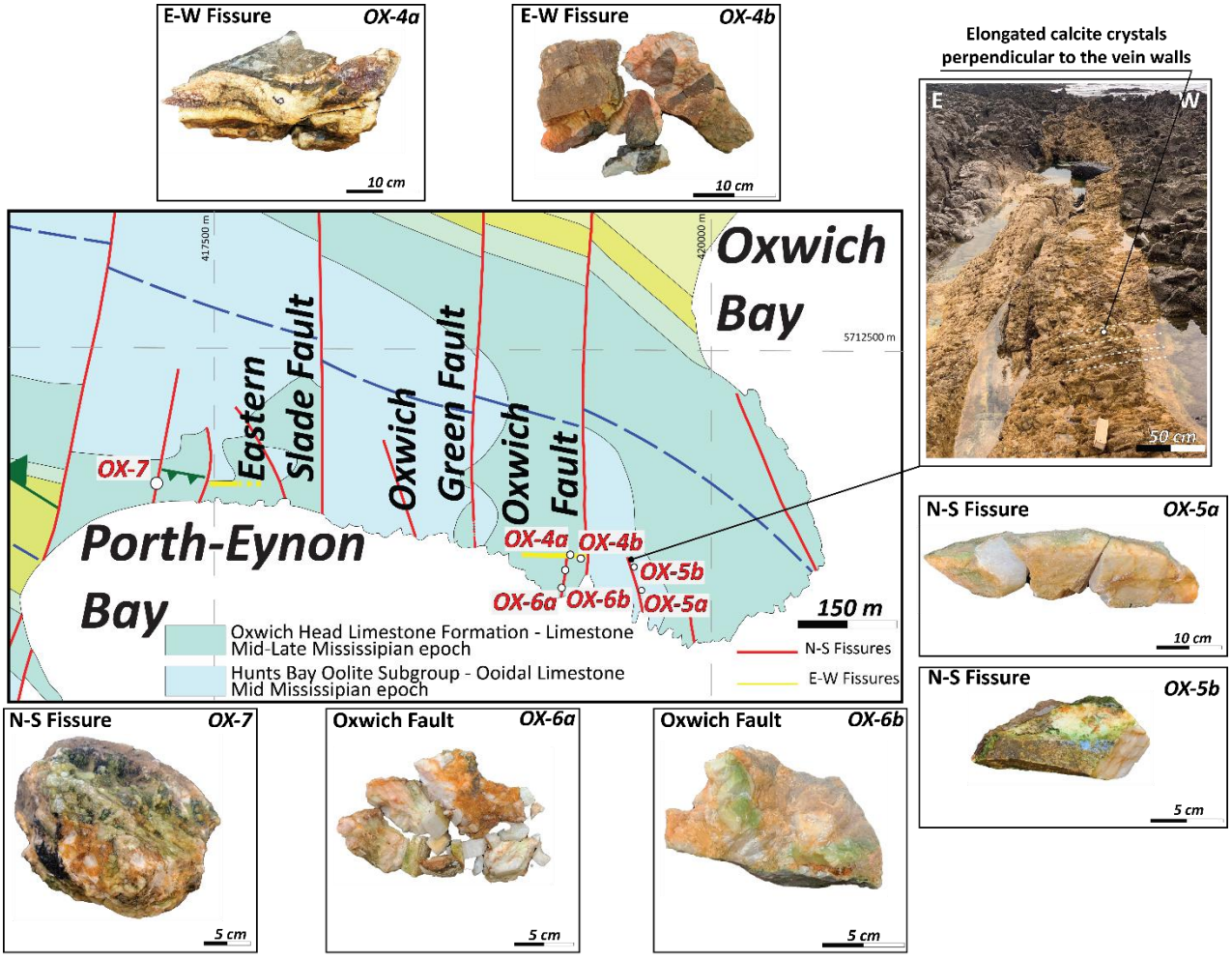

Figure 63: The hand specimen photos of samples with their descriptions and corresponding locations on the map. (Datum: WSG84 UTM Zone). OX-5a and OX-5b samples from the outcrop above.

Table 6: Sample locations and descriptions.

Sample ID	Easting	Northing	Description
OX-4a	419252	5711088	**E-W trending fault** containing cockade texture
OX-4b	419345	5711087	
OX-5a	419625	5710858	Fissure at the eastermost side of the study area not containing cockade texture
OX-5b	419608	5710923	
OX-6a	419187	5711043	**Western Oxwich Fault** containing cockade texture
OX-6b	419579	5710936	
OX-7	417133	5711479	Fissure at the westermost side of the study area containing cockade texture

The sampling sites were selected from east to west to represent fissures with and without cockade textures. Samples OX-4 a-b and OX-6 a-b were taken from carbonate rims of cockades in east-west trending fissures and from the Western Oxwich fault, respectively (Figure 64). Sample OX-4 a-b displays a cockade texture characterised by alternating layers of carbonate rims with blocky and elongated shapes (refer to Figure 25 for an outcrop photo and Figure 56 d for a thin section photo). Samples OX-6 a-b were collected from the carbonate rims of a large cockade texture in the Western Oxwich fault (see Figure 31 b for an outcrop photo and Figure 55 b for a thin section photo). The OX-5 a-b samples were obtained from a fissure at the westernmost side of the study area. This fissure contains large, elongated carbonate crystals oriented perpendicular to the north-south trending fissure walls and does not exhibit cockade texture (see Figure 65 for the outcrop photo). Finally, the OX-7 sample was collected from a fissure with cockade texture at the easternmost part of the study area (see Figure 31 a for the outcrop photo).

As the analysed carbonate samples were exposed to the surface, potential weathering effects were considered. However, the measurements were performed on sections prepared from the interior parts of the samples, rather than directly exposed surfaces, to minimise alteration. Additionally, petrographic selection ensured that only well-preserved, sealed inclusions were analysed, reducing the impact of post-depositional weathering on the recorded fluid inclusion microthermometry results and stable isotope analyses.

6.1.2 Methods

6.1.2.1 Fluid Inclusion Microthermometry

This study involved preparing doubly polished wafers of vein calcite (~250 µm thick) for fluid inclusion microthermometry. The microthermometric data was obtained using a Linkham THM600 heating-freezing stage at Cardiff University's School of Earth and Environmental Sciences. Calibration at low temperatures was performed using synthetic fluid inclusion standards from Syn Flinc, ensuring a temperature accuracy of ±0.5°C. Repeated measurements of the CO_2 melting point confirmed this accuracy, and additional ice-melting temperature measurements in secondary inclusions demonstrated internal consistency within the same uncertainty range. To minimise potential damage to fluid inclusions, wafers were fragmented into multiple 1–4 mm chips, preserving the integrity of inclusion populations across the sample. Optical microscopy was used to identify fluid inclusion assemblages.

The microthermometric procedure began with a preliminary heating step at 110°C for 5 minutes to remove water vapour from the chamber. The samples were then cooled to -150°C at a rate of 50°C/min, followed by a 5-minute hold to induce freezing. If freezing did not occur, the samples were cycled between -180°C and -90°C (10–15 times) to promote nucleation. After freezing, inclusions were heated at 10°C/min until reaching -57°C, and the rate was then reduced to 0.1°C/min near the CO_2 melting point (-56°C). Once CO_2 melting was complete, the heating rate was restored to 10°C/min until the expected T_{fm} (first melting temperature) and T_m (final ice-melting temperature) were reached. For the final heating runs, the rate was initially set to 20°C/min, and as vapour bubbles became active or daughter minerals started dissolving, the heating rate was reduced to 5°C/min to ensure accurate recording of homogenisation temperatures.

Several factors influence the accuracy of microthermometric data, including instrumental precision, phase transition hysteresis, and potential post-entrapment modifications. Calibration with Syn Flinc standards ensured a temperature precision of ±0.5°C across all measurements. Additionally, careful selection of fluid inclusions aimed to minimise the effects of necking-down, leakage, or stretching, which can alter homogenisation temperatures and salinity estimates. Despite these precautions, some degree of post-entrapment modification remains a consideration, particularly in recrystallised calcites. The small size of certain fluid inclusions posed an additional challenge in determining first melting temperatures (T_{fm}) and final ice-melting temperatures (T_m), as phase transitions were often subtle. To mitigate this, repeated measurements were conducted at a reduced heating rate (0.1°C/min near phase transitions) to improve accuracy. The uncertainty in T_{fm} and T_m measurements is estimated to be ±0.5°C, consistent with standard

microthermometric procedures (Goldstein and Reynolds, 1994). However, the selection of well-preserved secondary inclusions, along with consistency across multiple measurements, supports the reliability of the obtained data.

To estimate the pressure conditions and determine other parameters of the mineral formation medium, microthermometry data and the total concentration of salts in fluid inclusions, along with their affiliation with a particular water–salt system, were analysed using the software package AqSo_NaCl (Bakker, 2018). The equation of Bodnar and coauthors (1985) below was used to calculate salinities of liquid-rich fluid inclusions by measuring ice-melting temperatures, where θ represents the measured final ice melting temperature:

$$salinity\ (wt\%\ NaCl) = 1.78\ \times \theta - 0.0442 \times \theta^2 + 0.0005572 \times \theta^3\ \ . \qquad (6)$$

6.1.2.2 Stable Isotopes

The analysis of stable carbon and oxygen isotopes serves as a crucial method for understanding fluid-rock interactions and identifying the specific types of fluids involved in dissolution and precipitation processes within fault zones. The $^{13}C/^{12}C$ ratio plays a pivotal role in pinpointing the carbon source (Stahl, 1977). A depletion in ^{13}C suggests a connection to organic complex evolution (Labaume et al., 2001), while slight variations in $\delta^{13}C$ compositions can indicate an open system (Hausegger et al., 2010), along with a decline in $\delta^{18}O$ values (Marquer and Burkhard, 1992). The $^{18}O/^{16}O$ ratio, influenced by precipitation temperature and the oxygen isotopic composition of the precipitation fluid, enables the tracking of water movement (Clark and Fritz, 1997). Diverse $^{18}O/^{16}O$ ratios imply precipitation across varying temperatures and/or $\delta^{18}O$-water values (Labaume et al., 2001). Additionally, low $\delta^{18}O$ values compared to the host rock suggest precipitation from higher-temperature fluids or those with a lower $\delta^{18}O$ composition (Hausegger et al., 2010), possibly due to water salinity, freshwater input, and local evaporation. Rainwater tends to be ^{16}O-enriched due to the evaporation preference of the lighter ^{16}O from seawater. However, identifying the precise source or contributors from mixed sources remains challenging and subject to interpretation, given the typical variability or overlap in source compositions.

Several factors contribute to uncertainty in stable isotope analysis, including post-entrapment modifications, sample preparation, and instrumental precision. Petrographic analysis revealed evidence of recrystallisation in many of the sampled calcites, indicating the influence of secondary processes. While

care was taken to prioritise carbonate phases least affected by late-stage alteration, complete exclusion of secondary overprints was not possible. Therefore, the obtained isotopic data should be interpreted with consideration of potential post-depositional modifications, including partial isotopic resetting due to fluid interaction or recrystallisation. Uncertainties also arise from methodological factors such as sample extraction, weighing precision, and instrumental calibration. The analysis was conducted using a mass spectrometer, with gas conversion and separation steps introducing minor but unavoidable systematic errors. To monitor analytical precision, an internal standard (BCT63-Carrara Marble) was used, yielding a reproducibility of ≤ 0.04‰ (1 s.d.) for $\delta^{18}O$ and ≤ 0.03‰ (1 s.d.) for $\delta^{13}C$.

Pulverised carbonate samples, ranging from 5 to 100 µg, were extracted using a dental drill from the hand specimens. These samples underwent a reaction with 100% phosphoric acid at 60°C, using a gas bench connected to a mass spectrometer. Subsequently, the carbon dioxide produced during this reaction underwent analysis using a mass spectrometer. Variations in reaction temperatures across different laboratories are standard laboratory protocols. However, higher reaction temperatures expedite the analysis due to increased production of ^{16}O gas, resulting in more negative values as the temperature rises. It is essential to correct for the fractionation factor, α, for calcite, which decreases by 0.12 per mil (‰) for every 1°C increase in temperature. To ensure accuracy, oxygen isotope values were corrected using the phosphoric acid fractionation factors outlined by Kim et al. (2007) and Rosenbaum and Sheppard (1986). The results were reported in ‰ using the δ notation on the Vienna Pee Dee Belemnite (VPDB) scale. The analysis utilised the MAT 253/Kiel IV carbonate device at Cardiff University's School of Earth and Environmental Sciences (Appendix 4).

A total of seven carbonate samples were analysed to ensure a statistically robust dataset for assessing fluid temperatures and $\delta^{18}O$ values. The observed isotopic variations are consistent across multiple samples and mineral phases, reinforcing the reliability of the inferred precipitation conditions. However, additional sampling of coeval mineral phases would further refine the interpretations.

The $\delta^{18}O$ of a solid phase of carbonates, such as calcite and dolomite, is usually reported in PDB (heavy standard), while the $\delta^{18}O$ of liquid phases (e.g., seawater, rainwater, generally the precipitating fluid) is usually reported in VSMOW (Vienna Standard Mean Ocean Water, light standard). The interconversion equation for calcite is as follows (Friedman and O'Neil, 1977):

$$\delta^{18}O\ VSMOW = (1.03091 \times \delta^{18}O\ VPDB) + 30.91 \quad . \qquad (7)$$

6.2 Fluid Inclusion-Results

A set of 7 samples collected from fissures in Oxwich (Figure 63) representing the carbonate cements were analysed, and a total of 140 inclusions were measured using the methods outlined above, of which 102 yielded usable data (Figure 64) (Appendix 3.1). Due to site restrictions in Oxwich Natural Reserve, oversampling was avoided to minimise disturbance, and the number of analysed inclusions reflects the maximum achievable dataset while ensuring data reliability. The microthermometry analyses aimed to yield data from the secondary fluid inclusions, mostly isolated in the centre of the crystals, trapped along the growth zones of carbonate crystals, keeping their original shapes and away from intercrystalline fractures. Cockade textures are typically devoid of primary fluid inclusions due to their exposure to secondary geological processes of replacement and recrystallisation; however, they contain useful secondary inclusions, which can provide valuable insights into the post-depositional conditions they experienced (Moncada et al., 2012).

The results of microthermometry analysis on fluid inclusions from the seven samples are summarised in Table 7. Detailed results for each fluid inclusion are provided in Appendix 3.2. A representative result for each sample, including homogenisation temperatures (T_h °C), final ice-melting temperature (T_m °C), liquid and vapour size (µm), and calculated salinity (%), is presented for the samples listed in the second row of the table. Salinities of liquid-rich fluid inclusions were calculated using Bodnar's equation (1993) based on the measured final ice-melting temperatures. Determining first melting temperatures (T_{fm} °C) and final ice melting temperatures (T_m °C) was challenging due to the small size of the fluid inclusions. Nonetheless, meticulous care was taken to ensure accuracy in salinity calculations. The representative measurement of each sample, as presented in the second row, is used to plot isochore diagrams. These measurements include the homogenisation temperatures (T_h °C) and final ice melting temperatures (T_m °C) together.

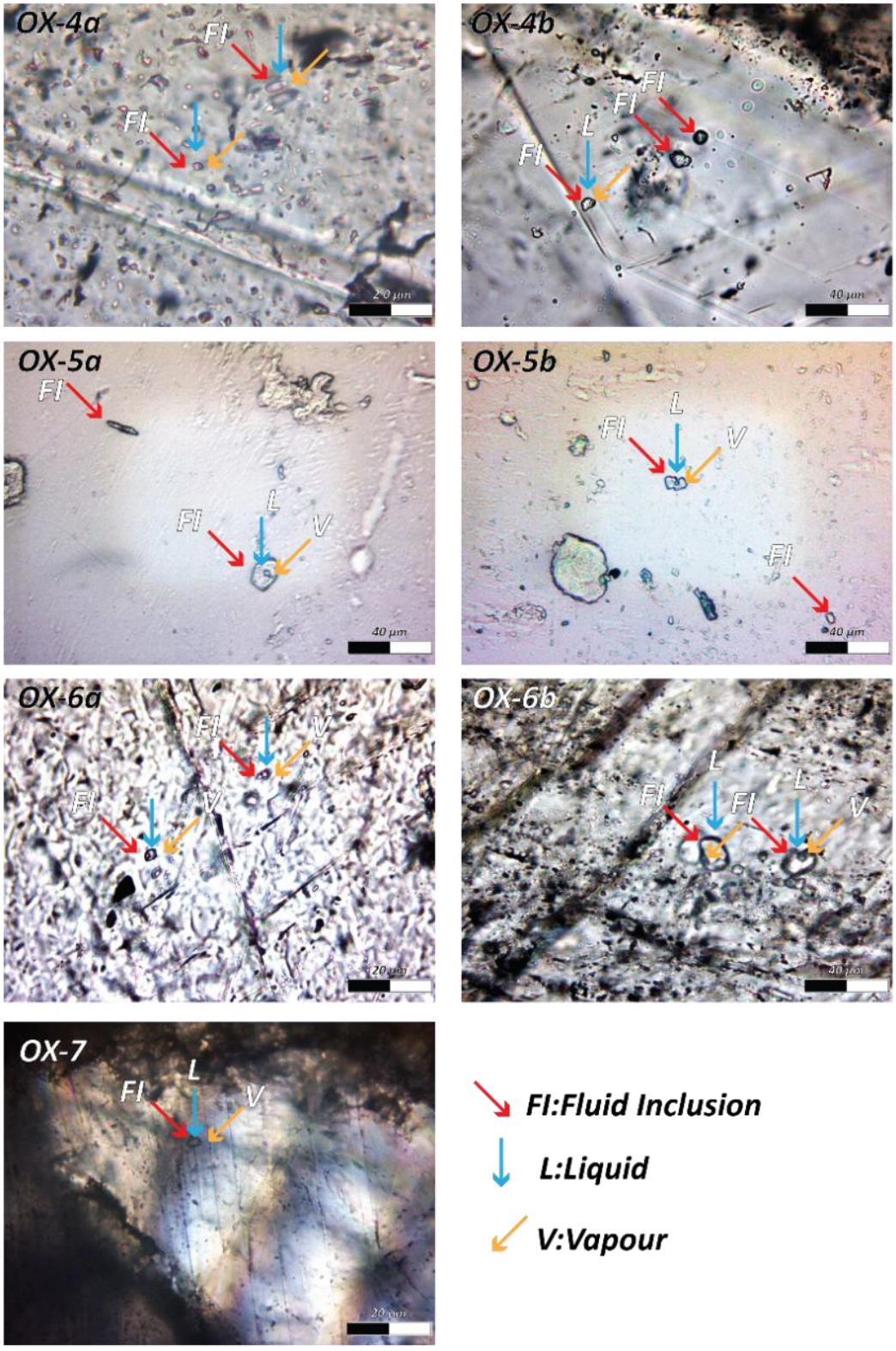

Figure 64: The fluid inclusion photos in carbonate crystals from double polished thin sections collected from fissures in Oxwich. All photos represent the plane-polarised light with condenser for higher resolution.

Table 7: Summary of fluid inclusion microthermometry results for the liquid-rich fluid inclusions present in the Oxwich sample.

Sample ID	# FI (n)	T_h °C	T_m °C	L (µm)	V (µm)	L Ratio (%)	Salinity (NaCl %)
OX-4a	17	182-268 **258**	-5.6 - -6.1 **-5.6**	2.4-5.6 **5.6**	0.8-2.2 **2.2**	67.7-77.6 **71.8**	**8,68**
OX-4b	17	182-276 **236**	-6.0 - -6.7 **-6.0**	2.6-8.3 **6.1**	0.9-2.5 **1.7**	71.6-79.8 **78.2**	**9,21**
OX-5a	9	81-93 **89**	-5.2 - -7.2 **-5.2**	3.2-8.8 **7.0**	0.7-1.8 **1.6**	69.2-83.1 **81.4**	**8.14**
OX-5b	9	85-128 **101**	-49 - -5.1 **-4.9**	2.1-6,4 **6.4**	0.8-2.4 **2.4**	69.4-77.1 **72.7**	**7.73**
OX-6a	21	155-248 **238**	-1.8 - -2.1 **-2.1**	2.3-8.2 **8.2**	0.4-2.7 **2.7**	66.0-85.5 **75.22**	**3.54**
OX-6b	8	232-285 **280**	0.5 - -1.0 **-0.5**	3.1-9.7 **9.7**	1.2-4.3 **4.2**	64.9-74.2 **69.8**	**0.88**
OX-7	21	198-278 **264**	-6.8 **-6.8**	1.9-7.5 **7.5**	0.5-2,1 **2.1**	69.6-83.3 **78.1**	**10.24**

Pressure corrections were not applied to estimate formation temperatures (T_f) from homogenisation temperatures (T_h), as formation pressures were unknown. Considering pressures were likely 30 MPa or less (Kelly and Rye, 1979), pressure corrections are unlikely to exceed 20°C, meaning that if applied, the actual formation temperatures (T_f) would be at most 20°C higher than the recorded homogenisation temperatures (T_h). According to Wright and coauthors (2009), field evidence, such as sedimentary infills in open spaces, suggests that the fissures in Oxwich remained open after formation rather than imploding or sealing instantaneously. Moreover, the open nature of these fissures, filled with red sediment from above, and the common occurrence of this relationship suggests that complete sealing of mineralised fissures was rare (Frenzel and Woodcock, 2014; Hardman et al., 2020). Therefore, we assume that homogenisation temperatures (T_h) obtained from fluid inclusion microthermometry analyses are equivalent to formation temperatures (T_f). The isochore plot illustrates pressure, molar volume, and density values for each sample (Figure 65). The calculation for isochore plots is presented in the Appendix 3.2.

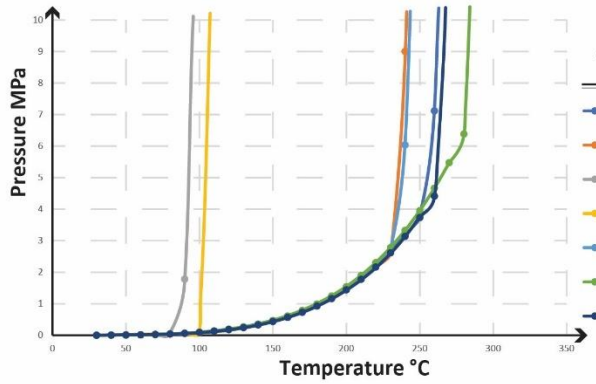

Sample ID	Tf (°C)	P (MPa)	Molar Volume (cm3/mol)	Density g/cm3
OX-4a	258	4.34	22.14	0.9
OX-4b	236	2.95	21.41	0.9
OX-5a	89	0.06	18.69	1.02
OX-5b	101	0.02	18.83	1.01
OX-6a	238	3.17	21.78	0.85
OX-6b	280	6.38	23.84	0.76
OX-7	264	4.71	22.19	0.87

Figure 65: The isochores and pressure, molar volume, and density values of representative fluid inclusions for each sample.

Based on the fluid inclusion microthermometry results and yielded pressure values on the carbonate samples, the analyses performed on samples from fissures including cockade texture (OX-4a, OX-4b, OX-6a, OX-6b, and OX-7) have higher homogenisation temperatures (T_h), ranging from 155°C to 285 °C, and pressure values, ranging from 2.95 MPa to 6.38 MPa. In contrast, the samples (OX-5a and OX-5b) taken from large elongate carbonate crystals perpendicular to the N-S trending fissure walls, which do not include cockade texture, have lower homogenisation temperature (T_h), ranging from 81°C to 128 °C, and pressure values, ranging from 0.02 MPa to 0.06 MPa. As the analysed carbonate samples were exposed at the surface, potential weathering effects were considered.

6.3 Stable Isotope-Results

Carbon and oxygen isotope analyses were conducted on carbonate samples associated with carbonate cement and cockade texture rims surrounding central fragments in fissures at Oxwich. These results were compared with data from previously published literature (Table 8 and Figure 68). The published data represent carbon and oxygen isotopic compositions from the host rock, which is also the host rock of this study. All samples originate from the Pembroke Limestone Group, a typical platform carbonate succession widely exposed in South Wales and deposited during the early Carboniferous Period. The published analyses include data from oolites and the surrounding carbonate cement (Table 8). The stratigraphic positions of the host rocks, their locations, and petrographic examples from both this study and previous literature are summarised in Figure 67 (Searl, 1989; Waters et al., 2007; Raven, 2023).

The $\delta^{13}C$ VPDB and $\delta^{18}O$ SMOW values from Oxwich and the literature (Searl, 1989; Raven, 2022) are listed in Table 8. The seven samples representing carbonate cement from Oxwich have relatively uniform C and O isotope compositions with $\delta^{13}C$ VPDB ranging from -4.60 ± 0.2 to 0.10 ± 0.2 ‰, and δ^{18} O VPDB ranging from -11.36 ± 0.2 to -6.42 ± 0.2 ‰. The $\delta^{18}O$ SMOW values are calculated as ranging from 19.21 ± 0.2 to 24.30 ± 0.2 ‰ using the equations of Friedman and O'Neil (1977) (Appendix 4). The C and O isotope compositions of both ooids and carbonate cements from previously published literature also correspond with the stable isotope compositions in the current study.

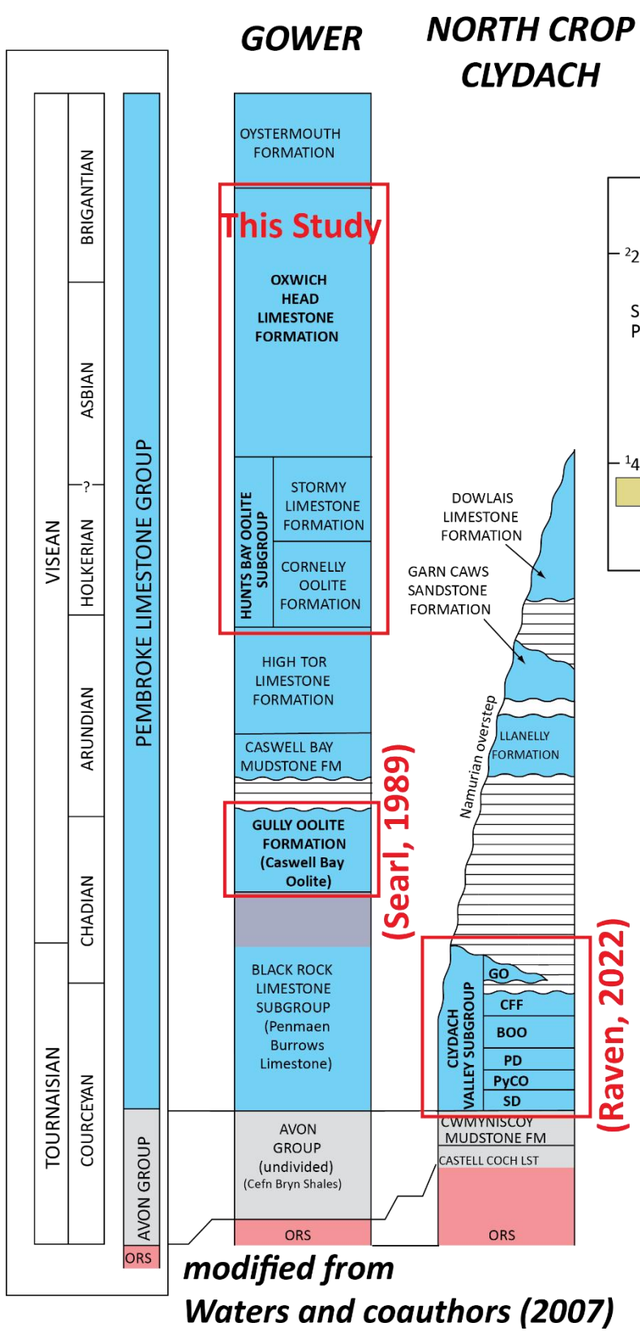

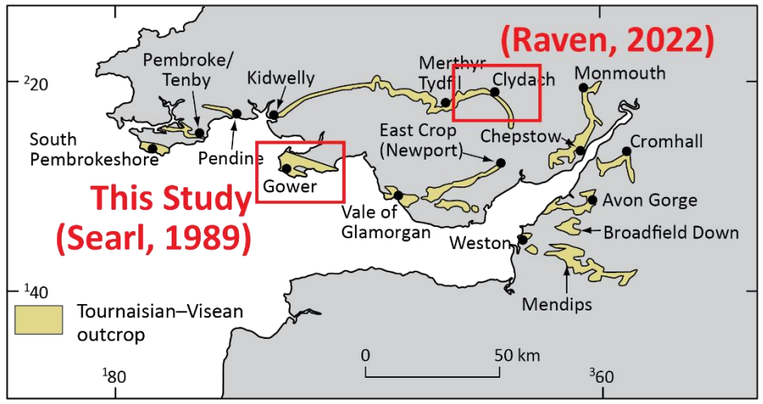

Dolomitised part of division indicated

Pembroke Limestone Group

Avon Group

Old Red Sandstone Group

Unconformity/disconformity

Divisions of Clydach Valley Subgroup :

GO	**Gilwern Oolite Formation**
CFF	Coed Ffyddlwn Formation
BOO	Blaen Onnen Oolite Formation
PD	Pantydarren Formation
PyCO	**Pwll-y-Cwm Oolite Formation**
SD	Sychnant Dolomite Formation

Gully Oolite Fm (Searl, 1989)

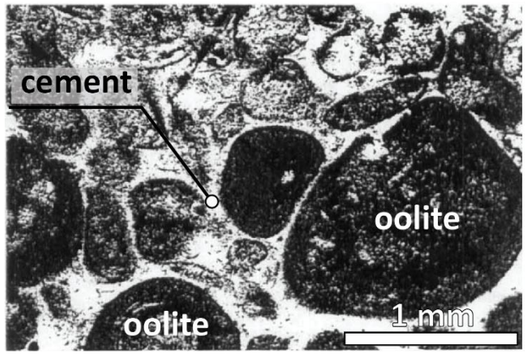

Gilwen Oolite Fm (Raven, 2022)

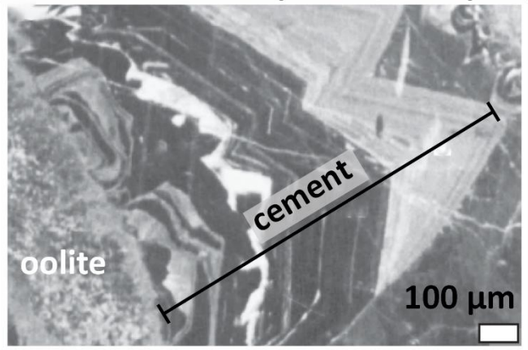

Pwll-y-Cwm Oolite Fm (Raven, 2022)

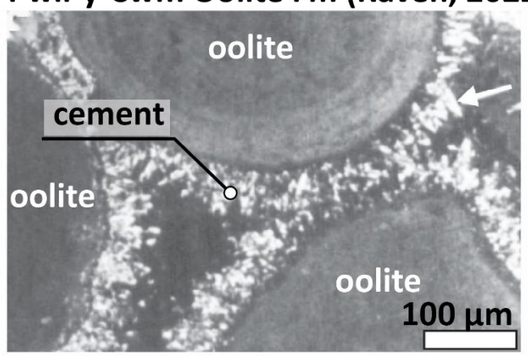

Figure 66: Stratigraphic columns illustrating the Lower Carboniferous of Gower and North Crop at Clyddach, South Wales, adapted from Waters and coauthors (2007). Red rectangles indicate the host rock of this study and those referenced in the literature (Searl, 1989; Raven, 2022). on stratigraphic columns and a map. The field photo from the Gully Oolite Formation is taken from Searl (1989) and the thin section photos of Gilwen Oolite and Pwll-Cwm Oolite Formations are taken from Raven (2022).

Table 8: Summary of stable isotope results from Oxwich and the literature (Searl, 1989 and Raven, 2022)

Sample ID	Locality	Formation	Sample Type	$\delta^{13}C$ (‰) VPDB	$\delta^{18}O$ (‰) VPDB	$\delta^{18}O$ VSMOW(‰)
OX-4a	Gower-Oxwich	Oxwich Head Limestone Formation	Cement	0.80 ± 0.2	-11.36 ± 0.2	19.21 ± 0.2
OX-4b	Gower-Oxwich	Oxwich Head Limestone Formation	Cement	-4.60 ± 0.2	-6.85 ± 0.2	21.03 ± 0.2
OX-5a	Gower-Oxwich	Hunts Bay Ooolite Subgroup	Cement	-2.13 ± 0.2	-8.94 ± 0.2	21.71 ± 0.2
OX-5b	Gower-Oxwich	Hunts Bay Ooolite Subgroup	Cement	-1.50 ± 0.2	-8.54 ± 0.2	22.12 ± 0.2
OX-6a	Gower-Oxwich	Oxwich Head Limestone Formation	Cement	-4.56 ± 0.2	-7.63 ± 0.2	22.05 ± 0.2
OX-6b	Gower-Oxwich	Oxwich Head Limestone Formation	Cement	-0.74 ± 0.2	-6.42 ± 0.2	23.86 ± 0.2
OX-7	Gower-Oxwich	Oxwich Head Limestone Formation	Cement	0.10 ± 0.2	-9.59 ± 0.2	24.30 ± 0.2
Searl, 1989_1	Gower	Gully Oolite Formation	Ooids	-3.17 ± 0.2	-6.73 ± 0.2	23.98 ± 0.2
Searl, 1989_2	Gower	Gully Oolite Formation	Cement	1.23 ± 0.2	-4.91 ± 0.2	25.86 ± 0.2
Searl, 1989_3	Gower	Gully Oolite Formation	Cement	-0.53 ± 0.2	-5.1 ± 0.2	25.66 ± 0.2
Searl, 1989_4	Gower	Gully Oolite Formation	Cement	-3.68 ± 0.2	-8.52 ± 0.2	22.14 ± 0.2
Raven, 2022_17856	Daren Ddu (South)	Gilwern Oolite Formation	Ooids	-3.81 ± 0.2	-6.61 ± 0.2	24.10 ± 0.2
Raven, 2022_17844	Daren Ddu (South)	Gilwern Oolite Formation	Cement	-5.48 ± 0.2	-6.74 ± 0.2	23.97 ± 0.2
Raven, 2022_17905	Craig y Cilau	Pwll-y-Cwm Oolite Formation	Cement	-4.16 ± 0.2	-6.23 ± 0.2	24.50 ± 0.2
Raven, 2022_17844	Daren Ddu (South)	Gilwern Oolite Formation	Cement	-2.75 ± 0.2	-7.73 ± 0.2	22.95 ± 0.2
Raven, 2022_18325	Viaduct	Gilwern Oolite Formation	Cement	-3.25 ± 0.2	-8.83 ± 0.2	21.82 ± 0.2

The results are plotted on the $\delta^{13}C$ VPDB vs. $\delta^{18}O$ SMOW diagram by Hoefs and coauthors (1997) (Figure 67). The stable carbon and oxygen isotope values from both the current study and the host rock data from the literature are clustered near the values of marine carbonates. This indicates that the fluids responsible for the precipitation of carbonates in the fissures, cockade rims, concentric lamellae of ooids, and the cement separating the ooids in the host rock were primarily derived from marine carbonate sources.

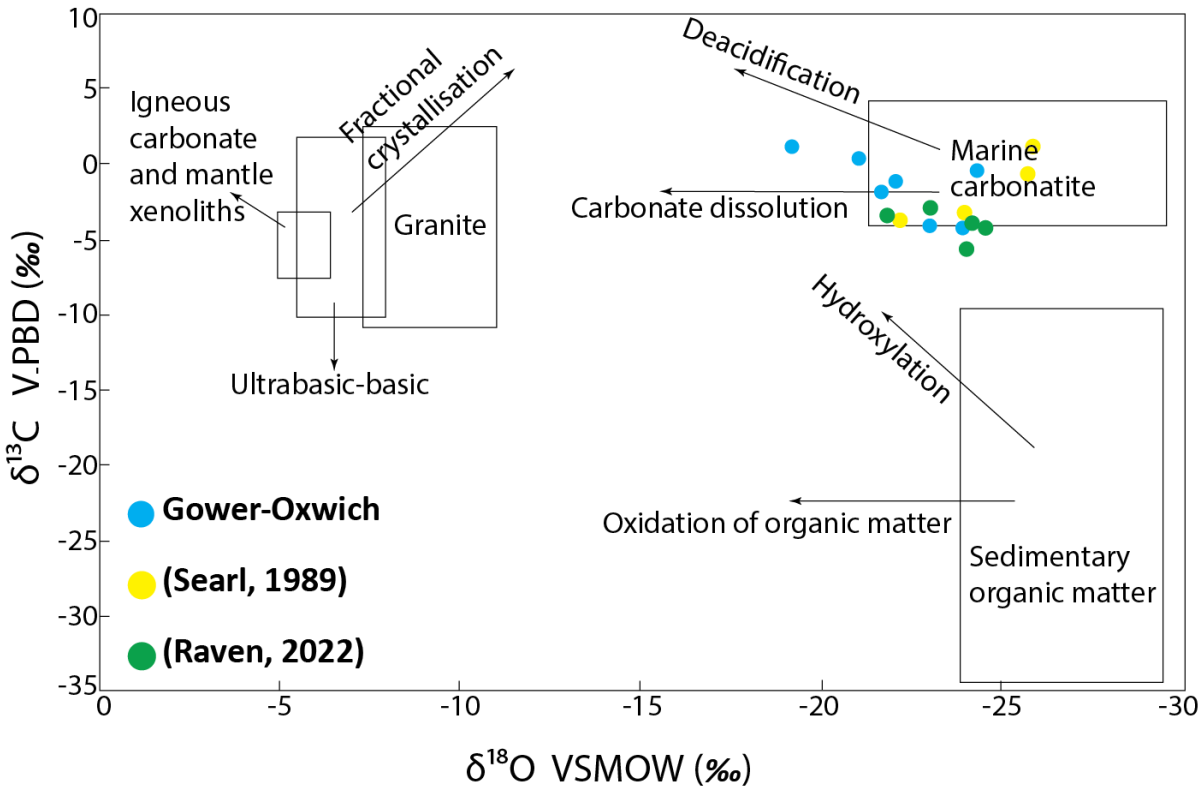

Figure 67: Carbon and oxygen isotope compositions of carbonates from Oxwich. Literature carbon and oxygen isotope values are from Searl (1989) and Raven (2022). The areas of mantle reservoirs are from Hoefs and coauthors (1997) and Demény and coauthors (2004). The area of marine carbonate reservoir is from Veizer and coauthors (1999).

6.4 Discussion and Conclusion

No primary or secondary fluid inclusions suitable for microthermometry analyses were identified in the samples from the Gicik field. This absence likely reflects the fine-grained nature of the rims forming the cockades, which has implications for both growth rate and pressure conditions. Rapid precipitation of silica from hydrothermal fluids often results in extremely fine-grained, microcrystalline, or amorphous silica phases, which may lack the well-defined cavities required for fluid inclusion entrapment (Moncada et al., 2012; Saunders, 1990). Additionally, fine-grained rim growth may indicate high supersaturation conditions, where rapid nucleation dominates over crystal growth, leading to dense microcrystalline textures that do not favour fluid inclusion preservation (Herrington and Wilkinson, 1993). Furthermore, if growth occurred under fluctuating pressure conditions, particularly in a seismogenic environment, the mechanical stress and episodic fluid pulses could have further hindered fluid inclusion entrapment or preserved only secondary inclusions in later overgrowths (Simmons and Browne, 2000). Therefore, the absence of measurable fluid inclusions in the Gicik samples suggests rapid rim growth under high supersaturation conditions and/or pressure fluctuations associated with episodic fluid flow.

In Oxwich, fluid inclusion microthermometry and carbon and oxygen stable isotope analyses were conducted to investigate the palaeo-fluid environment responsible for the precipitation of carbonate rims around central clasts in cockade textures. These analyses provided valuable insights into the formation mechanisms of these textures. The impact of secondary processes, particularly recrystallisation, on the carbonate rims has been discussed at both macroscopic and microscopic scales in Chapters 4 and 5. While the primary goal was to determine the original fluid geochemistry, pervasive recrystallisation in Oxwich has inevitably influenced the results. Consequently, the analytical data from the rims of cockades likely reflect post-depositional geological processes.

The temperature range of 155°C to 285°C obtained from the rims of cockades aligns with the formation conditions of cockade texture bearing breccias summarised by Frenzel and Woodcock (2014). Their study, which compiled 106 reported occurrences across various deposit types, shows that cockade textures typically develop in near-surface, low- to mid-temperature vein-style mineralisation, with formation temperatures ranging from 50°C to 350°C. The values observed at Oxwich fall within this range, reinforcing their consistency with previously documented cockade formation conditions. Stable carbon and oxygen isotope data indicate that the fluids responsible for carbonate precipitation were derived from marine carbonates, with no evidence of magmatic fluid mixing. The temperatures obtained from microthermometry analyses exceed the typical diagenetic temperature range for calcite (up to 200°C,

according to Machel, 2005). This temperature increase is interpreted as the result of a regionally elevated geothermal gradient, likely caused by hydrothermal activity along reactivated Variscan cross-faults during Mesozoic extension. Fault-related infills on the Gower Peninsula provide further evidence of early Cretaceous hydrothermal activity, interpreted as coeval with tectonic events related to the opening of the North Atlantic Ocean (Doré et al., 1999; Ault et al., 2016). Given the marine carbonate origin of these fluids, their elevated temperatures are more likely a result of prolonged circulation within a geothermal system rather than direct magmatic influence. In contrast, lower homogenisation temperatures (81°C to 128°C) were recorded in elongated carbonate crystals oriented perpendicular to fissure walls, which do not exhibit cockade textures. This distinction suggests that cockade formation was influenced by higher-temperature conditions than other carbonate precipitates associated with lower-temperature fluids.

Stable isotope data from this study and previous research suggest that the carbonate cements surrounding central fragments in cockade textures share a common marine carbonate origin with those enclosing oolites in the Pembroke Limestone Group (Figure 68). In oolitic limestone, oolite separation occurs due to the force of crystallisation, where internal pressure from crystal growth displaces grains, rather than through episodic seismic activity (Figure 67). Since oolitic limestones form in sedimentary environments without direct tectonic influence, their grain separation cannot be attributed to seismic processes. Given the isotopic similarity between cockade carbonate rims and late-stage cement oolite surrounding cement, it is plausible that the force of crystallisation also contributed to the displacement and separation of central fragments in cockade textures. Although episodic hydrothermal fluid influxes associated with fault activity likely played a role in cockade rim formation, their development is not necessarily restricted to seismic events. Instead, prolonged diagenetic processes, such as neomorphic transformations, recrystallisation, and replacement, may have also influenced rim formation over time. Therefore, attributing all cockade rim growth solely to seismic activity may oversimplify their formation history.

The obtained microthermometric and stable isotope data provide valuable constraints on palaeo-fluid conditions, but their interpretation must account for uncertainties arising from secondary geological processes. As petrographic and microthermometric analyses have demonstrated, the carbonate rims in cockade textures have undergone extensive recrystallisation, meaning that the measured values do not reflect their original formation conditions but instead record the cumulative effects of post-depositional modifications. Specifically, the elevated homogenisation temperatures (155°C to 285°C) recorded in secondary fluid inclusions exceed the typical diagenetic temperature range for calcite. This suggests that these samples were exposed to slightly higher temperatures during secondary processes. This has been

attributed to an increased geothermal gradient during Mesozoic extension, which led to the heating of fluids derived from adjacent platform limestones. Stable isotope values confirm that these fluids originated from marine carbonates, with no evidence of magmatic input.

While methodological controls were applied to minimise analytical errors, including calibration procedures and careful sample selection, the recorded temperatures and salinity estimates inherently reflect the influence of secondary processes. Additionally, fluid inclusion selection was carefully managed to avoid the effects of necking-down, leakage, or stretching, which can alter homogenisation temperatures and salinity estimates. Since these features commonly develop due to secondary modifications, special attention was given to excluding altered inclusions during data collection to ensure the reliability of results. To further reduce uncertainties, all analyses, including both stable isotope and fluid inclusion studies, were conducted on interior sections of the samples, avoiding directly exposed surfaces. This approach ensured that only well-preserved, sealed inclusions were analysed, minimising the potential impact of surface weathering. Despite these uncertainties, the consistency of the obtained values with previous literature supports the reliability of the interpretations while emphasising the need for careful evaluation of their geological implications.

Chapter 7: Formation of Cockade Texture at Oxwich and Gicik

Cockade texture is a fault-fill texture in which clasts are completely surrounded by spheroidal hydrothermal overgrowth rims (Adams, 1920; Bastin, 1950; Kutina and Sedlackova, 1961; Genna et al., 1996; Leroy et al., 2000; Frenzel and Woodcock, 2014; Cox and Munroe, 2016). Cockade texture bearing breccias are a distinctive type of fault breccia infill, commonly associated with hydrothermal systems and epithermal deposits. They have been studied as indicators of mineralisation sequences (Leroy et al., 2000), syntectonic mineral growth (Genna et al., 1996), and potential records of seismic cycles (Berger and Herwegh, 2019; Masoch et al., 2019).

Existing breccia classifications fail to adequately categorize cockade texture-bearing breccias as cement-supported breccias. To address this, a detailed review of breccia classification provided that both genetic and non-genetic classification systems are widely used to interpret breccia formation in fault zones. Despite their methodological differences, they are often applied together to infer formation mechanisms. For instance, terminology from genetic classifications (e.g., Jébrak, 1997) and non-genetic classifications (e.g., Woodcock and Mort, 2008) are frequently employed within the same breccia classification frameworks, demonstrating how breccia types from distinct systems are used interchangeably to interpret formation environments (e.g., Chauvet, 2019; Rhys et al., 2020). Cockade texture-bearing breccias exemplify these classification challenges, as their formation involves both primary deformation and secondary modification processes. Additionally, their characteristic open voids, which may remain unfilled or be infilled by matrix and cement, are often overlooked in classification schemes. While genetic classifications tend to omit post-formational changes, non-genetic systems generally do not account for void percentage, despite its critical role in fluid migration and breccia connectivity. To improve classification accuracy, genetic approaches should integrate secondary processes, and non-genetic classifications should consider void abundance. Addressing these gaps will enhance our understanding of breccia evolution and its role in fluid flow and mineralisation in fault zones.

As cockade textures became a focus of economic geology, particularly due to their frequent occurrence in breccias within epithermal deposits (Genna et al., 1996), the term cockade breccia began to be used interchangeably with cockade texture. Frenzel and Woodcock (2014) addressed this issue in the context of fault-related nomenclature and classification, suggesting that "cockade breccia" is a pragmatic term unlikely to cause misinterpretation. However, as demonstrated in this study, cockade textures often co-exist with other primary and secondary deformation-related textures within the same breccia. Therefore, directly using a single texture to define an entire breccia type, especially when its formation mechanisms

are still debated, may lead to oversimplification and misinterpretation of the geological processes involved. To avoid such ambiguities, this study distinguishes between the term “cockade texture” and the broader term “cockade texture bearing breccia”. When referring specifically to the texture itself, we use "cockade texture", whereas when discussing the breccia as a whole, we adopt the term "cockade texture-bearing breccia" to provide a geologically consistent terminology.

7.1 Geological Context of Oxwich and Gicik

This study investigates the formation of cockade textures by integrating field observations, microstructural analyses, and geochemical techniques. Understanding their development provides insights into hydrothermal ore deposition and fault-controlled deformation. The discussion explores these mechanisms in the context of cockade breccias from Oxwich and Gicik, two localities with contrasting geological settings.

The structural evolution of Oxwich is characterised by multiple deformation phases. Following the deposition of Lower Carboniferous platform limestones, the region underwent Variscan orogenic deformation in the Late Carboniferous, leading to the development of folds, thrust faults, and cross-faults (George, 1940; Roberts, 1979; Wright et al., 2009). During the Mesozoic extension, associated with the opening of the North Atlantic Ocean (Dore et al., 1999), the region experienced renewed tectonic activity. This event led to the formation of previously undocumented E-W trending faults (Figure 27), along which hydrothermal fluids circulated, as evidenced by mineralisation patterns (Ault et al., 2016). Cockade textures in Oxwich occur in both N-S trending cross-faults and newly developed E-W trending faults, suggesting that mineralisation was influenced by multiple structural phases.

The Gicik deposit is classified as a low-sulphidation epithermal gold mineralisation (Çil, 2019), characterised by colloform banding, crustification, lattice bladed, and cockade textures, typical of low-sulphidation epithermal systems. Mineralisation is hosted in silicified NE–SW trending veins, which are structurally controlled by NE–SW trending oblique faults with strike-slip and reverse components. These faults acted as fluid conduits, facilitating hydrothermal circulation and mineral deposition. Later deformation resulted in the formation of NW–SE and NNE–SSW trending faults, which cut and displaced both the mineralised veins and earlier faults (Çil, 2019). Field mapping confirms that NE–SW faults predate mineralisation, while subsequent NNW–SSE and NW–SE faults developed after mineralisation, potentially as a result of structural inversion (Figure 52 and Figure 53). The collinearity between mineralised veins and earlier faults suggests that the veins containing cockade texture-bearing breccias originally formed in an extensional regime but were later overprinted by compressional stress, leading to structural reactivation.

7.2 Mechanisms of Cockade Texture Formation

The formation mechanisms of cockade textures remain a subject of ongoing debate, with recent studies primarily focusing on four processes: clast suspension in ascending fluids, repeated rotation and accretion, partial metasomatic replacement, and force of crystallisation (Figure 69). These mechanisms are intrinsically linked to the geological setting, fluid dynamics, and structural evolution of fault zones. A key aspect in evaluating these mechanisms is whether they adequately explain the characteristic separation of core clasts within cockade breccias, as the central fragments do not touch each other. Dynamic fluid conditions, including episodic deformation and hydrothermal activity, are integral to the clast suspension and repeated rotation-accretion models, potentially linking cockade breccias to seismic events. Conversely, the force of crystallisation model proposes that cockade textures can also form in static fluid environments, suggesting that their occurrence does not necessarily indicate tectonic activity. Additionally, partial metasomatic alteration can modify or overprint primary mineralogical features, further complicating the interpretation of their formation history within structural and economic geology.

Suspension in fluid: Cockade textures with complete rims and separated central clasts form when clasts are temporarily suspended in either highly viscous, dense mineralizing fluids (Jobson et al., 1994) or rapidly ascending, low-viscosity hydrothermal fluids within dilatational cavities (Dill and Weber, 2010; Cox and Munroe, 2016) (Figure 69 a).

Repeated rotation and accretion: Cockades form through the repeated fracturing of a partially cemented breccia, primarily along the boundaries between individual clasts, followed by the growth of a partial layer of new cement (Frenzel and Woodcock, 2014) (Figure 69 b).

Partial metasomatic alteration: Cockade textures develop through the partial inward replacement of central clasts, which leads to the absence of contact points between the residual cores of the clasts (Kutina and Sedlackova, 1961) (Figure 69 c).

Force of crystallisation: Cockade textures form due to the force exerted during crystal growth into a nanometre-thick solution film, resulting in the gradual separation of central fragments (Von Weissenbach, 1836; Cotta, 1859, 1870; Beck, 1903; Teber, 1918; Lingern, 1919; Bastin, 1925; Wiltschko and Morse, 2001) (Figure 69 d).

.

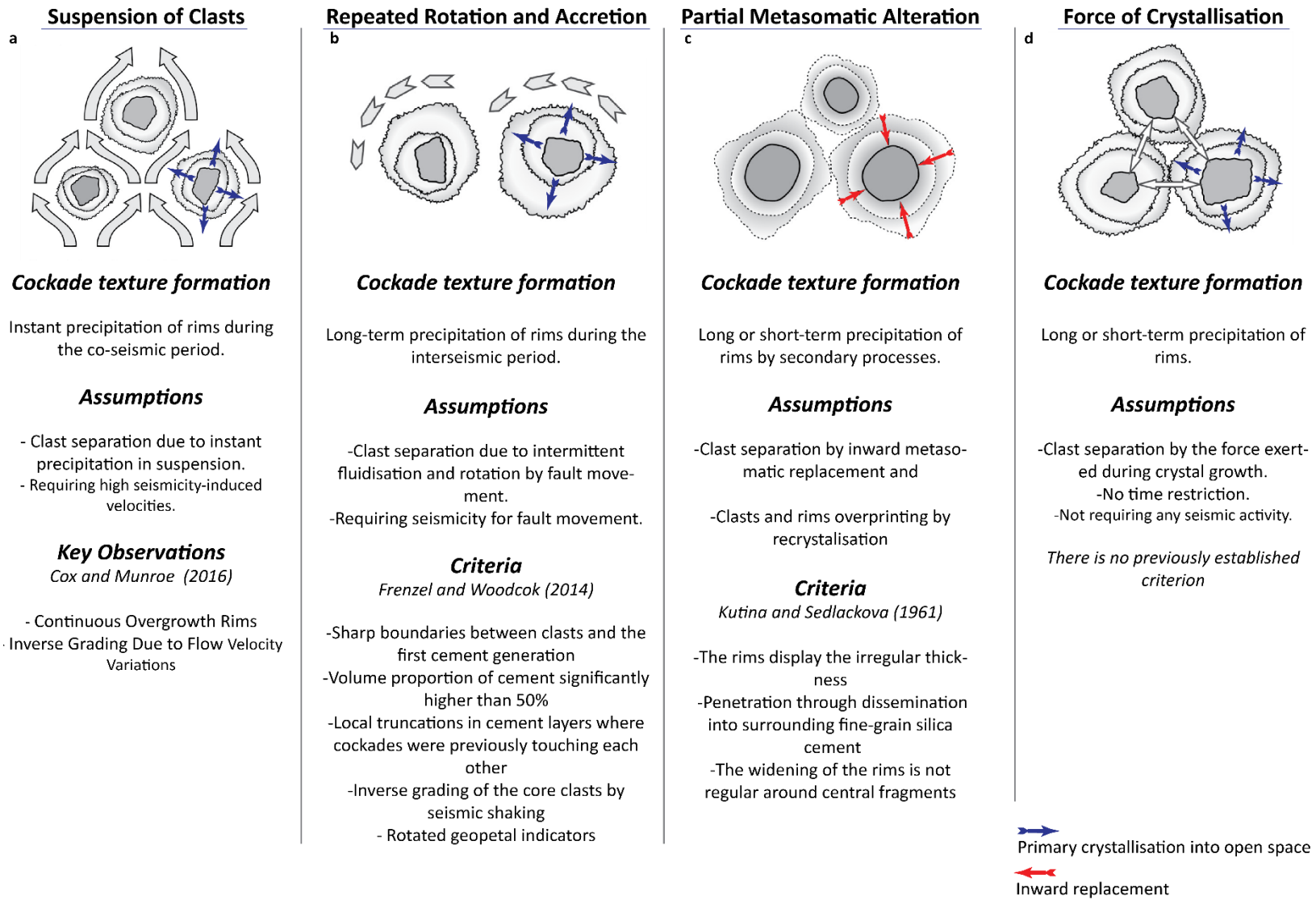

Figure 69: The mechanisms invoked for the formation of cockade texture, with their assumptions and mode of rim occurrences (based on Frenzel and Woodcock, (2014)).

7.3 Key Observations from Oxwich

7.3.1 Macroscopic Observations

Field observations from Oxwich indicate that fluid suspension models requiring high-viscosity or high-velocity hydrothermal fluids are not supported by geological evidence. The absence of significant argillaceous material in fault fills contradicts the hypothesis that a dense mineralizing fluid maintained clasts in suspension (Dill and Weber, 2010). Additionally, no field evidence suggests post-depositional removal of fine-grained material, which would be expected if clasts had initially been suspended and later settled (Spurr, 1926; Farmin, 1938; Jobson et al., 1994; Cox and Munroe, 2016). Hydrodynamic calculations indicate that sustaining clast suspension would require fluid velocities of up to 20 m/s, depending on clast size (~5 cm in diameter), a typical size for cockades (Leroy et al., 2000; Frenzel and Woodcock, 2014). However, such high velocities are not realistic for prolonged periods, particularly for larger clasts, such as the ~1.5-metre-sized central fragment observed at the East Oxwich Fault (Figure 28 d and Figure 28 e). The fluid velocities required to keep a clast of this size in suspension would be orders of magnitude higher than those calculated for 5 cm-diameter clasts, making long-term fluid suspension an implausible formation mechanism. Moreover, no evidence of size grading was observed within cockade texture-bearing breccias, suggesting that while episodic changes in flow energy may have occurred, they did not result in the particle sorting typically associated with fluid suspension mechanisms.

Field observations from Oxwich do not provide evidence supporting the rotation-accretion hypothesis. No truncation of outgrowth rims, rotated geopetal sediment structures, or reverse size grading were identified in field exposures. Instead, clear examples of unrotated geopetal sediment deposits were documented, which contradict the features expected from granular flow or seismic shaking-induced clast migration (Figure 34 c) (Möbius et al., 2001). A key observation from Oxwich is the vertical transition from jigsaw-fit crackle breccia to mosaic breccia and finally to cockade texture-bearing breccia within a single vein (Figures 26 and Figure 33). This pattern, which follows an increase in aperture, strongly suggests that clasts remained stationary as the vein progressively widened, rather than being mobilised and rotated. This structural progression further challenges the applicability of the rotation-accretion model proposed by Frenzel and Woodcock (2014).

The force of crystallisation appears to be the most viable mechanism for cockade texture formation at Oxwich. Experimental studies demonstrate that crystal growth within confined spaces can generate pressures exceeding 30 MPa, which is sufficient to induce dilation and expand vein walls (Wiltschko and Morse, 2001; Zheng et al., 2018, 2019). Additionally, the presence of well-defined crystal growth faces

within fissures suggests that cockade textures developed in fluid-filled open spaces, rather than through an incremental crack-seal process. The observed transition from crackle breccia to mosaic breccia and finally to cockade textures within a single fissure further supports a crystallisation-driven mechanism, rather than one controlled by repeated seismic reactivation.

7.3.2 Microscopic Observations

Thin section analysis of cockade rims at Oxwich reveals alternating layers of red-stained micritic calcite and euhedral sparry calcite, reflecting variations in mineral precipitation conditions (Figure 55). The central clasts originate from the limestone wall rock, with rims displaying either blocky or fibrous crystal morphologies. The micritic calcite within the rims is interpreted as having formed through diagenetic recrystallisation of a metastable carbonate precursor, a process common in carbonate-dominated systems (Wright and Tucker, 1991; Gierlowski-Kordesch, 2010). Blocky sparry calcite growth is associated with episodic hydrothermal pulses, where sudden changes in fluid pressure and chemistry cause rapid nucleation and precipitation (Oliver and Bons, 2001). In contrast, fibrous sparry calcite layers suggest competitive crystal growth, where lower degrees of fluid supersaturation led to the formation of elongated crystal morphologies (Oliver and Bons, 2001).

Cockade rim layers at Oxwich exhibit irregular thickness and gradational contact relationships between rim layers, supporting a partial metasomatic alteration by recrystallisation (Figures 55 a1-a2 and d1-d3). This suggests that recrystallisation acted as a secondary overprinting mechanism, modifying the rims rather than replacing them through direct mineral substitution.

Importantly, no rotated geopetal indicators or local truncations were observed in thin sections. The absence of these features at the microscopic scale further challenges the idea that cockade textures formed through repeated fault movement. Instead, the combination of micritic and sparry calcite textures suggests that cockade rims initially grew in open spaces, with subsequent partial inward recrystallisation acting as a secondary diagenetic modification. This highlights the necessity of distinguishing between primary growth and secondary overprinting when interpreting cockade textures in carbonate-hosted fault breccias.

7.3.3 Fluid Geochemistry at Oxwich

Fluid inclusion microthermometry and stable isotope analyses were conducted to assess the palaeo-fluid conditions responsible for cockade carbonate rim formation (Table 7 and Table 8). These data provide key constraints on fluid sources, temperature conditions, and post-depositional processes affecting cockade textures.

Microthermometric analyses indicate that cockade textures experienced temperatures ranging from 155°C to 285°C, which aligns with low- to mid-temperature hydrothermal systems (Frenzel and Woodcock, 2014). However, these values likely reflect post-depositional geological processes rather than primary formation conditions. As discussed in Chapter 5, pervasive recrystallisation has significantly altered the carbonate rims, meaning that the recorded temperatures and salinity estimates may not represent the original fluid geochemistry. While the primary objective was to reconstruct the conditions under which the cockade textures initially formed, secondary modifications, particularly diagenetic overprinting, have influenced the geochemical signatures obtained from these analyses.

The homogenisation temperatures obtained from secondary fluid inclusions (T_h: 155°C - 285°C) exceed the typical diagenetic temperature range for calcite (~200°C) (Machel, 2005), suggesting that cockade formation was influenced by an elevated regional geothermal gradient rather than standard burial diagenesis. The recorded elevated temperatures are interpreted as a result of geothermal heating during Mesozoic extension, consistent with hydrothermal fluid circulation along reactivated Variscan cross-faults (Doré et al., 1999; Ault et al., 2016). Similar fault-related hydrothermal infills on the Gower Peninsula further support evidence of early Cretaceous hydrothermal activity, likely associated with tectonic events related to the opening of the North Atlantic Ocean. Notably, homogenisation temperatures for elongated carbonate crystals (T_h: 81°C - 128°C), which do not exhibit cockade textures, are significantly lower than those recorded for cockade rims (Figures 66 and Table 7). This suggests that cockade textures formed under higher-temperature conditions than other lower-temperature carbonate precipitates within the same system.

Stable carbon and oxygen isotope data confirm that the fluids responsible for carbonate precipitation were derived from marine carbonates, with no evidence of magmatic fluid input. This suggests that geothermal fluid circulation played a primary role in heating the system, rather than direct magmatic activity. Additionally, stable isotope data indicate similarities between carbonate cockade rims and carbonate cement separating oolite in the limestone of the Pembroke Limestone Group (Searl, 1989; Raven, 2022) (Figure 67 and Figure 68). In oolitic limestones, grain separation occurs due to the force of crystallisation,

rather than through episodic seismic activity (Figure 67 and Figure 68). Given this isotopic similarity, it is plausible that crystallisation pressure also contributed to the displacement and separation of central clasts in cockade textures. While episodic hydrothermal pulses associated with fault activity likely influenced cockade rim growth, their development is not necessarily restricted to seismic events. Instead, prolonged diagenetic processes, such as neomorphic transformations, recrystallisation, and replacement, may have played a significant role over time.

To ensure the reliability of the geochemical interpretations, careful methodological controls were applied to minimise analytical uncertainties. Fluid inclusion selection was carefully managed to avoid the effects of necking-down, leakage, or stretching, which could alter homogenisation temperatures and salinity estimates. Since these features commonly develop due to secondary modifications, special attention was given to excluding altered inclusions during data collection. Additionally, all analyses including both stable isotope and fluid inclusion studies were conducted on interior sections of the samples, avoiding directly exposed surfaces to minimise the effects of surface weathering and contamination.

Despite these challenges, the consistency of the obtained values with previous literature supports their overall reliability. However, this underscores the need for a cautious approach when interpreting fluid inclusion and stable isotope data, particularly in systems affected by post-depositional modifications. Careful petrographic and geochemical analyses are essential to distinguish primary depositional signatures from secondary overprinting, ensuring that interpretations of palaeo-fluid conditions remain robust.

7.4 Key Observations from Gicik

7.4.1 Macroscopic Observations

Field observations from Gicik indicate that partial inward metasomatic replacement was the dominant mechanism for cockade texture formation, with additional evidence suggesting some influence from rotation and accretion processes (Kutina and Sedlackova, 1961; Rieder, 1969; Frenzel and Woodcock, 2014). Several macroscopic features support the role of metasomatic replacement, including the absence of sharp contact points between residual core clasts and their surrounding rims, the irregular thickness of the rims, and the variable distribution of sulphide-rich outer rims (Figure 48 g). These observations suggest that rim development occurred progressively through selective mineral replacement along grain boundaries, rather than by direct cementation around clasts within an open void.

Further macroscopic evidence supporting metasomatic replacement comes from the gradational transitions between core clasts and their overgrowth rims, rather than the sharp, well-defined contacts typically associated with direct precipitation. This feature is particularly significant, as metasomatic alteration and recrystallisation commonly result in diffuse boundaries between altered and unaltered material. Additionally, local truncations on cockade rims were observed, which have previously been interpreted as evidence of the rotation and accretion model (Frenzel and Woodcock, 2014). However, despite these truncations, no conclusive field evidence supporting the suspension in fluid or rotation-accretion models was identified, as no structural indicators suggest that the central fragments underwent significant rotation or shearing. In particular, the absence of rotated geopetal infill structures or inverse grading within breccia layers suggests that neither seismic shaking (Genna et al., 1996) nor co-seismic fluidisation (Cox and Munroe, 2016) significantly contributed to clast organisation.

A key macroscopic observation at Gicik is the coexistence of cockade textures with other hydrothermal vein textures, including colloform, comb, and lattice-bladed replacement textures (Figures 43 and Figure 44). The close spatial association of these textures within the same veins suggests that cockade texture formation was influenced by a combination of primary open-space precipitation and metasomatic overprinting. This interpretation aligns with the episodic nature of hydrothermal fluid flow in low-sulphidation epithermal systems, where cycles of mineral growth and subsequent alteration occur in response to transient changes in fluid pressure, temperature, and chemistry.

7.4.2 Microscopic Observations

Microscopic examination of cockade textures in Gicik reveals that, although primary growth textures are present, they have undergone significant overprinting due to recrystallisation. The most prominent textural indicators of this process include mosaic, feathery, plumose, and ghost sphere textures, which are commonly associated with silica gel precursors and high-temperature recrystallisation (>180°C) (Dong et al., 1995; Camprubí and Albinson, 2007; Taksavasu et al., 2018; Zeeck et al., 2021) (Figure 57). These observations suggest that the initial formation of cockade rims involved the rapid deposition of silica gel, followed by progressive recrystallisation into microcrystalline quartz.

A key microscopic observation is the presence of local truncations along the rims, which may indicate some degree of rotation and accretion during rim growth (Frenzel and Woodcock, 2014). However, these truncations coexist with clear evidence of metasomatic alteration, including replacement along grain boundaries, irregular rim thickness, and diffuse contact relationships between the central clasts and their surrounding rims (Kutina and Sedlackova, 1961) (Figure 57). The simultaneous occurrence of these features suggests that cockade textures in Gicik developed through both repeated rotation-accretion and inward metasomatic replacement, rather than being controlled by a single dominant process.

The overprinting of primary cockade structures by secondary recrystallisation processes has important implications for interpreting fluid evolution and tectonic conditions at Gicik. The textural complexity observed at the microscopic scale indicates that cockade formation was not a single stage process, but rather involved multiple episodes of mineral growth and alteration by recrystallisation. These findings emphasize the need for careful petrographic analysis when using cockade textures as sequential records of hydrothermal fluid fluxes, as overprinting by secondary processes can obscure primary features and complicate their geological interpretation in hydrothermal breccias with cockade texture.

The presence of silica gel-derived textures in cockade rims suggests that their initial formation was influenced by pressure fluctuations and rapid temperature changes. Episodic fracturing of the host rocks likely triggered sudden pressure drops, leading to the precipitation of amorphous silica, which subsequently recrystallised into chalcedony and eventually quartz (Henley and Hughes, 2000; Brown, 1986). This transformation process is well-documented in epithermal systems and is frequently linked to cyclic hydrothermal pulses. Microscopic observations from Gicik suggest that highly dense, gel-like silica fluids played a crucial role in the formation of cockade textures. The recrystallisation textures observed in these breccias—mosaic, feathery, plumose, and ghost spheres—indicate that silica-gel-like fluids, rather than thin hydrothermal films along crystal edges, were involved in their development. These textural

features suggest that the original precipitate was noncrystalline, highly viscous, and gel-like silica, similar to systems documented by Dong and coauthors (1995), Taksavasu and coauthors (2018), and Zeeck and coauthors (2021). Silica gel precipitation in hydrothermal systems typically results from the advection of silica-saturated fluids, where rapid pressure and temperature changes lead to gel-like phase transitions. Several mechanisms have been proposed for silica-gel precipitation in fault-controlled hydrothermal systems, including coseismic pore-fluid pressure drops (Henley and Hughes, 2000), frictional heating (Kirkpatrick et al., 2013), and dissolution-precipitation creep (Rutter and Elliott, 1976). These processes suggest that mechanical and chemical interactions within the fault zone contributed to the precipitation and stabilisation of silica-gel-like fluids (Williams and Fagereng, 2022). This type of silica represents an intermediate phase in the silica precipitation cycle, occurring after amorphous silica deposition and before the final crystallisation of quartz (Camprubí and Albinson, 2007; Kirkpatrick et al., 2013; Williams and Fagereng, 2022). The infiltration and precipitation of these highly viscous silica gel-like hydrothermal solutions into the fracture system at Gicik may provide an alternative explanation for clast separation in cockade textures. Instead of purely mechanical processes such as fluid suspension or rotation and accretion, the presence of silica gel suggests that clasts may have been displaced by the gradual solidification and expansion of gel-like fluids within the breccia matrix. This mechanism could be particularly relevant in low-sulphidation epithermal systems, where episodic hydrothermal pulses facilitate silica-gel precipitation and subsequent recrystallisation (Figure 70).

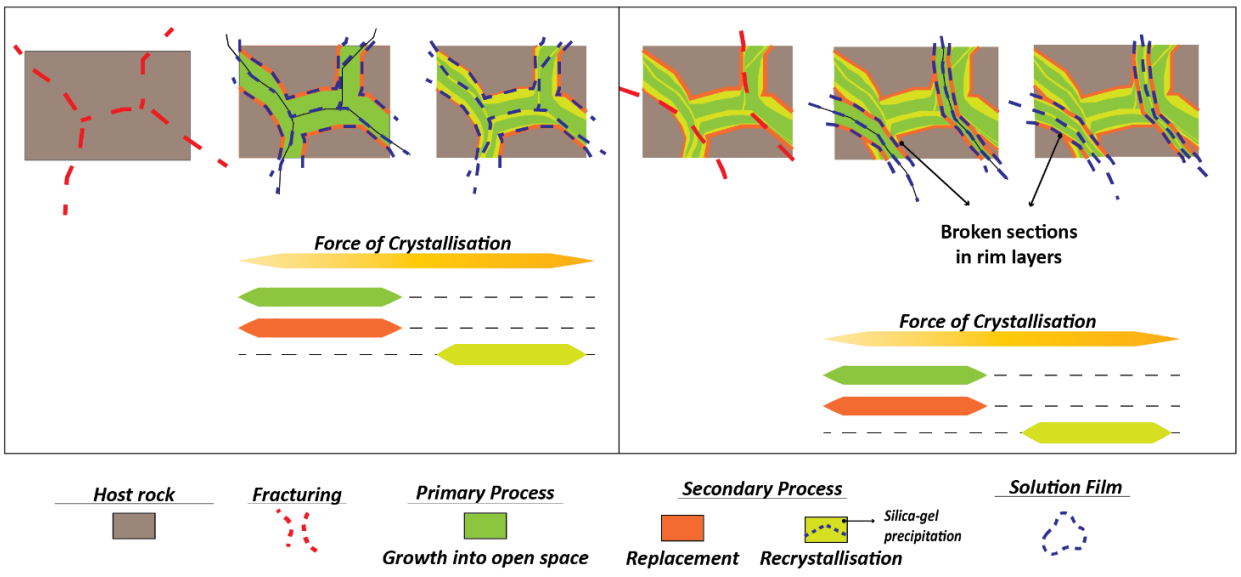

Figure 68: The schematic model for the formation of cockade texture by the silica-gel mechanism.

7.4.3 Fluid Geochemistry at Gicik

Hydrothermal alteration in Gicik is estimated to have occurred at temperatures ranging between 150° and 250°C, based on mineral assemblages observed in hydrothermally altered volcanic wall rocks (Çil, 2019). This temperature range aligns with low- to intermediate-temperature epithermal systems, where mineralisation is controlled by episodic hydrothermal fluid circulation (Reyes, 1990; Hedenquist et al., 2000; Camprubí and Albinson, 2007). Fluid inclusion studies conducted on vein quartz from Gicik by Besbelli and Varol (2002) yielded homogenisation temperatures (T_h) between 140° and 240°C, which closely correspond to the alteration-based temperature estimates provided by Çil (2019) (Figure 72 b3). In contrast to Oxwich, no primary or secondary fluid inclusions suitable for microthermometry analyses were identified in cockade texture samples from Gicik. This absence is likely a consequence of the fine-grained nature of the cockade rims, which influenced both growth rates and the pressure conditions under which these textures developed.

The lack of measurable fluid inclusions in cockade rims at Gicik suggests that their formation occurred under rapid precipitation conditions, primarily controlled by hydrothermal processes. One of the most critical factors influencing this precipitation is the high degree of supersaturation in silica-rich fluids. Rapid silica precipitation from hydrothermal solutions likely resulted in the formation of extremely fine-grained, microcrystalline, or amorphous silica phases, preventing the entrapment of fluid inclusions. The lack of trapped inclusions suggests that mineral growth occurred under conditions where nucleation rates outpaced crystal growth, leading to dense microcrystalline textures (Moncada et al., 2012; Saunders, 1990).

Another factor contributing to the absence of fluid inclusions may be fluctuating pressure conditions associated with episodic hydrothermal pulses. In seismogenic environments, rapid pressure fluctuations during fault activity can lead to transient fluid flow and sudden depressurisation, triggering immediate silica precipitation. Such conditions not only prevent the formation of primary fluid inclusions but may also destroy pre-existing inclusions or limit their preservation to secondary growth phases (Simmons and Browne, 2000). Additionally, if precipitation occurred under high geothermal gradients and dynamic hydrothermal flux, the rapid growth of fine-grained silica cement would have further impeded fluid inclusion entrapment (Herrington and Wilkinson, 1993). These observations indicate that cockade textures at Gicik developed primarily under high supersaturation conditions and fluctuating pressure regimes, leading to rapid episodic precipitation of silica rims.

7.5 Fractal Dimensions of Cockade Textures

Fractal dimension analysis was employed in this study to provide a quantitative approach for differentiating between cockade rims formed by primary and secondary processes. The method was chosen to address the subjectivity in describing mineral structures and textures, which often relies on qualitative terminology (Longley and Batty, 1989). To achieve this, a database was created using well-documented examples compiled by Frenzel and Woodcock (2014), and selected images were digitised for fractal dimension calculations. However, several methodological challenges limited the ability to systematically distinguish between primary and secondary formation processes. The box-counting method required the delineation of continuous, uninterrupted boundary lines, which proved problematic for rims affected by secondary processes. These modifications often disrupted the continuity of rim structures, making it impossible to apply the method consistently to altered rims. Additionally, the resolution of the source images significantly impacted the delineation of rims, introducing further uncertainty in the results. Consequently, the initial objective of using fractal dimension analysis to systematically differentiate primary and secondary textures could not be fully achieved.

Despite these limitations, the results showed a general trend of decreasing fractal dimensions from central fragments to outermost rims, particularly in silica-dominated systems (Figure 59 and Figure 60). This decline in complexity suggests that rims grew into open spaces, aligning with the proposed formation mechanisms of crystallisation pressure, rotation and accretion, and fluid suspension, but not with inward metasomatic replacement. The decrease in fractal dimension values implies a transition from an irregular, constrained growth pattern to smoother, more ordered growth, which is expected in open-space crystallisation. While sporadic increases in fractal dimension were observed in carbonate-dominated systems, they could not be directly linked to secondary processes. Additionally, variations in fractal dimension between central fragments and rims, including intermittent increases and occasional higher values in outer rims, were not systematically interpretable. The only clear observation was that central fragments generally exhibited higher fractal dimensions than outermost rims, with a notable exception in Wright and coauthors (2009), which was likely an artefact of image resolution rather than a true geological trend. Ultimately, while fractal dimension analysis provided some insights into rim growth patterns, its effectiveness in distinguishing between primary and secondary processes remains limited due to methodological constraints.

7.6 Cockade Texture Formation at Oxwich

The formation of concentric rims at Oxwich (Figure 72 a) was significantly influenced by recrystallisation, as evidenced by widespread carbonate recrystallisation textures. The separation of central fragments in cockade textures can primarily be explained by the force exerted during initial crystal growth, which was later modified by secondary recrystallisation. Previous studies indicate that N-S trending fissures at Oxwich developed perpendicular to the fold-and-thrust belt during the late stages of Variscan deformation in the Late Carboniferous (George, 1940; Roberts, 1979; Wright et al., 2009). These fissures were later reactivated during Mesozoic extension, coinciding with tectonic and seafloor spreading events associated with the opening of the North Atlantic Ocean (Brooks et al., 1988; Dore et al., 1999).

Ault and coauthors (2016) provide further support for this Mesozoic reactivation hypothesis, using low-temperature thermochronometric data from fault-related features on the Gower Peninsula, which document Early Cretaceous hydrothermal fluid circulation within originally N-S trending Variscan cross-faults (Figure 71 a). Their findings suggest that the Lower Carboniferous limestone host rock (Early Carboniferous Pembroke Limestone Group) was buried to depths of up to 4 km due to Variscan crustal thickening from the Late Carboniferous to the Early Permian (Figure 72 a). The maximum formation age for the cockade texture is constrained between the Late Permian and Early Triassic, based on the maximum depositional age of the infill sediments (Ault et al., 2016) (Figure 71 c and Figure 72 a1). Consequently, post-depositional processes influencing these fissures include burial diagenesis following their formation in the Late Carboniferous to Early Permian, with successive rim accretions affected by elevated geothermal gradients during Mesozoic extension (Figure 71 a; Figure 72 a2 and Figure 72 a3).

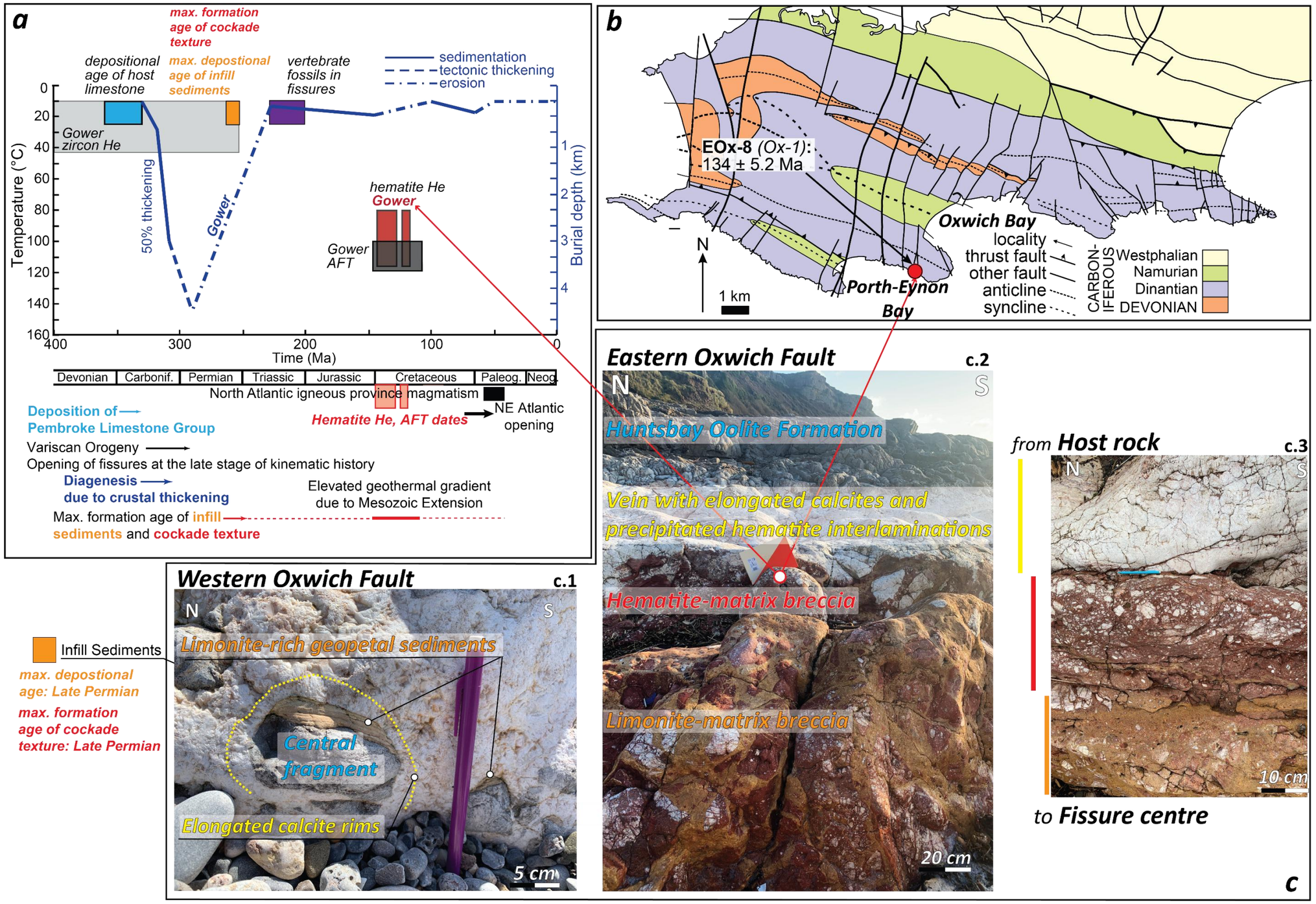

Figure 69: a) Burial history curve for Gower over the last ~400 m.y. and timing of major geological events involved in the formation of cockade texture in Oxwich (modified from Ault and coauthors (2016)); b) Simplified geologic map of Gower peninsula showing the location of low-temperature thermochronology data obtained from hematite rich breccia modified from Ault and coauthors (2016), time scale below indicates the paragenesis of geological events; c) (1) Field photo from Western Oxwich fault showing the unrotated geopetal infill sediment on the central fragment of a cockade texture (419193.67 m E 5711059.01 m N) (2-3) The field photo showing the paragenesis of the fissure fill. Red arrows show the location of the thermochronology sample on the map and the results on the burial history curve (Ault et al., 2016).

7.7 Cockade Texture Formation at Gicik

At Gicik, the formation of concentric cockade rims (Figure 72 b) was primarily driven by partial metasomatic alteration, as evidenced by prevalent replacement and recrystallisation textures. The force of crystallisation can explain the separation of central fragments, while the presence of cockade rims growing into open spaces suggests that episodic fracturing under fluid-dominated conditions played a role, potentially triggered by seismic activity. Additionally, the presence of local truncations on rims (Figure 72 b2) further supports this interpretation. However, no field evidence, such as rotated geopetal infill or reverse grading, was found to support the repeated rotation and accretion model.

Previous studies have demonstrated that gold mineralisation in Gicik is associated with NE-SW trending veins containing cockade textures (Çil, 2019). This mineralisation occurred within Early Eocene (55.0 ± 0.17 Ma, $40^{Ar}/39^{Ar}$) medium-K calc-alkaline and metaluminous volcanic units, including agglomerates and flow-banded andesitic to dacitic lavas (Figure 72 b1). These units are part of the Turkish segment of the Mesozoic–Cenozoic Western Tethyan Metallogenic Belt, a region known for its epithermal deposits (Çil, 2019). The formation of cockade textures is interpreted as contemporaneous with mineralisation and alteration, with hydrothermal breccia-hosted sericite yielding a maximum age of Early Eocene (44.14 ± 0.14 Ma, $40^{Ar}/39^{Ar}$) (Figure 72 b2). The maximum formation age for the cockade texture is further constrained to the Late Eocene, based on the age of alteration of the host rock (Çil, 2019).

The co-occurrence and proportions of alteration minerals in hydrothermally modified volcanic wall rocks suggest formation temperatures between 150°C and 250°C at depths below 300 m (Reyes, 1990; Hedenquist et al., 2000; Camprubí and Albinson, 2007; Çil, 2019). Fluid inclusion studies of vein quartz in Gicik by Besbelli and Varol (2002) yielded homogenisation temperatures (T_h) between 140°C and 240°C, aligning with the alteration-based temperature estimates from Çil (2019) (Figure 72 b3). This suggests that hydrothermal fluids controlled the precipitation of successive rims.

The cockade textures at Gicik are consistent with numerous reported occurrences of cockade breccias associated with temperatures ranging from 50°C to 350°C in vein-style mineralisation (Frenzel and Woodcock, 2014). These conditions are prevalent in near-surface environments, particularly in the upper portions of epithermal veins (Buchanan, 1981; Sillitoe, 1993).

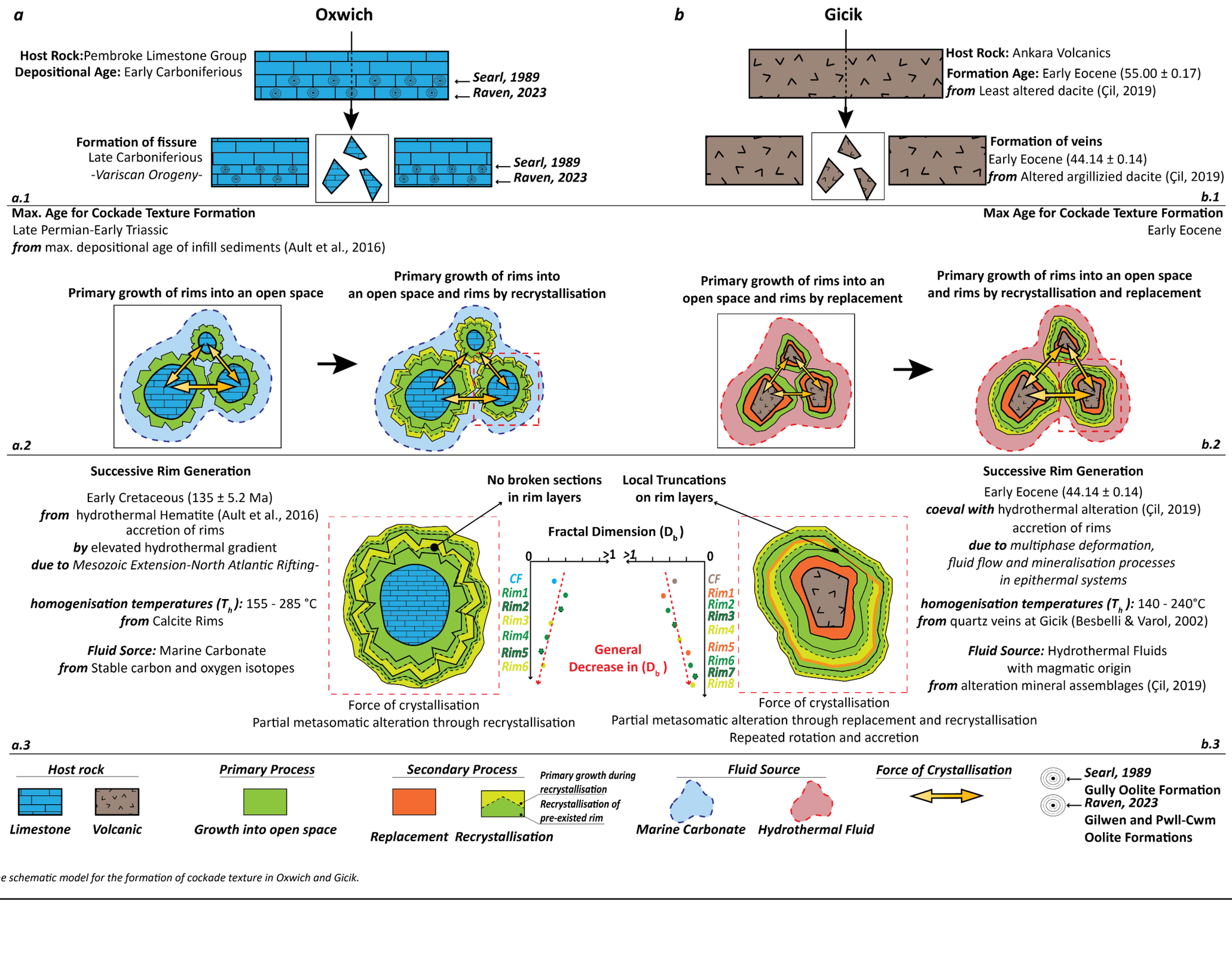

Figure 70: The schematic model for the formation of cockade texture in Oxwich and Gicik.

7.8 Summary

In conclusion, the formation mechanisms of cockade textures at Oxwich and Gicik show similarities and differences influenced by their distinct geological settings. At Oxwich, the formation of rims involved the force of crystallisation and partial metasomatic alteration through recrystallisation. There is no evidence supporting mechanisms that involve suspension in fluid and repeated rotation and accretion. At Gicik, the formation mechanisms of cockades include the force of crystallisation and partial metasomatic alteration through replacement and recrystallisation. The only evidence supporting the episodic fracturing is the presence of local truncations on the rims; however, no evidence indicates that the central fragments are rotated or sheared relative to each other in cockade-bearing breccias at Gicik. In both localities, the central fragments without rotation and the well-defined overgrowth faces of rims, particularly in Oxwich, suggest that the fracture opening and rim precipitation occurred slowly and within an open space consistently filled with fluids, consistent with the force of crystallisation mechanism. These findings underscore the importance of local geological history and fluid dynamics in determining the formation mechanisms of cockade textures in different settings.

The selection of Oxwich and Gicik as study sites provides a valuable comparative framework for evaluating the formation mechanisms of cockade textures in different geological settings. Despite their contrasting lithologies and tectonic histories, both sites exhibit well-developed cockade textures, allowing for an assessment of shared and distinct formation processes. Oxwich, a carbonate-hosted system, represents a setting where the force of crystallisation and partial metasomatic recrystallisation played a dominant role in cockade formation. In contrast, Gicik, a silica-dominated low-sulphidation epithermal system, demonstrates additional influences of metasomatic replacement and episodic hydrothermal fracturing. The comparison of these localities offers insights into how cockade textures develop under varying temperatures, fluid composition, and structural conditions. Moreover, this study bridges the gap between carbonate- and silica-rich systems by demonstrating that while similar textural features may arise, their underlying mechanisms can differ due to variations in fluid-rock interactions, tectonic influences, and mineralogical environments. By addressing these two sites, this research highlights the necessity of considering both primary growth and secondary modification processes in the interpretation of cockade textures, ultimately contributing to a more comprehensive understanding of their formation across diverse geological settings.

Chapter 8: Conclusions

This thesis investigates the formation mechanisms of cockade textures in cement-dominated breccias, addressing two primary objectives. The first objective was to explain why the central fragments of cockades do not touch each other, which is directly related to their formation mechanisms. The second objective was to assess the reliability of using successive rims of cockade textures to infer the timing of sequential geological events, particularly in paleoearthquake studies (Berger and Herwegh, 2019; Masoch et al., 2019). These studies may misinterpret the temporal relationships between successive rims due to secondary geological processes, including replacement and recrystallisation, that alter the rims around central fragments. The research encompasses findings from two distinct localities: Oxwich, a carbonate-dominated system, and Gicik, a silica-dominated system.

The results indicate that multiple mechanisms contribute to cockade formation, with local geological conditions playing a key role in determining which processes dominate. Cockade textures can form through rotation and accretion, partial metasomatic alteration (including recrystallisation and replacement), and the force of crystallisation. Additionally, at Gicik, the infiltration and subsequent precipitation of highly viscous silica gel-like hydrothermal solutions within fracture systems represent an alternative explanation for clast separation, which could lead to the formation of cockade textures in low-sulphidation epithermal systems (Figure 70). These findings challenge the idea that a single mechanism is responsible for cockade formation and highlight the importance of considering multiple interacting processes.

The fractal dimension analysis applied in this study provided quantitative evidence supporting open-space precipitation as a key factor in cockade formation. A general trend of decreasing fractal dimension values from central fragments to rims was observed in silica-dominated systems, while occasional increases were noted in carbonate-dominated systems. This trend indicates a transition from irregular, confined growth to more ordered, open-space growth, consistent with the proposed formation mechanisms. These findings reinforce the importance of numerical approaches in evaluating the textural complexity of geological features and distinguishing primary depositional structures from secondary modifications.

In Oxwich, fluid inclusion microthermometry and stable isotope geochemistry provided additional constraints on the palaeo-fluid conditions responsible for cockade formation. The homogenisation temperatures (155°C–285°C) from carbonate rims are consistent with previously documented cockade textures, while stable isotope data indicate that the fluids responsible for precipitation were derived from marine carbonates, with no evidence of magmatic fluid input. However, pervasive recrystallisation has

altered the isotopic signatures, suggesting that the measured geochemical data primarily reflect post-depositional modifications rather than the original fluid composition. Furthermore, the similarity between cockade textures and oolitic limestone cementation in the Pembroke Limestone Group supports the force of crystallisation as a viable mechanism for fragment separation, without requiring seismic activity.

Although the rotation-accretion model is widely cited in the literature and is often used to infer seismic activity in paleoearthquake studies (Frenzel and Woodcock, 2014; Berger and Herwegh, 2019), observations made during the course of this thesis at Oxwich differ from those of previous studies. These differences are likely due to the availability of newly exposed outcrops. Although successive rims of cockades can be associated with seismic deformation when both fracturing events and rim precipitation occur simultaneously, the later metasomatic alteration can significantly modify these rims over time. This work reveals that replacement and recrystallisation continuously overprint cockade rims, meaning that the preserved structures may not always directly reflect the original deformation conditions. However, the findings of this study indicate that successive rims are often modified by replacement and recrystallisation during their formation, challenging the assumption that each rim directly corresponds to a discrete deformation event.

The classification of cockade texture-bearing breccias presents significant challenges within existing breccia classification frameworks. Traditional genetic classifications focus on breccia formation processes but often overlook secondary modifications, while non-genetic classifications, although process-agnostic, frequently fail to account for void percentage, which influences fluid migration and breccia evolution. Given that cockade texture-bearing breccias result from both primary deformation and secondary modification, a more integrated classification approach is necessary. To improve classification accuracy, genetic classifications should incorporate post-formational changes, while non-genetic systems should consider void abundance to better reflect breccia evolution in hydrothermal systems.

Additionally, as cockade textures became a focus of economic geology, particularly in epithermal deposits, the term "cockade breccia" began to be used interchangeably with "cockade texture". However, this study demonstrates that cockade textures often coexist with other deformation-related textures within the same breccia, making it problematic to define an entire breccia type based on a single texture. To avoid misinterpretation, this thesis distinguishes "cockade texture", which refers specifically to the texture, from "cockade texture-bearing breccia", which describes breccias that contain cockade textures but may also include other fault-related structures. This distinction ensures a more precise and geologically consistent terminology, reducing ambiguity in breccia classification.

This thesis suggests that cockade texture should be defined as a fault-fill texture formed through fluid-rock interaction processes at shallow crustal depths. This definition acknowledges the complex interplay between primary and secondary processes, including crystallisation pressure, metasomatic alteration, and episodic fluid flux. The term "fluid-rock interaction process" encompasses any chemical or physical interaction between fluids (e.g., meteoric, fossil, or magmatic) and central clasts, including both primary growth and secondary overprinting mechanisms. By refining the classification of cockade textures, this study provides a more comprehensive genetic framework that integrates multiple formation mechanisms and improves their interpretation in structural and economic geology. A more precise approach to their classification will enhance our understanding of their role in hydrothermal mineralisation, fault zone evolution, and their broader implications for structural geology.

Future Work

Because cockades are common in fault zones exhumed from earthquake nucleation temperatures (150°C–350°C), the successive rim precipitation around central fragments may record the timing of sequential events. This is useful for studying different phases of seismic cycles in paleoearthquake research or correlating mineralisation with deformation in vein-type deposits. This interpretation assumes that rim precipitation occurs rapidly in open spaces coinciding with seismic activity. However, this study has shown that secondary processes, such as replacement and recrystallisation, continuously modify the rims of cockade textures, overprinting previously formed rims. Additionally, there is evidence that rim precipitation can occur slowly from a solution film consistently surrounded by fluids between the rim crystals without requiring seismic activity. Emphasising the roles of partial metasomatic alteration and crystallisation forces in rim precipitation could be crucial for a more comprehensive understanding of cockade texture formation and its applications. Therefore, future research should focus on quantifying the relative contributions of primary and secondary processes to the formation of cockade textures by exploring their interactions in different settings, ensuring more accurate geological interpretations.

The cathodoluminescence (CL) technique can provide detailed information on the growth history of the rims of cockade textures. By examining the luminescence properties of minerals alongside related mineral textures, it is possible to identify different generations of cement and reconstruct the fluid flow history. Moreover, clumped isotope analyses can determine more precise temperature and pressure conditions during the formation of cockade textures by providing insights into the palaeotemperature conditions of the fluids involved at the time of successive rim precipitation. Additionally, the internal rim textures of cockades alongside the external accompanying vein textures in the Oxwich and Gicik locations indicate that the fluctuations from central fragments to outermost rims in fractal dimension values might result from the effect of the secondary processes, such as replacement and recrystallisation. Therefore, the value of fractal dimensions, by coupling the detailed growth history and the paleotemperature conditions of the rims using cathodoluminescence and clumped isotopes, might serve as a quantitative indicator, which may shed light on mineral distributions by revealing primary and secondary growth features, e.g., recrystallisation and replacement.

Future research should address several key areas to enhance understanding of fault breccia classification. Current genetic and non-genetic classifications have limitations due to overarching criteria that present exceptions and difficulties in field application. There is a need for more comprehensive data from natural examples and better integration of chemical and physical processes, which often overprint each other.

Existing classifications do not adequately address fault rocks dominated by crystalline cement, like cockade texture-bearing breccias, because they focus primarily on syn-deformation factors but neglect interseismic or non-seismic processes such as compaction, cementation, replacement, recrystallisation, and dissolution. Future studies should incorporate these processes to better understand the final architecture of fault breccias. Therefore, by addressing these gaps, future research can provide a more comprehensive and accurate classification of fault breccias, leading to improved interpretations of their formation mechanisms and their role in hydrothermal ore deposition.

Cockade textures are often associated with hydrothermal ore deposits, making them of significant interest in economic geology. Future investigations should consider the combined effect of the force of crystallisation and partial metasomatic alteration through replacement and recrystallisation, mechanisms which can operate together, with or without requiring seismic activity, and prioritise examining the internal rim textures of cockades alongside the external accompanying vein textures while revealing the sequence of mineralisation through the correlation of outgrowth rims with episodic deformation events. These textures provide insights into both primary and secondary processes, often overprinting with each other during the formation of cockade texture. Additionally, investigating the economic value of minerals, particularly through replacement found within rims of cockade textures, and understanding how the formation processes influence mineral distribution could enhance the understanding of the mineralisation history of associated hydrothermal deposits.

References

Ach, J. A. (1982). The petrochemistry of the Ankara volcanics, central Turkey. *MSc. thesis, State University of New York at Albany*. 146 pp.

Ach, J. A., & Wilson, F. H. (1986). Potassium-Argon ages of volcanic rocks from near Ankara, central Turkey. *Isochron/West, Bulletin of Isotopic Geochronology*, *47*, 15–17.

Adams, S. F. (1920). A microscopic study of vein quartz. *Economic Geology*, 15(8), 623–664. https://doi.org/10.2113/gsecongeo.15.8.623

Ahmad, S. N., & Rose, A. W. (1980). Fluid inclusions in porphyry and skarn ore at Santa Rita, New Mexico. *Economic Geology*, *75*(2), 229–250. https://doi.org/10.2113/gsecongeo.75.2.229

Akyürek, B., Bilginer, E., Akbaş, B., Hemşin, N., Pehlivan, Ş., Sunu, O., Soysal, Y., Dauer, E., Çatal, E., Sözeri, B., Yıldırım, H., & Hakyemez, Y. (1984). Ankara-Elmadağ-Kalecik Dolayının Temel Jeoloji Özellikleri. *Jeoloji Mühendisliği Dergisi*, *8*(2), 31–46.

Allen, M., Brown, G. J., & Miles, N. J. (1995). Measurement of boundary fractal dimensions: review of current techniques. *Powder Technology*, *84*(1), 1–14. https://doi.org/10.1016/0032-5910(94)02967-S

Astin, T. R., & Scotchman, I. C. (1988). The diagenetic history of some septarian concretions from the Kimmeridge Clay, England. *Sedimentology*, *35*(2), 349–368. https://doi.org/10.1111/j.1365-3091.1988.tb00952.x

Ault, A. K., Frenzel, M., Reiners, P. W., Woodcock, N. H., & Thomson, S. N. (2016). Record of paleofluid circulation in faults revealed by hematite(U-Th)/He and apatite fission-track dating: An example from Gower Peninsula fault fissures, Wales. *Lithosphere*, *8*(4), 379–385. https://doi.org/10.1130/L522.1

Balay-Karperien, A. (2004). Defining Microglial Morphology: Form, Function, and Fractal Dimension. *MSc thesis. Charles Sturt University*. 246pp.

Barclay, W.J., Davies, J.R., Hillier, R.D., & Waters, R.A.. (2015) .Lithostratigraphy of the Old Red Sandstone successions of the Anglo-Welsh Basin. Nottingham, UK*, British Geological Survey*, 96pp.

Bastin, E. S. (1925). Primary native silver ores of South Lorrain and Cobalt, Ontario. *Economic Geology*, *20*(1), 1–24. https://doi.org/10.2113/gsecongeo.20.1.1

Bateman, A. M. (1924). Angular inclusions and replacement deposits (with discussion by J. E. Spurr and L. C. Graton). *Economic Geology*, *19*(6), 504–520. https://doi.org/10.2113/gsecongeo.19.6.504

Bates, R. L., & Jackson, J. A. (1987). *Glossary of geology* (3rd ed.). American Geological Institute.

Baumann, G., Barth, A., & Nonnenmacher, T. F. (1994). Measuring Fractal Dimensions of Cell Contours: Practical Approaches and their Limitations. In *Fractals in Biology and Medicine* (pp. 182–189). Birkhäuser Basel. https://doi.org/10.1007/978-3-0348-8501-0_15

Beck, R. (1903). *In: Lehre von den Erzlagerstätten* (2nd ed.). Gebrüder Bornträger, Berlin.

Becker, G. F., & Day, A. L. (1916). Note on the Linear Force of Growing Crystals. *The Journal of Geology*, *24*(4), 313–333. https://doi.org/10.1086/622342

Berger, A., & Herwegh, M. (2019). Cockade structures as a paleo-earthquake proxy in upper crustal hydrothermal systems. *Scientific Reports*, *9*(1), 1–9. https://doi.org/10.1038/s41598-019-45488-2

Bérubé, D., & Jébrak, M. (1996). Fractal descriptors for the classification of Sudbury breccias. Geological Association of Canada-Mineralogical Association of Canada. *In Annual Meeting AL tracs, Winnipeg* (Vol. 21).

Besbelli, A., & Varol, B. (2002). Clay Mineralisation In Hydrothermally Altered Tekke Volcanics (Çubuk, Ankara NE). *Bulletin Of The Mineral Research And Exploration (MTA Dergisi)*, *125*(1902), 121–137.

Blenkinsop, T. (2000). *Deformation Microstructures and Mechanisms in Minerals and Rocks*. Kluwer Academic Publishers. p.168 . https://doi.org/10.1007/0-306-47543-X

Blenkinsop, T. G., Oliver, N. H. S., Dirks, P. G. H. M., Nugus, M., Tripp, G., & Sanislav, I. (2020). Structural geology applied to the evaluation of hydrothermal gold deposits. In J. V. Rowland and D. A. Rhys (Eds.), *Applied structural geology of ore-forming hydrothermal systems* (Vol. 21, pp. 1–23). Society of Economic Geologists. https://doi.org/10.5382/rev.21.01

Block, A., von Bloh, W., & Schellnhuber, H. J. (1990). Efficient box-counting determination of generalized fractal dimensions. *Physical Review A*, *42*(4), 1869–1874. https://doi.org/10.1103/PhysRevA.42.1869

Bobis, R. E. (1994). A review of the description, classification and origin of quartz textures in low sulphidation epithermal veins. *Journal of Geological Society of Philippines*, *49*, 15–39.

Bodnar, R. J., Burnham, C. W., & Sterner, S. M. (1985). Synthetic fluid inclusions in natural quartz. III. Determination of phase equilibrium properties in the system H_2O-NaCl to 1000°C and 1500 bars. *Geochimica et Cosmochimica Acta*, *49*(9), 1861–1873. https://doi.org/10.1016/0016-7037(85)90081-X

Bons, P. D. (2001). The formation of large quartz veins by rapid ascent of fluids in mobile hydrofractures. *Tectonophysics*, *336*(1–4), 1–17. https://doi.org/10.1016/S0040-1951(01)00090-7

Bons, P. D., & Jessell, M. W. (1997). Experimental simulation of the formation of fibrous veins by localized dissolution-precipitation creep. *Mineralogical Magazine*, *61*(404), 53–63. https://doi.org/10.1180/minmag.1997.061.404.06

Boullier, A. M., & Robert, F. (1992). Palaeoseismic events recorded in Archaean gold-quartz vein networks, Val d'Or, Abitibi, Quebec, Canada. *Journal of Structural Geology*, 14(2), 161–179. https://doi.org/10.1016/0191-8141(92)90057-W

Bozkurt, E., & Mittwede, S. K. (2001). Introduction to the geology of Turkey - A synthesis. *International Geology Review*, *43*(7), 578–594. https://doi.org/10.1080/00206810109465034

Brenchley, P. J., & Rawson, P. F. (2006). *The Geology of England and Wales* (2nd edition). The Geological Society.

Brooks, M., Trayner, P. M., & Trimble, T. J. (1988a). Mesozoic reactivation of Variscan thrusting in the Bristol Channel area, UK. *Journal of the Geological Society*, *145*(3), 439–444. https://doi.org/10.1144/gsjgs.145.3.0439

Brown, K. L. (1986). Gold deposition from geothermal discharges in New Zealand. *Economic Geology*, *81*(4), 979–983. https://doi.org/10.2113/gsecongeo.81.4.979

Buczkowski, S., Hildgen, P., & Cartilier, L. (1998a). Measurements of fractal dimension by box-counting: a critical analysis of data scatter. *Physica A: Statistical Mechanics and Its Applications*, *252*(1–2), 23–34. https://doi.org/10.1016/S0378-4371(97)00581-5

Buczkowski, S., Kyriacos, S., Nekka, F., & Cartilier, Lo. (1998b). The modified box-counting method: Analysis of some characteristic parameters. *Pattern Recognition*, *31*(4), 411–418. https://doi.org/10.1016/S0031-3203(97)00054-X

Buerger, M. J., & Maury, J. L. (1927). Tin ores of Chocaya, Bolivia. *Economic Geology*, 22(1), 1–13. https://doi.org/10.2113/gsecongeo.22.1.1

Caine, J. S., Evans, J. P., & Forster, C. B. (1996). Fault zone architecture and permeability structure. *Geology*, *24*(11), 1025–1028. https://doi.org/10.1130/0091-7613(1996)024<1025:FZAAPS>2.3.CO;2

Camprubí, A., & Albinson, T. (2007). Epithermal deposits in Mexico—Update of current knowledge, and an empirical reclassification. In *Geology of Mexico: Celebrating the Centenary of the Geological Society of Mexico*. Geological Society of America. https://doi.org/10.1130/2007.2422(14)

Carr, J. R., & Benzer, W. B. (1991). On the practice of estimating fractal dimension. *Mathematical Geology*, *23*(7), 945–958. https://doi.org/10.1007/BF02066734

Cathles, L. M., & Smith, A. T. (1983). Thermal constraints on the formation of Mississippi Valley-type lead-zinc deposits and their implications for episodic basin dewatering and deposit genesis. *Economic Geology*, 78(5), 983–1002. https://doi.org/10.2113/gsecongeo.78.5.983

Chauvet, A. (2019). Structural control of ore deposits: The role of pre-existing structures on the formation of mineralised vein systems. *Minerals, 9*(1), 56. https://doi.org/10.3390/min9010056

Chester, F. M., Friedman, M., & Logan, J. M. (1985). Foliated cataclasites. *Tectonophysics*, *111*(1–2), 139–146. https://doi.org/10.1016/0040-1951(85)90071-X

Clark, I. D., & Fritz, P. (1997). *Environmental Isotopes in Hydrogeology*. Lewis Publishers. p.342. https://doi.org/10.1201/9781482242911

Cleal, C. J., & Thomas, B. A. (1996). South Wales. In *British Upper Carboniferous Stratigraphy* (pp. 57–107). Springer Netherlands. https://doi.org/10.1007/978-94-011-0587-3_4

Cocks, L. R. M., & Fortey, R. A. (1982). Faunal evidence for oceanic separations in the Paleozoic of Britain. *Journal of the Geological Society*, *139*(4), 465–478. https://doi.org/10.1144/gsjgs.139.4.0465

Cocks, L. R. M., Mckerrow, W. S., & Van Staal, C. R. (1997). The margins of Avalonia. *Geological Magazine*, *134*(5), 627–636. https://doi.org/10.1017/S0016756897007425

Converse, D. R., Holland, H. D., & Edmond, J. M. (1984). Flow rates in the axial hot springs of the East Pacific Rise (21°N): Implications for the heat budget and the formation of massive sulfide deposits. *Earth and Planetary Science Letters*, 69(1), 159–175. https://doi.org/10.1016/0012-821X(84)90084-3

Correns C.W. (1949). Growth and dissolution of crystals under linear pressure. *Discuss Faraday Society* 5:267–271

Cossey, P. J., & Adams, A. E. (2004). Introduction to British Lower Carboniferous stratigraphy. *Geological Conservation Review Series*, 29, 1-13.

Cotta, B., (1859). Lehre von den Erzlagerstätten. J.G. Engelhardt, Freiberg.

Cotta, B., (1870). A treatise on ore deposits. In: Prime, F. (Ed.), Translation of 2nd German. Van Nostrand, New York.

Cox, S. F., & Munroe, S. M. (2016). Breccia formation by particle fluidization in fault zones: Implications for transitory, rupture-controlled fluid flow regimes in hydrothermal systems. *American Journal of Science*, *316*(3), 241–278. https://doi.org/10.2475/03.2016.02

Çil, A. (2019). *Surface characteristics, mineralogy and geochemistry of the Gicik low–sulphidation epithermal AU deposit* (Ankara province, Central Anatolia) (Master's thesis, Middle East Technical University).

Danielsson, P.-E. (1980). Euclidean distance mapping. *Computer Graphics and Image Processing*, *14*(3), 227–248. https://doi.org/10.1016/0146-664X(80)90054-4

Demény, A., Sitnikova, M. A., & Karchevsky, P. I. (2004). Stable C and O isotope compositions of carbonatite complexes of the Kola Alkaline Province: Phoscorite–carbonatite relationships and source compositions. In *Phoscorites and Carbonatites from Mantle to Mine: The Key Example of the Kola Alkaline Province* (pp. 193–220). The Mineralogical Society.https://doi.org/10.1180/MSS.10.12

De Nevers, N. (1970). *Fluid mechanics* (1st ed., pp. 1–514). Addison-Wesley

Derjaguin, B. V., & Churaev, N. V. (1986). Flow of nonfreezing water interlayers and frost heaving. Cold Regions Science and Technology, 12(1), 57–66. https://doi.org/10.1016/0165-232X(86)90020-0

Dickson, J. A. D. (1993). Inorganic Calcite Morphology: Roles of Fluid Chemistry and Fluid Flow: Discussion. Journal of Sedimentary Petrology, 63(3), 560–561.

Dill, H. G., & Weber, B. (2010). Variation of colour, structure, and morphology of fluorite and the origin of the hydrothermal F-Ba deposits at Nabburg-Wölsendorf, SE Germany. *Neues Jahrbuch für Mineralogie-Abhandlungen*, 187(2), 113–132. https://doi.org/10.1127/0077-7757/2010/0170

Dong, Morrison, G., & Jaireth, S. (1995a). Quartz textures in epithermal veins, Queensland - classification, origin, and implication. Economic Geology, 90(6), 1841–1856. https://doi.org/10.2113/gsecongeo.90.6.1841

Dönmez, M., Akçay, A. E., Türkecan, A., Satır, M., Evcimen, Ö., Atakay, E., & Görmüş, T. (2009). Ankara ve Yakın Çevresi Geç Kretase− Tersiyer Volkanitlerinin Stratigrafisi ve Yeni Yaş Bulguları. *Türkiye Jeoloji Kurultayı, Bildiri Özleri Kitabı*, 62.

Doré, A. G., Lundin, E. R., Jensen, L. N., Birkeland, Ø., Eliassen, P. E., & Fichler, C. (1999). Principal tectonic events in the evolution of the northwest European Atlantic margin. In Geological Society, London, petroleum geology conference series (Vol. 5, No. 1, pp. 41-61*). The Geological Society of London*. https://doi.org/10.1144/0050041

Dowling, K., & Morisson, G. (1989). Application of Quartz Textures to the Classification of Gold Deposits Using North Queensland Examples. In *The Geology of Gold Deposits* (pp. 342–355). Society of Economic Geologists. https://doi.org/10.5382/Mono.06.26

Dubuc, B., Zucker, S. W., Tricot, C., Quiniou, J. F., & Wehbi, D. (1989). Evaluating the fractal dimension of surfaces. *Proceedings of the Royal Society of London. A. Mathematical and Physical Sciences*, *425*(1868), 113–127. https://doi.org/10.1098/rspa.1989.0101

Durney, D. W. (1972). A major unconformity in the Archaean, Jones Creek, Western Australia. *Journal of the Geological Society of Australia*, *19*(2), 251–259. https://doi.org/10.1080/14400957208527886

Dutch, S. I. (1993). Linear Richardson plots from non-fractal data sets. *Mathematical Geology*, *25*(6), 737–751. https://doi.org/10.1007/BF00893176

Eichhubl, P., & Boles, J. R. (2000). Rates of fluid flow in fault systems: Evidence for episodic rapid fluid flow in the Miocene Monterey Formation, coastal California. *American Journal of Science*, 300(7), 571–600. https://doi.org/10.2475/ajs.300.7.571

Einaudi, M. T., Hedenquist, J. W., & Inan, E. E. (2003). Sulfidation State of Fluids in Active and Extinct Hydrothermal Systems: Transitions from Porphyry to Epithermal Environments. In *Volcanic,*

Geothermal, and Ore-Forming Fluids: Rulers and Witnesses of Processes within the Earth (pp. 285–313). Society of Economic Geologists. https://doi.org/10.5382/SP.10.15

Everett, D. H. (1961). The thermodynamics of frost damage to porous solids. *Transactions of the Faraday Society*, *57*, 1541. https://doi.org/10.1039/tf9615701541

Farmin, R. (1938). Dislocated inclusions in gold-quartz veins at Grass Valley, California. *Economic Geology*, *33*(6), 579–599. https://doi.org/10.2113/gsecongeo.33.6.579

Faulkner, D. R., Jackson, C. A. L., Lunn, R. J., Schlische, R. W., Shipton, Z. K., Wibberley, C. A. J., & Withjack, M. O. (2010). A review of recent developments concerning the structure, mechanics and fluid flow properties of fault zones. *Journal of Structural Geology*, *32*(11), 1557–1575. https://doi.org/10.1016/j.jsg.2010.06.009

Fisher, R. V. (1961). Proposed classification of volcaniclastic sediments and rocks. *Bulletin of the Geological Society of America*, *72*(9), 1409–1414. https://doi.org/10.1130/0016-7606(1961)72[1409:PCOVSA]2.0.CO;2

Fletcher, R. C., & Merino, E. (2001). Mineral growth in rocks: kinetic-rheological models of replacement, vein formation, and syntectonic crystallisation. *Geochimica et Cosmochimica Acta*, 65(21), 3733-3748.

Flook, A. G. (1979). The characterisation of textural and structural profiles by the automated measurement of their fractal dimensions. *2nd European Symposium of Particle Characterisation*, 591–599.

Fournier, R. O. (1985). The Behavior of Silica in Hydrothermal Solutions. In *Geology and Geochemistry of Epithermal Systems* (pp. 45–61). Society of Economic Geologists. https://doi.org/10.5382/Rev.02.03

Fowler, A. D., & Roach, D. E. (1993). Dimensionality analysis of time-series data: Nonlinear methods. *Computers and Geosciences*, *19*(1), 41–52. https://doi.org/10.1016/0098-3004(93)90041-3

Frenzel, M., & Woodcock, N. H. (2014). Cockade breccia: Product of mineralisation along dilatational faults. *Journal of Structural Geology*, *68*(PA), 194–206. https://doi.org/10.1016/j.jsg.2014.09.001

Friedman, I., & O'Neil, J. R. (1977). Compilation of stable isotope fractionation factors of geochemical interest. In *Data of geochemistry* (6th ed., Professional Paper 440-KK, pp. 1–12). U.S. Geological Survey. https://doi.org/10.3133/pp440kk

Friend, P. F., Williams, B. P. J., Ford, M., & Williams, E. A. (2000). Kinematics and dynamics of Old Red Sandstone basins. *Geological Society, London, Special Publications*, *180*(1), 29–60. https://doi.org/10.1144/GSL.SP.2000.180.01.04

Gaskell, D. R. (1992). *An introduction to transport phenomena in materials engineering* (pp. 1–613). Macmillan.

Gayer, R., & Jones, J. (1989). The Variscan foreland in south Wales. *Proceedings - Ussher Society*, *7*(2), 177–179.

Genna, A., Jébrak, M., Marcoux, E., & Milési, J. P. (1996). Genesis of cockade breccias in the tectonic evolution of the Cirotan epithermal gold system, West Java. *Canadian Journal of Earth Sciences*, *33*(1), 93–102. https://doi.org/10.1139/e96-010

George, G. T. (2021). *The geology of South Wales: A field guide* (3rd ed., 314 pp.). Geoserv Publishing.

George, T. N. (1940). The structure of Gower. *Quarterly Journal of the Geological Society*, *96*(1–4), 131–198. https://doi.org/10.1144/GSL.JGS.1940.096.01-04.06

George, T. N. (1970). South Wales, British Regional Geology. London: HMSO.

Gerber, D., Wilen, L. A., Poydenot, F., Dufresne, E. R., & Style, R. W. (2022). Stress accumulation by confined ice in a temperature gradient. *Proceedings of the National Academy of Sciences*, *119*(31). https://doi.org/10.1073/pnas.2200748119

Gierlowski-Kordesch, E. H. (2010). Chapter 1 Lacustrine Carbonates. In *Developments in Sedimentology-Carbonates in Continental Settings* (Vol. 61, pp. 1–101). Elsevier. https://doi.org/10.1016/S0070-4571(09)06101-9

Gillespie, M. R., Barnes, R. P., & Milodowski, A. E. (2011). *British Geological Survey scheme for classifying discontinuities and fillings* (p. 15). British Geological Survey.

Gillespie, P. A., Howard, C. B., Walsh, J. J., & Watterson, J. (1993). Measurement and characterisation of spatial distributions of fractures. *Tectonophysics*, *226*(1–4), 113–141. https://doi.org/10.1016/0040-1951(93)90114-Y

Gilpin, R. R. (1979). A model of the “liquid-like” layer between ice and a substrate with applications to wire regelation and particle migration. *Journal of Colloid and Interface Science*, *68*(2), 235–251. https://doi.org/10.1016/0021-9797(79)90277-7

Goldstein, R. H., & Reynolds, T. J. (1994). Systematics Of Fluid Inclusions In Diagenetic Minerals - Sepm Short Course 31 . *SEPM (Society for Sedimentary Geology)*. https://doi.org/10.2110/scn.94.31

Gonzalez, L. A., Carpenter, S. J., & Lohmann, K. C. (1992). Inorganic Calcite Morphology: Roles of Fluid Chemistry and Fluid Flow. *SEPM Journal of Sedimentary Research*, *Vol. 62*(3), 382–399. https://doi.org/10.1306/D426790B-2B26-11D7-8648000102C1865D

Gonzato, G. (1998). A practical implementation of the box counting algorithm. *Computers and Geosciences*, *24*(1), 95–100. https://doi.org/10.1016/S0098-3004(97)00137-4

Groom, N. (2020). *The Story of Avalonia, When England and Wales Collided with Scotland*. https://www.youtube.com/watch?v=MZuUiXyM74Mandt=2059s

Gülyüz, N., Shipton, Z. K., Kusçu, İ., Lord, R. A., Kaymakcı, N., Gülyüz, E., & Gladwell, D. R. (2018). Repeated reactivation of clogged permeable pathways in epithermal gold deposits: Kestanelik epithermal vein system, NW Turkey. *Journal of the Geological Society*, *175*(3), 509–524. https://doi.org/10.1144/jgs2017-039

Hardman, K., Holdsworth, R. E., Dempsey, E., & McCaffrey, K. (2020). Nature and significance of rift-related, near-surface fissure-fill networks in fractured carbonates below regional unconformities. *Journal of the Geological Society*, 177(6), 1168-1185. https://doi.org/10.1144/jgs2020-074

Hausegger, S., Kurz, W., Rabitsch, R., Kiechl, E., & Brosch, F.-J. (2010). Analysis of the internal structure of a carbonate damage zone: Implications for the mechanisms of fault breccia formation and fluid flow. *Journal of Structural Geology*, *32*(9), 1349–1362. https://doi.org/10.1016/j.jsg.2009.04.014

Hedenquist, J. W., Arribas, A. R., & Gonzalez-Urien, E. (2000). Exploration for Epithermal Gold Deposits. In *Gold in 2000* (pp. 245–277). Society of Economic Geologists. https://doi.org/10.5382/Rev.13.07

Helvacı, C., Yücel Öztürk, Y., Satr, M., & Shang, C. K. (2014). U-Pb zircon and K-Ar geochronology reveal the emplacement and cooling history of the Late Cretaceous Beypazar granitoid, central Anatolia, Turkey. *International Geology Review*, *56*(9), 1138–1155. https://doi.org/10.1080/00206814.2014.921795

Henley, R. W., & Hughes, G. O. (2000). Underground Fumaroles: “Excess Heat” Effects in VeinFormation. *Economic Geology*, *95*(3), 453–466. https://doi.org/10.2113/gsecongeo.95.3.453

Higgins, M. W. (1971). Cataclastic rocks. *United States Geological Survey*, *687*, 97. https://doi.org/10.1007/springerreference_4979

Hoefs, J. (1997). Variations of stable isotope ratios in nature. In *Stable Isotope Geochemistry* (pp. 65–168). Springer. https://doi.org/10.1007/978-3-662-03377-7_3

Horák, J. M. (1993). *The Late Precambrian Coedana and Sarn Complexes, NW Wales – a geochemical and petrological study.* University of Wales.

Hounslow, M. W. (1997). Significance of localized pore pressures to the genesis of septarian concretions. *Sedimentology*, *44*(6), 1133–1147. https://doi.org/10.1046/j.1365-3091.1997.d01-64.x

Howells, M. F. (2007). *British Regional Geology: Wales*. British Geological Survey.

James, D. M. D. (1987). Tectonics and sedimentation in the Lower Paleozoic back-arc basin of S. Wales, UK: some quantitative aspects of basin development. *Norsk Geologisk Tidsskrift*, *67*(4), 419–428.

Jébrak, M. (1997). Hydrothermal breccias in vein-type ore deposits: A review of mechanisms, morphology and size distribution. *Ore Geology Reviews*, *12*(3), 111–134. https://doi.org/10.1016/S0169-1368(97)00009-7

Jobson, D. H., Boulter, C. A., & Foster, R. P. (1994). Structural controls and genesis of epithermal gold-bearing breccias at the Lebong Tandai mine, Western Sumatra, Indonesia. *Journal of Geochemical Exploration*, *50*(1–3), 409–428. https://doi.org/10.1016/0375-6742(94)90034-5

Jourdan, A.-L. V., Mullis, J., Ramseyer, K., & Spiers, C. J. (2009). Evidence of growth and sector zoning in hydrothermal quartz from Alpine veins. *European Journal of Mineralogy*, *21*(1), 219–231. https://doi.org/10.1127/0935-1221/2009/0021-1881

Kaymakcı, N., Inceöz, M., Ertepinar, P., & Koç, A. (2010). Late Cretaceous to Recent kinematics of SE Anatolia (Turkey). *Geological Society Special Publication*, *340*(April), 409–435. https://doi.org/10.1144/SP340.18

Kaymakcı, N., Özçelik, Y., White, S. H., & Van Dijk, P. M. (2009). Tectono-stratigraphy of the Çankırı Basin: Late Cretaceous to early Miocene evolution of the Neotethyan Suture Zone in Turkey. *Geological Society, London, Special Publications*, *311*(1), 67–106. https://doi.org/10.1144/SP311.3

Kellaway, G. A., & Welch, F. B. A. (1955). The Upper Old Red Sandstone and Lower Carboniferous rocks of Bristol and the Mendips compared with those of Chepstow and the Forest of Dean. *Bulletin of the Geological Survey Great Britain*, *9*, 1–21.

Kelling, G. (1988). Silesian sedimentation and tectonics in the South Wales Basin: A brief review. In B. M. Besly & G. Kelling (Eds.), *Sedimentation in a synorogenic basin complex: The Upper Carboniferous of Northwest Europe* (pp. 38–42). Blackie.

Keskin, M., Genç, Ş. C., & Tüysüz, O. (2008). Petrology and geochemistry of post-collisional Middle Eocene volcanic units in North-Central Turkey: Evidence for magma generation by slab breakoff following the closure of the Northern Neo-Tethys Ocean. *Lithos*, *104*(1–4), 267–305. https://doi.org/10.1016/j.lithos.2007.12.011

Ketin, İ. (1966). Tectonic units of Anatolia. *Maden Tetkik ve Arama Bulletin*, *66*, 23–34.

Killick, A. M. (2003). Fault rock classification: An aid to structural interpretation in mine and exploration geology. *South African Journal of Geology*, *106*(4), 395–402. https://doi.org/10.2113/106.4.395

Kim, S.-T., Mucci, A., & Taylor, B. E. (2007). Phosphoric acid fractionation factors for calcite and aragonite between 25 and 75 °C: Revisited. *Chemical Geology*, *246*(3–4), 135–146. https://doi.org/10.1016/j.chemgeo.2007.08.005

Kjelstrup, S., Ghoreishian Amiri, S. A., Loranger, B., Gao, H., & Grimstad, G. (2021). Transport coefficients and pressure conditions for growth of ice lens in frozen soil. *Acta Geotechnica*, *16*(7), 2231–2239. https://doi.org/10.1007/s11440-021-01158-0

Klinkenberg, B. (1994). A review of methods used to determine the fractal dimension of linear features. *Mathematical Geology*, *26*(1), 23–46. https://doi.org/10.1007/BF02065874

Knauth, L. P. (1994). Chapter 7. PETROGENESIS OF CHERT. In *Silica* (pp. 233–258). De Gruyter. https://doi.org/10.1515/9781501509698-012

Kuşcu, İ., Tosdal, R. M., & Gençalioğlu-Kuşcu, G. (2019). Porphyry-Cu deposits of Turkey. In F. Pirajno, T. Ünlü, C. Dönmez, & M. Şahin (Eds.), *Mineral resources of Turkey* (Vol. 16, pp. 211–247). Springer. https://doi.org/10.1007/978-3-030-02950-0_8

Kutina, J., & Sedlackova J. (1961). The role of replacement in the origin of some cockade textures. *Economic Geology*, *56*(1), 149–176. https://doi.org/10.2113/gsecongeo.56.1.149

Labaume, P., Sheppard, S. M. F., & Moretti, I. (2001). Fluid flow in cataclastic thrust fault zones in sandstones, Sub-Andean Zone, southern Bolivia. *Tectonophysics*, *340*(3–4), 141–172. https://doi.org/10.1016/S0040-1951(01)00144-5

Lambart, S. (2018). Experimental investigation of the pressure of crystallisation of $Ca(OH)_2$: Implications for the reactive cracking process. *Geochemistry, Geophysics, Geosystems, 19*(11), 1–11. https://doi.org/10.1029/2018GC007609

Laznicka, P. (1989). Breccias and ores. Part 1: History, organization and petrography of breccias. *Ore Geology Reviews*, *4*(4), 315–344. https://doi.org/10.1016/0169-1368(89)90009-7

Leroy, J. L., Hubé, D., & Marcoux, E. (2000). Episodic deposition of Mn Minerals in cockade breccia structures in three low-sulfidation epithermal deposits: A mineral stratigraphy and fluid-inclusion approach. *Canadian Mineralogist*, *38*(5), 1125–1136. https://doi.org/10.2113/gscanmin.38.5.1125

Liebovitch, L. S., & Toth, T. (1989). A fast algorithm to determine fractal dimensions by box counting. *Physics Letters A*, *141*(8–9), 386–390. https://doi.org/10.1016/0375-9601(89)90854-2

Lindgren, W. (1919). *In: Mineral Deposits* (2nd ed.). McGraw-Hill Book Company.

Longley, P. A., & Batty, M. (1989). Fractal measurement and line generalization. *Computers and Geosciences*, *15*(2), 167–183. https://doi.org/10.1016/0098-3004(89)90032-0

Lydon, J.W., 1984, Ore deposit models: Volcanogenic massive sulphide deposits. Part 1: A descriptive model: *Geoscience Canada*, 11, 195–202.

Lydon, J. W. (1988). Ore deposit models: Volcanogenic massive sulphide deposits. Part 2: Genetic models. *Geoscience Canada, 15*(1), 43–65. https://doi.org/10.4095/127921

Magloughlin, J. F., & Spray, J. G. (1992). Frictional melting processes and products in geological materials: introduction and discussion. *Tectonophysics*, *204*(3–4), 197–204. https://doi.org/10.1016/0040-1951(92)90307-R

Macdonald, K. C., Becker, K., Spiess, F. N., & Ballard, R. D. (1980). Hydrothermal heat flux of the black smoker vents on the East Pacific Rise. *Earth and Planetary Science Letters*, 48(1), 1–7. https://doi.org/10.1016/0012-821X(80)90168-4

Maliva, R. G., & Siever, R. (1988). Diagenetic replacement controlled by force of crystallisation. *Geology*, 16(8), 688–691. https://doi.org/10.1130/0091-7613(1988)016

Marquer, D., & Burkhard, M. (1992). Fluid circulation, progressive deformation and mass-transfer processes in the upper crust: the example of basement-cover relationships in the External Crystalline Massifs, Switzerland. *Journal of Structural Geology*, *14*(8–9), 1047–1057. https://doi.org/10.1016/0191-8141(92)90035-U

Masoch, S., Fondriest, M., Preto, N., Secco, M., & Di Toro, G. (2019). Seismic cycle recorded in cockade-bearing faults (Col de Teghime, Alpine Corsica). *Journal of Structural Geology*, *129*(September). https://doi.org/10.1016/j.jsg.2019.103889

McKerrow, W. S., Mac Niocaill, C., & Dewey, J. F. (2000). The Caledonian Orogeny redefined. *Journal of the Geological Society*, *157*(6), 1149–1154. https://doi.org/10.1144/jgs.157.6.1149

Means, W. D., & Li, T. (2001). A laboratory simulation of fibrous veins: some first observations. *Journal of Structural Geology*, *23*(6–7), 857–863. https://doi.org/10.1016/S0191-8141(00)00158-9

Meng, Q., Hooker, J., & Cartwright, J. (2017). Early overpressuring in organic-rich shales during burial: evidence from fibrous calcite veins in the Lower Jurassic Shales-with-Beef Member in the Wessex Basin, UK. *Journal of the Geological Society*, *174*(5), 869–882. https://doi.org/10.1144/jgs2016-146

Merino, E., Canals, A., & Fletcher, R. C. (2006). Genesis of self-organized zebra textures in burial dolomites: Displacive veins, induced stress, and dolomitization. *Geologica Acta*, *4*(3), 383–393.

Mitchell, W. I. (Ed.). (2004). The geology of Northern Ireland: Our natural foundation (2nd ed., 318 pp.). Geological Survey of Northern Ireland.

Mithen, J. P., & Sear, R. P. (2014). Computer simulation of epitaxial nucleation of a crystal on a crystalline surface. *The Journal of Chemical Physics*, *140*(8). https://doi.org/10.1063/1.4866035

Möbius, M. E., Lauderdale, B. E., Nagel, S. R., & Jaeger, H. M. (2001). Size separation of granular particles. *Nature*, *414*(6861), 270–270. https://doi.org/10.1038/35104697

Moix, P., Beccaletto, L., Kozur, H. W., Hochard, C., Rosselet, F., & Stampfli, G. M. (2008). A new classification of the Turkish terranes and sutures and its implication for the paleotectonic history of the region. *Tectonophysics*, *451*(1–4), 7–39. https://doi.org/10.1016/j.tecto.2007.11.044

Moncada, D., Mutchler, S., Nieto, A., Reynolds, T. J., Rimstidt, J. D., & Bodnar, R. J. (2012). Mineral textures and fluid inclusion petrography of the epithermal Ag-Au deposits at Guanajuato, Mexico:

Application to exploration. *Journal of Geochemical Exploration*, *114*, 20–35. https://doi.org/10.1016/j.gexplo.2011.12.001

Mort, K., & Woodcock, N. H. (2008). Quantifying fault breccia geometry: Dent Fault, NW England. *Journal of Structural Geology*, *30*(6), 701–709. https://doi.org/10.1016/j.jsg.2008.02.005

Nash, J. T., & Theodore, T. G. (1971). Ore fluids in the porphyry copper deposit at Copper Canyon, Nevada. *Economic Geology*, *66*(3), 385–399. https://doi.org/10.2113/gsecongeo.66.3.385

Nemčok, M., Gayer, R., & Miliorizos, M. (1995). Structural analysis of the inverted Bristol Channel Basin: implications for the geometry and timing of fracture porosity. *Geological Society, London, Special Publications*, *88*(1), 355–392. https://doi.org/10.1144/GSL.SP.1995.088.01.20

Newhouse, W. H. (1940). Openings due to movement along a curved or irregular fault plane. *Economic Geology*, *35*(3), 445–464. https://doi.org/10.2113/gsecongeo.35.3.445

Noiriel, C., Renard, F., Doan, M., & Gratier, J. (2010). Intense fracturing and fracture sealing induced by mineral growth in porous rocks. *Chemical Geology*, *269*(3–4), 197–209. https://doi.org/10.1016/j.chemgeo.2009.09.018

Okay, A. I., & Göncüoğlu, C. (2004). The Karakaya Complex: A review of data and concepts. *Turkish Journal of Earth Sciences*, *13*(2), 77–95.

Okay, A. I., & Şahintürk, Ö. (1997). Geology of the Eastern Pontides. In A. G. Robinson (Ed.), *Regional and petroleum geology of the Black Sea and surrounding region* (AAPG Memoir No. 68, pp. 291–311). American Association of Petroleum Geologists.

Okay, A. I., & Tüysüz, O. (1999). Tethyan sutures of northern Turkey. *Geological Society Special Publication*, *156*(June), 475–515. https://doi.org/10.1144/GSL.SP.1999.156.01.22

Okay, A. I., Tüysüz, O., Satir, M., Özkan-Altiner, S., Altiner, D., Sherlock, S., & Eren, R. H. (2006). Cretaceous and Triassic subduction-accretion, high-pressure-low- temperature metamorphism, and continental growth in the Central Pontides, Turkey. *Bulletin of the Geological Society of America*, *118*(9–10), 1247–1269. https://doi.org/10.1130/B25938.1

Oliver, N. H. S., & Bons, P. D. (2001). Mechanisms of fluid flow and fluid–rock interaction in fossil metamorphic hydrothermal systems inferred from vein–wallrock patterns, geometry and microstructure. *Geofluids*, *1*(2), 137–162. https://doi.org/10.1046/j.1468-8123.2001.00013.x

Orford, J. D., & Whalley, W. B. (1983). The use of the fractal dimension to quantify the morphology of irregular-shaped particles. *Sedimentology*, *30*(5), 655–668. https://doi.org/10.1111/j.1365-3091.1983.tb00700.x

Orford, J. D., & Whalley, W. B. (1987). The quantitative description of highly irregular sedimentary particles: The use of the fractal dimension. In J. R. Marshall (Ed.), *Clastic particles: Scanning electron microscopy and shape analysis of sedimentary and volcanic clasts* (pp. 267–280). Van Nostrand Reinhold.

Ostapenko, G. T. (1976). Excess pressure on the solid phases generated by hydration (according to experimental data on hydration of periclase). *Geochemistry International, 13*(3), 120–138.

Pettyjohn, E. S., & Christiansen, E. B. (1948). Effect of particle shape on free-settling rates of isometric particles. Chemical Engineering Progress, 44(3), 157–172.

Perelló, J. A. (1994). Geology, porphyry CuAu, and epithermal CuAuAg mineralisation of the Tombulilato district, North Sulawesi, Indonesia. *Journal of Geochemical Exploration*, *50*(1–3), 221–256. https://doi.org/10.1016/0375-6742(94)90026-4

Phillips, W. R., & Griffen, D. T. (1981). *Optical mineralogy: The nonopaque minerals* (671 pp.). W. H. Freeman and Company.

Philips, W. J. (1972). Hydraulic fracturing and mineralisation. *Journal of the Geological Society*, *128*(4), 337–359. https://doi.org/10.1144/gsjgs.128.4.0337

Posepný, F. (1895). The Genesis of Ore Deposits. In *American Institute of Mining Engineers*, pp. 45–50.

Prior, D. J. (1987). Syntectonic porphyroblast growth in phyllites: textures and processes. *Journal of Metamorphic Geology*, *5*(1), 27–39. https://doi.org/10.1111/j.1525-1314.1987.tb00367.x

Putnis, A. (2009). Mineral replacement reactions. *Reviews in Mineralogy and Geochemistry, 70*(1), 87–124. https://doi.org/10.2138/rmg.2009.70.3

Putnis, A., & Putnis, C. V. (2007). The mechanism of reequilibration of solids in the presence of a fluid phase. *Journal of Solid State Chemistry*, *180*(5), 1783–1786. https://doi.org/10.1016/j.jssc.2007.03.023

Rabayrol, F., Hart, C. J. R., & Thorkelson, D. J. (2019). Temporal, spatial and geochemical evolution of late Cenozoic post-subduction magmatism in central and eastern Anatolia, Turkey. *Lithos*, *336–337*(2019), 67–96. https://doi.org/10.1016/j.lithos.2019.03.022

Ramsay, J. G. (1980). The crack-seal mechanism of rock deformation. *Nature*, *284*(5752), 135–139. https://doi.org/10.1038/284135a0

Ramsay, J. G., & Huber, M. I. (1983). *The techniques of modern structural geology: Strain analysis* (Vol. 1, 307 pp.). Academic Press.

Raven, M. J. (2023). Carbon and oxygen isotope characteristics of the Clydach Valley Subgroup, Courceyan, South Wales-Mendip shelf, UK. *Depositional Record*, *9*(3), 573–606. https://doi.org/10.1002/dep2.209

Rice, S. P., Robertson, A. H. F., & Ustaömer, T. (2006). Late Cretaceous-Early Cenozoic tectonic evolution of the Eurasian active margin in the Central and Eastern Pontides, northern Turkey. *Geological Society, London, Special Publications*, *260*(1), 413–445. https://doi.org/10.1144/GSL.SP.2006.260.01.17

Rice, S. P., Robertson, A. H. F., Ustaömer, T., Inan, N., & Tasli, K. (2009). Late cretaceous-Early Eocene tectonic development of the Tethyan suture zone in the Erzincan area, Eastern Pontides, Turkey. *Geological Magazine*, *146*(4), 567–590. https://doi.org/10.1017/S0016756809006360

Richards, J. P. (2015). Tectonic, magmatic, and metallogenic evolution of the Tethyan orogen: From subduction to collision. *Ore Geology Reviews*, *70*, 323–345. https://doi.org/10.1016/j.oregeorev.2014.11.009

Rieder, M. (1969). Replacement and cockade textures. *Economic Geology*, *64*(5), 564–567. https://doi.org/10.2113/gsecongeo.64.5.564

Rhys, D. A., Lewis, P. D., & Rowland, J. V. (2020). Structural controls on ore localization in epithermal gold-silver deposits: A mineral systems approach. *Reviews in Economic Geology, 21*, 1–36.

Robert G. Loucks. (1999). Paleocave Carbonate Reservoirs: Origins, Burial-Depth Modifications, Spatial Complexity, and Reservoir Implications. *AAPG Bulletin*, *83*. https://doi.org/10.1306/E4FD426F-1732-11D7-8645000102C1865D

Robert L. Folk. (1959). Practical Petrographic Classification of Limestones. *AAPG Bulletin*, *43*. https://doi.org/10.1306/0BDA5C36-16BD-11D7-8645000102C1865D

Roberts, J. C. (1979). Jointing and minor tectonics of the south gower Peninsula between mumbles head and Rhossilli Bay, South Wales. *Geological Journal*, *14*(2), 1–14. https://doi.org/10.1002/gj.3350140202

Robertson, A. H. F., Parlak, O., & Ustaömer, T. (2021). Late Paleozoic extensional volcanism along the northern margin of Gondwana in southern Turkey: implications for Palaeotethyan development. In *International Journal of Earth Sciences* (Vol. 110, Issue 6). Springer Berlin Heidelberg. https://doi.org/10.1007/s00531-021-02051-7

Robie, R. A., & Hemingway, B. S. (1995). *Thermodynamic properties of minerals and related substances at 298.15 K and 1 bar (10^5 pascals) pressure and at higher temperatures* (U.S. Geological Survey Bulletin No. 2131). U.S. Government Printing Office. https://doi.org/10.3133/b2131

Roedder, E. (1984). Fluid inclusions. In P. H. Ribbe (Ed.), *Reviews in Mineralogy* (Vol. 12, pp. 10–98). Mineralogical Society of America.

Rogers, A. F. (1917). A Review of the Amorphous Minerals. *The Journal of Geology*, *25*(6), 515–541. https://doi.org/10.1086/622518

Rosenbaum, J., & Sheppard, S. M. F. (1986). An isotopic study of siderites, dolomites and ankerites at high temperatures. *Geochimica et Cosmochimica Acta*, *50*(6), 1147–1150. https://doi.org/10.1016/0016-7037(86)90396-0

Sander, M. V., & Black, J. E. (1988). Crystallisation and recrystallisation of growth-zoned vein quartz crystals from epithermal systems; implications for fluid inclusion studies. *Economic Geology*, *83*(5), 1052–1060. https://doi.org/10.2113/gsecongeo.83.5.1052

Sarkar, N., & Chaudhuri, B. B. (1994). An efficient differential box-counting approach to compute fractal dimension of image. *IEEE Transactions on Systems, Man, and Cybernetics*, *24*(1), 115–120. https://doi.org/10.1109/21.259692

Saunders, J. A. (1994). Silica and gold textures in bonanza ores of the Sleeper Deposit, Humboldt County, Nevada; evidence for colloids and implications for epithermal ore-forming processes. *Economic Geology*, *89*(3), 628–638. https://doi.org/10.2113/gsecongeo.89.3.628

Scherer, G. W. (1999). Crystallisation in pores. *Cement and Concrete Research*, *29*(8), 1347–1358. https://doi.org/10.1016/S0008-8846(99)00002-2

Schmid, R. (1981). Descriptive nomenclature and classification of pyroclastic deposits and fragments: Recommendations of the IUGS Subcommission on the Systematics of Igneous Rocks. *Geology*, *9*(1), 41. https://doi.org/10.1130/0091-7613(1981)9<41:DNACOP>2.0.CO;2

Schneider, C. M., Kesselring, T. A., Andrade, J. S., & Herrmann, H. J. (2012). Box-covering algorithm for fractal dimension of complex networks. *Physical Review E*, *86*(1), 016707. https://doi.org/10.1103/PhysRevE.86.016707

Scholle, P. A., & Ulmer-Scholle, D. S. (2003). *A colour guide to the petrography of carbonate rocks* (Vol. 77, 459 pp.). American Association of Petroleum Geologists. https://doi.org/10.1306/M77973

Scholz, C. H. (2019). *The Mechanics of Earthquakes and Faulting*. Cambridge University Press. https://doi.org/10.1017/9781316681473

Schuiling, R. D., & Wensink, H. (1962). Porphyroblastic and poikiloblastic textures: The growth of large crystals in a solid medium. *Neues Jahrbuch für Mineralogie Monatshefte*, 1962(6), 247–254.

Scotese, C. R., & McKerrow, W. S. (1990). Revised World maps and introduction. *Geological Society, London, Memoirs*, *12*(1), 1–21. https://doi.org/10.1144/GSL.MEM.1990.012.01.01

Searl, A. (1989). Diagenesis of the Gully Oolite (Lower Carboniferous), South Wales. In *Geological Journal* (Vol. 24).

Şengör, A. M. C., & Yilmaz, Y. (1981). Tethyan evolution of Turkey: A plate tectonic approach. *Tectonophysics*, *75*(3–4). https://doi.org/10.1016/0040-1951(81)90275-4

Sheldon, H. A., & Micklethwaite, S. (2007). Damage and permeability around faults: Implications for mineralisation. *Geology*, *35*(10), 903–906. https://doi.org/10.1130/G23860A.1

Sherlock, R. L., Tosdal, R. M., Lehrman, N. J., Graney, J. R., Losh, S., Jowett, E. C., & Kesler, S. E. (1995). Origin of the McLaughlin Mine sheeted vein complex; metal zoning, fluid inclusion, and isotopic evidence. *Economic Geology*, 90(8), 2156-2181.

Shukla, M. K., & Sharma, A. (2018). A brief review on breccia: it's contrasting origin and diagnostic signatures. *Solid Earth Sciences*, *3*(2), 50–59. https://doi.org/10.1016/j.sesci.2018.03.001

Sibley, D. N., Llombart, P., Noya, E. G., Archer, A. J., & MacDowell, L. G. (2021). How ice grows from premelting films and water droplets. *Nature Communications*, *12*(1), 239. https://doi.org/10.1038/s41467-020-20318-6

Sibson, R. H. (1977). Fault rocks and fault mechanisms. *Journal of the Geological Society*, *133*(3), 191–213. https://doi.org/10.1144/gsjgs.133.3.0191

Sibson, R. H. (1981). Fluid flow accompanying faulting: Field evidence and models. In D. W. Simpson & P. G. Richards (Eds.), Earthquake prediction: An international review (Maurice Ewing Series, Vol. 4, pp. 593–603). American Geophysical Union. https://doi.org/10.1029/ME004p0593

Sibson, R. H. (1982). Fault zone models, heat flow, and the depth distribution of earthquakes in the continental crust of the United States. *Bulletin of the Seismological Society of America, 72*(1), 151–163.

Sibson, R. H. (1986). Brecciation processes in fault zones: Inferences from earthquake rupturing. *Pure and Applied Geophysics PAGEOPH*, *124*(1–2), 159–175. https://doi.org/10.1007/BF00875724

Sibson, R. H. (1990). Conditions for fault-valve behaviour. *Geological Society Special Publication*, *54*, 15–28. https://doi.org/10.1144/GSL.SP.1990.054.01.02

Sillitoe, R. H. (1985). Ore-related breccias in volcanoplutonic arcs. *Economic Geology*, *80*(6), 1467–1514. https://doi.org/10.2113/gsecongeo.80.6.1467

Sillitoe, R. H., & Hedenquist, J. W. (2003). Linkages between Volcanotectonic Settings, Ore-Fluid Compositions, and Epithermal Precious Metal Deposits. In *Volcanic, Geothermal, and Ore-Forming Fluids: Rulers and Witnesses of Processes within the Earth* (pp. 315–343). Society of Economic Geologists. https://doi.org/10.5382/SP.10.16

Simmons, S. F., and Christenson, B. W. (1994). Origins of calcite in a boiling geothermal system. *American Journal of Science*, *294*(3), 361–400. https://doi.org/10.2475/ajs.294.3.361

Simmons, S. F., White, N. C., & John, D. A. (2005). Geological Characteristics of Epithermal Precious and Base Metal Deposits. In *One Hundredth Anniversary Volume*. Society of Economic Geologists. https://doi.org/10.5382/AV100.16

Sipahi, F., Kaygusuz, A., Saydam Eker, Vural, A., & Akpınar. (2018). Late Cretaceous arc igneous activity: the Eğrikar Monzogranite example. *International Geology Review*, *60*(3), 382–400. https://doi.org/10.1080/00206814.2017.1336120

Skarbek, R. M., Savage, H. M., Kelemen, P. B., & Yancopoulos, D. (2018). Competition Between Crystallisation-Induced Expansion and Creep Compaction During Gypsum Formation, and Implications for Serpentinization. *Journal of Geophysical Research: Solid Earth*, *123*(7), 5372–5393. https://doi.org/10.1029/2017JB015369

Spry, A. (1969). *Metamorphic textures.* Elsevier. (P. Press., Ed.; 1st edition, p. 350).

Spurr, J. E. (1926). Successive banding around rock fragments in veins. *Economic Geology*, *21*(6), 519–537. https://doi.org/10.2113/gsecongeo.21.6.519

Srivastava, D. C., Lisle, R. J., & Vandycke, S. (1995). Shear zones as a new type of palaeostress indicator. *Journal of Structural Geology*, *17*(5), 663–676. https://doi.org/10.1016/0191-8141(94)00084-D

Stahl, W. J. (1977). Carbon and nitrogen isotopes in hydrocarbon research and exploration. *Chem. Geol. (Netherlands)*, *2*, 121–149.

Taber, S. (1918). The mechanics of vein formation. *Trans. Am. Inst. Min. Eng.*, *140*, 1189–1222.

Taksavasu, T., Monecke, T., & Reynolds, T. (2018). Textural Characteristics of Noncrystalline Silica in Sinters and Quartz Veins: Implications for the Formation of Bonanza Veins in Low-Sulfidation Epithermal Deposits. *Minerals*, *8*(8), 331. https://doi.org/10.3390/min8080331

Talmadge, S. B. (1929). The significance of “unsupported inclusions.” *Economic Geology*, *24*(6), 601–610. https://doi.org/10.2113/gsecongeo.24.6.601

Tankut, A. (1985). Ankara dolaylarındaki Neojen yaşlı volkaniklerin jeokimyası. *Türkiye Jeoloji Bülteni*, *28*(1973), 55–66.

Torsvik, T. H., and Rehnström, E. F. (2003). The Tornquist Sea and Baltica–Avalonia docking. *Tectonophysics*, *362*(1–4), 67–82. https://doi.org/10.1016/S0040-1951(02)00631-5

Van Alstine, R. E. (1944). The fluorspar deposits of Saint Lawrence, Newfoundland. *Economic Geology*, *39*(2), 109–132. https://doi.org/10.2113/gsecongeo.39.2.109

Varol, E., Temel, A., Yürür, T., Gourgaud, A., & Bellon, H. (2014). Petrogenesis of the Neogene bimodal magmatism of the Galatean Volcanic Province, Central Anatolia, Turkey. *Journal of Volcanology and Geothermal Research*, *280*(April 2019), 14–29. https://doi.org/10.1016/j.jvolgeores.2014.04.014

Veizer, J., Ala, D., Azmy, K., Bruckschen, P., Buhl, D., Bruhn, F., Carden, G. A. F., Diener, A., Ebneth, S., Godderis, Y., Jasper, T., Korte, C., Pawellek, F., Podlaha, O. G., & Strauss, H. (1999). 87Sr/86Sr, δ13C and δ18O evolution of Phanerozoic seawater. *Chemical Geology*, *161*(1–3), 59–88. https://doi.org/10.1016/S0009-2541(99)00081-9

Von Weissenbach, C. G. A. (1836). *Abbildungen merkwürdiger Gangverhältnisse aus dem sächsischen Erzgebirge* (XIII, 63 pp.). Leopold Voss.

Voss, R. F. (1986). Characterisation and Measurement of Random Fractals. *Physica Scripta*, *T13*, 27–32. https://doi.org/10.1088/0031-8949/1986/T13/004

Waters, C. N., Browne, M. A. E., Dean, M. T., & Powell, J. H. (2007). *Lithostratigraphical framework for Carboniferous successions of Great Britain (Onshore)*. British Geological Survey Research Report (RR/07/01). British Geological Survey, Nottingham.

Waters, C. N., Millward, D., & Thomas, C. W. (2014). The millstone grit group (Pennsylvanian) of the Northumberland-Solway Basin and Alston Block of northern England. *Proceedings of the Yorkshire Geological Society*, *60*(1), 29–51. https://doi.org/10.1144/pygs2014-341

Watts, N. L. (1978). Displacive calcite: Evidence from recent and ancient calcretes. *Geology*, *6*(11), 699. https://doi.org/10.1130/0091-7613(1978)6<699:DCEFRA>2.0.CO;2

Webber, J. B. W., Dore, J. C., Strange, J. H., Anderson, R., & Tohidi, B. (2007). Plastic ice in confined geometry: the evidence from neutron diffraction and NMR relaxation. *Journal of Physics: Condensed Matter*, *19*(41), 415117. https://doi.org/10.1088/0953-8984/19/41/415117

Weyl, P. K. (1959). Pressure solution and the force of crystallisation: a phenomenological theory. *Journal of Geophysical Research*, 64(11), 2001-2025.

White, J. D. L., & Houghton, B. F. (2006). Primary volcaniclastic rocks. *Geology*, *34*(8), 677. https://doi.org/10.1130/G22346.1

Wickham, J. S. (1973). An estimate of strain increments in a naturally deformed carbonate rock. *American Journal of Science*, 273(1), 23–47.

Wickham, J. S., & Elliott, D. (1970). Rotation and strain history in folded carbonates, Front Royal area, northern Virginia. *Transactions of the American Geophysical Union, 51*(4), 422.

Williams, R. T., & Fagereng, Å. (2022). The role of quartz cementation in the seismic cycle: A critical review. *Reviews of Geophysics, 60*(1), e2021RG000768. https://doi.org/10.1029/2021RG000768

Wilson, D., Davies, J. R., Fletcher, C. J. N., & Smith, M. (1990). *Geology of the South Wales Coalfield, part VI, the country around Bridgend* (2nd ed.). British Geological Survey.

Wiltschko, D. V., & Morse, J. W. (2001). Crystallisation pressure versus "crack seal" as the mechanism for banded veins. *Geology*, *29*(1), 79. https://doi.org/10.1130/0091-7613(2001)029<0079:CPVCSA>2.0.CO;2

Wise, D. U., Dunn, D. E., Engelder, J. T., Geiser, P. A., Hatcher, R. D., Kish, S. A., Odom, A. L., & Schamel, S. (1984). Fault-related rocks: Suggestions for terminology. *Geology*, *12*(7), 391. https://doi.org/10.1130/0091-7613(1984)12<391:FRSFT>2.0.CO;2

Wolterbeek, T. K. T., van Noort, R., & Spiers, C. J. (2018). Reaction-driven casing expansion: potential for wellbore leakage mitigation. *Acta Geotechnica*, *13*(2), 341–366. https://doi.org/10.1007/s11440-017-0533-5

Woodcock, N. H., & Mort, K. (2008). Classification of fault breccias and related fault rocks. *Geological Magazine*, *145*(3), 435–440. https://doi.org/10.1017/S0016756808004883

Wright, V. P., & Tucker, M. E. (1991). Calcretes: An Introduction. In V. P. Wright and M. E. Tucker (Eds.), *Calcretes* (Vol. 2, pp. 1–22). Blackwell. https://doi.org/10.1002/9781444304497.ch

Wright, V. P., Zarza, A. M. A., Sanz, M. E., & Calvo, J. P. (1997). Diagenesis of Late Miocene micritic lacustrine carbonates, Madrid Basin, Spain. *Sedimentary Geology*, *114*(1–4), 81–95. https://doi.org/10.1016/S0037-0738(97)00059-6

Wright, V., Woodcock, N. H., & Dickson, J. A. D. (2009). Fissure fills along faults: Variscan examples from Gower, South Wales. *Geological Magazine*, *146*(6), 890–902. https://doi.org/10.1017/S001675680999001X

Yardley, B. W. D. (1974). Porphyroblasts and 'Crystallisation Force': Discussion of Some Theoretical Considerations. *Geological Society of America Bulletin*, *85*(1), 61. https://doi.org/10.1130/0016-7606(1974)85<61:PACFDO>2.0.CO;2

Yigit, O. (2009). Mineral deposits of Turkey in relation to Tethyan metallogeny: Implications for future mineral exploration. *Economic Geology*, *104*(1), 19–51. https://doi.org/10.2113/gsecongeo.104.1.19

Zeeck, L. R., Monecke, T., Reynolds, T. J., Tharalson, E. R., Pfaff, K., Kelly, N. M., & Hennigh, Q. T. (2021). Textural Characteristics of Barren and Mineralised Colloform Quartz Bands at the Low-Sulfidation Epithermal Deposits of the Omu Camp in Hokkaido, Japan: Implications for Processes Resulting in Bonanza-Grade Precious Metal Enrichment. *Economic Geology*, *116*(2), 407–425. https://doi.org/10.5382/econgeo.4795

Zheng, X., Cordonnier, B., & McBeck, J. (2019). Mixed-mode strain localization generated by hydration reaction at crustal conditions. *Journal of Geophysical Research: Solid Earth, 124*(5), 4507–4522. https://doi.org/10.1029/2018JB017008

Zhang, R., Liu, S., Zhang, L., & Zhang, J. (2021). Rheological behaviour and filtration of water-based drilling fluids containing graphene oxide. *ACS Omega, 6*(45), 30529–30538. https://doi.org/10.1021/acsomega.1c04398

Zheng, X., Cordonnier, B., Zhu, W., Renard, F., & Jamtveit, B. (2018). Effects of Confinement on Reaction-Induced Fracturing During Hydration of Periclase. *Geochemistry, Geophysics, Geosystems*, *19*(8), 2661–2672. https://doi.org/10.1029/2017GC007322

Appendices

Appendices 1

Appendix 1.1: The fissure outcrop map of Western-Slade fault in Oxwich.

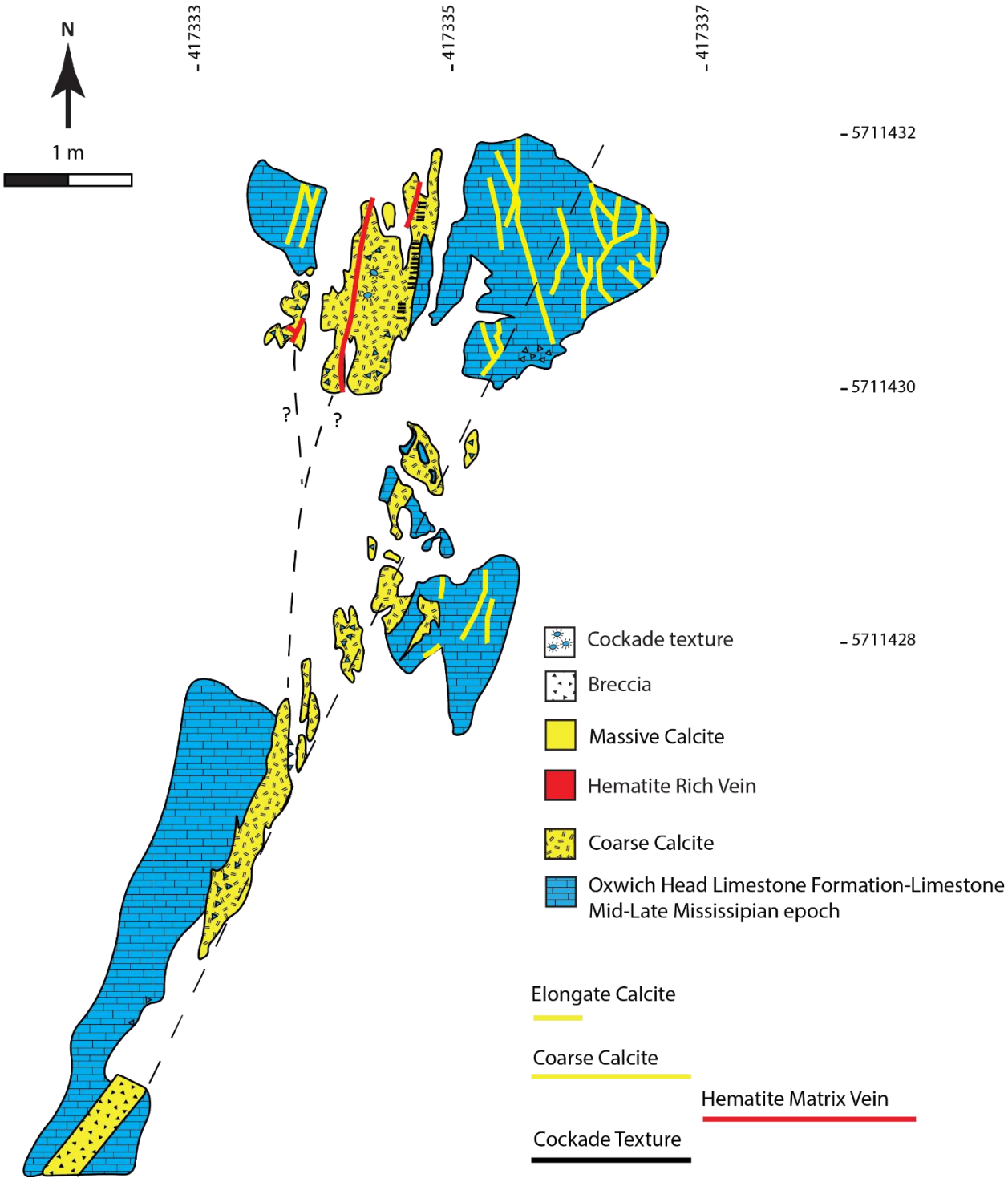

Appendix 1.2 The fissure outcrop map of Eastern-Slade fault in Oxwich.

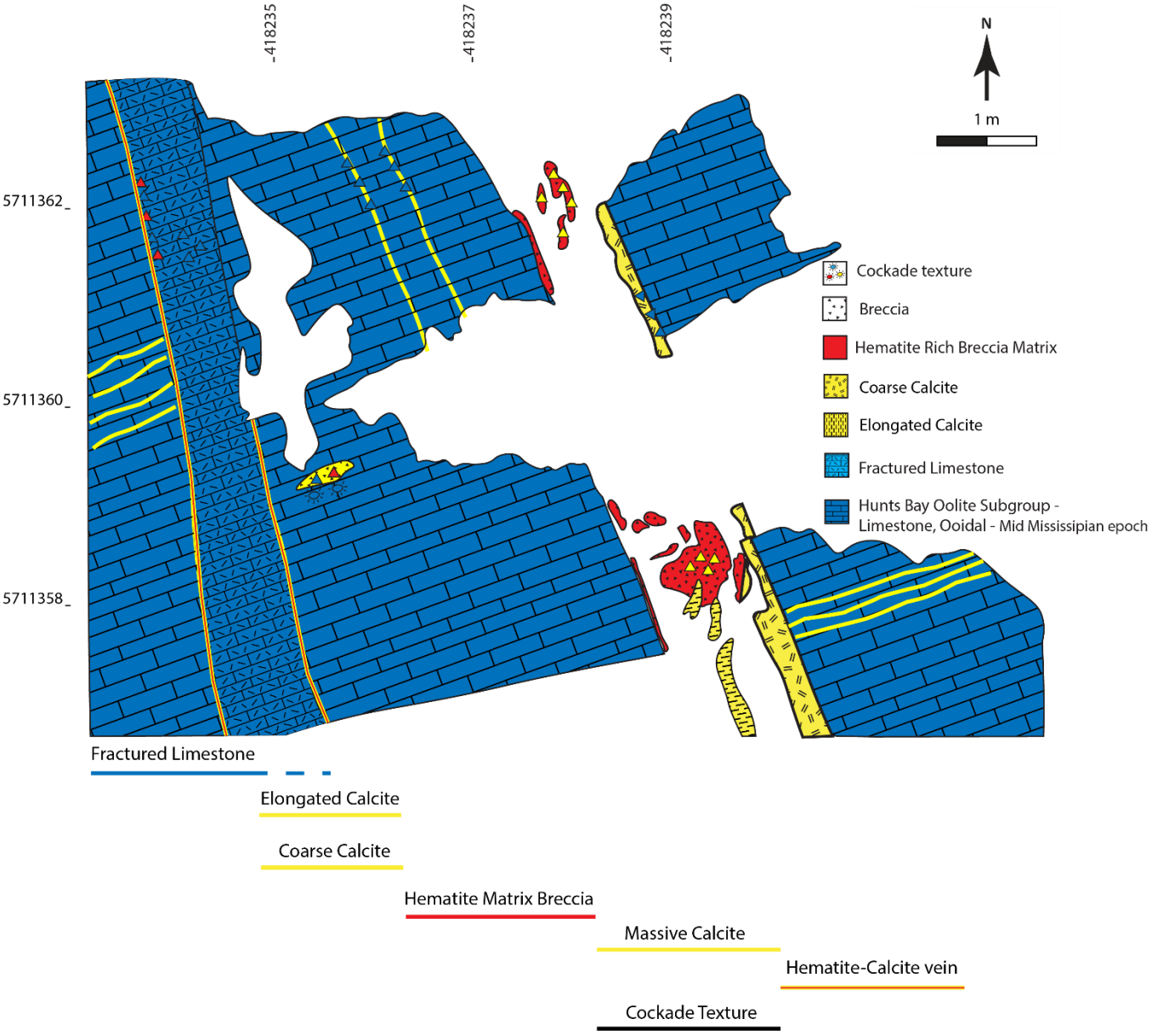

Appendix 1.3 The fissure outcrop map of Oxwich-Green fault in Oxwich.

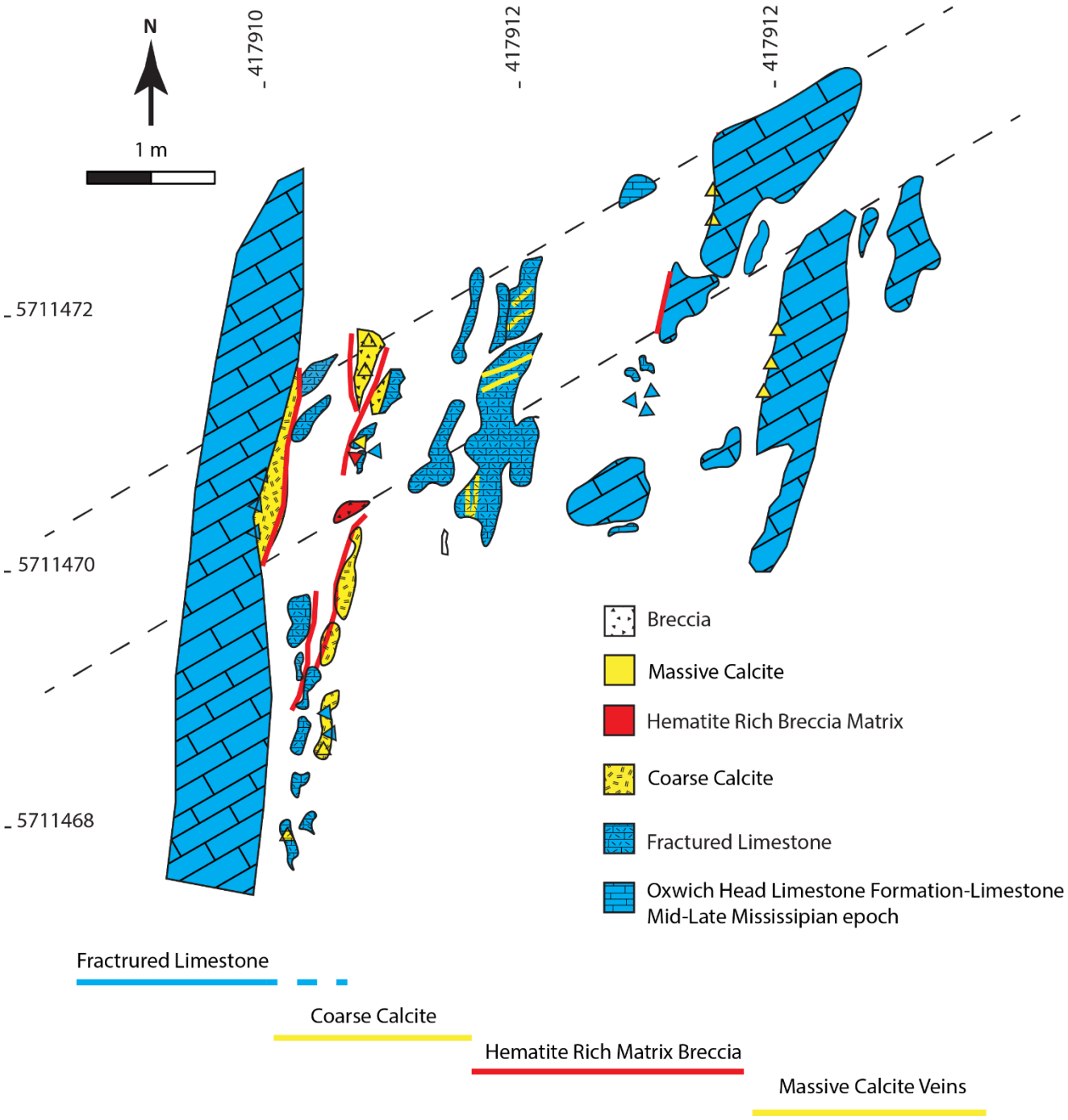

Appendix 1.4 The fissure outcrop map of Western-Oxwich fault in Oxwich.

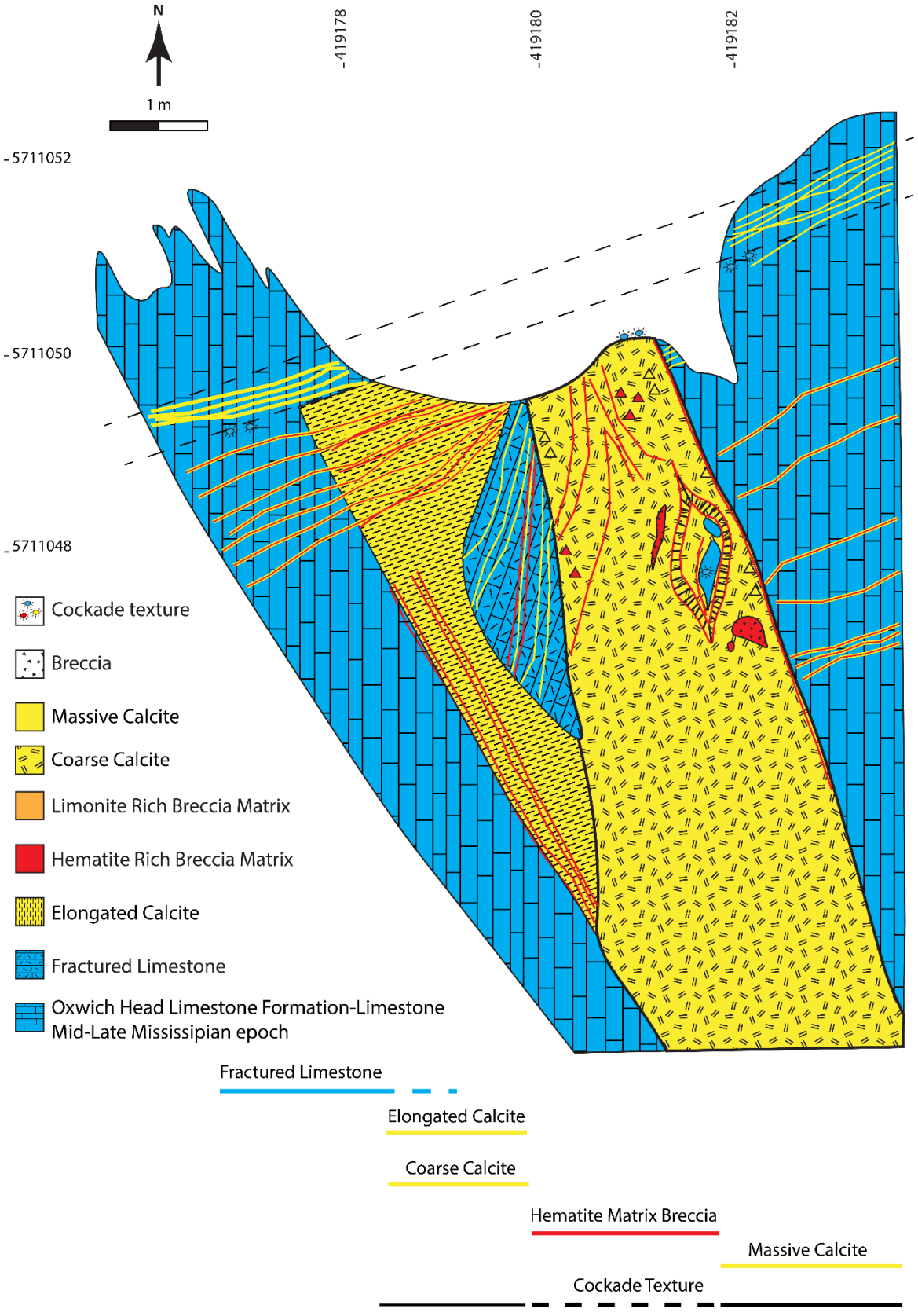

Appendix 1.5 The fissure outcrop map of Eastern-Oxwich fault in Oxwich.

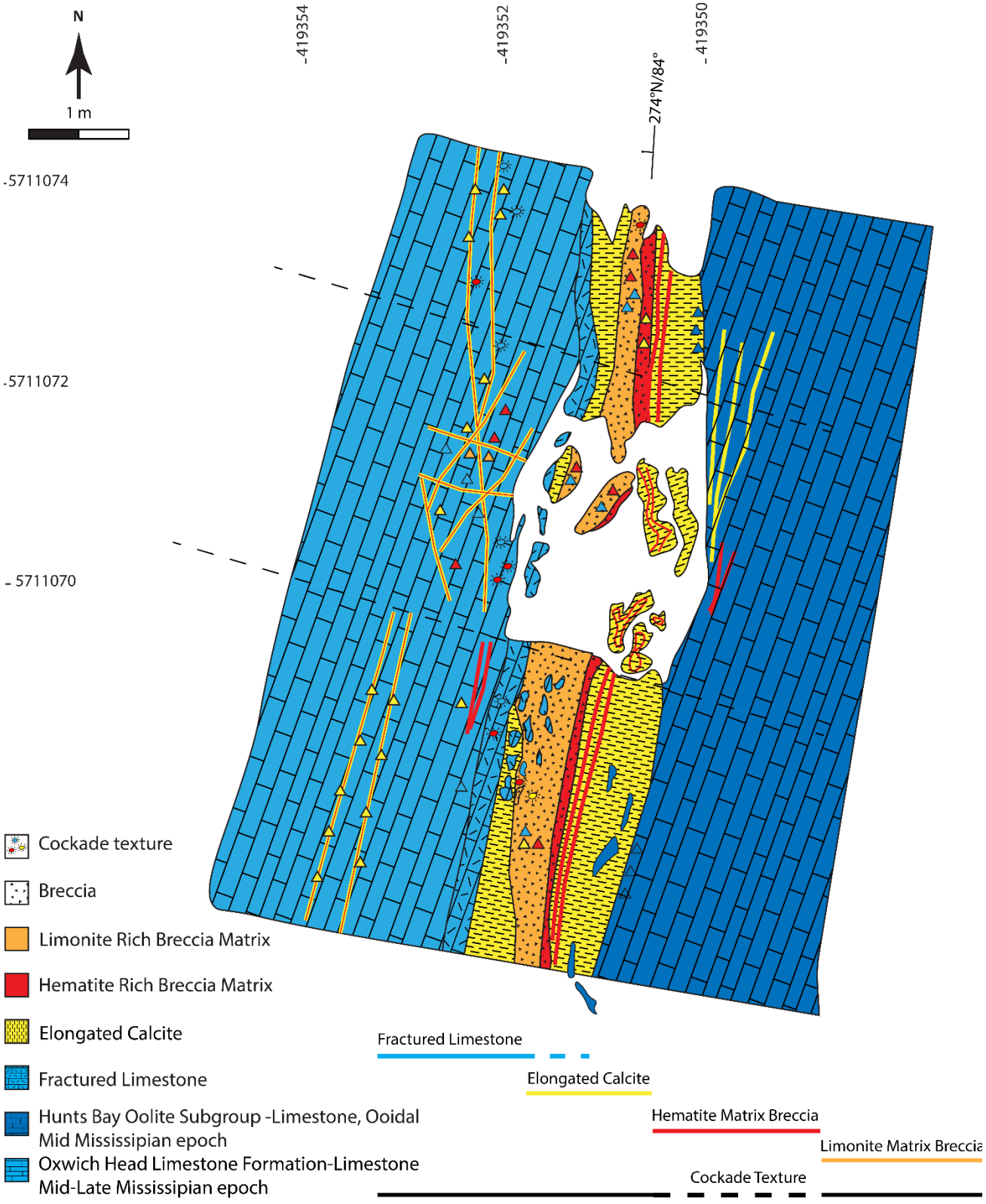

Appendix 1.6 The outcrop map of Q-1 Vein segment in Gicik.

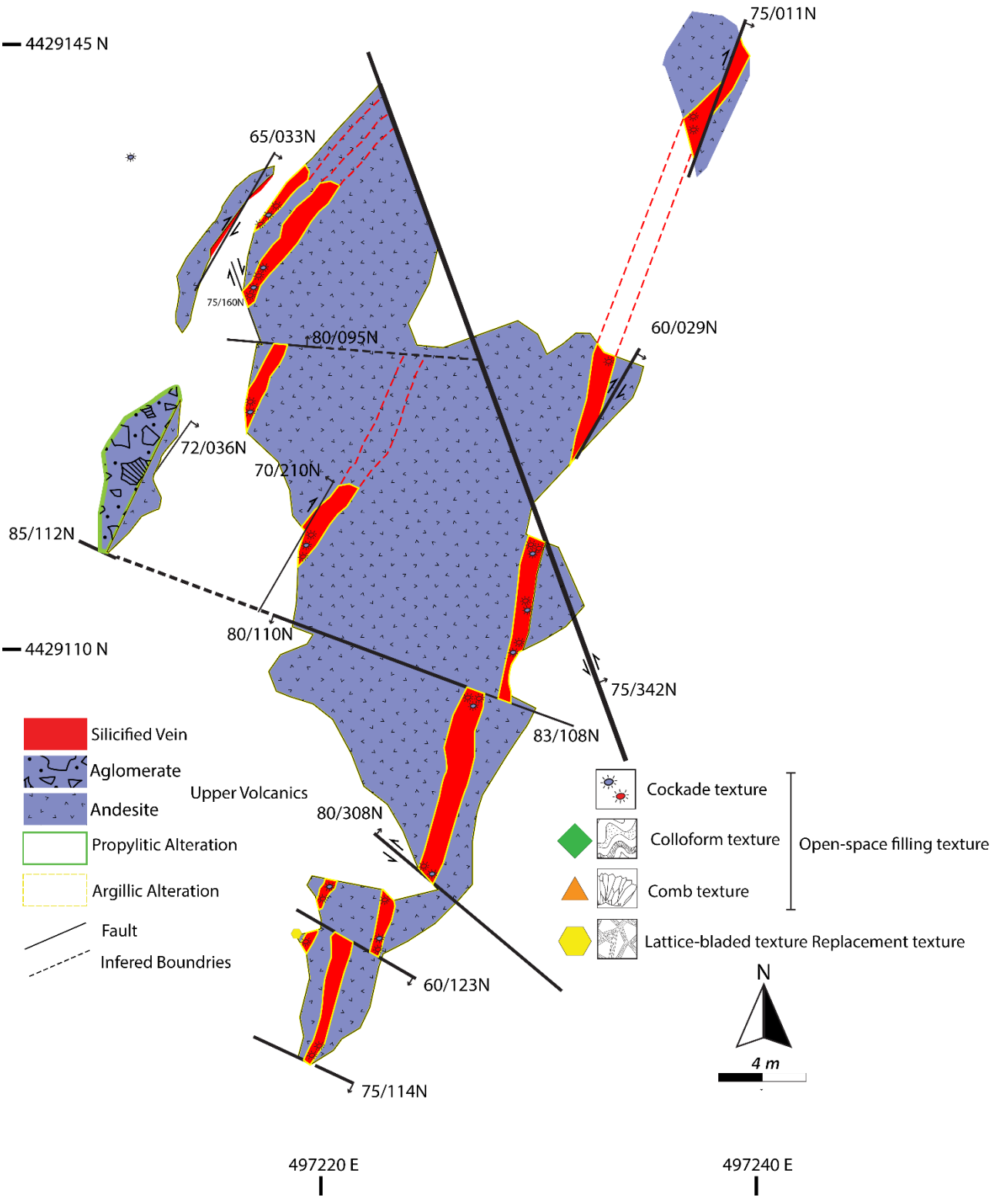

Appendix 1.7 The outcrop map of Q-2 Vein segment in Gicik.

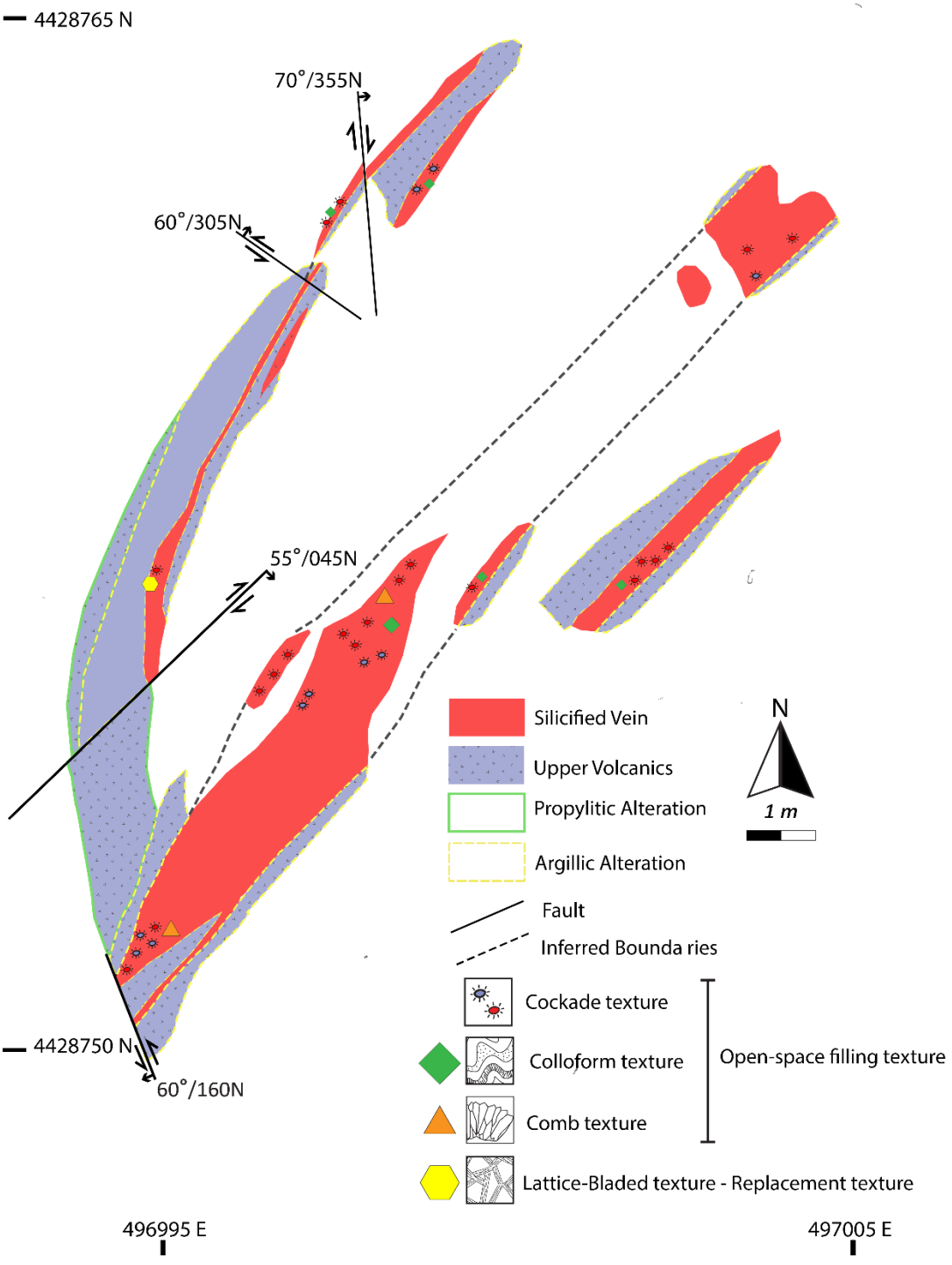

Appendix 2 The Fractal dimension values calculation for a database and Gicik with their standard deviations and r^2 values.

Epithermal Pb-Zn-(Cu,Ag,Au,Sn) veins

Reference	Outline (0.1 mm)	Scale	Fractal Dimension (D_B)	STANDARD DEVIATION (σ) for D_B	r^2 for D_B
Watson, 1943	Central Fragment	Macroscopic	1.0608	0.0033	0.994
	Rim1	Macroscopic	1.0373	0.0018	0.9961
Kutina and Sedlackova, 1961	Central Fragment	Macroscopic	1.0948	0.0032	0.9937
	Rim1	Macroscopic	1.0556	0.0034	0.9958
Rieder, 1969	Central Fragment	Macroscopic	1.083	0.0030	0.996
	Rim1	Macroscopic	1.049	0.0032	0.9952
	Rim2	Macroscopic	1.0601	0.0031	0.9947
Munoz et al, 1994	Central Fragment	Macroscopic	1.1029	0.0034	0.996
	Rim1	Macroscopic	1.0816	0.0031	0.9961
Spurr, 1926	Central Fragment	Macroscopic	1.1069	0.0047	0.9965
	Rim1	Macroscopic	1.051	0.0038	0.9956
	Rim2	Macroscopic	1.0505	0.0044	0.9947
Buerger and Maury, 1927	Central Fragment	Macroscopic	1.0654	0.0041	0.9952
	Rim1	Macroscopic	1.0557	0.0032	0.9899
Munoz et al, 1997	Central Fragment	Macroscopic	1.0532	0.0036	0.9942
	Rim1	Macroscopic	1.0454	0.0034	0.9958

Epithermal Au-(Ag,Cu) veins

Reference	Outline (0.1 mm)	Scale	Fractal Dimension (D_B)	STANDARD DEVIATION (σ) for D_B	r^2 for D_B
Gibson, 1990	Central Fragment	Macroscopic	1.1046	0.0029	0.9963
	Rim1	Macroscopic	1.0899	0.0029	0.9963
Tanner, 2012	Central Fragment	Macroscopic	1.0864	0.0040	0.9941
	Rim1	Macroscopic	1.0572	0.0041	0.9956
Berger and Herwegh, 2019	Central Fragment	Microscopic	1.1283	0.0038	0.9956
	Rim1	Microscopic	1.0886	0.0038	0.995
	Rim2	Microscopic	1.0913	0.0036	0.9952
	Rim3	Microscopic	1.0986	0.0038	0.9946
	Rim4	Microscopic	1.0985	0.0036	0.9946
	Rim5	Microscopic	1.0577	0.0037	0.9936
Masoch et al, 2019	Central Fragment	Microscopic	1.0691	0.0027	0.9941
	Rim1	Microscopic	1.0592	0.0029	0.9941
	Rim2	Microscopic	1.047	0.0030	0.9953
Jobson et al, 1994	Central Fragment	Macroscopic	1.0617	0.0028	0.9964
	Rim1	Macroscopic	1.0775	0.0033	0.9962
	Rim2	Macroscopic	1.0548	0.0036	0.9956
Genna et al, 1996	Central Fragment	Macroscopic	1.0495	0.0027	0.996
	Rim1	Macroscopic	1.0223	0.0019	0.9978
	Rim2	Macroscopic	1.0241	0.0020	0.9985
Leroy et al,2000	Central Fragment	Macroscopic	1.0682	0.0024	0.9968
	Rim1	Macroscopic	1.0475	0.0024	0.997
	Rim2	Macroscopic	1.0388	0.0021	0.998
	Rim3	Macroscopic	1.0199	0.0019	0.9981
	Rim4	Macroscopic	1.0353	0.0028	0.9966
Grancea et al,2002	Central Fragment	Macroscopic	1.0893	0.0043	0.994
	Rim1	Macroscopic	1.0522	0.0038	0.9913
Squires ,2005	Central Fragment	Macroscopic	1.0599	0.0038	0.9954
	Rim1	Macroscopic	1.0442	0.0037	0.9957
	Rim2	Macroscopic	1.0485	0.0032	0.9961
Cox and Munroe, 2016	Central Fragment	Microscopic	1.0642	0.0019	0.9978
	Rim1	Microscopic	1085	0.0029	0.9952
	Rim2	Microscopic	1.0478	0.0026	0.997
	Rim3	Microscopic	1.0333	0.0022	0.9974
	Central Fragment	Macroscopic	1.1064	0.0034	0.9962
	Rim1	Microscopic	1.0232	0.0030	0.9971
	Rim2	Microscopic	1.312	0.0027	0.9912

Fluorite-Barite vein

Reference	Outline (0.1 mm)	Scale	Fractal Dimension (D_B)	STANDARD DEVIATION (σ) for D_B	r^2 for D_B
VanAlstine,1944	Central Fragment	Macroscopic	1.0565	0.0028	0.9937
	Rim1	Macroscopic	1.0444	0.0036	0.996
	Rim2	Macroscopic	1.0379	0.0035	0.9963

Low-T Calcite veins

Reference	Outline (0.1 mm)	Scale	Fractal Dimension (D_B)	STANDARD DEVIATION (σ) for D_B	r^2 for D_B
Wright et al, 2009	Central Fragment	Macroscopic	1.0209	0.0019	0.9978
	Rim1	Macroscopic	1.046	0.0027	0.9961
	Rim2	Macroscopic	1.0492	0.0027	0.9954
Frenzel and Woodcock, 2014	Central Fragment	Macroscopic	1.1308	0.0036	0.9948
	Rim1	Macroscopic	1.1155	0.0024	0.9953
	Rim2	Macroscopic	1.0937	0.0032	0.9959
	Rim3	Macroscopic	1.0439	0.0038	0.9953
	Rim4	Macroscopic	1.0556	0.0026	0.9952

Gicik Low-Sulfidation Epithermal System

	Outline (0.1 mm)	Scale	Fractal Dimension (D_B)	STANDARD DEVIATION (σ) for D_B	r^2 for D_B
Cockade 1	Central fragment	Macroscopic	1.1593	0.0064	0.9884
	Rim1	Macroscopic	0.9755	0.0049	0.9901
	Rim2	Macroscopic	0.9655	0.0040	0.9917
	Rim3	Macroscopic	1.1026	0.0049	0.9936
	Rim4	Microscopic	0.9913	0.0046	0.9914
	Rim5	Microscopic	1.0863	0.0038	0.9914
Cockade 2	Central fragment	Microscopic	1.0948	0.0041	0.9941
	Rim1	Microscopic	1.0056	0.0039	0.9871
	Rim2	Microscopic	1.0606	0.0043	0.9931
	Rim3	Microscopic	1.064	0.0041	0.99
	Rim4	Microscopic	1.0495	0.0044	0.9942
Cockade 3	Central fragment	Microscopic	1.0801	0.0030	0.9962
	Rim1	Microscopic	1.0556	0.0034	0.9949
	Rim2	Macroscopic	1.0525	0.0036	0.9959
Cockade 4	Central fragment	Macroscopic	1.0692	0.0043	0.9948
	Rim1	Macroscopic	1.0625	0.0039	0.9894
	Rim2	Macroscopic	1.0531	0.0038	0.9896
Cockade 5	Central fragment	Macroscopic	1.1136	0.0040	0.9964
	Rim1	Macroscopic	1.0655	0.0053	0.9948
	Rim2	Macroscopic	1.0702	0.0038	0.9959
Cockade 6	Central fragment	Macroscopic	1.0783	0.0041	0.9933
	Rim1	Macroscopic	1.0642	0.0046	0.9927
	Rim2	Macroscopic	1.0682	0.0039	0.9932
Cockade 7	Central fragment	Macroscopic	1.0768	0.0043	0.9932
	Rim1	Macroscopic	1.0712	0.0037	0.9955
	Rim2	Macroscopic	1.0616	0.0035	0.9947
Cockade 8	Central fragment	Macroscopic	1.0793	0.0035	0.9963
	Rim1	Macroscopic	1.074	0.0030	0.9932
	Rim2	Macroscopic	1.0031	0.0030	0.9966
Cockade 9	Central fragment	Microscopic	1.0577	0.0034	0.9956
	Rim1	Microscopic	0.9935	0.0038	0.9942
	Rim 2	Microscopic	1.0479	0.0032	0.9916

Appendices 3

Appendix 3.1 The Fluid inclusion results of measured 102 fluid inclusions.

Sample-ID	T_h (°C)	T_m (°C)	Liquid (µm)	Vapour (µm)	(L)Ratio (%)	*Salinity* (NaCl %)*
OX-4a	222		1.80	4.52	71.5	
OX-4a	234		1.80	4.50	71.4	
OX-4a	268		0.80	2.40	75.0	
OX-4a	190		1.70	4.40	72.1	
OX-4a	228		1.30	4.50	77.6	
OX-4a	182		2.00	4.20	67.7	
OX-4a	**258**	**-5.60**	**2.20**	**5.60**	**71.8**	***8.7***
OX-4a	270		0.90	2.50	73.5	
OX-4a	269		1.00	2.70	73.0	
OX-4a	268		1.30	3.40	72.3	
OX-4a	272		1.70	5.40	76.1	
OX-4a	267		1.20	3.10	72.1	
OX-4a	264		0.80	2.60	76.5	
OX-4a	262		1.10	3.70	77.1	
OX-4a	263		1.40	3.50	71.4	
OX-4a	265		1.20	3.40	73.9	
OX-4a	184	-6.10	1.00	3.00	75.0	*9.3*
OX-4b	242		2.4	8.2	77.4	
OX-4b	275	-6.3	1.9	4.8	71.6	*9.6*
OX-4b	265		1.8	5.4	75.0	
OX-4b	**236**	**-6**	**1.7**	**6.1**	**78.2**	***9.2***
OX-4b	262		2.5	7.2	74.2	
OX-4b	242		1.6	6.3	79.7	
OX-4b	268		0.9	2.8	75.7	
OX-4b	272		1.2	3.8	76.0	
OX-4b	270		1.4	4.1	74.5	
OX-4b	274		1.8	4.6	71.9	
OX-4b	200	-6.7	1.6	5	75.8	*10.1*
OX-4b	182		2.1	8.3	79.8	
OX-4b	232		2.4	7.9	76.7	
OX-4b	278		2.2	7.6	77.6	
OX-4b	227		1.9	6.6	77.6	
OX-4b	276		1	2.6	72.2	
OX-4b	245		1.2	3.4	73.9	
OX5a	93		1.6	4.8	75.0	

Sample-ID	T_h (°C)	T_m (°C)	Liquid (µm)	Vapour (µm)	(L)Ratio (%)	*Salinity* (NaCl %)*
OX5a	95	-5.4	1.8	6.8	79.1	*8.4*
OX5a	98	-7.1	1.8	8.8	83.0	*10.6*
OX5a	97	-7.2	1.1	5.1	82.3	*10.7*
OX5a	84	-5.4	0.8	3.3	80.5	*8.4*
OX5a	87		1.6	3.6	69.2	
OX5a	89	-5.2	1.6	7	81.4	*8.1*
OX5a	88	-6.2	1.6	5.4	77.1	*9.5*
OX5a	81		0.7	3.2	82.1	
OX-5b	101	-4.9	2.4	6.4	72.7	*7.7*
OX-5b	128		1.5	4.5	75.0	
OX-5b	100	-5.1	1.7	5.7	77.0	*8.0*
OX-5b	85		1.5	3.4	69.4	
OX-5b	86		2.1	6.1	74.4	
OX-5b	84		0.8	2.1	72.4	
OX-5b	92		1.2	3.8	76.0	
OX-5b	98		1.8	4.6	71.9	
OX-5b	102		1.6	4.2	72.4	
OX6a	155		0.6	3.5	85.4	
OX6a	158		0.4	2.3	85.2	
OX6a	155		0.7	2.8	80.0	
OX6a	157		1.2	3.5	74.5	
OX6a	152		1.8	3.5	66.0	
OX6a	186		1.3	4.4	77.2	
OX6a	179		1.4	4.9	77.8	
OX6a	178		1.4	4.7	77.0	
OX6a	177		1.3	3.3	71.7	
OX6a	157		1.3	3.4	72.3	
OX6a	183		0.8	2.4	75.0	
OX6a	182		1	2.8	73.7	
OX6a	212		1.8	4.3	70.5	
OX6a	208		2	5.1	71.8	
OX6a	238	-2.1	2.7	8.2	75.2	*3.5*
OX6a	217		1.3	4.5	77.6	
OX6a	211		1.2	3.5	74.5	
OX6a	242	-1.8	1.8	6.1	77.2	*3.1*
OX6a	205		1.8	4.6	71.9	
OX6a	212		1.2	3.6	75.0	
OX6a	192		1	2.4	70.6	

Sample-ID	T_h (°C)	T_m (°C)	Liquid (µm)	Vapour (µm)	(L)Ratio (%)	*Salinity* (NaCl %)*
OX6b	285	-1	3	6	66.7	*1.7*
OX6b	282	-0.6	2.7	5	64.9	*1.1*
OX6b	274	-0.2	4.3	8.5	66.4	*0.4*
OX6b	280	-0.5	4.2	9.7	69.8	*0.9*
OX6b	232		1.2	3.1	72.1	
OX6b	261		1.5	3.8	71.7	
OX6b	278	-0.7	4.2	8.9	67.9	*1.2*
OX6b	281	-0.2	1.8	5.2	74.3	*0.4*
OX7	224	-6.8	1.1	4.2	79.2	*10.2*
OX7	221	-7	1	5	83.3	*10.5*
OX7	264		1	2.9	74.4	
OX7	267		1.7	3.9	69.6	
OX7	267		0.7	2.6	78.8	
OX7	268		0.8	2.4	75.0	
OX7	266		0.6	2.1	77.8	
OX7	270		0.8	3	78.9	
OX7	272		1.6	4.5	73.8	
OX7	271		0.9	2.7	75.0	
OX7	278		1.5	4.3	74.1	
OX7	264	-6.8	2.1	7.5	78.1	*10.2*
OX7	185		0.7	2.2	75.9	
OX7	228		1.2	4.1	77.4	
OX7	186		0.5	1.9	79.2	
OX7	192		1.1	2.8	71.8	
OX7	215		1.6	4	71.4	
OX7	213		1	3.6	78.3	
OX7	212		1.6	4.9	75.4	
OX7	201		1	3.1	75.6	

*The equation of (Bodnar et al., 1985), below, was used to calculate salinities of liquid-rich fluid inclusions from measuring ice-melting temperatures.

$$Salinity\ (wt\%\ NaCl) = 1.78\ \times \theta - 0.0442 \times \theta^2 + 0.0005572 \times \theta^3 \qquad (6)$$

Appendix 3.2 AqSo_NaCl: computer program to calculate p-T-V-x properties in the H_2O-NaCl system applied to fluid inclusion research and pore fluid calculation and results for each sample is presented below for isocore plot.

Sample ID = **OX-4a**

Molar Volume = 21.40652 cm3/mol

Density = 0.8988247 g/cm3

x(NaCl) = 0.0303183

Homogenisation conditions: 236 Celsius and 2.945023 MPa

Temperature	*Pressure*	*xNaCl(liq)*	*V(liq)*	*frac(liq)*	*V(vap)*	*frac(vap)*
(°C)	**(MPa)**	**(fraction)**	**(cm^3/mol)**	**(fraction)**	**(cm^3/mol)**	**(fraction)**
30	0.004	0.026	18.120	0.818	654447.100	0.182
40	0.007	0.026	18.198	0.822	383834.700	0.178
50	0.011	0.026	18.283	0.826	234076.100	0.174
60	0.019	0.026	18.376	0.830	148024.900	0.170
70	0.029	0.026	18.476	0.834	96769.950	0.166
80	0.045	0.026	18.583	0.839	65184.850	0.161
90	0.066	0.026	18.698	0.844	45097.530	0.156
100	0.096	0.026	18.820	0.850	31950.050	0.150
110	0.135	0.026	18.950	0.856	23118.760	0.144
120	0.187	0.026	19.089	0.862	17046.920	0.138
130	0.255	0.026	19.236	0.868	12783.970	0.132
140	0.341	0.026	19.393	0.875	9734.011	0.125
150	0.449	0.026	19.559	0.883	7514.278	0.117
160	0.584	0.026	19.734	0.891	5873.451	0.109
170	0.749	0.026	19.920	0.899	4643.164	0.101
180	0.949	0.026	20.117	0.908	3708.551	0.092
190	1.189	0.026	20.326	0.917	2989.921	0.083
200	1.475	0.026	20.548	0.927	2431.139	0.073
210	1.812	0.026	20.783	0.938	1992.093	0.062
220	2.206	0.026	21.033	0.949	1643.751	0.051
230	2.664	0.026	21.299	0.961	1364.838	0.039
240	3.192	0.026	21.583	0.974	1139.587	0.026
250	3.797	0.026	21.886	0.988	956.190	0.012
260	7.124	0.026	22.144	1.000	0.000	0.000
270	20.823	0.026	22.144	1.000	0.000	0.000
280	34.492	0.026	22.144	1.000	0.000	0.000
290	48.216	0.026	22.144	1.000	0.000	0.000
300	62.010	0.026	22.144	1.000	0.000	0.000

Sample ID = **OX-4b**

Molar Volume = 21.40652 cm3/mol

Density = 0.8988247 g/cm3

x(NaCl) = 0.0303183

Homogenisation conditions: 236 Celsius and 2.945023 MPa

Temperature	*Pressure*	*xNaCl(liq)*	*V(liq)*	*frac(liq)*	*V(vap)*	*frac(vap)*
(°C)	**(MPa)**	**(fraction)**	**(cm^3/mol)**	**(fraction)**	**(cm^3/mol)**	**(fraction)**
30	0.00	0.03	18.13	0.85	667367.60	0.15
40	0.01	0.03	18.21	0.85	390435.20	0.15
50	0.01	0.03	18.30	0.85	237580.30	0.15
60	0.02	0.03	18.39	0.86	149990.70	0.14
70	0.03	0.03	18.49	0.86	97946.68	0.14
80	0.04	0.03	18.59	0.87	65936.22	0.13
90	0.07	0.03	18.71	0.87	45604.94	0.13
100	0.09	0.03	18.83	0.88	32308.08	0.12
110	0.13	0.03	18.96	0.89	23379.68	0.11
120	0.19	0.03	19.09	0.89	17241.50	0.11
130	0.25	0.03	19.24	0.90	12931.52	0.10
140	0.34	0.03	19.39	0.91	9847.30	0.09
150	0.44	0.03	19.55	0.91	7602.14	0.09
160	0.58	0.03	19.72	0.92	5942.17	0.08
170	0.74	0.03	19.91	0.93	4697.34	0.07
180	0.94	0.03	20.10	0.94	3751.58	0.06
190	1.18	0.03	20.30	0.95	3024.36	0.05
200	1.46	0.03	20.52	0.96	2458.91	0.04
210	1.79	0.03	20.74	0.97	2014.67	0.03
220	2.19	0.03	20.99	0.98	1662.25	0.02
230	2.64	0.03	21.24	0.99	1380.13	0.01
240	9.01	0.03	21.41	1.00	0.00	0.00
250	23.79	0.03	21.41	1.00	0.00	0.00
260	38.53	0.03	21.41	1.00	0.00	0.00
270	53.33	0.03	21.41	1.00	0.00	0.00
280	68.21	0.03	21.41	1.00	0.00	0.00
290	83.16	0.03	21.41	1.00	0.00	0.00
300	98.21	0.03	21.41	1.00	0.00	0.00

Sample ID = **OX-5a**

Molar Volume = 18.68796 cm3/mol

Density = 1.021503 g/cm3

x(NaCl) = 0.0265857

Homogenisation conditions: 88.99958 Celsius and 0.0635729 MPa

Temperature	*Pressure*	*xNaCl(liq)*	*V(liq)*	*frac(liq)*	*V(vap)*	*frac(vap)*
(°C)	**(MPa)**	**(fraction)**	**(cm^3/mol)**	**(fraction)**	**(cm^3/mol)**	**(fraction)**
30	0.00	0.03	18.12	0.97	657019.00	0.03
40	0.01	0.03	18.20	0.98	385151.00	0.02
50	0.01	0.03	18.29	0.98	234776.10	0.02
60	0.02	0.03	18.38	0.98	148418.00	0.02
70	0.03	0.03	18.48	0.99	97005.42	0.01
80	0.04	0.03	18.59	0.99	65335.20	0.01
90	1.79	0.03	18.69	1.00	0.00	0.00
100	17.36	0.03	18.69	1.00	0.00	0.00
110	33.58	0.03	18.69	1.00	0.00	0.00
120	50.46	0.03	18.69	1.00	0.00	0.00
130	67.87	0.03	18.69	1.00	0.00	0.00
140	85.80	0.03	18.68	1.00	0.00	0.00
150	104.22	0.03	18.68	1.00	0.00	0.00
160	123.10	0.03	18.68	1.00	0.00	0.00
170	142.39	0.03	18.68	1.00	0.00	0.00
180	162.05	0.03	18.68	1.00	0.00	0.00
190	182.05	0.03	18.68	1.00	0.00	0.00
200	202.35	0.03	18.67	1.00	0.00	0.00
210	222.91	0.03	18.67	1.00	0.00	0.00
220	243.69	0.03	18.67	1.00	0.00	0.00
230	264.66	0.03	18.67	1.00	0.00	0.00
240	285.80	0.03	18.67	1.00	0.00	0.00
250	307.06	0.03	18.66	1.00	0.00	0.00
260	328.43	0.03	18.66	1.00	0.00	0.00
270	349.87	0.03	18.66	1.00	0.00	0.00
280	371.37	0.03	18.66	1.00	0.00	0.00
290	392.89	0.03	18.65	1.00	0.00	0.00
300	414.41	0.03	18.65	1.00	0.00	0.00

Sample ID = **OX-5b**

Molar Volume = 18.83191 cm3/mol

Density = 1.010636 g/cm3

x(NaCl) = 0.025161

Homogenisation conditions: 100.9997 Celsius and 0.0992784 MPa

Temperature	*Pressure*	*xNaCl(liq)*	*V(liq)*	*frac(liq)*	*V(vap)*	*frac(vap)*
(°C)	**(MPa)**	**(fraction)**	**(cm^3/mol)**	**(fraction)**	**(cm^3/mol)**	**(fraction)**
30	0.00	0.03	18.12	0.96	653163.50	0.04
40	0.01	0.03	18.20	0.97	383177.10	0.03
50	0.01	0.03	18.28	0.97	233726.00	0.03
60	0.02	0.03	18.37	0.98	147828.00	0.02
70	0.03	0.03	18.47	0.98	96651.88	0.02
80	0.04	0.03	18.58	0.99	65109.33	0.01
90	0.07	0.03	18.70	0.99	45046.47	0.01
100	0.10	0.03	18.82	1.00	31913.96	0.00
110	14.65	0.03	18.83	1.00	0.00	0.00
120	31.05	0.03	18.83	1.00	0.00	0.00
130	48.01	0.03	18.83	1.00	0.00	0.00
140	65.43	0.03	18.83	1.00	0.00	0.00
150	83.27	0.03	18.83	1.00	0.00	0.00
160	101.51	0.03	18.83	1.00	0.00	0.00
170	120.11	0.03	18.83	1.00	0.00	0.00
180	139.05	0.03	18.83	1.00	0.00	0.00
190	158.28	0.03	18.83	1.00	0.00	0.00
200	177.77	0.03	18.83	1.00	0.00	0.00
210	197.49	0.03	18.83	1.00	0.00	0.00
220	217.41	0.03	18.83	1.00	0.00	0.00
230	237.49	0.03	18.83	1.00	0.00	0.00
240	257.72	0.03	18.83	1.00	0.00	0.00
250	278.06	0.03	18.83	1.00	0.00	0.00
260	298.50	0.03	18.83	1.00	0.00	0.00
270	319.01	0.03	18.83	1.00	0.00	0.00
280	339.57	0.03	18.83	1.00	0.00	0.00
290	360.16	0.03	18.83	1.00	0.00	0.00
300	380.76	0.03	18.83	1.00	0.00	0.00

Sample ID = **OX-6a**

Molar Volume = 21.77812 cm3/mol

Density = 0.848021 g/cm3

x(NaCl) = 0.0112126

Homogenisation conditions: 238 Celsius and 3.165679 MPa

Temperature	*Pressure*	*xNaCl(liq)*	*V(liq)*	*frac(liq)*	*V(vap)*	*frac(vap)*
(°C)	**(MPa)**	**(fraction)**	**(cm^3/mol)**	**(fraction)**	**(cm^3/mol)**	**(fraction)**
30	0.00	0.01	18.10	0.83	617943.00	0.17
40	0.01	0.01	18.17	0.83	365014.20	0.17
50	0.01	0.01	18.25	0.84	223996.10	0.16
60	0.02	0.01	18.34	0.84	142330.90	0.16
70	0.03	0.01	18.44	0.85	93346.00	0.15
80	0.05	0.01	18.55	0.85	62993.37	0.15
90	0.07	0.01	18.67	0.86	43616.59	0.14
100	0.10	0.01	18.80	0.86	30905.55	0.14
110	0.14	0.01	18.94	0.87	22358.44	0.13
120	0.19	0.01	19.09	0.88	16480.71	0.12
130	0.26	0.01	19.24	0.88	12355.27	0.12
140	0.35	0.01	19.41	0.89	9405.30	0.11
150	0.46	0.01	19.59	0.90	7259.67	0.10
160	0.60	0.01	19.78	0.91	5674.49	0.09
170	0.77	0.01	19.99	0.92	4486.43	0.08
180	0.98	0.01	20.20	0.93	3584.12	0.07
190	1.23	0.01	20.43	0.94	2890.36	0.06
200	1.52	0.01	20.68	0.95	2350.84	0.05
210	1.87	0.01	20.94	0.96	1926.80	0.04
220	2.27	0.01	21.22	0.97	1590.21	0.03
230	2.74	0.01	21.52	0.99	1320.53	0.01
240	6.04	0.01	21.78	1.00	0.00	0.00
250	20.34	0.01	21.78	1.00	0.00	0.00
260	34.68	0.01	21.78	1.00	0.00	0.00
270	49.10	0.01	21.78	1.00	0.00	0.00
280	63.61	0.01	21.78	1.00	0.00	0.00
290	78.17	0.01	21.78	1.00	0.00	0.00
300	92.80	0.01	21.78	1.00	0.00	0.00

Sample ID = **OX-6b**

Molar Volume = 23.84079 cm3/mol

Density = 0.7602605 g/cm3

x(NaCl) = 0.0027261

Homogenisation conditions: 280 Celsius and 6.386023 MPa

Temperature	*Pressure*	*xNaCl(liq)*	*V(liq)*	*frac(liq)*	*V(vap)*	*frac(vap)*
(°C)	**(MPa)**	**(fraction)**	**(cm^3/mol)**	**(fraction)**	**(cm^3/mol)**	**(fraction)**
30	0.00	0.00	18.09	0.76	598535.40	0.24
40	0.01	0.00	18.16	0.76	354903.40	0.24
50	0.01	0.00	18.24	0.76	218526.30	0.24
60	0.02	0.00	18.33	0.77	139216.60	0.23
70	0.03	0.00	18.43	0.77	91463.46	0.23
80	0.05	0.00	18.54	0.78	61785.21	0.22
90	0.07	0.00	18.66	0.78	42799.55	0.22
100	0.10	0.00	18.80	0.79	30329.65	0.21
110	0.14	0.00	18.94	0.79	21939.83	0.21
120	0.20	0.00	19.10	0.80	16169.53	0.20
130	0.27	0.00	19.26	0.81	12120.12	0.19
140	0.36	0.00	19.44	0.81	9225.34	0.19
150	0.47	0.00	19.63	0.82	7120.51	0.18
160	0.61	0.00	19.83	0.83	5565.92	0.17
170	0.79	0.00	20.05	0.84	4401.01	0.16
180	1.00	0.00	20.28	0.85	3516.37	0.15
190	1.25	0.00	20.53	0.86	2836.20	0.14
200	1.55	0.00	20.79	0.87	2307.19	0.13
210	1.90	0.00	21.07	0.88	1891.33	0.12
220	2.31	0.00	21.38	0.90	1561.12	0.10
230	2.78	0.00	21.71	0.91	1296.47	0.09
240	3.33	0.00	22.06	0.92	1082.48	0.08
250	3.96	0.00	22.45	0.94	908.00	0.06
260	4.67	0.00	22.87	0.96	764.61	0.04
270	5.48	0.00	23.33	0.98	645.86	0.02
280	6.39	0.00	23.84	1.00	546.79	0.00
290	18.11	0.00	23.84	1.00	0.00	0.00
300	29.94	0.00	23.84	1.00	0.00	0.00

Sample ID = **OX-7**

Molar Volume = 22.18629 cm3/mol

Density = 0.8738597 g/cm3

x(NaCl) = 0.0339543

Homogenisation conditions: 264 Celsius and 4.713054 MPa

Temperature	*Pressure*	*xNaCl(liq)*	*V(liq)*	*frac(liq)*	*V(vap)*	*frac(vap)*
(°C)	**(MPa)**	**(fraction)**	**(cm^3/mol)**	**(fraction)**	**(cm^3/mol)**	**(fraction)**
30	0.00	0.03	18.14	0.82	677806.60	0.18
40	0.01	0.03	18.22	0.82	395744.90	0.18
50	0.01	0.03	18.31	0.83	240387.90	0.17
60	0.02	0.03	18.40	0.83	151560.60	0.17
70	0.03	0.03	18.50	0.83	98884.55	0.17
80	0.04	0.03	18.60	0.84	66534.47	0.16
90	0.06	0.03	18.72	0.84	46008.85	0.16
100	0.09	0.03	18.84	0.85	32593.17	0.15
110	0.13	0.03	18.96	0.85	23587.58	0.15
120	0.18	0.03	19.10	0.86	17396.67	0.14
130	0.25	0.03	19.24	0.87	13049.29	0.13
140	0.33	0.03	19.39	0.87	9937.82	0.13
150	0.44	0.03	19.55	0.88	7672.40	0.12
160	0.57	0.03	19.72	0.89	5997.18	0.11
170	0.73	0.03	19.90	0.90	4740.74	0.10
180	0.93	0.03	20.09	0.90	3786.08	0.10
190	1.17	0.03	20.29	0.91	3051.99	0.09
200	1.45	0.03	20.50	0.92	2481.22	0.08
210	1.78	0.03	20.72	0.93	2032.82	0.07
220	2.17	0.03	20.96	0.94	1677.15	0.06
230	2.62	0.03	21.21	0.96	1392.47	0.04
240	3.14	0.03	21.47	0.97	1162.66	0.03
250	3.74	0.03	21.76	0.98	975.64	0.02
260	4.42	0.03	22.06	0.99	822.29	0.01
270	12.98	0.03	22.19	1.00	0.00	0.00
280	26.55	0.03	22.19	1.00	0.00	0.00
290	40.12	0.03	22.19	1.00	0.00	0.00
300	53.73	0.03	22.19	1.00	0.00	0.00

Appendix 4 The assay results for stable isotope analyses in Oxwich.

Sample-ID	*$\delta^{13}C$ VPDB*	*d $^{13}C/^{12}C$ Std Dev*	*$\delta^{18}O$ VPDB*	*d $^{18}O/^{16}O$ Std Dev*	*$\delta^{18}O$ VSMOW**
OX-4a	0.796	0.013	-11.357	0.014	*19.212*
OX-4a	0.781	0.021	-11.333	0.016	*19.237*
OX-4a	0.752	0.019	-11.37	0.025	*19.198*
OX-4b	-4.55	0.014	-6.779	0.024	*23.931*
OX-4b	-4.61	0.04	-6.844	0.035	*23.864*
OX-4b	-4.562	0.012	-6.745	0.025	*23.966*
OX-5a	-2.13	0.017	-8.937	0.029	*21.707*
OX-5a	-2.115	0.024	-8.923	0.032	*21.721*
OX-5a	-2.102	0.01	-9.004	0.02	*21.638*
OX-5b	-1.501	0.021	-8.539	0.024	*22.117*
OX-5b	-1.529	0.021	-8.594	0.023	*22.060*
OX-5b	-1.476	0.02	-8.515	0.008	*22.142*
OX-6a	-4.557	0.021	-7.633	0.021	*23.051*
OX-6a	-4.39	0.012	-7.693	0.028	*22.989*
OX-6a	-4.316	0.012	-7.785	0.02	*22.894*
OX-6b	-0.743	0.011	-6.423	0.03	*24.298*
OX-6b	-0.72	0.016	-6.426	0.028	*24.295*
OX-6b	-0.777	0.018	-6.413	0.016	*24.309*
OX-7	0.097	0.011	-9.588	0.021	*21.036*
OX-7	0.077	0.02	-9.515	0.011	*21.111*
OX-7	-0.062	0.018	-9.552	0.032	*21.073*

*The interconversion equations from $\delta^{18}O$ VPDB to $\delta^{18}O$ VSMOW are as follows (Friedman and O' Neil, 1977):

$$\delta\,^{18}O\ \ VSMOW = (1.03091 \times \delta\,^{18}O\ \ VPDB) + 30.91 \qquad (7)$$